Phase Matching and Coherence of High-Order Harmonic Generation in Hollow Waveguides

by

Amy Louise Lytle

B.A., The College of Wooster, 2001

A thesis submitted to the

Faculty of the Graduate School of the

University of Colorado in partial fulfillment

of the requirements for the degree of

Doctor of Philosophy

Department of Physics

2008

This thesis entitled:
Phase Matching and Coherence of High-Order Harmonic Generation in Hollow Waveguides
written by Amy Louise Lytle
has been approved for the Department of Physics

Margaret Murnane

Prof. Henry Kapteyn

Date _____

The final copy of this thesis has been examined by the signatories, and we find that both the content and the form meet acceptable presentation standards of scholarly work in the above mentioned discipline.

Lytle, Amy Louise (Ph.D., Physics)

Phase Matching and Coherence of High-Order Harmonic Generation in Hollow Waveguides

Thesis directed by Prof. Margaret Murnane

Over the last twenty years, high-order harmonic generation has emerged as a scientifically useful, temporally and spatially coherent source of extreme ultraviolet light. Because of the nature of the generation process, the harmonics are emitted in a series of attosecond bursts, creating a spectroscopic and imaging tool with high temporal and spatial resolving power. The coherence and short time-duration, in combination with the accessibility of this table-top source, have made high harmonic generation a truly unique light source, opening possibilities for new science.

The current limitation to this source is its brightness, limited mainly through poor phase matching of the nonlinear conversion process. This thesis presents work performed toward better understanding of the physics and the engineering of high harmonic generation, specifically in a waveguide geometry. First is a survey of the relevant theory and review of previous work on high harmonic generation and phase matching techniques. Presented next are selected experimental results related to optimizing the harmonic photon yield in hollow waveguides, including a measurement of the photon yield at 45 eV, measurements of the density-dependent energy loss in the driving laser beam, and a study of the effects of modulation depth in the technique of quasi-phase matching using hollow waveguides with a modulated inner diameter.

Counterpropagating light is used for the first time as a tool for measuring the in-situ coherence length of the harmonic generation process. Through this measurement of the coherence length, several other quantities can be inferred. The ionization level at which different harmonic orders are generated can be determined, giving insight into the

temporal dynamics of high harmonic generation. Intensity variations caused by energy loss in the driving laser beam due to ionization or refraction, or by interference between coupled modes of the waveguide, are measured. The dynamic nature of the coherence length of high harmonic generation makes an in-situ measurement of this kind crucial for any implementation of quasi-phase matching.

Finally, all-optical quasi-phase matching of high harmonic generation is demonstrated by using trains of counterpropagating pulses for periodic correction of the phase mismatch. Enhancements of more than two orders of magnitude are demonstrated at high photon energies, where conventional phase matching techniques are currently not possible. All-optical quasi-phase matching is also shown to be selective in terms of enhanced bandwidth, and can even isolate one of the two electronic trajectories contributing to harmonic emission. These advances have the potential for improving the harmonic flux at high photon energies that cannot currently be phase matched, and for permitting manipulation of the temporal and spectral structure of the harmonic emission.

Dedication

For Etienne.

Acknowledgements

A body of work the magnitude of a PhD career cannot be completed alone. In the case of my own, there were many extraordinary people who supported and assisted me through the last several years. I may have been the common thread in the work presented here, but friends, family, and colleagues contributed in ways that are impossible to quantify. A partial list includes: Margaret Murnane and Henry Kapteyn, my tireless advisors, who shared their support and considerable expertise, helping me to learn and achieve more than I thought possible; The Kapteyn-Murnane research group members, many of whom contributed significantly to this work, and all of whom were good friends and colleagues: Dave Gaudiosi, Ra'anan Tobey, Luis Miaja-Avila, Mark Siemens, Xiaoshi Zhang, Daisy Raymondson, Richard Sandberg, Tenio Popmintchev, Mike Grisham, Paul Arpin, Nick Wagner, Ariel Paul, Arvinder Sandhu, Oren Cohen, and Sterling Backus; Barry Walker, for help with the modulated waveguide measurements; Don Jacobs, Shila Garg, and John Lindner, still my models for great scientists and educators; The JILA staff, particularly Rachael Tearle; The National Science Foundation, for a greatly appreciated fellowship; My family, for the love they express in so many ways; Most of all my appreciation goes to Etienne Gagnon, for more reasons than I can fit into a PhD thesis.

Contents

Chapter

Tables

Table

Figures

Figure

Chapter 1

Introduction

1.1 High-Order Harmonic Generation as a Source of Coherent EUV/ Soft X-Ray Light

The ability of the laser to produce intense and coherent light has precipitated a revolution in science and technology. From spectroscopy to data storage, from communications to laser cooling, the laser has infiltrated not only our laboratories, but our society. With the invention of the laser came the advent of nonlinear optics, and together they quickly expanded the range of frequencies over which it is possible to generate coherent light. The motivation to generate coherent light at short wavelengths and high photon energies has grown stronger. However, the production of coherent light at VUV, EUV, and soft x-ray frequencies becomes difficult for a number of reasons. These frequencies are strongly absorbed by any material, making the construction of optics challenging, and the choice of gain or nonlinear media is quite limited. In addition, the power requirement for obtaining laser action follows a λ^{-4} scaling with wavelength [2], placing high demands on pump sources. Lasers in the EUV, with wavelengths as short as 10 nm, have been demonstrated with useful pulse energies [3], but are limited in the available frequencies to a few electronic excitation transitions, and have yet to be developed into commercially available products. Alternative sources of EUV and soft x-ray light include synchrotron light sources [4] and free-electron laser (FEL) accelerator facilities [5]. However, these large scale facilities are quite expensive and have limited

accessibility to researchers.

High-order harmonic generation (HHG) is a nonlinear optical process for upconverting coherent light from visible frequencies up to EUV and soft x-ray frequencies. This technique for producing short wavelength light was made possible by the development of ultrafast, high intensity laser sources [6, 7] that can routinely produce visible light pulse with peak intensities of 10^{15} to 10^{18} W/cm^2. Sources based on HHG have a convergence of several attractive qualities in comparison with sources mentioned above. HHG is fully temporally and spatially coherent [8, 9] and it can be used to produce coherent radiation ranging from the UV up to photon energies > 1 keV [10]. It is an ultrafast pulse source, with pulse durations from femtoseconds to attoseconds [11–13], and it is accessible, since it is produced with a tabletop laser system. Demonstrated applications of HHG include studies surface dynamics [14], high-resolution imaging [15,16], molecular dynamics [17–19], as well as static molecular structure [20], and attosecond dynamics [21, 22].

As with any harmonic generation process, the main technical obstacle to a high conversion efficiency for HHG is the difference in the phase velocities between the fundamental and harmonic fields due to dispersion of the nonlinear material. Because of this phase mismatch, the phase of the fundamental field will shift by π rad relative to the harmonic field as it propagates. This means that harmonic light generated early in the nonlinear medium will be exactly out of phase with harmonic light generated a certain propagation distance later. This dephasing distance is called the coherence length. This destructive interference limits the total achievable coherent buildup of the harmonic field. Balancing of the major dispersion terms to minimize the phase mismatch of HHG has led to bright HHG sources up to ~ 100 eV, or $\lambda \approx 12$ nm. Photon yields here are on the order of 10^{11} $photons/sec$ [23–25], allowing studies of the kind listed above.

In high harmonic generation, the situation becomes complicated for generation

at high photon energies (200 eV and above). Because the laser generating the harmonic light also ionizes the medium, a large dispersion results from the free electrons. Once the fraction of ionization increases above about 5%, conventional phase matching techniques are no longer possible. Typical coherence lengths range from a few millimeters at lower photon energies to a few microns at the highest observed photon energies. New techniques for raising the conversion efficiency for HHG are crucial to extending this source to high photon energies.

The density of free electrons can also change rapidly, both in time and in space. In time, the ionization fraction can ramp up rapidly during the ultrafast pulse. In space, the intensity can vary strongly due to refraction of the plasma and other nonlinear effects. The dynamic nature of the phase mismatch is difficult to model accurately, and even more difficult to compensate accurately. Phase matching is transient at best under conditions where the phase mismatch changes rapidly. The absence of experimental techniques for measuring the local phase mismatch also limits further progress.

Quasi-phase matching (QPM) is an alternative method for compensating for the phase mismatch to improve conversion efficiency. In this technique, the phase of the driving laser is corrected at a periodicity equal to twice the coherence length, so that the destructive interference is eliminated. Several proposals [26–32] and demonstrations [33–36] of QPM of HHG have been published to date. However, many of these have technical limitations, or limited scaling to higher conversion efficiency. One of the reasons for this is that there has not been an easy, in-situ technique for measuring the dynamically changing coherence length of HHG.

In this thesis, I present new work using counterpropagating light for accurate measurements of the local coherence length. This information provides previously unknown information about the dynamics of HHG. Measurement of the coherence length is then used for a demonstration of efficient QPM using multiple counterpropagating pulses. This technique is found to be flexible, customizable to the measured conditions,

and scalable both in terms of the enhancement factor and the phase mismatch it may compensate.

1.2 Contents

The structure of this thesis is as follows: Chapter 2 contains a survey of the many different physical processes involved in HHG, including the physics of electron rescattering, and nonlinear optical effects that influence HHG. Coupling and propagation of light in hollow waveguides is reviewed, since this is the geometry used for the nonlinear interaction region. The mechanisms for phase matching and quasi-phase matching of HHG are reviewed, along with proposals and previous demonstrations. Finally, the effect of counterpropagating light on high harmonic generation is discussed, along with the basic process for all-optical QPM.

The general experimental setup for generation and detection of harmonic light is outlined in Chapter 3, and selected results are presented from exploratory work on generating bright HHG from hollow waveguides. One of the main advantages of using a hollow waveguide over a free-focus for HHG is its ability to maintain a high intensity over a longer propagation distance. In order to characterize this, the density-dependent energy loss of the driving laser beam is measured and simulated under a range of conditions. An estimate of the absolute photon yield at 45 eV is presented along with a short discussion of optimization of the yield. Finally, quasi-phase matching using hollow waveguides with a modulated inner diameter is characterized. The enhancement of HHG at high photon energies ($200-300$ eV) is reproduced, and the optimal modulation depth is investigated.

Chapter 4 includes experimental results related to the use of counterpropagating light both to probe and to quasi-phase match the process of HHG. Counterpropagating pulses are used to probe the coherence of HHG, and provide a previously inaccessible measurement of the local coherence length of the generation process. They are also used

to study the spatial and temporal dynamics of the harmonic generation process. Since the local phase mismatch is sensitive to the local intensity, measurement of the coherence length provides information about intensity fluctuations present in the waveguide. These variations are shown to be caused both by energy loss and the interference of propagating modes of the waveguide. A two-pulse probing technique overcomes difficulties discovered in the measurement of coherence with only one pulse. Counterpropagating pulses are also used to implement an all-optical quasi-phase matching technique. Enhancement is shown for emission from two different noble gases, helium and argon, for photon energies that cannot be conventionally phase matched for the driving laser wavelength used. Studies of the effect of this technique on the spectral and temporal structure of the harmonic emission are also presented.

The final chapter includes a summary of the major experimental results, and a discussion of possible avenues for future research on high harmonic generation using counterpropagating light.

Three appendices describe work done in areas indirectly related to HHG. The first is a demonstration and analysis of a cavity geometry change in a Ti:sapphire femtosecond laser that allows a variation of the repetition rate and pulse energy obtainable. The second contains specifications and an analysis of a grazing-incidence, dichroic beamsplitter, designed to transmit the HHG driving laser wavelength, 800 nm, and to reflect harmonic photon energies in the range $\sim$35-100 eV. The third appendix is an alignment procedure for a Ti:sapphire oscillator of the kind used in our research group. It is intended as an introduction to alignment and the characteristic behavior of these lasers for those unfamiliar with their operation.

Chapter 2

Background and Theory

2.1 Introduction

This chapter reviews the theoretical models and previous work relevant to the measurements described in Chapters 3 and 4. An understanding of high-order harmonic generation as an extreme nonlinear optical process, requires a description at both the atomic and macroscopic levels. First, the origin of the microscopic nonlinear polarization of the medium that leads to harmonic emission must be considered. Second, it is necessary to understand how the macroscopic polarization evolves with propagation through an extended medium. Other important considerations are effects due to nonlinear optical processes, inescapable at the intensities involved, including plasma defocusing and blue-shifting of harmonic fields. To understand the propagation effects, the major sources of dispersion in the present regime of HHG are described, and experimental background on previous efforts to phase match and quasi-phase match HHG are summarized. Harmonic generation is found to depend sensitively on the coupling into hollow waveguides and propagation of the intense laser beam that drives the process. A discussion of propagation in hollow waveguides provides some insight into these effects. Finally, the effects of counterpropagating light on HHG are described, particularly those relevant to the probing and quasi-phase matching techniques discussed in Chapter 4.

2.2 High-Order Harmonic Generation: Single-Atom Response

The discovery of the processes of above-threshold ionization [37] and high-order harmonic generation [38, 39] required a new description for the response of atoms to strong fields. In particular, experimental studies of HHG showed a spectrum of harmonic emission peaks at odd multiples of the driving frequency. The strength of the peaks decreased rapidly for the first few harmonic orders, then leveled out for several orders in a *plateau* region, then sharply decreased at specific cutoff photon energy. Empirical and numerical [40] studies agreed on the shape of the plateau and location of cutoff, but a cohesive physical picture was still lacking. A quantum and then semi-classical analytical theory was developed by Kulander et al. [41] and Corkum [42], which accurately describes the main observable characteristics of high-order harmonic generation. It is also an intuitive and useful description of the physical processes involved. This theory outlines three basic steps in the generation of high harmonic radiation:

(1) Tunneling ionization of an atom by an intense laser field.

(2) The electron, now free of the atom, is driven by the electrical force of the sinusoidal laser field.

(3) The electron may recombine with the ion to its ground state, the system emitting a photon with energy equal to the ionization potential of the atom and the kinetic energy of the electron at recombination.

This model was subsequently expanded into a semi-analytical, quantum mechanical model by Lewenstein et al. [43]. This model quite accurately describes characteristics of HHG seen experimentally, as well as providing a rigorous description of the picure of the semi-classical theory. In this theory, the emission of harmonic radiation from an oscillating dipole is given as a product of three probability amplitudes, corresponding to the three steps described above.

Step 1: Ionization

In a theoretical sense, high-order harmonic generation is fundamentally different from low-order harmonic generation because of the process of optical ionization. Once the electric field of the laser has a strength comparable to the Coulomb field of the atom ($\sim 10^{11}\ V/m$), the laser field is no longer a small perturbation to the polarization of the nonlinear material, and the atom can be ionized. While the induced polarization of low-order nonlinear processes can be developed using perturbation theory [44], this approximation breaks down with increasing field strength.

Depending on the strength of the electric field, there are three basic models for photoionization: multiphoton ionization, tunneling ionization, and above-barrier ionization [45]. A parameter defined by Keldysh [46] classifies which of these three mechanisms is dominant. The Keldysh parameter is defined as:

$$\gamma = \sqrt{\frac{I_p}{2U_p}}, \tag{2.1}$$

where I_p is the ionization potential of the atom and U_p is the ponderomotive energy. The ponderomotive energy is the time-average of the kinetic energy obtained by an electron in an oscillating electric field:

$$U_p = \frac{e^2 E_0^2}{4m\omega^2} = \frac{e^2 I}{2m\epsilon_0 c\omega^2}, \tag{2.2}$$

where e is the electron charge, E_0 is the amplitude of the laser field, m is the electron mass, ω is the frequency of the laser field, ϵ_0 is the permittivity of free space, and c is the speed of light. U_p is proportional to the laser intensity and the square of the laser wavelength: $U_p[eV] \approx 9.3\ 10^{-14}\ I_0[W/cm^2]\ \lambda^2[\mu m^2]$.

Multiphoton ionization is the dominant mechanism for laser intensities at which $\gamma \gg 1$. In this case, the ionization can be modeled as the absorption of enough photons by the atom for the electron to reach an energy level higher than the ionization potential. For $\gamma \leq 1/2$, the appropriate model becomes tunneling ionization. In this case, the laser

electric field distorts the Coulomb potential strongly enough to form a potential barrier through which part of the electron wavefunction may leak into the continuum (see Fig. 2.1). This process can occur when the laser frequency is small enough that the field is approximately constant during the tunneling process. Another, more intuitive way to express the Keldysh parameter is $\gamma = T_l/\tau_t$, where T_l is the period of the oscillating laser field, and τ_t is the tunneling time. Tunneling ionization can only occur when the laser period is shorter than the tunneling time. This is the regime in which HHG takes place. The intensity at which tunneling ionization becomes dominant, for a laser wavelength of 0.8 μm, in neutral argon gas ($I_p = 15.78\ eV$), is 5 10^{14} W/cm^2. In the third regime, above-barrier ionization, the intensity is strong enough that the Coulomb potential is suppressed below the ionization threshold, and the electron is essentially no longer bound.

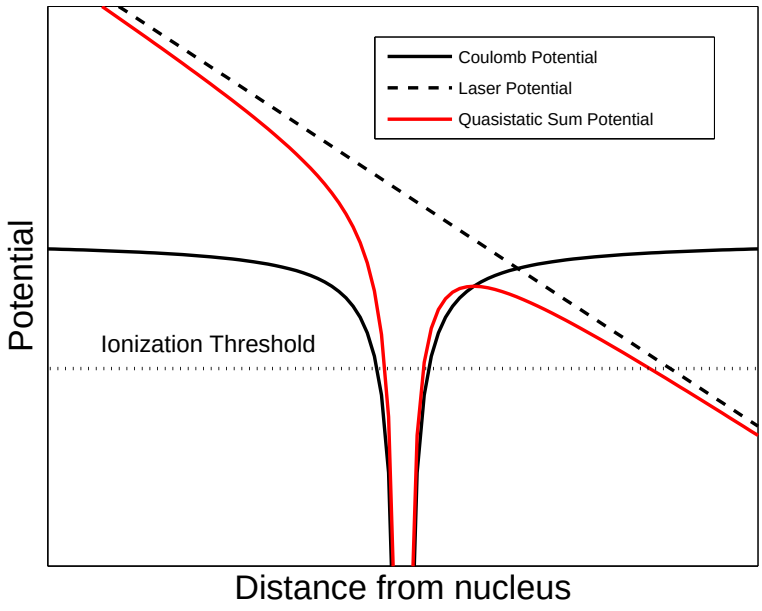

Figure 2.1: Atomic Coulomb potential when distorted by an intense laser field, in the tunneling regime.

The probability for tunneling photoionization of an atom is the first step of the three-step model outlined above. Ionization rates for the tunneling regime were developed by Ammosov, Delone, and Krainov [47], and later generalized to arbitrarily complex atoms and ions by including the effect of the Coulomb potential of the ion [48,49]. The rate of ionization from the ground state can be expressed as:

$$\omega(t) = \omega_p |C_{n^*}|^2 \left(\frac{4\omega_p}{\omega_t}\right)^{2n^*-1} \exp\left(-\frac{4\omega_p}{3\omega_t}\right), \tag{2.3}$$

where

$$\omega_p = I_p/\hbar$$
$$\omega_t = (eE(t)) / (2mI_p)^{1/2}$$
$$n^* = Z (I_H/I_p)^{1/2}$$
$$|C_{n^*}|^2 = 2^{2n^*} [n^*\Gamma(n^*+1)\Gamma(n^*)]^{-1}$$

For Eqn. 2.3 and the definitions following it, I_p is the ionization potential of the atom, $\hbar$ is Planck's constant divided by 2π, $E(t)$ is the electric field of the laser, m is the electron mass, Z is the ion charge after ionization, I_H is the ionization potential of atomic hydrogen, and $\Gamma(x)$ is the Gamma function.

The fraction of atoms ionized (or alternatively, the density of free electrons) is given by:

$$\eta(t) = \exp\left[-\int_{-\infty}^{t} \omega(t')dt'\right]. \tag{2.4}$$

This value is important particularly for estimates of phase mismatch, since, as will be shown in more detail below, the phase mismatch is sensitively dependent on the relative proportions of neutral atoms and free electrons. Figure 2.2 shows a sample calculation of the fraction of singly ionized argon as a function of time during a 25 fs pulse with peak intensity 5 10^{14} W/cm^2. The stepwise nature of the curve results from the fact that ionization occurs strongly at the peak of field amplitude, which occurs at every half cycle. It is important to note that the fraction of ionization is quite sensitive to

the intensity at the time of ionization. Figure 2.2 shows the variation in time within an ultrafast pulse. The ionization fraction will also depend on spatial variations in the intensity, making models of laser beam propagation important to modeling free electron density.

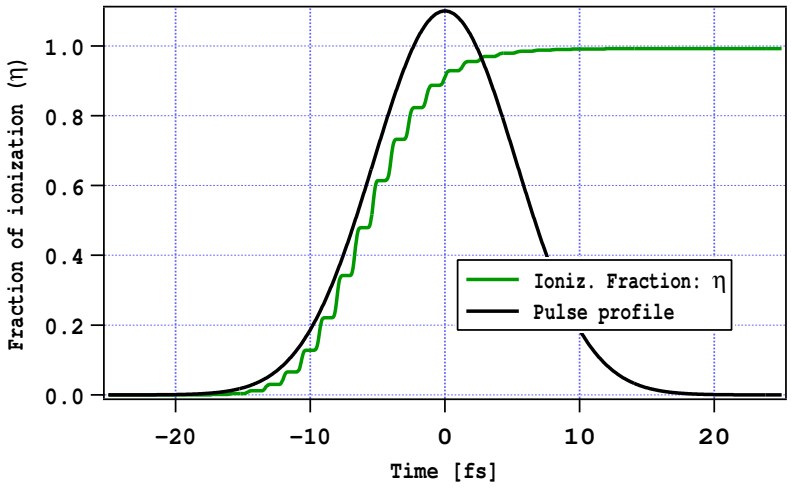

Figure 2.2: Fraction of ionization of argon as a function of time within a 25 fs pulse of peak intensity 5 10^{15} W/cm^2.

Steps 2 & 3: Rescattering and Recombination

Once the atom is ionized, the semi-classical three step model assumes the electron starts with zero velocity, then is driven purely by the oscillating electric field of the laser. The kinetics are calculated using the classical equations of motion. Under the influence of a sinusoidal laser field $E(t) = E_0 \cos(\omega t)$, the velocity of the electron is

$$v(t, t_0) = \frac{-eE_0}{mw} \left(\sin(\omega t) - \sin(\omega t_0)\right), \tag{2.5}$$

and its position is

$$x(t, t_0) = \frac{eE_0}{mw^2} \left(\cos(\omega t_0) - \cos(\omega t) - \sin(\omega t_0)\left(\omega t - \omega t_0\right)\right). \tag{2.6}$$

The electron's specific path in the continuum depends on the phase of the driving laser at the time of ionization, $\phi_0 = \omega t_0$. Figure 2.3 shows the path of the electron for

several different values of the laser phase at the time of ionization. In this plot, the phase value of 0 rad represents the peak of the laser field. For phase values $0 < \phi_0 < \pi/2$, a linearly polarized laser field will first carry the electron away from the ion, then, when the field changes direction, drive it back toward the vicinity of the ion, then recombine. A few of these trajectories are shown as the colored curves in Fig. 2.3. These paths recross the x axis with a nonzero slope, indicating that the electron encounters the ion with a nonzero kinetic energy. At $\phi_0 = 0$, the electron has exactly zero kinetic energy when it reaches the ion (black curve, labeled 0 rad). For phase values $\pi/2 \leq \phi_0 \leq \pi$, the electron will never reencounter the ion, but be driven away by the laser. A few of these trajectories are shown in black on Fig. 2.3. This cycle repeats itself for the next half-cycle of the electric field: phase values $\pi < \phi_0 \leq 2\pi$. Again, recombination is possible only for $\pi < \phi_0 < 3\pi/2$. Since the field reverse direction, the electrons are driven in the opposite direction.

Harmonic emission, then, is most likely to occur twice within a single optical cycle. The electron can reencounter the parent ion multiple times (see, e.g., the blue curve in Fig. 2.3), providing multiple opportunities for recombination at varying times within the optical cycle. However, the quantum nature of the electron makes recombination increasingly unlikely. The electron wavepacket spreads transversely with respect to the direction of its motion, at a rate of $\sim 1.5\ \mathring{A}/fs$ [42]. The probability of recombination increases for a larger parent ion or a shorter laser wavelength. Higher collision cross sections [50] of nonlinear gaseous media increase the probability of recombination, so that larger rare gas atoms have a higher nonlinear susceptibility. Only linear polarization of the laser field is used for HHG. Even a slight ellipticity will steer the electron away from the parent ion, reducing the chances of recombination.

The velocity of the electron at the time it reencounters the parent ion determines the energy imparted to the high harmonic photon. Figure 2.4 shows the kinetic energy of the electron at recollision as a function of the phase value at which it was ionized. Again,

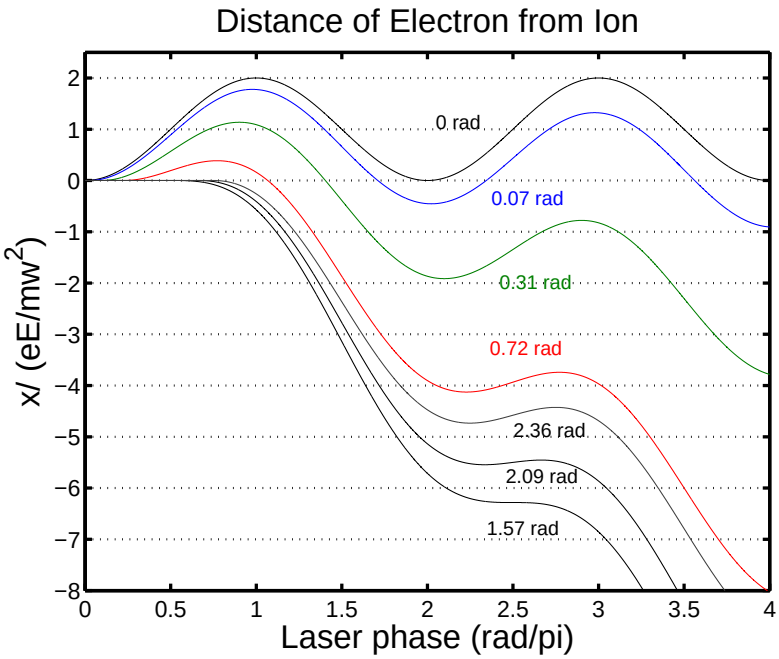

Figure 2.3: Possible paths for the electron during rescattering as a function of laser phase (time), and several selected values of the phase of the laser at ionization (or, equivalently, time at ionization). Intersection with the x-axis indicates a possible opportunity for recombination.

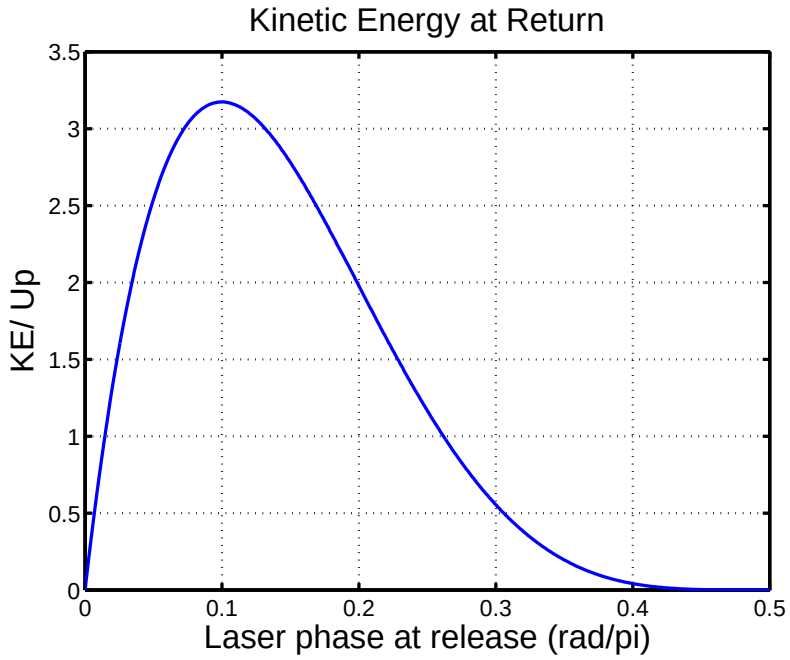

Figure 2.4: Kinetic energy at the return of the electron to the parent ion, as a function of phase of the laser at ionization.

phase values are plotted only for $0 < \phi_0 < \pi/2$, for which the electron path reencounters the ion. Kinetic energy values are given in terms of U_p, the ponderomotive energy. The graph shows that for each value of the return kinetic energy, there are two values of the phase at which the electron was originally released. At the peak of the curve is the highest return kinetic energy, $KE \approx 3.17U_p$, at $\phi_0 \approx 0.09\pi$. These features are further illustrated in a plot of the electron trajectories, Fig. 2.5. This plot shows trajectories for the singular path of the highest kinetic energy, as well as the two paths that return to the ion with $KE = 1.5U_p$. The middle green curve represents the trajectory that contributes to the highest photon energy that can be generated with a sinusoidal driver field. This is known as the "cutoff" photon energy. The red and blue curves represent what are called the "short" and "long" trajectories, respectively, for generating photon energies that are smaller than the cutoff. The short and long trajectories are most distinct at low harmonic orders and throughout the plateau region, and converge at the cutoff.

If the electron recombines with the ion into its ground state, the system will emit a photon with energy equal to the ionization potential of the atom plus the return kinetic energy of the electron. Using the largest possible return kinetic energy from Fig. 2.4, the cutoff photon energy is given by:

$$h\nu_{max} = I_p + 3.17U_p. \tag{2.7}$$

This equation describes the highest observable photon energy, assuming a perfectly sinusoidal field (a less than accurate assumption for ultrafast pulses $< 30\ fs$ [51]), and emission from the first encounter with the ion. The cutoff rule has, however, been well borne out as a general rule both by experiment and theory [40–43,52]. Since $U_p \propto I\lambda^2$, a higher cutoff may be obtained by increasing either the intensity or the wavelength. Each of these changes, however, reduces the brightness of harmonic emission, albeit in very different ways. A higher intensity increases the dephasing of the coherent buildup of the

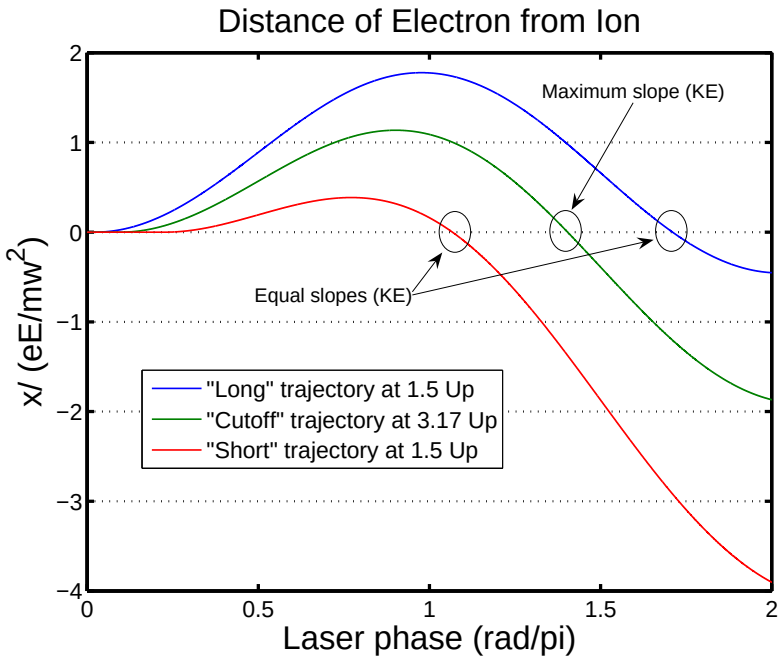

Figure 2.5: Possible paths for the electron during rescattering, indicating the origin of the "cutoff" photon energy, as well as the "long" and "short" trajectories contributing to a photon energy below cutoff.

harmonic field, which will be described in greater detail below. A larger wavelength, on the other hand, will cause the electron to spend a longer time in the continuum, reducing the probability of recombination due to the spread of the electron wavepacket.

Intensity-Dependent Phase

Since high-harmonic generation is a coherent process, the phase of the emitted harmonic light depends in part on the phase of the laser field. However, there is a second, significant component to the phase of the harmonic emission that depends on the intensity. The dipole phase, also called the intrinsic phase, is the phase accumulated by the electron wavefunction as it propagates in the continuum. The total phase of the harmonic field, the sum of these two components, is given by

$$\phi_q = q\omega t_r - \frac{1}{\hbar} S(t_0, t_r), \tag{2.8}$$

in which t_0 and t_r are the ionization and recombination times, respectively, q is the

harmonic order, ω is the angular frequency of the laser field, and $S(t_0, t_r)$ is the quasi-classical action [53], which can be approximated as:

$$S(t_0, t_r) = \int_{t_0}^{t_r} dt \left(\frac{p(t_0, t_r)^2}{2m} + I_p \right). \tag{2.9}$$

In Eqn. 2.9, $p(t_0, t_r)$ is the momentum of the electron at ionization, m is the mass of the electron, and I_p is the ionization potential of the atom. The two components of the phase described by Eqn. 2.8 correspond to: 1) the phase of the laser field at the time of recombination, t_r, and 2) the intrinsic phase.

A direct implication of Eqn. 2.8 is that each of the two trajectories that contributes to a given harmonic order q acquires a different phase, since each corresponds to a different time of recombination, t_r. Also, the dependence of the phase on the action means that the intrinsic phase is intensity dependent. Combining Eqns. 2.5 and 2.8 makes this intensity dependence explicit:

$$\phi_q = \frac{2U_p}{\hbar\omega} \int_{\phi_0}^{\phi_r} d\phi \left(\sin(\phi) - \sin(\phi_0)\right)^2 + \frac{I_p}{\hbar\omega}(\phi_r - \phi_0), \tag{2.10}$$

where $\phi_0 = \omega t_0$, $\phi_r = \omega t_r$, and $U_p \propto I$ (Eqn. 2.2). The dependence of the harmonic phase on the intensity is given by the derivative:

$$\frac{\partial \phi_q}{\partial I} = \frac{2K}{\hbar\omega} \frac{\partial U_p}{\partial I} = \frac{K e^2}{\hbar m \epsilon_0 c \omega^3}, \tag{2.11}$$

using the definition for U_p, Eqn. 2.2. K is the solution of the integral in Eqn. 2.10, a dimensionless constant whose value depends on the trajectory of the electron [54]. Figure 2.6 shows the dependence of K on ϕ_0, the phase at the time of ionization. The black vertical line at $\phi_0 = 0.09\pi$ *rad* indicates the phase at cutoff (cf. Fig. 2.4). Long trajectories originate with $\phi_0 < 0.09\pi$ *rad*, and short trajectories for $\phi_0 > 0.09\pi$ *rad*. In general, for a given kinetic energy contribution to the harmonic photon energy, the long trajectory has a much larger value of K than does the short trajectory. For example, for the plateau harmonic which is generated with a kinetic energy component of $1.5U_p$,

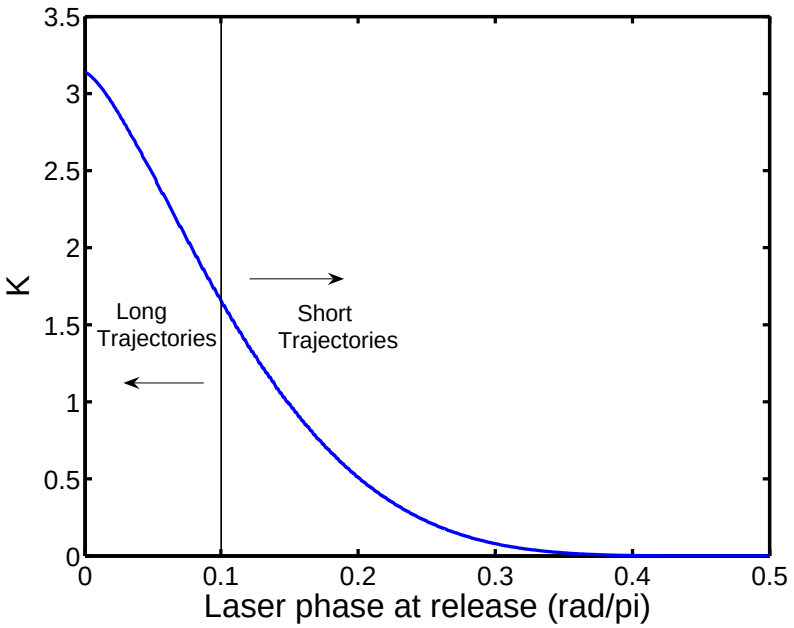

Figure 2.6: Values of K as a function of release phase.

$K_{long} = 2.89$, while $K_{short} = 0.323$. The phase of the long trajectories are thus much more sensitive to the intensity than are the short.

Figure 2.7 shows the intensity dependent phase for the short and long trajectories as a function of intensity for $q = 31$, using a full analytical model. The slopes of the the two curves are determined by the value of the dimensionless constant K. This plot illustrates the rapid accumulation of phase with increasing intensity of the long trajectory compared to the short.

The intrinsic phase can have a significant effect on the temporal and spectral structure of HHG. One of these effects occurs with a short driving laser pulse, in which the intensity changes significantly between half-cycle peaks. On the leading edge of the pulse, a changing intensity from peak to peak results in both a higher generated photon energy and intrinsic phase shift with time. This causes an inherent negative chirp in the harmonic emission, particularly for the photon energies near cutoff, where the emission

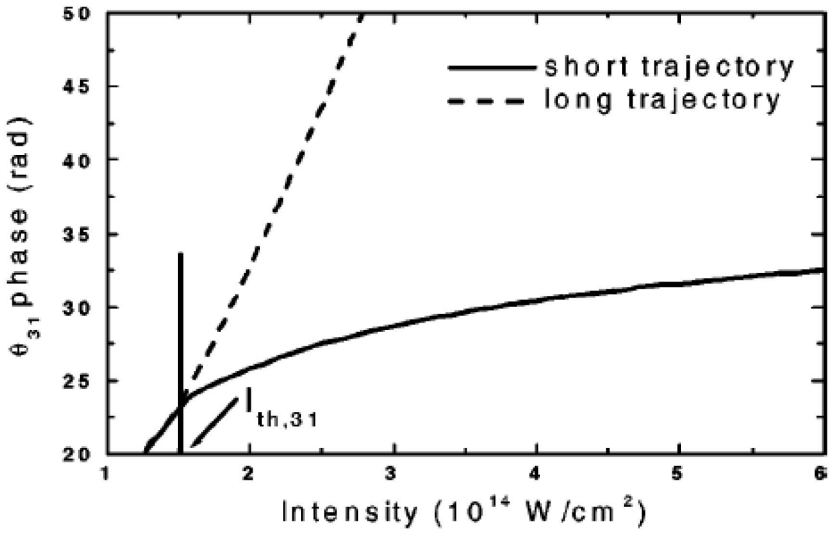

Figure 2.7: Harmonic phase of the 31^{st} harmonic generated in argon, as a function of the intensity. $I_{th,31}$ indicates the threshold intensity for generating the 31^{st} harmonic. The curves show a stronger dependence on intensity of the phase of the emission from the long trajectory. Reproduced from Ref. [55].

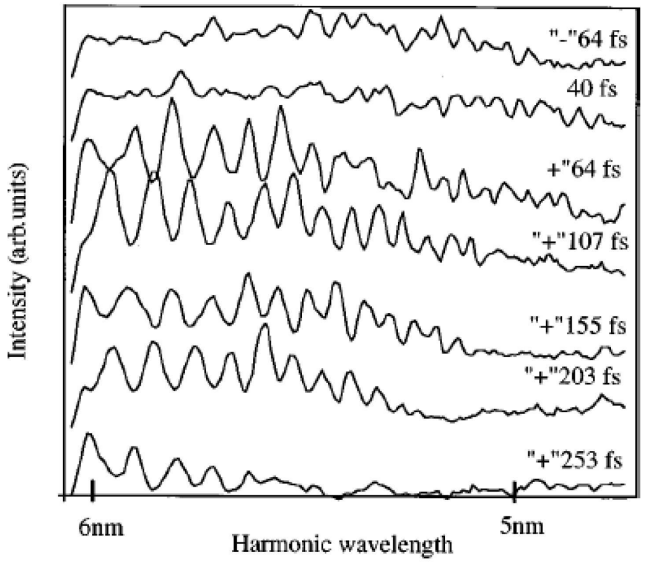

Figure 2.8: Harmonic spectra generated in argon with driving laser pulses of varying chirp. Reproduced from Ref. [56].

is limited to a few trajectories. The temporal structure of the HHG may be controlled by varying the chirp of the driving laser pulse, as shown in Ref. [56]. Figure 2.8 shows several harmonic spectra generated using driving laser pulses of varying chirp. The appearance of strong harmonic peaks indicates the role of intrinsic phase in the spectral structure of HHG.

2.3 Macroscopic Phase Effects

Equally important to the microscopic, or single-atom, effects on the properties of high-order harmonic generation are the macroscopic, or propagation effects. There are several physical processes which affect the spectral, spatial, and temporal properties of HHG, and below are descriptions of a few that are most relevant to the data presented in Chapters 3 and 4. Emitted harmonics are frequently blue-shifted in frequency under certain experimental conditions, either due to self-phase modulation caused by ionization, or non-adiabatic effects of the ultrafast laser pulse. The propagating laser beam is also greatly affected by the process of ionization through energy loss and a tendency to defocus in the presence of the generated plasma. Finally, the spatial profile and coherence properties of HHG are largely determined by propagation effects. One of the most significant processes affecting the conversion efficiency of HHG, dephasing between the fundamental and harmonic fields, will be addressed in the following section.

Self-Phase Modulation

Self-phase modulation (SPM) is a common occurrence whenever ultrafast pulses interact with matter. The ultrafast pulse induces a time-varying index of refraction in the material it propagates through, due to a nonlinear interaction, which in turn varies the instantaneous frequency of the laser pulse. For a pulse with a high and rapidly varying intensity, this frequency variation can significantly change the laser spectrum. Two main nonlinear processes vary the index of refraction in the case of the ultrafast pulses used to drive high harmonic generation.

The intensity-dependent index of refraction is a third order nonlinear process, also called the optical Kerr effect, which easily becomes significant at the intensities used for HHG. The nonlinear index is expressed as

$$n(t) = n_0 + n_2 I(t), \tag{2.12}$$

in which n_2 is referred to as the nonlinear index coefficient and $I(t)$ is the time evolution of the intensity of the ultrafast pulse. Since the index of refraction of the material depends on intensity, the index of the material rapidly changes in time as the pulse propagates through. The instantaneous phase of the laser pulse is given by

$$\phi(t) = \omega_0 t - \frac{2\pi}{\lambda_0} n(t) L, \tag{2.13}$$

where ω_0 and λ_0 are the center frequency and wavelength of the pulse, respectively, and L is the length propagated in the medium. This phase shift, which is time-dependent, causes a shift in the instantaneous frequency of the pulse:

$$\omega(t) = \frac{d\phi}{dt} = \omega_0 - \frac{2\pi L n_2}{\lambda_0} \frac{dI(t)}{dt}. \tag{2.14}$$

For a typical ultrafast pulse, the temporal shape is similar to a Gaussian or hyberbolic secant squared. On the rising edge of the pulse, $\frac{dI(t)}{dt} > 0$, causing a shift toward lower frequencies, while the falling edge ($\frac{dI(t)}{dt} < 0$) is shifted toward higher frequencies.

At modest intensities, HHG occurs only near the peak of the pulse, so that harmonic light is emitted symmetrically toward the rising and falling edges of the pulse. In this case, the frequency shift will be translated symmetrically to the spectrum of each harmonic peak. When the intensity is higher, however, harmonic generation can be limited to only the rising edge of the pulse. The main reason for this is that the gas medium can become almost completely ionized by the peak of the pulse (see, e.g., Fig. 2.2). In this case, the harmonic light should be red-shifted, since the frequencies of the laser pulse are also red-shifted. However, the ionization itself causes a time-varying

refractive index which tends to dominate the third-order effect, and causes a blue-shift of the harmonic peaks.

Ionization-Induced Blue-Shifting

Blue-shifting of the harmonic frequencies has been extensively studied through experimental observation [55–58] and modeling [55, 59, 60]. The rapid ionization of the gas medium is one of the main causes of this phenomenon, called ionization-induced blue-shifting. The time-dependent index of refraction of a plasma depends on the density, and is given by

$$n_p(t) = \sqrt{1 - \frac{\omega_p^2(t)}{\omega^2}} \approx 1 - \frac{\omega_p^2(t)}{2\omega^2}, \tag{2.15}$$

where ω is the angular frequency of the laser field,

$$\omega_p(t) = \sqrt{\frac{N_e(t)e^2}{\epsilon_0 m}} \tag{2.16}$$

is the plasma frequency, and $N_e(t)$ is the free electron density. (For a derivation of the plasma index, see Ref. [61] or [62].) The approximate value of Eqn. 2.15 holds for $\omega^2 \gg \omega_p^2$. As the free electron density, $N_e(t)$, increases with time during ionization by the ultrafast pulse, the plasma index decreases. Since the plasma dispersion is anomalous, a decreasing index results in a greater phase shift. At the same time, the number of neutral atoms is proportionately decreased, and so this normal dispersion contribution to the index is decreased. The time-dependent index due to the free electron plasma in terms of the fraction of ionization, $\eta(t)$, is

$$n_p(t) = 1 - \eta(t)\frac{N_{atm}Pe^2}{2\omega^2 P_{atm}\epsilon_0 m}, \tag{2.17}$$

since $N_e(t) = \eta(t)N_{atm}P/P_{atm}$, where N_{atm} is the number density at 1 atm, and P/P_{atm} is the fractional pressure with respect to atmospheric pressure. The instantaneous frequency shift of the laser field due to the increasing plasma is:

$$\omega(t) = \omega_0 - \frac{2\pi L}{\lambda_0}\frac{dn_p(t)}{dt} = \omega_0 + \frac{2\pi L}{\lambda_0}\frac{d\eta(t)}{dt}\left(\frac{N_{atm}Pe^2}{2\omega^2 P_{atm}\epsilon_0 m}\right). \tag{2.18}$$

Note in this case that the increasing free electron density causes a shift to *higher* frequencies *throughout* the duration of the pulse. Figure 2.2 shows that the ionization level increases throughout the pulse, since the plasma lifetime ($\sim ns$) is significantly longer than the typical ultrafast pulse ($\sim fs$). This causes an overall blue-shift of the laser frequencies that is proportional to the ionization rate. For low intensities, when the final ionization fraction is significantly smaller than 1, the strongest blue-shifting will occur, symmetrically, near the peak of the pulse where the ionization rate is high. On the other hand, when the gas is fully ionized by the peak of the pulse, for very intense pulses like the one shown in Fig. 2.2, the strongest blueshifting will occur on the rising edge of the pulse.

While ionization-induced blue-shifting can also directly shift the harmonic frequencies, the dominant effect is indirect, by shifting the fundamental laser frequency. The reason for this can be seen in Eqn. 2.18: the time-dependent frequency is proportional to λ, thus the indirect shift is a factor of q stronger.

Non-Adiabatic Blue-Shifting

The rapidly changing intensity of the ultrafast pulse contributes to a second significant blue-shifting process. However, in this case there is a direct shift in the harmonic frequencies. This blue-shifting results from the intensity-dependent phase of the harmonic light, and is referred to as non-adiabatic blue-shifting [55]. For this process, the degree of blue-shifting varies with the harmonic order and contributions from different trajectories. This contrasts with ionization induced blue-shifting, which affected the harmonics indirectly through a frequency shift of the laser field, and is independent of both harmonic order and trajectory contribution. In non-adiabatic blue-shifting, there is a significant difference in the degree of frequency shift with harmonic order, particularly for harmonic orders well below cutoff. For mid-plateau harmonics, there is a large difference in the intensity-dependent phase accumulated by the long and short trajectories that contribute to them. This difference decreases toward the cutoff, where the

phase variation between the long and short trajectories disappears.

Non-adiabatic blue-shifting can be described starting with Eqn. 2.8, for the phase of the harmonic emission. The time derivative of the phase is the instantaneous frequency:

$$\omega(t) = \frac{d\phi_q}{dt} = q\omega_0 - \frac{Ke^2}{\hbar m\epsilon_0 c\omega^3}\frac{dI(t)}{dt}, \tag{2.19}$$

using Eqn. 2.11 for the intensity dependence of the harmonic phase. Like self-phase modulation, and unlike ionization-induced blue-shifting, the frequency shifting will be symmetric about the peak of the pulse, especially for pulses of modest intensity. However, this effect is strongest for very intense pulses, when harmonics are generated on the rising edge of the pulse, where the intensity varies most rapidly.

This blue-shifting can be detected in the spectral content of the harmonic emission. Since the value of K is larger for long trajectories, the long trajectories will be blue-shifted more strongly than the short trajectories. This can lead to a splitting of the harmonic peaks within the plateau. Figure 2.9 shows the result of a calculation performed by Kan et al. [60] using the Lewenstein model for HHG. Figure 2.9a) shows the harmonic spectrum for a 150 fs pulse with a peak intensity of 10^{15} W/cm^2, displaying two main separated peaks corresponding to the long and short trajectories, in which the long trajectory appears at a higher frequency than the short. The temporal structure of the emission of the 55^{th} harmonic order is shown in Fig. 2.9b), clearly showing the emission in the rising edge of the pulse.

Figure 2.10 shows an harmonic spectrum generated in 5 torr argon, using a 27 fs pulse with a peak intensity of $\sim$ 5 10^{14} W/cm^2. The harmonics shown are within the plateau region; for the peak intensity used, the cutoff is around the 61^{st} order. A clear double peak structure is visible for each of the harmonic orders shown. The capability to distinguish emission from the different trajectories in the spectral data provides information about the temporal structure of the emission, and can be used

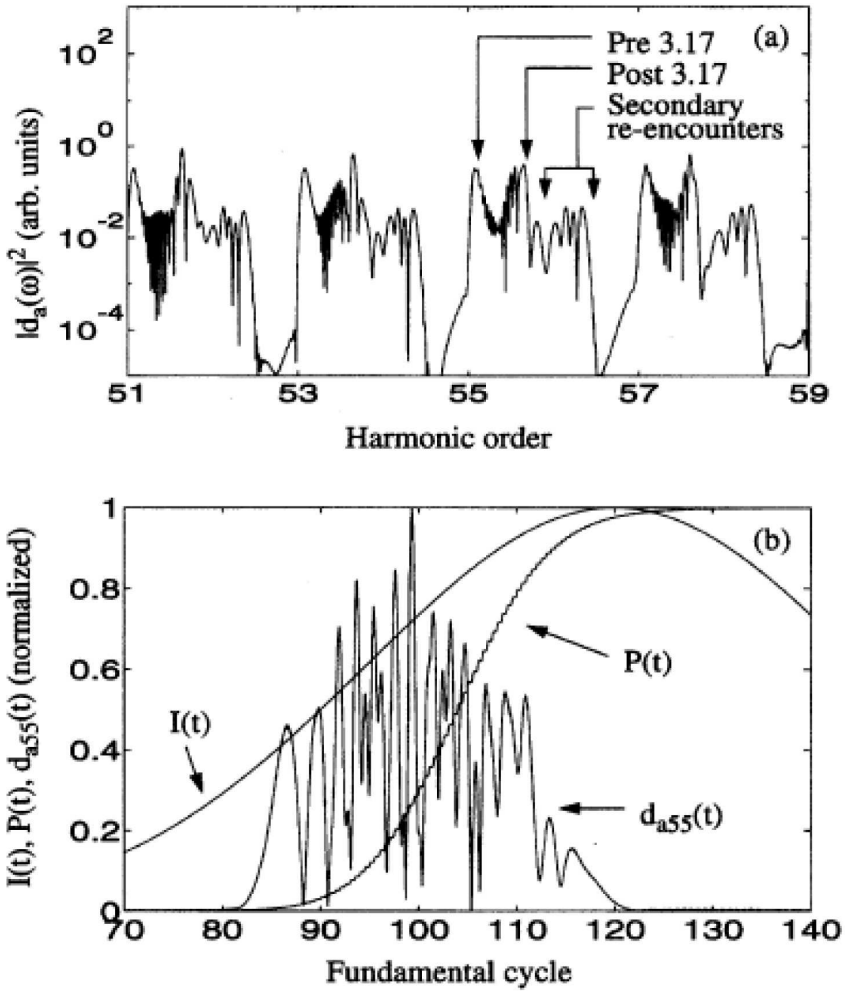

Figure 2.9: Calculated spectral (a) and temporal (b) structure of the 55^{th} harmonic order generated by a 150 fs pulse with a peak intensity of 10^{15} W/cm^2. Different electron trajectories appear with different frequencies, due to the intensity-dependent phase of harmonic emission. Reproduced from Ref. [60].

as an indicator for the use of counterpropagating pulses to manipulate HHG, discussed further in Chapter 4.

The properties of HHG are not only affected strongly by the temporally varying intensity of the ultrafast laser pulse, but they are also affected by the spatially varying intensity of the laser beam. Two of the spatial effects are ionization-induced defocusing of the laser beam, and a different divergence in the harmonic emission from each of the

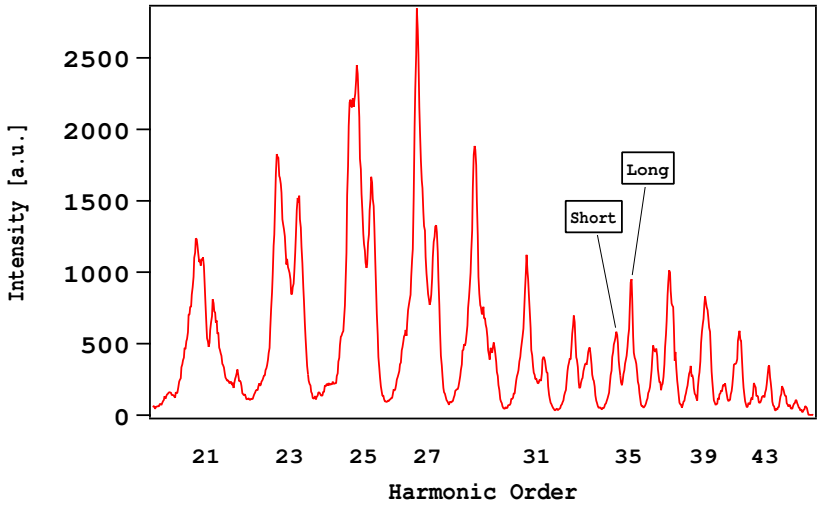

Figure 2.10: Harmonic spectra generated in 5 torr argon, with a 27 fs pulse with a peak intensity of $\sim 5\ 10^{14} W/cm^2$, showing peak splitting due to non-adiabatic blue-shifting. The two peaks correspond to emission from the long and short electron trajectories.

two main trajectories which contribute to harmonic emission.

Ionization-Induced Defocusing

Ionization-induced defocusing is a mechanism that can change the propagation of the intense laser beam used to generate high harmonics [63,64]. Because of the refraction of the free electrons that are generated during ionization, the beam can diverge more quickly and lose the high intensity needed for HHG. In a free-focusing geometry, the laser beam is loosely focused through the gas medium. For a Gaussian laser mode, the intensity will be highest at the axis of propagation and fall off radially. The ionization rate is directly related to the intensity, meaning that the free electron density will be highest at the central axis of the propagating beam, and will fall off radially. From Eqns. 2.15 and 2.16, it can be seen that the plasma index is directly proportional to the free electron density. A significant radial change in the index will produce a lensing effect. However, since the dispersion of a plasma is anomalous, the high free electron density at the center will have a comparatively low index that increases radially outward, creating

a diverging lens. The strength of this effect can be quantified by what is called the defocusing length [63], given by

$$l_D = \frac{\lambda}{2}\frac{N_{cr}}{N_e}, \tag{2.20}$$

where $N_{cr} = \epsilon_0 m\omega^2/e^2$ is the critical free electron density, at which $\omega = \omega_p$. The defocusing length, l_D, is the propagation length in the presence of the plasma at which the divergence of the beam doubles. This effect becomes more prominent at higher intensities, as well as higher gas pressures, both of which increase the free electron density. This effect is counteracted by the use of hollow waveguides, which can partially refocus the light to maintain the intensity over a longer propagation distance.

Trajectory-Dependent Divergence

The second effect involving spatial phase variation is a different divergence between the long and short trajectories. For a Gaussian radial distribution of the intensity, there will be a corresponding radial difference in the accumulation of the intensity dependent phase (Eqn. 2.10). The long trajectories are more more sensitive to the intensity, and so the phase fronts for contributions from the long trajectories will be more strongly curved. Figure 2.11 shows the different phase fronts for the long, denoted as "τ_2 contribution," and short, denoted as "τ_1 contribution," trajectories. With a strongly curved phase front, the contribution from the long trajectories will be much more divergent, which has been confirmed both by calculation [65] and experiment [8].

These phase differences between emission from the two trajectories ultimately determine the coherence of the HHG beam. Studies of the temporal [8, 65] and spatial [9, 66–68] coherence of HHG sources show that interference between emission from the two trajectories tends to degrade both the temporal and spatial coherence of the emission. Coherence tends to improve when the conversion efficiency of one of the two trajectories is selectively enhanced through phase matching of the nonlinear conversion process. For free-focusing geometries, this is accomplished by placing the gas inter-

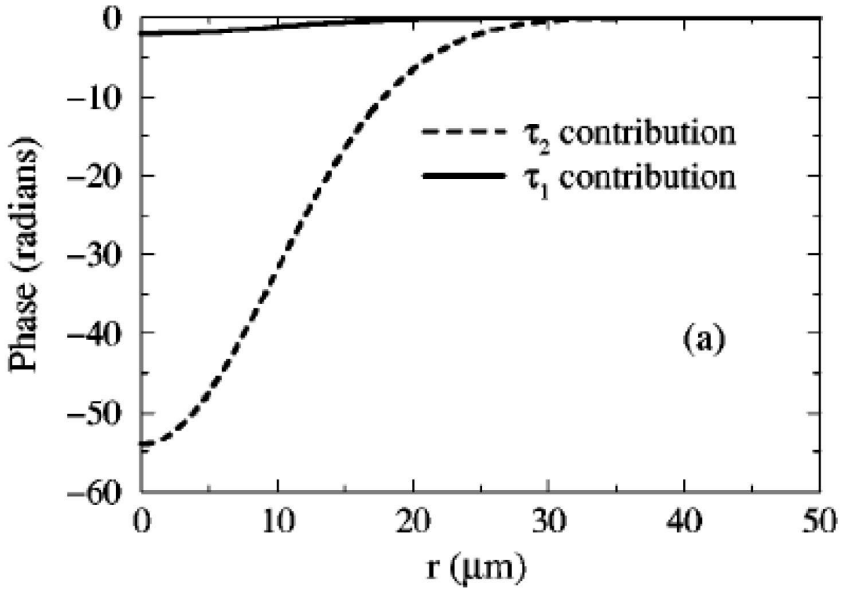

Figure 2.11: Phase fronts for the different trajectories that contribute to plateau harmonic orders. The stronger dependence of the harmonic phase on intensity leads to a greater curvature for the long (τ_2, dashed curve) compared to the short (τ_1, solid curve) trajectories. Reproduced from Ref. [65].

action region after the focus of the laser beam to avoid the Guoy phase shift at the focus [65, 67]. For HHG in a waveguide geometry, dispersion from the waveguide is independent of propagation distance and importantly, pressure, so that tuning of the pressure creates phase matching conditions for a single trajectory. Finally, all-optical quasi-phase matching with counterpropagating light in a hollow waveguide also can selectively enhance a single trajectory [69].

2.4 Phase Matching

The most significant macroscopic effect on the conversion efficiency and brightness of high harmonic generation is the phase mismatch between propagation of the fundamental and harmonic frequencies. Phase mismatch describes the degree to which dispersion causes the fundamental and harmonic frequencies to propagate at different

phase velocities through the nonlinear medium. Without compensation for this phase mismatch, the propagation length over which the harmonic field may sum coherently is limited, and so the total brightness of the harmonic source is likewise limited. Essentially, if the fundamental field propagates at a different phase velocity than the aggregate harmonic field, after a certain propagation distance the fundamental field will be exactly out of phase with the co-propagating harmonic field. At this point, subsequently generated harmonic light will begin to destructively interfere. The phase mismatch is expressed as the difference between the propagation vectors of the fundamental and q^{th} harmonic fields:

$$\Delta k = qk_0 - k_q, \tag{2.21}$$

in which k_0 is the propagation vector of the fundamental and k_q is that of the q^{th} harmonic order. A simple description of the harmonic field at the end of a nonlinear medium of length L is:

$$E_{HHG}(L) = \int_0^L E^0_{HHG}(z) \exp\left(i\Delta k z\right) dz, \tag{2.22}$$

in which $E^0_{HHG}(z)$ is the microscopic amplitude of the generated harmonic field as a function of propagation distance, z. Classical derivations of the nonlinear response adapted for high harmonic generation can be found in [54, 70]. The harmonic field will be maximal when $\Delta k = 0$, otherwise the strength of the field will oscillate sinusoidally with propagation distance. The periodicity of this oscillation is twice a characteristic length known as the coherence length:

$$L_c = \frac{\pi}{\Delta k}. \tag{2.23}$$

L_c describes the propagation distance between two locations of harmonic emission that are exactly out of phase. In other words, at the end of the coherence length, there is a π phase slip between the fundamental field and the harmonic field that was generated at the beginning of the coherence length. The intensity of the harmonic light detected

at the end of nonlinear medium of length L depends sensitively on the phase mismatch:

$$I_q = I_q^{max} \frac{\sin^2(\Delta kL/2)}{(\Delta kL/2)^2}, \tag{2.24}$$

which is plotted in Fig. 2.12, showing the sharp decrease in the obtainable harmonic intensity with increasing phase mismatch.

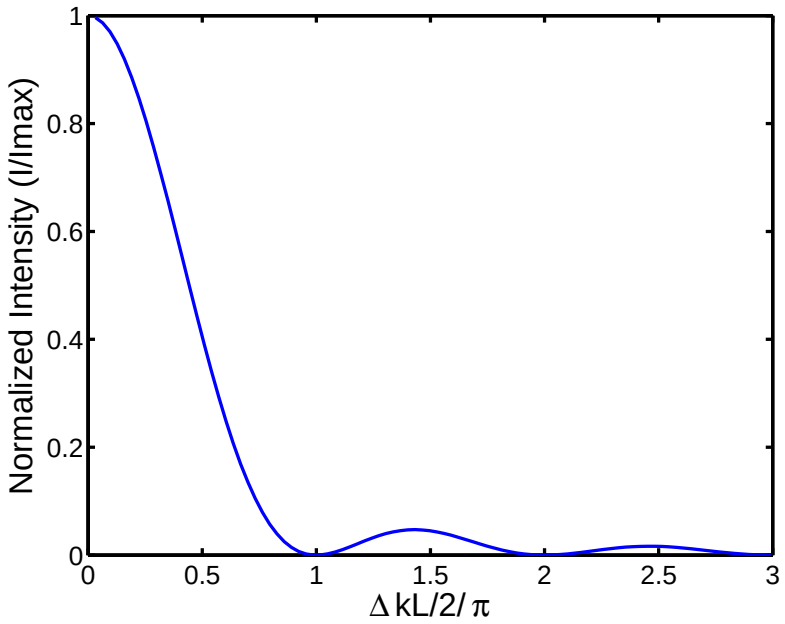

Figure 2.12: Harmonic intensity as a function of the phase mismatch.

When the phase mismatch is zero, the fundamental and harmonic fields are in phase throughout the medium, and the harmonic field grows linearly with distance. The harmonic intensity, then, grows quadratically with distance. Figure 2.13 illustrates the growth of harmonic intensity in two cases: for phase matching, and for a non-zero phase mismatch. Note than even after a single coherence length, the non-phase matched intensity is only 40% of the phase matched intensity.

In general, material dispersion of the nonlinear medium precludes phase matching, since different frequencies propagate with different phase velocities. In low-order nonlinear optical harmonic generation, such as second harmonic generation (SHG), phase

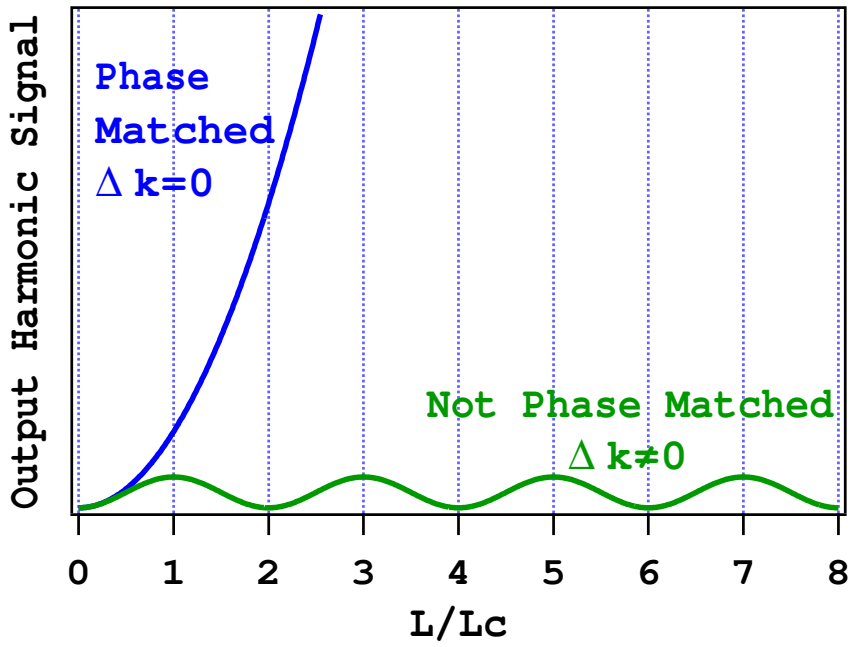

Figure 2.13: Harmonic intensity as a function of propagation distance, in the case of phase matching and a non-zero phase mismatch.

matching is most often achieved through the use of a birefringent crystal. The angles of the polarizations of the fundamental and harmonic fields with respect to the optic axis are tuned carefully so that the two fields propagate with the same phase velocity. Unfortunately this technique cannot be transferred to HHG. The nonlinear medium for HHG is most often a dilute, isotropic noble gas, for a couple of reasons. First, the high ionization potential of the noble gas atoms allows generation of higher photon energies (Eqn. 2.7), since the atoms can persist to a high instantaneous laser intensity before ionization. Second, high order harmonics are at frequencies which are strongly absorbed by any material, making a low pressure gas necessary to prevent excessive reabsorption of the harmonic photons.

Minimization of the phase mismatch in HHG has been studied extensively in the pursuit of maximizing the conversion efficiency [23, 71–76]. Two often-used tech-

niques for minimizing phase mismatch involve a balance of the main dispersion terms in HHG, in particular taking advantage of phase mismatch terms originating from the laser propagation geometry. In initial studies by L'Huillier and coworkers [71–73], high-order harmonics were generated by placing a gas jet at or near the focus of the laser beam. These studies were restricted to very low pressures and low intensities, and the dispersion from the neutral gas and free electrons were neglected. Instead, transient phase matching was achieved through a balance of the geometrical Guoy phase shift across the focus and the intrinsic phase shift through the variation of the intensity at the focus. Hollow waveguides were subsequently used for HHG by Murnane and Kapteyn [23, 74]. Guiding of the laser light extends the region of high intensity and may partially counteract the ionization-induced defocusing, while providing a new mechanism for minimizing the phase mismatch. In this case, the range of phase matching was extended to higher pressures, as the contributions from the neutral gas and free electron dispersion were taken into account. In fact, the hollow waveguide provides a mechanism for true phase matching over a long interaction distance by removing the transient nature of the Guoy phase shift and instead, providing a "plane wave" propagation geometry. Below are discussed three of the main contributions the phase mismatch: neutral gas and plasma dispersion, and geometrical corrections to the propagation vector.

Neutral gas dispersion

For the noble gas atoms used as the nonlinear medium for HHG, the resonance frequency is most often present somewhere between the fundamental and harmonic frequencies. Thus the index for the fundamental frequency is positive and for the harmonic frequency is negative. The phase mismatch contribution due to material dispersion, for harmonic order q, is simply

$$\Delta k = \frac{2\pi q}{\lambda_0}(n(\lambda_0/q) - n(\lambda_0)). \tag{2.25}$$

The index of refraction of noble gases, being very close to unity, are often reported

in the form $\delta(\lambda) = n(\lambda) - 1$, at STP (1 atm and 298 K) [77, 78], using the Sellmeier equation to express frequency dependence. The index scales linearly with pressure, so the index can be scaled by P/P_{atm}, or the ratio of the gas pressure relative to atmospheric pressure. For the fundamental wavelength of $\lambda_0 = 0.8\ \mu m$, $\delta(\lambda_0) \sim 10^{-5}$, and for harmonics $q > 21$, $\delta(\lambda_0/q) \sim -10^{-4}$ to -10^{-6}. Because of ionization, the density of neutral atoms is also scaled by the fraction of ionization, η, giving a phase mismatch between the fundamental and harmonic fields of:

$$\Delta k_N = \frac{2\pi q}{\lambda_0}\frac{P}{P_{atm}}\delta_n(1-\eta), \tag{2.26}$$

in which $\delta_n = \delta(\lambda_0/q) - \delta(\lambda_0)$ is the difference in the index of refraction between the fundamental and harmonic wavelengths. The dispersion of the resultant ions are often neglected for a couple of reasons: first, the resonance frequency is higher than that of neutral atoms, and second, by the time there is a significant population of ions, when $\eta > 0.1$, the free electron contribution to the phase mismatch is much greater than any other term.

Plasma dispersion

For the dispersion of the plasma, Eqn. 2.25 also applies, using Eqn. 2.17 for the plasma index. The electron number density, N_e, can be rewritten as $\eta N_{atm} P/P_{atm}$, in which N_{atm} is the atomic number density at STP. A substitution can also be made for the classical electron radius, $r_e = \frac{1}{4\pi\epsilon_0}\frac{e^2}{mc^2}$. Substituting and simplifying Eqn. 2.25 gives

$$\Delta k_{Pl} = \eta N_{atm} r_e \lambda_0 \frac{P}{P_{atm}}\frac{q^2-1}{q}. \tag{2.27}$$

Since $(q^2-1)/q \approx q$ when $q \gg 1$, this factor is often approximated for high orders.

Geometrical phase mismatch

Propagation of the driving laser mode also contributes to the phase mismatch through effects on the propagation vector. Two geometrical situations are common in HHG: a free Gaussian focus, and guiding through a hollow dielectric waveguide. A free

focus through a gas jet or a gas cell is commonly used in HHG experiments, and suffers from a phase shift across the focal region of π radians, called the Guoy phase shift. This phase shift is in the form of the arctangent near the focus:

$$\phi_{Guoy} = \arctan(z/b), \tag{2.28}$$

where $b = \omega w_o^2/2c$ is the Rayleigh range and w_0 is the $1/e^2$ intensity beam radius of the fundamental beam. The Guoy term for the harmonic light is smaller than that for the fundamental by a factor of $\approx \frac{1}{q^2}\frac{w_o(\lambda_0)^2}{w_o(\lambda_0/q)^2}$, and is therefore neglected for high harmonic orders. Thus the phase mismatch resulting from the Guoy phase is that from the effect on the fundamental field:

$$\Delta k_G = \frac{q\lambda_0}{\pi w_o^2}. \tag{2.29}$$

This large phase shift is often avoided by placing the interaction medium either before or after the focus.

The propagation of guided modes within a hollow waveguide will be discussed in more detail in Section 1.7. The correction to the propagation vector by guiding is constant through the interaction distance. Since high harmonic generation typically occurs only close to the central axis of the waveguide, where the intensity is highest, the harmonic light does not encounter the walls of the waveguide. The phase mismatch is therefore also given only in terms of the effect on the fundamental beam:

$$\Delta k_W = \frac{q u_{nm}^2 \lambda_0}{4\pi a^2}, \tag{2.30}$$

where a is the inner radius of the waveguide, and u_{nm} is the m^{th} root of the $(n-1)^{th}$ Bessel function of the first kind, specifying the coupled mode. Given a linearly polarized fundamental beam, n = 1 for the most strongly excited modes.

Although far from rigorous, these formulae are useful in practice for estimation of the phase mismatch and coherence length. However, several parameters are neglected, including the intensity-dependent phase of the harmonic field, which has been shown

to significantly affect the phase mismatch (e.g. see the results of Chapter 4 as well as Refs. [53, 73]). In addition, it is worth noting that although the phase mismatch can be expressed relatively simply in terms of the experimental parameters involved, these parameters themselves are often far from constant. For example, two of the terms are dependent on the ionization fraction, η, which can change drastically in time as well as both the propagation and radial directions. The phase mismatch is thus a dynamically changing quantity, and the phase matching techniques described below often can only correct for the phase mismatch within a limited temporal or spatial window. In the case of a free focus geometry in particular, the geometrical Guoy phase shift, as well as the gas density in a typical gas jet, also change with propagation and radial dimensions, allowing minimization of the phase mismatch over a limited volume.

Balancing Phase Mismatch: Free Focus and Hollow Waveguide

Phase matching of HHG can be achieved by balancing the various dispersion terms for a zero net phase mismatch. In the case of free focusing, the total phase mismatch is given by :

$$\Delta k = \Delta k_N + \Delta k_{Pl} + \Delta k_G = -\frac{2\pi q}{\lambda_0}\frac{P}{P_{atm}}\delta_n(1-\eta) + q\eta N_{atm} r_e \lambda_0 \frac{P}{P_{atm}} - \frac{q\lambda_0}{\pi w_o^2} \quad (2.31)$$

Recall that the geometrical term is valid only near the focus. Note that the neutral atoms and the geometrical phase mismatch are negative terms, while the free electron term is positive. These terms may be balanced by adjusting either the level of ionization through the peak intensity, or the gas pressure. In practice, this technique is only applicable for very low levels of ionization, at most a few percent (as will be shown below). At the intensities used in this situation, the variation of the intensity dependent phase of the harmonic emission with propagation is stronger than the dispersion of the free electrons. Thus the brightest emission from a free focus geometry is often achieved through balancing the Guoy phase and the intensity dependent phase.

The effect of the intensity dependent phase was investigated by L'Huillier and

coworkers [71, 73]. In particular, they showed that observed improvement in conversion efficiency as well as changes in the harmonic beam's divergence, through adjusting the location of the gas jet relative to the focus of the driving laser beam, can be explained through the effect of the intensity dependent phase. Figure 2.14 shows the on-axis dependence of the harmonic phase as a function of propagation distance relative to the focus. The long-dashed line shows the Guoy phase shift of the fundamental laser beam, the short-dashed line shows the calculated dipole phase, which varies with the on-axis intensity through the focus, and the solid line is the sum of the two. The phase mismatch will be minimal where the variation of the phase with propagation is minimal, i.e., at $\sim 3\ mm$ in the figure. Note that neither of these effects are dependent on the gas density.

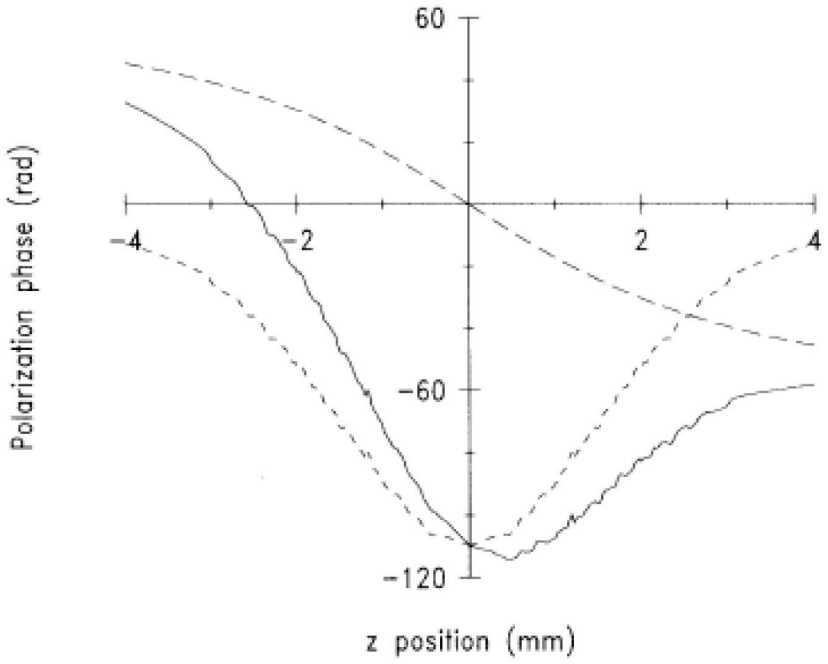

Figure 2.14: Dipole phase as a function of propagation distance. The long-dashed line shows the phase evolution of the fundamental through the focus due to the Guoy phase shift. The short-dashed line shows the evolution of the harmonic phase due to the intensity-dependent phase. The solid curve is the sum of the two contributions. Reproduced from Ref. [73].

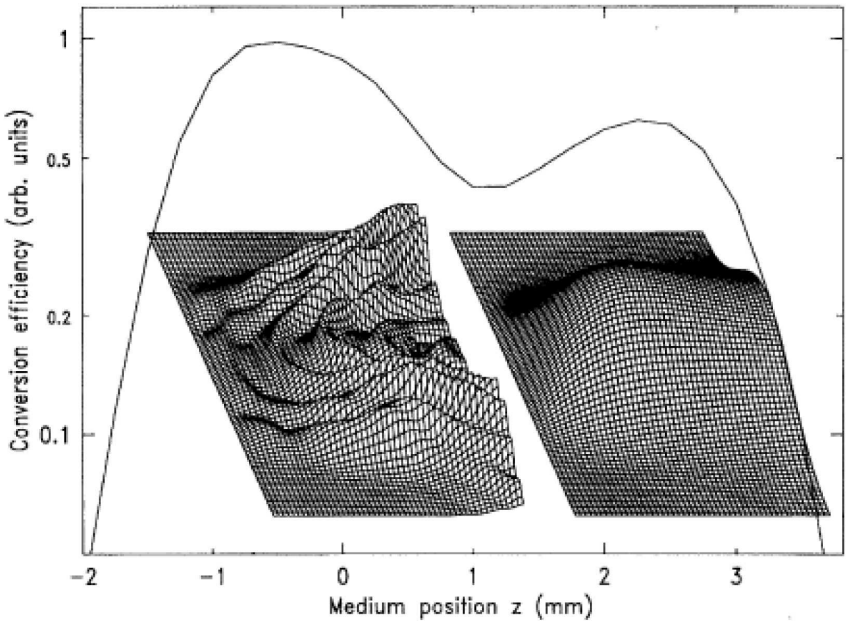

Figure 2.15: Conversion efficiency of HHG for the 45^{th} harmonic order as a function of the distance of the focus from the gas jet (z). The 3D plots illustrate the harmonic field at $z = -1$ and $z = 3mm$, as a function of the propagation distance and the transverse direction (azimuthal symmetry is assumed). Reproduced from Ref. [73].

A calculation of the conversion efficiency as a function of the distance, denoted by z, between the focus and a gas jet of width 0.8 mm FWHM is shown in Fig. 2.15. There are two local maxima in the conversion efficiency, one of which is in fact located near $z = 3$ mm, with another at $z = -1$ mm. Inset in the figure are 3D plots of the harmonic buildup at each of these two maxima as a function of both the propagation distance and the dimension perpendicular to the propagation axis. These insets reveal one of the realities of phase matching techniques in HHG, especially in the case of a free focus: its transient nature. The maximum in conversion efficiency at $z = 3$ mm occurs on-axis, as Fig. 2.14 predicts. The second maximum, however, at $z = -1$ mm, results from *off-axis* phase matching. This strong, off-axis emission results in an annular beam. In either case, the minimization of phase mismatch occurs only over a limited region, both in the propagation and radial directions. Predictions for the far-field harmonic

beam proflies have been verified closely through experiment [73].

In any case, maximization of the conversion efficiency of HHG using a free focusing geometry consists of making the coherence length of the process only at least as long as the width of the interaction region. For a free focus geometry, this width is limited, either due to the width of the gas jet used, the Rayleigh length, or the defocusing length of the driving laser beam.

In the case of hollow waveguides, the total phase mismatch caused by the three terms described above: neutral atoms, free electron plasma, and the guiding in the hollow waveguide, is given by the sum of these terms:

$$\Delta k = \Delta k_N + \Delta k_{Pl} + \Delta k_W = -\frac{2\pi q}{\lambda_0}\frac{P}{P_{atm}}\delta_n(1-\eta) + q\eta N_{atm} r_e \lambda_0 \frac{P}{P_{atm}} + \frac{q u_{nm}^2 \lambda_0}{4\pi a^2}, \quad (2.32)$$

For a hollow waveguide, the phase correction of the waveguide is the same sign as the free electron dispersion, in contrast with the Guoy phase.

There are three main advantages to using hollow waveguides over a free focus: the geometrical phase correction term is constant with propagation distance, the intensity can be maintained at a high level over a long propagation distance, and the gas may be contained conveniently at a well-defined pressure. The fact that two of the terms of Eqn. 2.32, for the neutral atoms and free electrons, depend on the pressure of the gas, while the waveguide term does not, indicates the experimental mechanism for phase matching. Pressured-tuned waveguide phase matching of HHG was reported in Rundquist et al., [23] and Durfee et al. [74]. These were the first publications to account for the dispersion of the neutral atoms and free electrons, both of which become significant at even low pressure and low ionization fraction. Also, this is the first demonstration of true phase matching of HHG, since the geometrical phase shift is constant with propagation distance. Phase matching could be achieved over a longer propagation distance due to the "plane wave" nature of the propagation geometry, in contrast with the transient phase matching of Figs. 2.14 and 2.15. Figure 2.16 shows the pressure tuning curves

for four different gases along with the predicted behavior. As the pressure is increased, there is a local maximum in the HHG signal when the phase mismatch is minimized.

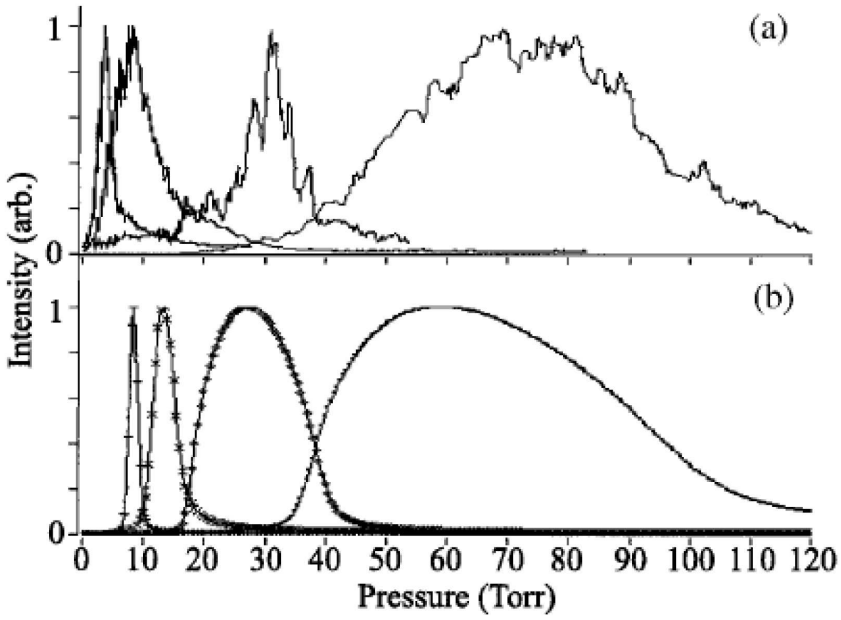

Figure 2.16: a) Measured and b) calculated pressure dependence of the harmonic yield for several gases. In order of increasing optimum pressure, the curves correspond to xenon, krypton, argon, and hydrogen. Reproduced from Ref. [74].

The dependence of the harmonic signal on pressure when phase matched is a $sinc^2$, since the phase mismatch is proportional to the pressure (Eqn. 2.24 and Fig. 2.12). However, the measured pressure-tuning curves are broadened in comparison with the prediction of a $sinc^2$ profile [70]. This is due to absorption of the gas, as well as the broadening effect of the rapidly changing phase mismatch.

Limits to Phase Matching

There are two major limitations to pressure-tuned phase matching: ionization and absorption. The above technique of pressure tuned phase matching works by balancing the contributions to the phase mismatch. The dispersion of the neutral atoms present cancels that from the free electrons and the waveguide. However, at a critical value

of the ionization fraction, η_{cr}, the dispersion from the remaining neutral atoms is not enough to balance the dispersion from the free electrons. This value may be estimated by equating Eqns. 2.26 and 2.27, and solving for the ionization fraction, η:

$$\eta_{cr} = \left[1 + \frac{\lambda_0^2 r_e N_{atm}}{2\pi\delta_n}\left(1 - \frac{1}{q^2}\right)\right]^{-1} \tag{2.33}$$

Since both phase mismatch terms are proportional to pressure, the critical ionization is independent of the pressure. Without the inclusion of the waveguide phase mismatch, Eqn. 2.33 gives an upper limit for the ionization fraction, since the sign of the waveguide term is the same as the free electron term. Table 2.1 shows the values of the critical ionization for the noble gases. The harmonic order quoted is the highest harmonic order which may be phase matched, assuming that the critical ionization is reached at the peak of a 25 fs pulse of center wavelength 0.8 μm. Ionization fractions were calculated used the ADK ionization rates (Eqn. 2.3).

Gas Species	η_{cr}	Harmonic order
He	0.005	91
Ne	0.011	69
Ar	0.048	35

Table 2.1: Critical ionization values for the noble gases, as well as the highest harmonic order that can be phase matched, generated at the peak of a 25 fs pulse of center wavelength 0.8 μm.

Once the ionization fraction is higher than critical, the dispersion from the free electron density will be the dominant component in the phase mismatch. This leads in general to a decreasing coherence length with harmonic order, since ever higher intensities are required to produce higher photon energies, and higher intensities result in a higher free electron density. The photon energy that can be generated before the ionization level reaches critical may be maximized in a couple of different ways. First, the shorter the driving laser pulse, the greater the probability that the electron will not be driven from the atom before the peak electric field within the pulse. Since

ionization occurs discretely at every half cycle, the fewer half cycles there are with sufficient amplitude for ionization before the peak of the pulse, the less the degree of ionization. This is why "few-cycle" laser pulses are useful for the generation of the highest photon energies [45, 79]. It is worth noting also that the ADK ionization rates overestimate the degree of ionization for few-cycle laser pulses, because the field envelope changes significantly between half-cycle peaks of the field within the pulse. Numerical estimates of this "non-adiabatic" effect can be found in Refs. [11] and [80].

The second method for phase matching higher photon energies works in essentially the same way as the first, by reducing the number of half-cycle peaks within a pulse. In this case, the technique is to use a longer wavelength in the driving laser pulse. Recall that the cutoff photon energy is proportional to the square of the driving laser wavelength (Eqn. 2.7), making this an advantageous scaling factor [81, 82]. Significant extension of the cutoff energy through the use of long driving wavelength was demonstrated in several experiments [81, 83, 84]. The disadvantage is that the electron spends more time in the continuum during rescattering, lowering the recombination cross-section. It was recently found both theoretically and experimentally that the single-atom yield scales as $\lambda^{-5.5\pm0.5}$, which greatly reduces the efficiency of HHG driven by longer wavelengths [85]. Recent experimental and theoretical work has shown that it is possible to extend true phase matching of the high harmonic generation process to significantly higher photon energies (in theory up to 1 keV) using long wavelength driving lasers [86]. However, the unfavorable single atom yield may limit applications of harmonics driven by long wavelength drivers to photon energies around 300 eV, even when perfectly phase matched.

The drawbacks to each of these techniques is the higher degree of technical difficulty in generating the driving laser pulse. Pulse compression techniques for generating few-cycle laser pulses are improving due to interest in the multiple applications of such short pulses, but still reduce the overall efficiency. Similarly, generation of intense laser

pulses at near- to mid-IR wavelengths require the use of nonlinear optical conversion techniques that also reduce overall efficiency. Each of these things places higher demands on the base laser system in terms of energy and beam quality.

The high intensities needed for the generation of very high harmonic orders lead to other limits on generating bright emission at high photon energies. Defocusing limits the interaction length, for a free focus geometry, and can lead to extra loss or the excitation of higher order modes in a hollow waveguide geometry. Strong ionization depletes the energy in the driving laser beam, reducing the intensity. Nonlinear optical effects, such as the optical Kerr effect, can become quite significant at high intensities, leading to a reshaping of the ultrashort pulse [87]. Even subtle changes in the phase front or the local intensity can alter the local phase matching conditions in ways difficult to predict. The major difficulty with improving conversion efficiency of HHG at high photon energies is this rapidly varying phase mismatch.

Finally, absorption plays a major role in the maximum obtainable conversion efficiency. Especially for VUV and EUV frequencies, strong absorption of the harmonic light becomes the ultimate limitation of the achievable flux. The strong absorption originates for the same reason that these photon energies are of particular interest: the valence electrons of many materials are bound with energies of $\sim 10-100\ eV$. Constant et al. [75] calculated that the maximum harmonic yield saturates once the interaction length is longer than a few absorption lengths, even for perfect implementation of phase matching. The result of their calculation is shown in Fig. 2.17. The overall optimization conditions predicted by this analysis are:

$$L_{int} < 3L_{abs},\ L_c > 5L_{abs} \tag{2.34}$$

This description of absorption-limited harmonic generation has been confirmed experimentally [75, 88]. Figure 2.18 shows the results of such a measurement. Because of the relationship expressed in Eqn. 2.34, in the case of strong absorption, the phase

matching condition may be relaxed so that L_c is simply much longer than L_{abs}. It is also worth noting in designing the region of gas density, whether this is a gas jet, or the pressure profile in a hollow waveguide. The absorption length places an upper limit on the length of the interaction region that will be practical for phase matching.

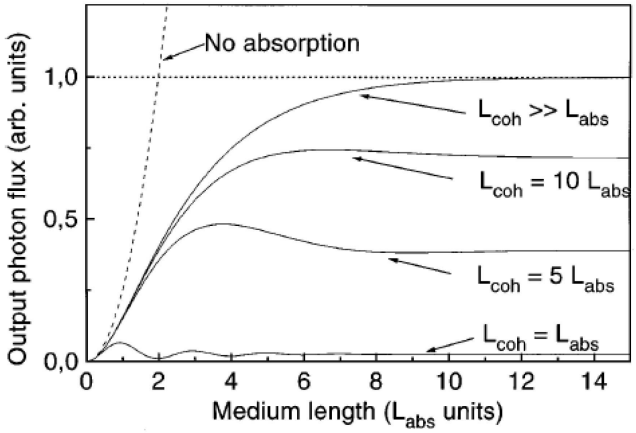

Figure 2.17: Phase matched HHG photon emission as a function of the propagation distance (in units of the absorption length, L_{abs}) in the presence of absorption. Reproduced from Ref. [75].

2.5 Quasi-Phase Matching

When full phase matching is impossible or inconvenient, a reasonable and efficient alternative is quasi-phase matching (QPM). Originally proposed [89, 90] soon after the demonstration of nonlinear optical harmonic generation, QPM can drastically improve the conversion efficiency of harmonic generation through a periodic correction to the phase mismatch. This periodic correction can take multiple forms, but among the most successful techniques is the use of periodically-poled ferromagnetic crystalline structures [91–93]. In this method, the spontaneous polarization of the crystal is reversed periodically, inverting the relative phase between the fundamental and harmonic fields. Ideally, this reversal happens at every coherence length, so that, on average, the phases of the two fields remain within π radians, the condition for continued coherent addition

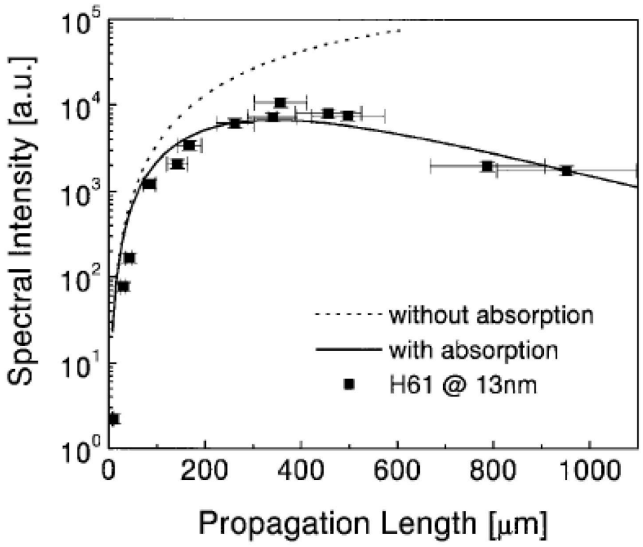

Figure 2.18: Measured (squares) and predicted (solid curve) brightness of the 61^{st} harmonic order generated in neon, as a function of propagation distance, showing the effect of absorption on the conversion efficiency. Reproduced from Ref. [88].

of the harmonic field. Reversal of the polarization at a periodicity of any odd number of coherence lengths will also improve the conversion efficiency, but scales down with an increasing number of coherence lengths per period. Figure 2.19 illustrates the harmonic growth as a function of propagation distance with the application of QPM. The black curve corresponds to the growth of harmonic signal in a periodically-poled nonlinear material. The dashed curve illustrates that this signal growth is essentially quadratic with distance, as in full-phase matching, except scaled by a factor of approximately $\pi^2/4$ [91].

The red curve describes a slightly different version of QPM. Instead of reversing the phase relationship at every coherence length, the harmonic emission is suppressed in every other coherence length. Essentially, the destructive interference which occurs at every other coherence length is suppressed, and only constructive interference between zones of similar phase occurs. It may be seen from the figure that the harmonic intensity achieved after a propagation distance L is the same as that achieved with QPM using

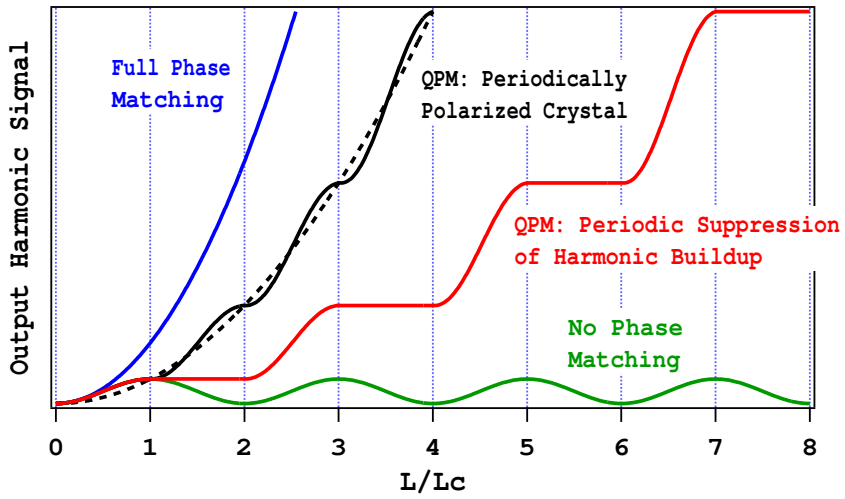

Figure 2.19: Harmonic intensity as a function of propagation distance, in the case of full phase matching (blue curve), traditional quasi-phase matching with periodically poled nonlinear crystal (black curve), quasi-phase matching through periodic suppression of the harmonic signal (red curve), and no phase matching (green curve).

periodic polarization after a propagation distance of $L/2$.

QPM using a periodically poled nonlinear crystalline structure is not applicable to high-order harmonic generation for the same reason that phase matching using birefringent materials is not applicable: the strong absorption of high harmonic frequencies by dense media. Several proposals and a few experimental demonstrations of techniques for QPM of HHG have appeared since the demonstration of HHG itself. These QPM techniques involve periodic modulation of either the gas density [26, 30, 36] or the driving laser intensity [27–29, 31, 32, 34, 35]. However, nearly all of these proposals neglect an important problem specific to QPM of HHG. Quasi-phase matching techniques are needed mainly for high photon energies that are generated at ionization levels that preclude true phase matching techniques. However, the high degree of ionization leads also to a rapidly varying phase mismatch that can be difficult to predict. In addition to the ionization, propagation effects in the waveguide, such as modebeating, ionization and guiding loss, refraction, and group velocity dispersion lead to a dynamically changing

laser intensity in both space and time along the propagation direction of the driving laser. These changes in turn result in a longitudinally-varying phase mismatch (coherence length). Most of the proposals simplistically assume a constant phase mismatch, which is often not realistic.

Three techniques for QPM of HHG have been successfully demonstrated experimentally to date. In the first approach, the driving laser intensity is varied by modulating the inner diameter of a hollow waveguide, while the gas pressure and laser intensity are tuned to match the coherence length to the waveguide modulation period [1, 29, 34, 35, 94]. When the intensity is modulated above and below the threshold for generating a given harmonic, and the periodicity is matched to the coherence length of the process, the process can be phase matched. Figure 2.20 shows a calculation by Ivan Christov of the harmonic signal as a function of propagation distance. Because of

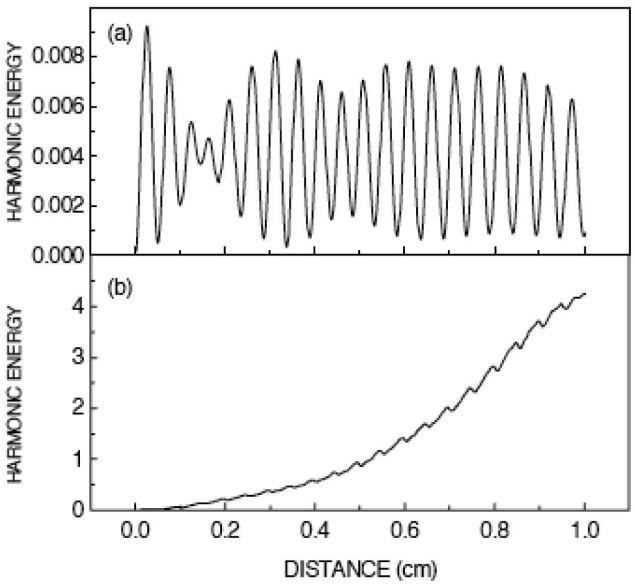

Figure 2.20: Energy of the 95^{th} harmonic order for a large phase mismatch in the case of a) a straight, unmodified waveguide, and b) a modulated waveguide. Reproduced from Ref. [29].

the variation of the phase mismatch with propagation distance, QPM using a modulated

waveguide structure only partially compensates for the phase mismatch. As a result, significant enhancements of 1-2 orders of magnitude were demonstrated. Figure 2.21 shows an enhancement of the harmonic signal from neon using modulated waveguides, at photon energies up to $\sim 284\ eV$. As can be seen in the figure, the enhancement

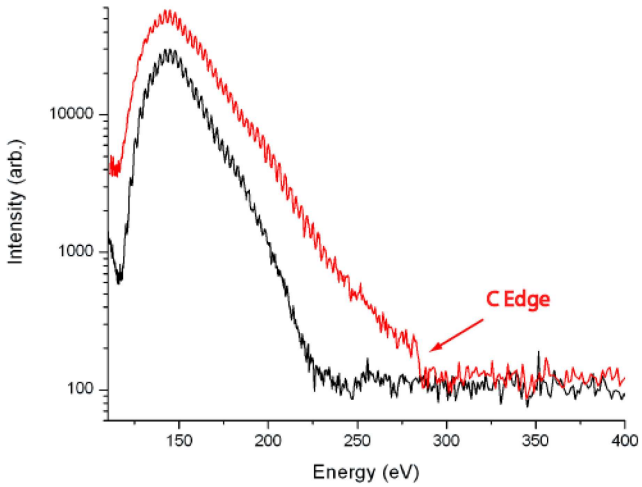

Figure 2.21: Measured harmonic emission from neon generated in straight (black curve) and modulated (red curve) waveguides. Reproduced from Ref. [35].

is broadband, rather than applying only to the cutoff harmonics. It is possible that QPM is partially achieved for plateau harmonics through modulation of the intensity-dependent phase. However, all these improvements are much less than is in principle possible under full phase matching conditions that coherently combine the emission over extended distances and many coherence lengths.

In analogy to periodic polarization of the nonlinear medium, multiple researchers have proposed modulation of the gas density as a method for quasi-phase matching of HHG [26, 30, 36]. Numerical simulations predict large enhancements of the conversion efficiency, but without a mechanisms for appropriate modulation of the density, experimental demonstrations were not possible. Recently, Seres, et al., [36] demonstrated this type of QPM by periodic modulation of the gas pressure in a free focus geometry.

Enhancement factors of ~ 4 were achieved at very short wavelengths of $\sim 2-5\ nm$ by optimizing the distance between two regions of high gas density along the axis of laser propagation. However, the scalability to higher enhancements appears to be limited in this geometry. The width of the gas jets were comparable to the Rayleigh range of the laser focus, limiting the number of gas jets that could be efficiently used.

2.6 Hollow Waveguides

Hollow waveguides were the geometry used for all the HHG data presented in Chapters 3 and 4. This geometry has several advantages over free focusing through a gas jet or gas cell. First, despite the relative lossiness of hollow waveguides in comparison to other types of waveguides, the guiding mechanism maintains a high laser intensity over a long distance, often several times the typical Rayleigh range of a free focus geometry. It also counteracts the decrease in intensity due to ionization-induced defocusing. These two consequences of the guiding maximize the interaction region between the laser field and the nonlinear medium. As shown above, the waveguide alters the propagation vector of the fundamental field so that there is effectively a slightly different index of refraction for a given excited mode of the waveguide. This phase effect contributes to the phase mismatch of the nonlinear generation process which allows a phase matching technique based on pressure tuning. As shown in the previous section, quasi-phase matching can be achieved through modulation of the inner diameter to influence the intensity and phase profile of the fundamental field. Hollow waveguides provide a convenient mechanism for gas management. Since HHG frequencies are readily absorbed by even a low pressure gas, it is imperative to limit the gas density to the region of high laser intensity, and reduce the density to a moderate vacuum ($10^{-6}\ torr$) elsewhere to allow propagation of the harmonic beam. Current designs for the hollow waveguide feature either long ($\sim cm$) regions of constant gas density, with short ($\sim 5\ mm$) differential pumping sections at the entrance and exit, or long pressure ramp regions. The small

inner bore ($\sim 150\ \mu m$) diameter of the waveguide guarantees a small conductance into the larger vacuum system. For a summary of pressure profiles in hollow waveguides, see Ref. [70]. Finally, the extended interaction region and the plane wave propagation of the fundamental light in a hollow waveguide facilitate phase matching techniques.

Hollow waveguides differ from the more common optical fiber used in communications in their index profile. Telecom fiber guides light using total internal reflection, in which the inner core of the fiber has a higher index (n_i) than the outer cladding material (n_o). Hollow waveguides have the reverse index profile, but when the wavelength of the light guided is much smaller than the diameter of the inner bore ($2a$, where a is the radius), then the light is guided through glancing-incidence reflection from the inner boundary. The following summarizes the description of low-loss mode propagation in dielectric waveguides by Marcatili and Schmeltzer [95]. In general, there are three main types of modes supported by hollow waveguides:

Circular electric modes: TE_{0m}, in which the field components are restricted to E_θ, H_r, and H_z.

Circular magnetic modes: TM_{0m}, in which the field components are restricted to H_θ, E_r, and E_z.

Hybrid modes: EH_{nm}, in which all field components may be present.

A linearly polarized, TEM_{00} Gaussian beam, when coupled into a hollow waveguide, will preferentially excite modes of the hybrid type, specifically the EH_{1m} modes. Linear polarization is maintained when $n = 1$. Modes with a linear polarization are also possible as a linear combination of TE_{0m} and EH_{nm} modes, but are attenuated more rapidly given the cladding index used in the present work. Inside the waveguide, the amplitude of the field will vary radially as

$$E_{1m}(r) = \sqrt{\frac{\mu_0}{\epsilon_0}} H_{1m} = J_0\left(u_{1m}\frac{r}{a}\right). \tag{2.35}$$

Again assuming that $\lambda \ll a$, as well as that the index of the cladding is real at the

propagating wavelength, the propagation constant can be written as:

$$\gamma_{1m} = \beta_{1m} + i\alpha_{1m}, \tag{2.36}$$

where

$$\beta_{1m} = \frac{2\pi}{\lambda}\left[1 - \frac{1}{2}\left(\frac{u_{1m}\lambda}{2\pi a}\right)^2\right] \tag{2.37}$$

is the phase constant, from which Eqn. 2.30 originates, and

$$\alpha_{1m} = \left(\frac{u_{1m}}{2\pi}\right)^2 \frac{\lambda^2}{a^3}\left(\frac{(n_o^2+1)}{2\sqrt{n_o^2-1}}\right) \tag{2.38}$$

is the attenuation constant. Since the value of u_{1m} increases with m, the mode with the smallest loss will be the "lowest-order" mode, EH_{11}, and attenuation will increase with higher order. Table 2.2 shows the attenuation parameters and phase velocities of several of the hybrid modes. Group velocities are calculated using Eqn. 2.42, defined below.

Mode	$1/e$ Attenuation	Phase Velocity	Group Velocity
EH_{11}	313 cm	1.00001c	0.999983c
EH_{12}	59 cm	1.00004c	0.999912c
EH_{13}	24 cm	1.00011c	0.999784c
EH_{14}	13 cm	1.0002c	0.999601c
EH_{15}	8.7 cm	1.0003c	0.999403c

Table 2.2: Attenuation constants, phase velocities, and group velocities for several of the low-order hybrid modes, for $\lambda = 0.8\ \mu m$ and $a = 75\ \mu m$.

Hollow Waveguide Coupling

The coupling of a free space propagating laser beam into a hollow waveguide can be described by the projection of the incident field profile onto the eigenmodes of the hollow waveguide. For a linearly polarized incident beam, the incident field distribution can be expressed as:

$$E_i(r) = \sum_{m=1}^{\infty} C_m E_{1m}(r) \tag{2.39}$$

where $E_{1m}(r)$ is given by Eqn. 2.35 and C_m is the coupling coefficient for the m^{th} mode, given by [96]:

$$C_m = \sqrt{\frac{2}{\pi}} \frac{1}{w_0} \int_0^a E_{1m}(r) L_{m-1}\left(\frac{2r^2}{w_0^2}\right) \exp\left(\frac{-r^2}{w_0^2}\right) 2\pi r dr, \tag{2.40}$$

where L_{m-1} is the Laguerre polynomial of the $(m-1)^{th}$ degree.

In practice, a free-space propagating laser beam is coupled into a hollow waveguide by placing the entrance to the waveguide at the focus of the beam, and choosing the appropriate beam waist in relation to the inner diameter of the waveguide. For most efficient coupling and lowest-loss propagation in the waveguide, the ideal coupling of a Gaussian TEM_{00} mode into a EH_{11} mode occurs for the beam waist w_0 at which $\frac{\partial C_1}{\partial w_0} = 0$. When this condition is satisfied, $w_0/a = 0.6435$, for which 98% of the energy is coupled into the EH_{11} mode.

Modebeating

The excitation of multiple modes in the waveguide is common, either through coupling parameters or laser-plasma interactions within the waveguide. Because each mode has a different phase velocity, the modes present will interfere, resulting in a variation of the intensity with propagation distance. In general, the on-axis intensity can be expressed as:

$$I(z) = \frac{\epsilon_0 c}{2} \left| \sum_m A_m \exp(i\gamma_{1m} z) \right|^2, \tag{2.41}$$

where A_m is the amplitude of excitation. Figure 2.22 displays the results of a two-dimensional analytical model that includes contributions from the first three lowest order modes, EH_{11}, EH_{12}, and EH_{13}. The energy of the beam is divided among the three modes: 70%, 20%, and 10%, respectively. Although a higher proportion of the energy can be coupled into the lowest order mode in practice, this plot illustrates the basic behavior of the slowly varying intensity modulations that result. The inclusion of only the first few modes shows oscillations of the largest periodicity. The periodicity from the interference between the EH_{11} and EH_{12} modes, at $\lambda = 0.8\ \mu m$, in a waveguide

of inner diameter 150 μm, is approximately 2.2 cm. The periodicity decreases as the difference in the values of m for the interfering modes increases. In other words, the fastest modulations appear for the interference between the lowest order mode with the highest order excited mode.

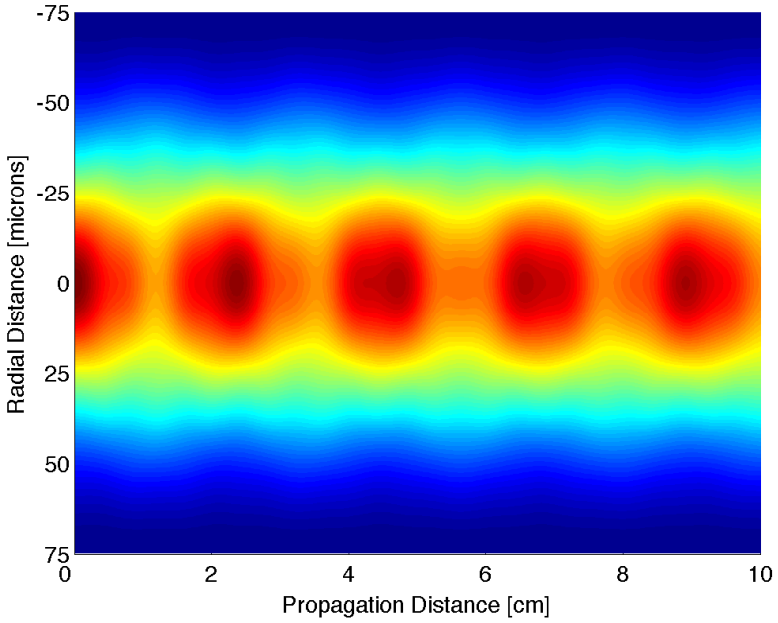

Figure 2.22: Analytically calculated intensity profile of a beam ($\lambda_0 = 0.8\ \mu m$) propagating through a hollow waveguide ($a = 75\ \mu m$), including the first three lowest order modes.

A numerical simulation, written by David Gaudiosi, of the coupling of a Gaussian beam into a hollow waveguide and its subsequent propagation illustrates the two-dimensional intensity profile in the waveguide. Figures 2.23 - 2.25 show the results of this simulation for three different coupling parameters: $R = 0.6, 0.6435$, and 0.7, where $R = w_0/a$ describes the size of the Gaussian beam relative to the inner radius of the waveguide. For a waveguide with $a = 75\ \mu m$, these correspond to $w_0 = 45, 48.25$, and 52.5 μm, which were within the typical range of beam waists used for the experimental work described in later chapters. A beam that is slightly smaller than optimal couples

more energy into the EH_{12} mode, resulting in the strong modulation with periodicity 2.2 cm. Optimal coupling, with 98% of the energy in the EH_{11} mode, still shows significant modulations in the intensity. The standard deviation of the on-axis intensity, for a Gaussian beam of peak intensity 9.57 x 10^{14} W/cm^2, is 26%. A beam slightly larger than optimal further reduces the appearance of long range modulations, but the standard deviation of the on-axis intensity fluctuation increases to 38%. This amplitude of intensity modulations can affect the local phase mismatch significantly.

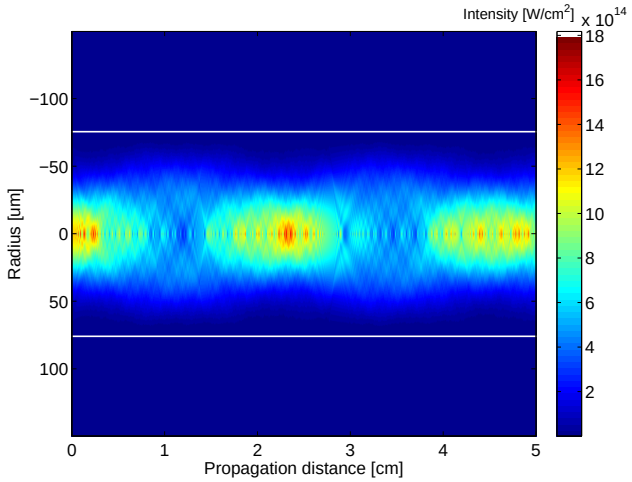

Figure 2.23: Numerical simulation of the intensity profile of a Gaussian beam, $\lambda = 0.8$ μm, coupled into and propagating in a hollow waveguide with inner diameter 150 μm. Coupling parameter: $R = w_0/a = 0.6$.

The above simulations simplistically assume vacuum within the waveguide. This assumption may be valid for low pressures and small degrees of ionization, but a significant increase in either the neutral density or the free electron density will alter the intensity profile. Nonlinear effects, such as SPM, will result in a radially varying phase for the propagating field. Several recent publications deal with the propagation of an intense, ultrashort pulse through an ionizing medium [97], and in a hollow waveguide [87, 98–101]. As discussed above, the free electrons are strongly dispersive and can defocus the propagating field.

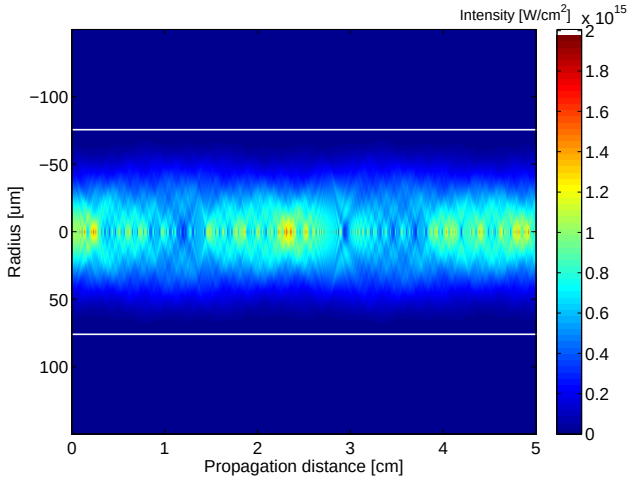

Figure 2.24: Numerical simulation of the intensity profile of a Gaussian beam, $\lambda = 0.8$ μm, coupled into and propagating in a hollow waveguide with inner diameter 150 μm. Coupling parameter: $R = w_0/a = 0.6435$ (optimal coupling into the EH_{11} mode).

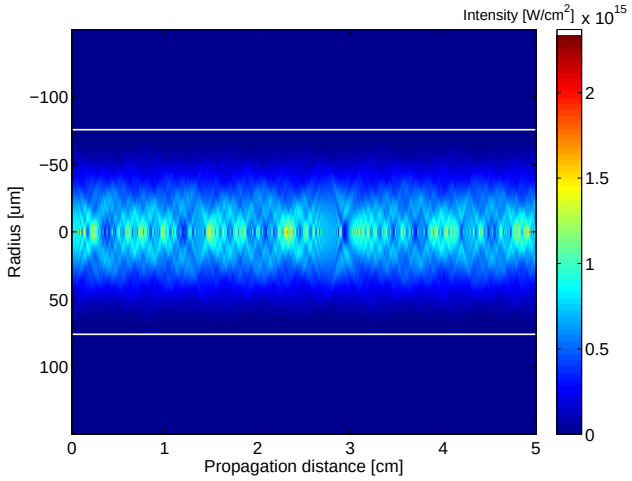

Figure 2.25: Numerical simulation of the intensity profile of a Gaussian beam, $\lambda = 0.8$ μm, coupled into and propagating in a hollow waveguide with inner diameter 150 μm. Coupling parameter: $R = w_0/a = 0.7$.

Experimentally, modulations in the intensity of the propagating laser beam translate to modulations in the brightness of the plasma emission, such as those shown in Ref. [32]. For the waveguide radius used, 150 μm, modulations are commonly observed in the plasma emission with propagation distance with a periodicity of roughly 2 cm. This is only a qualitative correspondence, since there is a complicated relationship between ionization and intensity, as well as between ionization and brightness of the plasma emission. However, this modulation is a good indication of the presence of modebeating, even when care is taken to select the correct waist size for optimal coupling. One reason for this could be the defocusing effect of the free electrons. Long range modulations occur for a slightly smaller than optimal focal spot size. In this case, the beam is able to diverge to a greater degree, resulting in a periodic focusing and defocusing. This effect may be mimicked by the presence of defocusing free electrons. The refraction of the free electrons will also result in a greater coupling of the field into the cladding of the waveguide, and an increased attenuation of the intensity with propagation.

Another limiting assumption of the above simulations is that they assume a CW propagation field. In HHG, the propagating field has a limited spatial extent along the propagation direction due to the short duration of the pulses. Because of the difference in group velocities between the modes, the original pulse will split into multiple pulses, each traveling at a slightly different group velocity. The group velocity for the hybrid modes is given by:

$$v_g = \left(\frac{\partial \beta_{1m}}{\partial \omega}\right)^{-1} = c\left[1 + \frac{1}{2}\left(\frac{u_{1m}.\lambda}{2\pi a}\right)^2\right]^{-1} \tag{2.42}$$

Group velocities for the first several modes are listed in Table 2.2. Once the separation of the pulses grows larger than the width of the pulse, the modes will no longer interact. For example, one can calculate the propagation distance over which the delay between the EH_{11} and higher order modes grows larger than the width of the pulse. The modes EH_{12}, EH_{13}, EH_{14}, and EH_{15} have a separation of 25 fs from the EH_{11} mode after a

propagation distance of 10.5 cm, 3.8 cm, 2.0 cm, and 1.3 cm, respectively. This effect may be a partial reason that the spatial coherence of HHG improves with waveguide length [68]. The EH_{11} mode has the largest group velocity and will be the first to encounter the atoms toward the end of the waveguide. In addition to acting as a spatial filter due to the loss of high order modes, the waveguide's isolation of the lowest order mode from other propagating modes may allow a more well-defined spatial phase profile.

These intensity variations can strongly affect the brightness of the harmonic generation process in multiple ways. The local field strength determines the ionization rate, or the single atom strength of the emission. When the amplitude of intensity variation is strong enough, the regions of strong emission will be limited to that where the intensity is sufficient for a significant ionization rate. In the case of strong modebeating, the harmonic emission may be limited to regions of ~ 1 cm length where the intensity is high (see e.g., Fig. 2.22). The intensity variation will also have a strong effect on the phase mismatch. The free electron density is strongly and nonlinearly dependent on the local intensity, both in space and in time. The phase of the harmonic emission is also quite sensitive to the local intensity, through the intrinsic phase, as described above in Section 2.2.

Quasi-Phase Matching with Modebeating

Recently, there has been some interest in the use of modebeating intensity variations as a method of quasi-phase matching HHG [31,32,102]. In contrast with modulated waveguides, the intensity modulations can be established by selection of the appropriate coupling conditions for excited multiple interfering modes. Pfeifer and Downer [32] show experimental measurements, as well as numerical models, of the modulation of plasma brightness due to modebeating between the first two lowest order modes. For the experiment, they use a waveguide of inner radius $a = 25.5$ μm, and observe a periodicity of ~ 2.6 mm. However, this publication does not examine how the phase mismatch evolves with the variation of the on-axis free electron density. With such strong modulation of

the intensity, the harmonic generation would be limited to the regions of high intensity, and the intrinsic phase would also be modulated. Although not specified, presumably the mechanism for phase matching would be to choose the periodicity such that the phase of the fundamental was the same for each generation region.

There are several limitations to this type of quasi-phase matching. Like with modulated waveguides, the intensity profile is fixed by the structure of the waveguide. For a given inner diameter, the periodicity established by interaction between the two lowest order modes is fixed. Thus tuning of the periodicity to maximize conversion efficiency is not possible. Shaping of the spatial profile of the incident beam might be used, however, to create a more complex, tunable beating pattern through excitation of higher order modes. Such shaping has already been shown to control HHG in waveguides [103]. Second, it is limited in how short a coherence length it may compensate efficiently. Shorter periodicity may be achieved with a smaller inner radius, but this limits the total gas density and thus the absolute photon number achievable. The attenuation constant, temporal separation of pulses, and phase mismatch also increase with a smaller waveguide radius.

Hooker and coworkers [31] consider, instead of interference from only the two lowest order modes, a more complex and realistic intensity modulation resulting from the interaction of several modes. In this case the intensity modulations of highest frequency are also of much smaller amplitude. They numerically simulate the coherent growth of the harmonic field, comparing the case of optimal coupling into the lowest order mode with an incident Gaussian beam with an incident beam of an Airy profile for which $w_0/a = 0.2$, coupling more of the laser energy into higher orders. In a subsequent publication [102], an experimental demonstration of bright emission from argon ions is attributed to quasi-phase matching of the nonlinear process through multimode modulation of the intensity. However, in neither publication do the authors include the effect of the presence of gas on the propagation of the laser in the waveguide. This

is especially important considering the intensities used, and the fact that they claim harmonic emission from singly ionized argon. The resulting, substantial free electron density is considered in relation to contributing to the bulk of the phase mismatch, but not in relation to how it would affect the on-axis intensity profile. Their own calculations predict that the ultimate conversion efficiency is quite sensitive to subtle differences in the intensity profile. Also, no measurements support the claim that multimode beating is the cause of the increase in conversion efficiency other than the measurement of flux itself. Considering the complex dynamics which result in a changing phase mismatch in both space and time, the assumption of a constant coherence length is dubious. Recent work [104] suggests that the mechanism for the generation of bright emission, and extension of the observed cutoff to the water window, from argon ions in waveguides is due to pulse compression [87].

2.7 Counterpropagating Light

Counterpropagating light can have a substantial effect on HHG in any geometry, and control of harmonic generation may be achieved through control of the counterpropagating field. The influence of counterpropagating light on HHG was first theoretically studied by Peatross and coworkers [27,28], and later developed further by Landreman et al., [105] and Cohen et al., [106]. The principal effect of a counterpropagating field is to suppress the coherent buildup of the harmonic field by establishing a rapid, stationary phase modulation. As will be shown in Chapter 4, this process can be exploited to study coherence properties of HHG in hollow waveguides, as well as to achieve a new quasi-phase matching technique. QPM using counterpropagating light turns out to be a flexible and highly selective tool for enhancement of the conversion efficiency.

Parallel Polarizations

To understand how counterpropagating pulses may suppress harmonic generation, consider two plane waves of the same frequency and parallel polarization that travel in

opposite directions. The electric field of the light may be written as:

$$E_T(z,t) = E_F \exp[i(kz - \omega t)] + E_C \exp[i(-kz - \omega t)] = E_{0T}(z) \exp[i(kz - \omega t + \phi(z))], \tag{2.43}$$

in which E_F and E_C are the amplitudes of the forward and counterpropagating fields, respectively, and

$$E_{0T}(z) = E_F \sqrt{1 + r^2 + 2r\cos(2kz)} \tag{2.44}$$

and

$$\phi(z) = -\arctan\left(\frac{r\sin(2kz)}{1 + r\cos(2kz)}\right), \tag{2.45}$$

$r = E_C/E_F$ being the field amplitude ratio. Both the field and the phase have a time-independent, sinusoidal variation in the propagation direction, with a periodicity of half the wavelength of the forward or counterpropagating fields. The peak-to-peak amplitude of the phase modulation is given by:

$$\Delta\phi = 2\arctan\left(\frac{r}{\sqrt{1 - r^2}}\right) \approx 2r, \tag{2.46}$$

where the approximation is true for $r \ll 1$. Coherent buildup of the harmonic field will be suppressed when the phase modulation translated to the harmonic field has an amplitude of π or greater. This condition is met when

$$r = \frac{\pi}{2q}. \tag{2.47}$$

For large q, it can be seen that the approximation $r \ll 1$ is valid, meaning that a counter-propagating field with an amplitude much smaller than that of the forward propagating field is sufficient to suppress coherent buildup of the harmonic signal. In fact, the higher the order of the harmonic, the smaller a counterpropagating field required to suppress its coherent buildup.

In addition to the direct phase modulation of the harmonic driving laser field, there is an indirect phase modulation through the intrinsic, or intensity-dependent

phase. This component arises through Eqn. 2.44, or the stationary modulation of the intensity. The peak-to-peak variation of the intensity is

$$\Delta I = \sqrt{4 I_F I_C}, \tag{2.48}$$

with I_F and I_C as the instantaneous forward and counterpropagating intensities. Combination with Eqn. 2.11 gives the peak-to-peak variation in the intensity-dependent phase:

$$\Delta\phi_p = \frac{2Ke^2 I_F r}{\hbar m \epsilon_0 c \omega^3}. \tag{2.49}$$

While Eqn. 2.47 describes a phase variation of the fundamental field, which then is transferred to the harmonic phase, Eqn. 2.50 describes a direct variation of the harmonic phase. The dependence on harmonic order enters through the parameter K, which varies with the release phase as shown in Fig. 2.6. The effect on a given harmonic order thus also depends on which trajectory contributes. Since the value of K is generally significantly higher for the long trajectories in comparison with the short, the harmonic emission from the long trajectories will be suppressed for a smaller value of r, or in other words, a lower counterpropagating intensity. An example of such a phase modulation is shown in Fig. 2.26a), displaying the difference in the modulation amplitude between the two trajectories. The condition for suppressing emission due to modulation of the intensity is when $\Delta\phi_p = \pi$, or when

$$K I_F r = \frac{\hbar m \epsilon_0 c \omega^3}{2\pi e^2}. \tag{2.50}$$

To show how the harmonic emission may be suppressed by the phase modulations, the microscopic effective emission may be modeled [28, 106]. This is the ratio between the generated harmonic fields without and with the presence of the counterpropagating light, for one period of the standing wave, $\Lambda = \lambda_0/2$:

$$\xi = \frac{1}{\Lambda}\int_0^{\Lambda} \exp[i\Delta\phi(z)]dz = \frac{1}{\Lambda}\int_0^{\Lambda} \exp\left[iA\cos\left(\frac{2\pi}{\Lambda}z\right)\right]dz = J_0(A), \tag{2.51}$$

in which A is the amplitude of the phase variation and $J_0(A)$ is the zero-order Bessel function of the first kind. This phase amplitude A is directly proportional to r, the field amplitude ratio, as can be seen in Eqns. 2.47 and 2.50. Figure 2.26, reproduced from Ref. [106], shows the effect of a weak counterpropagating pulse on HHG emission, from a calculation using the generalized Lewenstein model [43]. For these calculations, the medium was helium, and the driving laser pulse had a peak intensity of 10^{15} W/cm^2 and a FWHM pulse duration of 20 fs. Figures 2.26a) and b) confirm that the phase modulation is stronger for the long trajectories compared to the short, and that the phase amplitude A is directly proportional to the field amplitude ratio r. Figure 2.26d) shows the form of the microscopic effective emission factor ξ, illustrating that for the presence of even a small counterpropagating field, the harmonic emission is effectively suppressed. Notably, for some values of A, ξ is negative, corresponding to a phase shift of π in the harmonic phase. This is important for the implementation of QPM using counterpropagating light, which will be discussed further below.

Perpendicular Polarizations

Harmonic emission may also be suppressed under the influence of counterpropagating light with a polarization that is linear and perpendicular to the forward propagating driving field. In this case, the physical mechanism is different. Rather than creating a longitudinally varying phase that suppresses the coherent buildup of harmonic signal, the counterpropagating light lowers the probability of emission itself by creating a sinusoidally varying *ellipticity* in the driving laser field. As has been described in several studies of HHG (e.g. Refs. [107–109]), even a slight ellipticity in the fundamental field will reduce the probability of recombination due to the transverse spread of the electron wavefunction during rescattering. The advantage of using a perpendicular polarization for suppression of HHG with counterpropagating light is that it may be attenuated using a polarizer before it feeds back into the laser system.

The ellipticity induced by counterpropagating light was derived by Landreman et

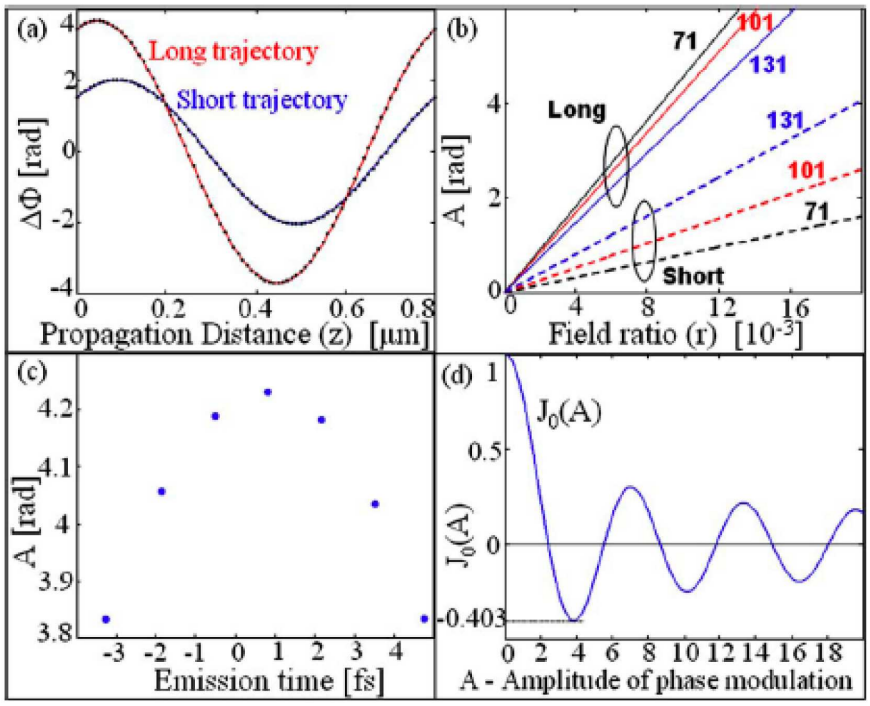

Figure 2.26: Influence of a weak counterpropagating field on the phase of HHG. a) Example of the intensity-dependent phase modulation, with a different amplitude for the two trajectories. Amplitude of the phase modulations calculated as a function of the field ratio, r. c) Amplitude of the phase oscillations for a particular contribution as a function of emission time. d) Bessel dependence of the microscopic effective emission factor on the amplitude of the phase modulation. Reproduced from Ref. [106].

al., [105]. In this case, the sum of the electric fields of the forward and counterpropagating beams can be written as:

$$E_T(z,t) = E_F \exp[i(kz - \omega t)] \begin{pmatrix} 1 \\ 0 \end{pmatrix} + rE_F \exp[i(-kz - \omega t)] \begin{pmatrix} 0 \\ 1 \end{pmatrix}, \tag{2.52}$$

where the vectors represent possible polarization orientations in the 2D transverse plane. Any two-component complex vector can be expressed in form:

$$\begin{pmatrix} a \\ b \end{pmatrix} = \exp(i\phi) \left[\begin{pmatrix} u \\ v \end{pmatrix} + i\epsilon \begin{pmatrix} v \\ -u \end{pmatrix} \right], \tag{2.53}$$

where u, v, ϕ, and ϵ are real quantities, so that the total electric field can be rewritten

as

$$E_T(z,t) = E_F \exp[-i\omega t] \exp(i\phi(z)) \left[\begin{pmatrix} u(z) \\ v(z) \end{pmatrix} + i\epsilon(z) \begin{pmatrix} v(z) \\ -u(z) \end{pmatrix} \right]. \tag{2.54}$$

The ellipticity of the electric field will evolve with propagation distance, the major and minor axes of the ellipse given by the two-component vectors in Eqn. 2.54, and the ellipticity given by $\epsilon(z)$. The ellipticity is defined as the ratio of the peak field in the direction of the minor axis and the peak field in the direction of the major axis, and is given by

$$\epsilon(z) = \frac{1 + r^2 + \sqrt{1 + r^4 + 2r^2 \cos(4kz)}}{2r \sin(2kz)} \tag{2.55}$$

The authors show both theoretically and experimentally that the suppression of HHG emission generally requires a larger field ratio, r, when using a counterpropagating field of perpendicular polarization compared to parallel polarization. Their calculations indicate that the ratio of intensities, I_F/I_C, needed to reduce the harmonic signal by 50% is roughly 10x greater for the perpendicular polarization when compared to the phase modulation of the fundamental field with a parallel polarization (of the type described by Eqn. 2.47).

Quasi-Phase Matching with Counterpropagating Pulses

Quasi-phase matching of HHG may be achieved by using counterpropagating pulses to suppress harmonic emission from the out-of-phase coherence lengths created by the phase mismatch between the fundamental and harmonic fields. As described in Section 2.5, when the phase mismatch is nonzero, the harmonic signal oscillates with a period of twice the coherence length. The harmonic field increases until the phase slip between the driving laser and harmonic fields reaches π radians, at which point the subsequently emitted harmonic field begins to interfere destructively. All-optical QPM using counterpropagating pulses is implemented by arranging for the overlap region of the colliding pulses to suppress emission from one or more coherence zones that would otherwise cause destructive interference (see Fig. 2.19).

Peatross and coworkers have shown that counterpropagating light can effectively suppress the coherent buildup of HHG in free-focus geometries through a gas jet [33,110] or a gas cell [111,112]. In Voronov et al. [33], efficient suppression of the harmonic signal was observed over well phase matched conditions. The interaction region consisted of a $\sim 300\ \mu m$ wide jet of argon gas, and the experimental conditions were adjusted for highest harmonic signal near the 23^{rd} harmonic order. The collision region (effective width $\sim 300\ \mu m$) of the driving laser pulse and a counterpropagating pulse of duration $1\ ps$ was scanned through the interaction region by adjusting a delay stage in the counterpropagating beam line. The results are shown in Fig. 2.27. The harmonic signal is strongly suppressed.

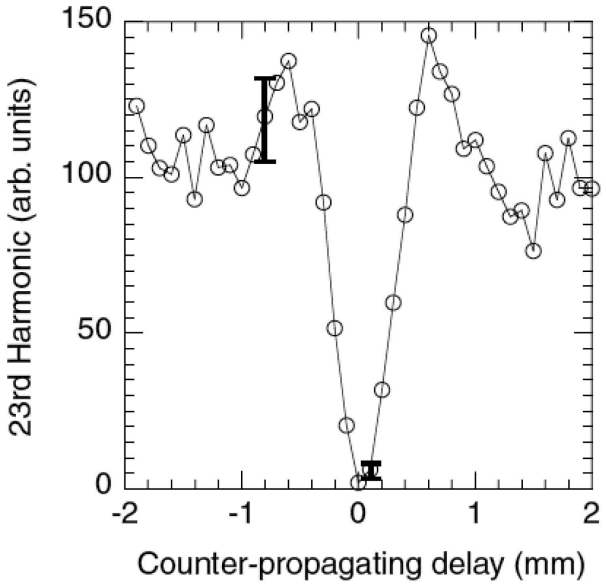

Figure 2.27: Scan of the collision point of the driving laser pulse with a counterpropagating pulse through a narrow gas jet. The harmonic signal is suppressed strongly in the presence of the counterpropagating light. Reproduced from Ref. [33].

The authors also demonstrate an enhancement of the harmonic signal for poor phase matching conditions. The focus was moved away from the gas nozzle to a region where the gas region is approximately $1\ mm$ wide, drastically reducing the harmonic

signal through dephasing. For the given experimental conditions, the authors estimate the presence of approximately three coherence zones. The scan of the collision region now results in a restoration of the harmonic signal (see Fig. 2.28) as the destructively interfering emission is now suppressed.

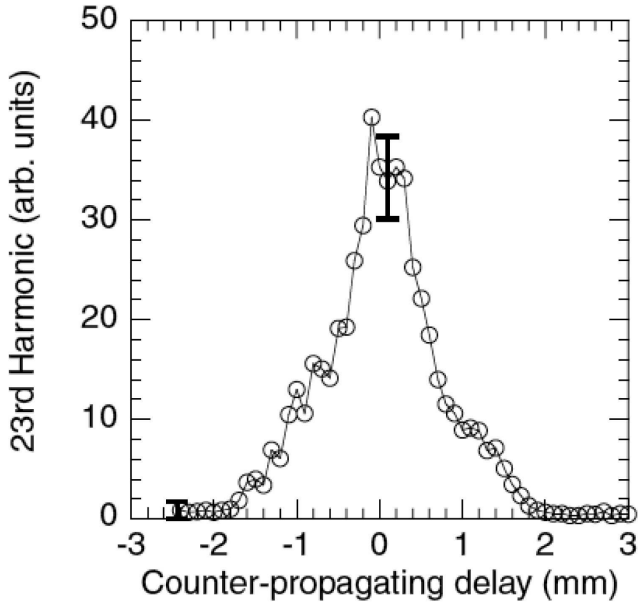

Figure 2.28: Scan of the collision point of the driving laser pulse with a counterpropagating pulse through a wider gas jet. The poorly-phase matching harmonic signal is restored through suppression of destructively interfering harmonic emission. Reproduced from Ref. [33].

Similar plots of suppression and restoration of the harmonic signal from neon are shown in Ref. [112]. In that experiment, the harmonics were generated in a gas cell of several cm, and the counterpropagating pulse had a duration of $\sim 10\ ps$, (effective width $\sim 3\ mm$). Measurements provided a rough estimate of the coherence length over a distance of 1 to $2L_c$. However, in all cases, the interaction medium was limited, either due to the width of the gas jet, the absorption depth of the gas, or the region of sufficient laser intensity. This ultimately limits the potential enhancement using counterpropagating pulses. While an enhancement of the harmonic signal was observed due to the

presence of counterpropagating light, this enhancement was not an improvement above other phase matching techniques. Moreover, they were unable to match the width of the counterpropagating pulse to the coherence length without the ability to measure the coherence length.

To implement all-optical QPM efficiently, a train of counterpropagating pulses is needed to suppress harmonic generation in several selected out-of-phase regions of the medium. Hollow waveguides provide an ideal medium for this technique, since the guiding provides an extended interaction region. A sequence of counterpropagating pulses can allow significant enhancement of the HHG signal if constructed appropriately. Each pulse must have the correct width for suppressing the out-of-phase harmonic emission from one coherence zone, and the sequence of pulses must have the correct spacing for suppressing consecutive out-of-phase coherence zones, while allowing in-phase zones to coherently add. Assuming a constant single-atom efficiency and a constant phase mismatch with propagation, the expected enhancement of harmonic intensity for a sequence of N pulses is $(N+1)^2$. However, as will be described in Chapter 4, a varying harmonic emission efficiency or phase mismatch can lead to significantly higher enhancements. In addition, it is predicted that for a correct ratio of the forward and counterpropagating fields, the counterpropagating light can cause an overall phase shift in the harmonic emission of π radians [106]. In this case, the out-of-phase coherence zone is partially converted to an in-phase coherence zone, further increasing the overall conversion efficiency.

The optimal shape of the counterpropagating pulses for QPM is that which most effectively suppresses destructive interference from out-of-phase zones. The overlap region between the counterpropagating and driving laser pulses corresponds to half the width of the longer counterpropagating pulse, since the pulses move in opposite directions. In other words, although the counterpropagating pulse may be, for example, 2 ps in duration, with a physical extent of ~ 600 μm, its overlap region with the forward

propagating pulse will be only $\sim 300\ \mu m$. This resulting overlap region is referred to as the "effective" width of the counterpropagating pulse. Thus, the optimal counterpropagating pulses will have a square temporal profile with effective width equal to a single coherence length. The enhancement due to a sequence of counterpropagating pulses was calculated in Ref. [106] for both a square pulse and a sech^2 pulse. This calculation is shown in Fig. 2.29, which plots the QPM efficiency factor: the generated total harmonic signal with the counterpropagating pulses, normalized to the signal generated under perfect phase matching. Two parameters were varied in order to find the optimal pulse shapes: the peak amplitude of the phase modulation, A_0, and the effective suppression width of the pulse, z_0. From the calculation, it was found that the optimal effective FWHM of a sech^2 pulse is $0.26L_c$, which, along with the optimal phase modulation amplitude, gives a harmonic efficiency factor of 0.14. Because of the extra phase shift of π radians induced by the counterpropagating field at the appropriate phase modulation amplitude, part of the emission in the out-of-phase zone is shifted to be in-phase, and adds to the total signal. This gives an efficiency that is 40% larger than simply completely suppressing the out-of-phase emission.

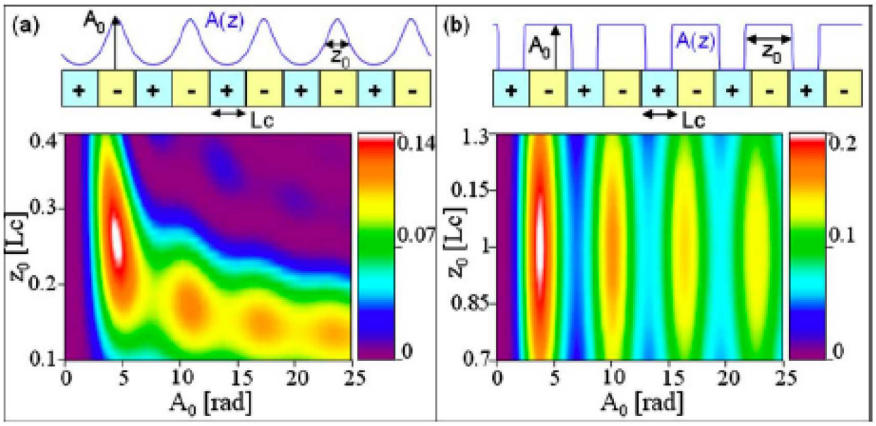

Figure 2.29: QPM efficiency factor for a) hyperbolic secant and b) square counterpropagating pulses as a function of pulse width and peak phase modulation amplitude. Reproduced from Ref. [106].

Chapter 3

Characterization of Waveguide High Harmonic Generation

3.1 Introduction

This chapter contains a general description of the laser system, the HHG waveguide setup, and the detection of EUV light. Also included are some selected experimental results from exploratory work on optimizing the conversion efficiency of HHG in waveguides. Specifically, the measurement and estimation of the photon yield of HHG from hollow waveguides at 45 eV is presented. Measurements are presented of the energy loss in the interaction medium within the hollow waveguide, and are compared with a simple numerical model of energy loss due to ionization. This model appears to account for a majority of the loss of energy in the driving laser beam. Finally, a brief characterization of the enhancement of the HHG signal from modulated hollow waveguides is presented.

3.2 Experimental Setup

Laser System

The laser source used was a Ti:sapphire amplifier system (KMLabs Red Dragon). This is a two-stage, multipass, chirped pulse amplification (CPA) system, operating at 1 kHz, capable of generating pulses as short as 20 fs, and pulse energies as large as 6 mJ. Although this system is more technically advanced than those described in Ref. [7], this reference is a very useful and detailed review, especially for a review of the components and overall design of this type of CPA laser system. The first stage pump

laser was an arclamp-pumped, frequency-doubled Nd:YLF laser (Quantronix Falcon) with a pulse energy of $\sim 20\ mJ$ and a pulse duration of $\sim 150\ ns$ at a wavelength of 527 nm. The first stage of amplification had a multipass (~ 10 passes) ring configuration of the folded type described in Ref. [113], used to minimized astigmatism. The second stage was pumped by either a Photonics Industries DM-40 or DM-50: both diode-pumped, frequency-doubled Nd:YLF lasers at 527 nm, with a pulse duration of ~ 150 ns and maximum pulse energies of 40 and 50 mJ, respectively. The second stage of amplification was a simple two pass configuration.

The front end of the laser system was a Ti:sapphire, Kerr-lens passively mode-elocked oscillator operating at a repetition frequency of $\sim$ 90 MHz. The prism-dispersion-compensated laser generated a bandwidth of typically $\sim 150\ nm$ tail-to-tail at a center wavelength of 780 nm, supporting a transform-limited pulse of about 10 fs. The repetition frequency of the oscillator was reduced to 1 kHz using a Pockels cell. A second Pockels cell pulse selector, placed before the entrance to the second stage, limited crosstalk of optical noise between the two stages due to amplified spontaneous emission.

The pulse duration at the output of the amplifier was typically $25 - 30\ fs$. The amplifier could be operated with no amplification in the second stage, in which case the amplified bandwidth typically supported a transform-limited pulse of 20 fs. However, uncompensated high-order dispersion prevented full compression. When the pulse was amplified further in the second stage, gain-narrowing of the spectrum tended to broaden the pulse duration as more energy was extracted. At an output of 4 mJ, the pulse duration was at least 30 fs. The pulse durations quoted were measured using SHG-FROG [114]. The output mode of the amplifier was characterized through a measurement of M^2, using a Spiricon M^2 Beam Propagation Analyzer. Typical M^2 values were ~ 1.1 without amplification in the second stage, at about 1 W total power, increasing to ~ 1.3 at 4 W total power.

The laser beam was coupled into the vacuum system through a thin (250 μm), anti-reflection coated sapphire window, with a clear aperture diameter of approximately 1 cm. The window was located between the focusing optics of the beam and the entrance to the waveguide, as far from the focus of the beam as possible without clipping the beam. This configuration minimized the accumulation of nonlinear phase, or "B-integral" [7], which would distort the phase front of the beam. The beam was focused with a curved mirror at near normal incidence, mounted on a translation stage for optimization of the coupling into the waveguide. A curved mirror was used, rather than a lens, to avoid further dispersion that would lengthen the duration of the ultrafast pulse.

Capillary Waveguide Setup

The guided-wave geometry for HHG has been shown in previous work [23, 74] to provide certain advantages over the gas jet or gas cell geometries. Since EUV and soft x-ray frequencies are strongly absorbed by bulk material, HHG beams must propagate in a vacuum of $\sim 10^{-4}$ torr or lower for a typical beam path of a few meters. Hollow core waveguides are a convenient vehicle for maintaining a constant pressure of dilute gas within a limited region, with short differential pumping regions that prevent reabsorption of the HHG photons. Although a hollow waveguide is more lossy than the more familiar step-index telecom fiber, the guiding properties of the capillary waveguide maintain the high intensity necessary for HHG over an interaction distance longer than is possible in a free-focus geometry. Finally, as described in Chapter 2, the guiding properties of the capillary result in a constant phase correction of the driving laser beam, which may be exploited to phase match the nonlinear HHG process.

Two suppliers were used for the hollow waveguide, or capillary, employed in the work here: Wilmad Glass Co., Inc. or Polymicro Technologies, LLC. The cladding material is fused silica, with an outer diameter of 1.2 mm and an inner diameter (ID) ranging from $100 - 400$ μm. For the majority of data presented (and unless indicated otherwise), 150 μm ID capillary was used. Until around April of 2005, the hollow

waveguides were mounted using an outer capillary to hold three separate sections of capillary. Variations in the inner bore of the outer capillary, as well as the relative orientations of the three segments of waveguide, resulted in significant variations in the coupling conditions and loss. In 2005, a modular, custom-designed, vacuum fixture was devised that holds the waveguide very straight using a v-groove design to minimize bending. The v-groove setup is designed to hold a single section of capillary, into which gas is injected through laser-drilled holes. This has resulted in much better coupling efficiencies and much more reproducible results. For more details on the v-groove and quantitative comparisons of the two designs, please see Ariel Paul's PhD Thesis [1].

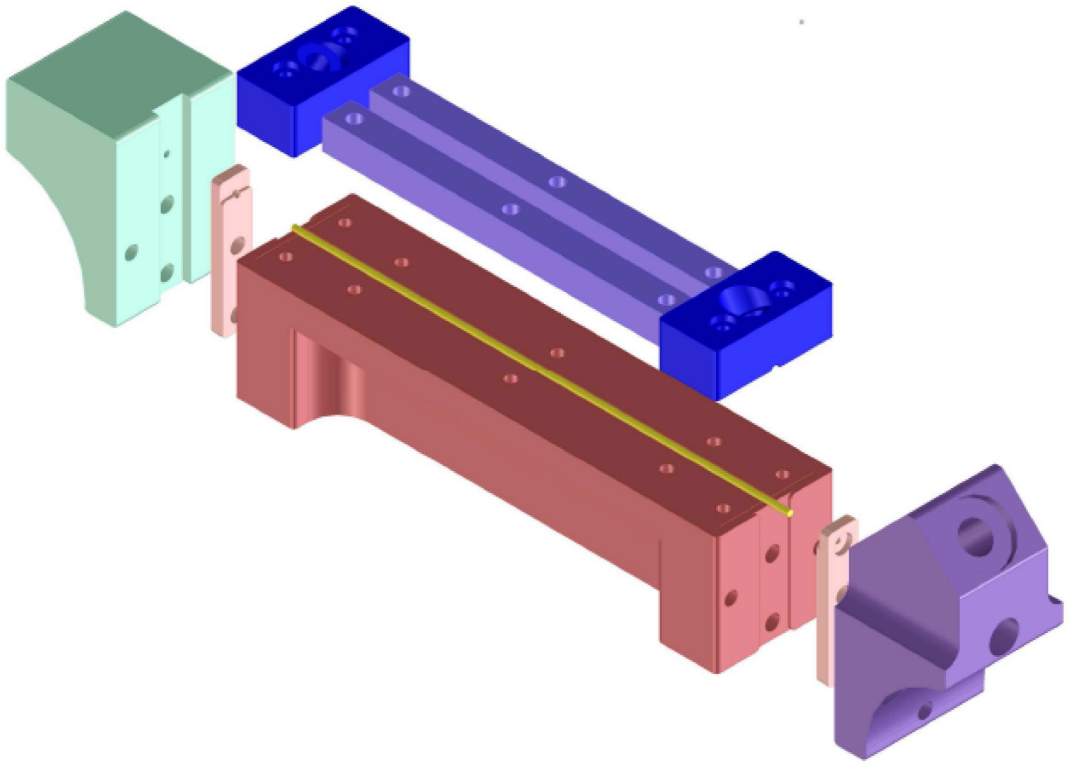

Figure 3.1: 3D rendering of the components of a v-groove vacuum fixture for mounting the hollow waveguides. Reproduced from [1].

Depending on the length of the central v-groove section, the waveguide mount can accommodate total waveguide lengths from $1.5 - 20$ cm. Waveguide lengths for

data presented in this thesis include 3.5, 6, and 11 *cm* total length, sometimes referred to as 2.5, 5, and 10 *cm* waveguides, respectively. The latter refers to the length of the constant-pressure section. Each waveguide also has two 5 *mm* sections used for differential pumping. With the development of the new v-groove apparatus and the ability to drill holes into the capillary for introducing gas, waveguides have since been produced as one piece, leading to the extra 1 *cm* of length. Gas is delivered into the hollow bore of the waveguide through small holes drilled into one side of the capillary using a focused CO_2 laser beam. Gas input blocks attach to the v-groove block, sealing over the hole in the waveguide to prevent contamination of the gas.

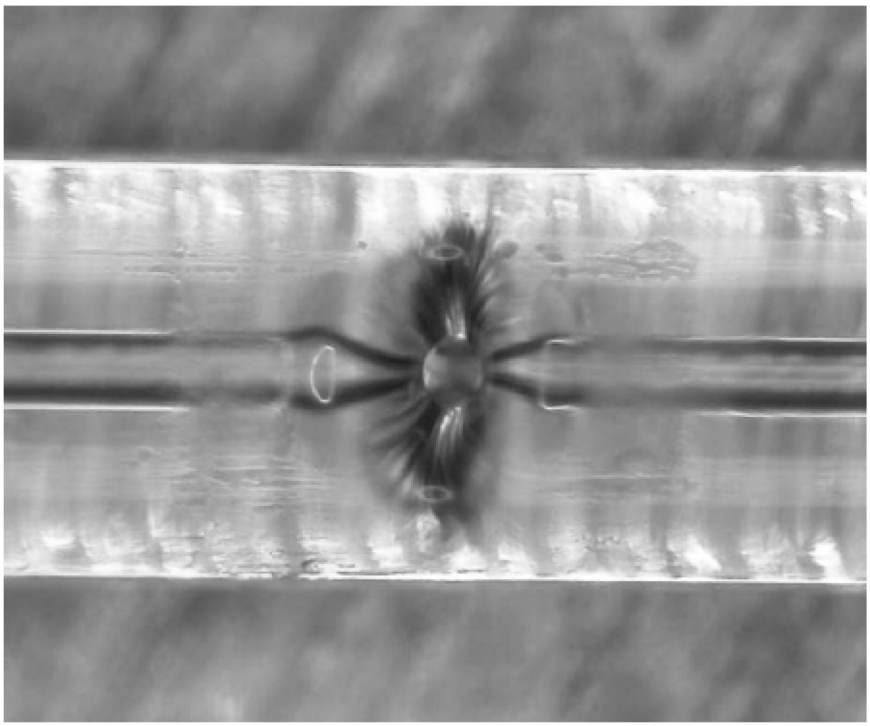

Figure 3.2: Image of a laser-drilled hole in the side of a hollow waveguide, used for gas delivery. The apparent tapering of the inner bore of the waveguide is a refraction effect due to the deformation of the outer surface of the waveguide. Reproduced from [1].

Modulated waveguides were constructed using a finely-tuned glassblowing lathe apparatus, in conjunction with a CO_2 laser. Details of this apparatus as well as examples

of its capabilities can be found in Ref. [1]. Smooth modulations are introduced to the inner diameter of the waveguide by focusing the CO_2 laser beam, at wavelength 10 μm, onto the capillary spinning in the lathe. The hollow core of the waveguide is kept at a gauge pressure of $50 - 100$ *torr*, so that as the fused silica softens, it is pushed outward slightly. This technique can create smoothly varying modulations in the waveguide up to a few % of the inner diameter. The same apparatus is used, under slightly different focusing conditions and while the waveguide is stationary, to ablate the fused silica to create the gas delivery and pumping holes. Figure 3.2 shows a magnified image of a laser-drilled hole in the side of a waveguide. The hole is roughly the same diameter as the inner diameter of the waveguide, 150 μm. The apparent tapering of the inner bore of the waveguide is simply a refraction effect due to the deformation of the outer surface of the waveguide. In fact, the inner bore of the waveguide is minimally altered, as was confirmed by examination under a microscope.

For the HHG described below, the nonlinear media were the noble gases: helium, neon, and argon, with 99.995% purity. The pressure of the gas introduced to the waveguide was controlled using either an electronic MKS Instruments Model 640A pressure controller – for ranges of pressure $1 - 110$ *torr*, or a Siemens sub-atmospheric pressure regulator (Model 43-20L) and constant differential relay (Model 63A) – for pressures ranging from 2 *torr* up to several hundred *torr*. Backing pressures for the exhaust were typically 10^{-2} - 10^{-3} *torr*, provided by roughing pumps of either oil or scroll pump design. Swagelok or Swagelok Ultratorr fittings were used for the vacuum connections for the gas lines, roughing pump lines, and between the tubing in the vacuum system. The noble gas was injected into the waveguide through laser-drilled holes at varying locations in the waveguide. Typically, the pressure profile was constant through the majority of the waveguide, with a ramp down in the 5 mm on either end of the waveguide. However, in several cases, the pressure was injected only at the entrance, only at the exit, or even only at some location in between, creating a pressure ramp profile in

the waveguide. The gas profile that was used will be indicated for data in this and the following chapter.

Coupling of the laser beam into the fiber was accomplished by adjustment of the orientation of the fiber, rather than the laser beam. This ensured that the alignment of the laser into the EUV spectrometer, and hence the co-propagating HHG beam, was not altered. The waveguide vacuum setup is supported on either side between clamps rigidly attached to two x-z translation stages, allowing horizontal and vertical adjustment of each end (see Fig. 3.4).

Detection of EUV

For nearly all measurements presented in this thesis, with the exception of the photon yield measurements, the EUV and soft x-ray light was characterized using a Kirkpatrick-Baez imaging, flat-field spectrometer (Hettrick Scientific) with an EUV and x-ray sensitive CCD camera (Andor Technology, model D0420-BN). The spectrometer consisted of two grazing incidence ($\sim 2-3°$), first surface gold coated, cylindrically curved mirrors, and a grazing incidence gratings. Two spectrometers were used: the older model spectrometer used contained both constant linespace and varied linespace, or survey, gratings, to allow efficient diffraction of wavelengths ranging from $\sim 10-300$ $\mathring{A}$. The newer model spectrometer used only survey gratings. The survey gratings were designed to have efficient (~ 0.1) first-order diffraction over a large range of wavelengths. The gratings were labeled A, B, and C, or SA, SB, and SC (survey gratings) corresponding to rough wavelength ranges of $10-30$, $30-90$, and $90-270$ $\mathring{A}$, respectively. Figure 3.3 shows the first order diffraction efficiency for replicas of the newer spectrometer's survey gratings, supplied by Hettrick Scientific. The spectrometer included the capability for adjusting the angle of incidence of the gratings, so that the camera could remain stationary while the grating could be tilted for detection of zero-order reflection vs. first-order diffraction, etc. Alignment of the spectrometer was accomplished while vented (at atmospheric pressure) using the IR laser light. The laser beam was aligned

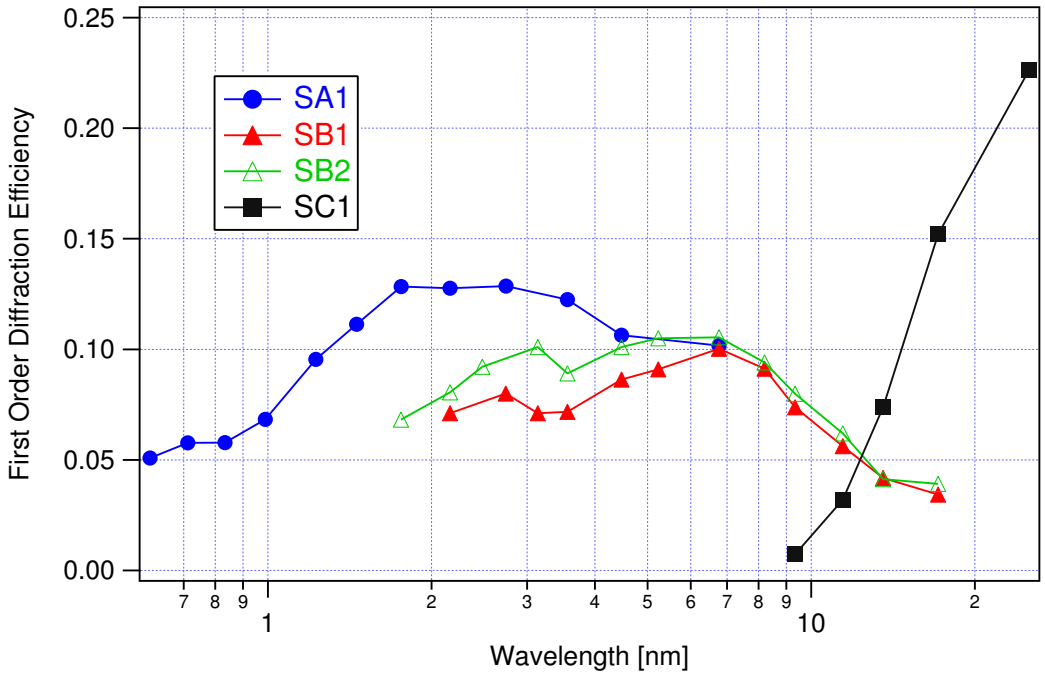

Figure 3.3: Comparison of the absolute first order diffraction efficiencies of the survey gratings, measured from replicas of the gratings used in the spectrometer. Incidence angle for these measurements was 88.75°.

to the grid of the optical table for repeatability, and the orientation of the spectrometer was adjusted manually to the laser beam and clamped into place. The CCD camera was mounted on an x-y translation stage so that the plane of the CCD could be adjusted to the image plane of the spectrometer. The CCD chip had a resolution of 256 x 1024, pixel size 26 μm, with the long side oriented vertically, along the diffraction axis.

The vacuum was maintained at a level of 10^{-6} *torr* (with no gas load present) using one 50 L/s (near the exit of the fiber) and one 17 L/s (at the spectrometer chamber) turbomolecular pump (Leybold and Pfeiffer), backed using scroll roughing pumps (Varian). The total propagation length of the vacuum line was determined by the imaging parameters of the spectrometer. The space between the waveguide setup and the spectrometer chamber was frequently used for plunger feedthroughs, which could accommodate anything from metal foil filters to mirrors to apertures. A series of

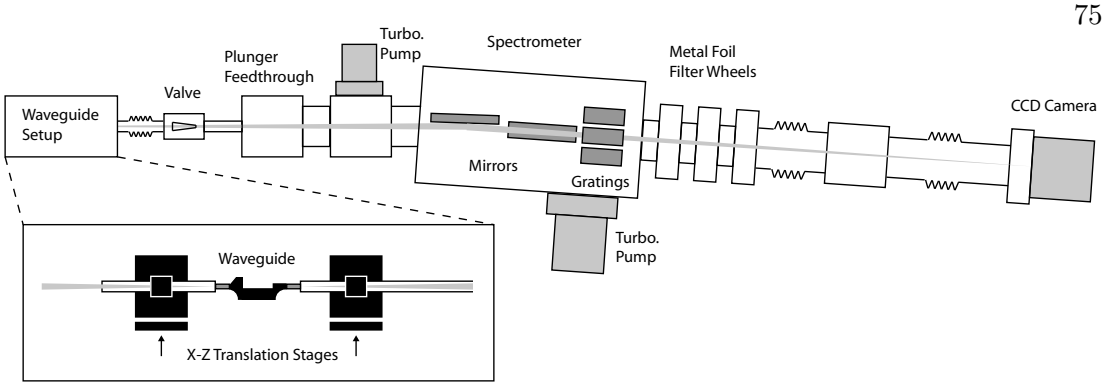

Figure 3.4: Experimental setup for generation, propagation, and detection of HHG under vacuum.

filter wheels [1] were located between the spectrometer chamber and the CCD camera for attenuation of all but the EUV and soft x-ray light incident on the camera. Figure 3.4 shows a schematic of the vacuum propagation and detection line, as well as an inset showing detail of the waveguide setup.

Thin metal foils were used as bandpass filters to allow detection of the harmonic signal while attenuating the co-propagating, intense driving laser beam. These were mounted either in a plunger vacuum feedthrough, or a vacuum filter wheel that could accomodate up to three different filters. Two filters were used for full attenuation of the driving laser, since often there were small holes in the filters. Attenuation of the laser was especially important when using either the CCD camera or the vacuum photodiode for detecting harmonic intensities. At the extreme laser intensities, saturation of the detectors or even optical damage is possible.

3.3 Absolute Harmonic Photon Yield

As a basis of comparison for the available photon yield from HHG by other researchers, the absolute photon yield at 45 eV was estimated using the laser system and hollow waveguide setup described above. For relatively high photon rates ($> 10^9$ $photons/sec$), the measurement was accomplished using a NIST Al_2O_3 vacuum pho-

todiode (serial no. 397) [115]. A basic schematic of the diode is shown in Fig. 3.5. Incident radiation generates photoelectrons from the aluminum oxide surface, that are

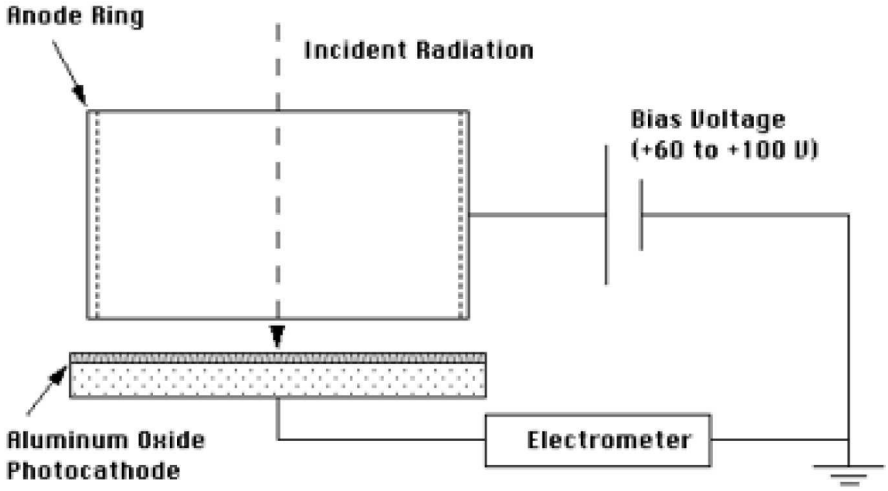

Figure 3.5: Schematic of the detection circuit of the Al_2O_3 NIST vacuum photodiode.

then accelerated to an anode ring held at a bias relative to ground. The resulting current is proportional to the rate of incident photons for a given photon energy. The quantum efficiency of the diode was measured in 2005, and the calibration is shown in Fig. 3.6.

Because both the quantum efficiency and the expected photon rates are so low, the expected currents are on the order of pA to nA. Such a small current can be measured using an electrometer (Keithley, Model 6517), with care taken to eliminate noise sources. The experimental setup for measuring absolute photon yield is shown in Fig. 3.7. The triaxial cable connecting the terminals of the diode to the electrometer was shielded within the chassis for the bias circuit and a braided shielding cable. Careful attention was paid to grounding the shielding as well as the appropriate places in the circuit to prevent a floating ground. A bias of 65.5 V was supplied using batteries to introduce minimal electrical noise. While measurements were conducted, all cables were held stationary to reduce triboelectric effects, caused by friction between the conducting wire and the surrounding insulator [116]. Noise measurements conducted using these

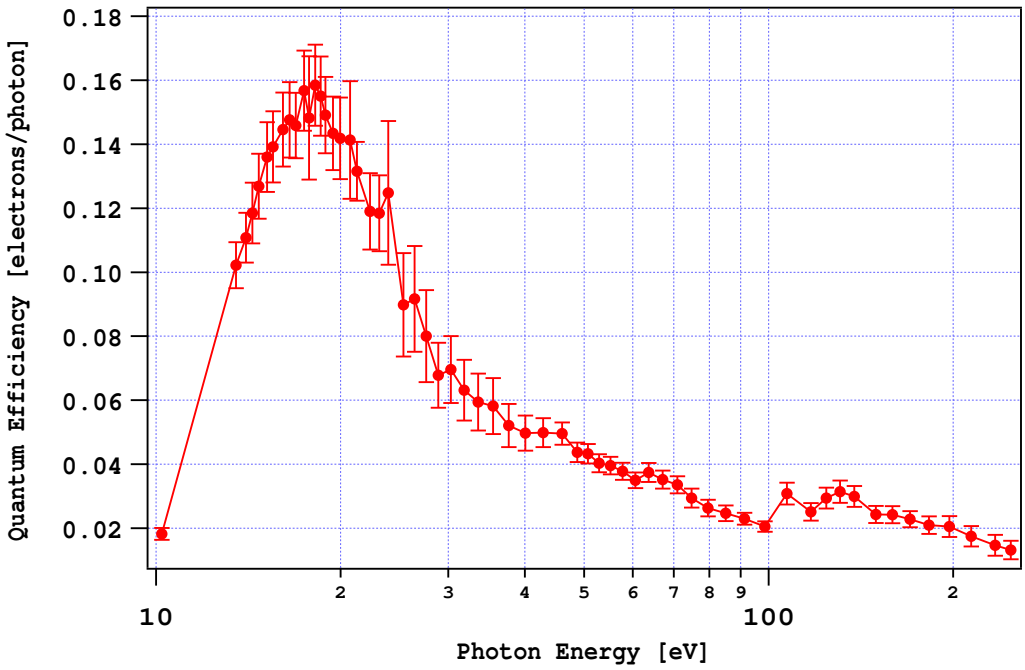

Figure 3.6: Quantum efficiency of the Al_2O_3 NIST vacuum photodiode, serial no. 397. Measured June 2005.

shielding precautions indicated that the electronic noise was reduced to approximately $\pm 0.05\ pA$ when sampled at a frequency of $\sim 1\ Hz$, however, longer scale drifts occurred on the order of 30 *min.*, causing a variation in the current of 0.5 pA. Even this drift amplitude was smaller than the standard deviation of the measured data, typically several pA. As an indication of the lower limit of the photon yield measurement, a measured current of 1 pA corresponds to a photon yield of 10^8 $photons/sec$ at a photon energy near 45 eV.

Thin metal foils were used as a bandpass filter in order to limit the region of emission measured, especially to attenuate the intense driving laser beam. Although the vacuum photodiode is normally non-responsive to visible radiation, at the high intensities used here, multiphoton ionization or optical damage could result.

The combined transmission of argon and the Al filter permitted a bandwidth near 45 eV including about 5 bright harmonic orders. A rough calibration of the transmission

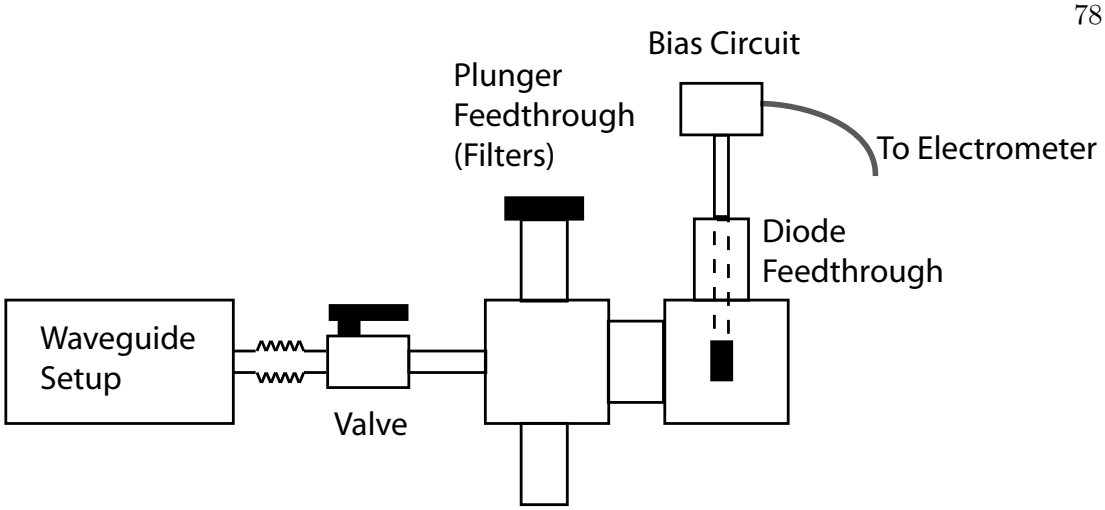

Figure 3.7: Experimental setup for photon yield measurement.

of the 150 nm aluminum filter indicated that it transmitted about 10% of the harmonic energy. The total harmonic yield was measured as a function of pressure for several input intensities, shown in Fig. 3.8. The energies listed in the graph indicate the transmitted pulse energy through the waveguide when under vacuum. Error bars in the plots show the standard deviation of the data averaged for each pressure. Each of these curves is broad, especially compared to the phase matching curve for argon from Ref. [74] (Fig. 2.16). The diode will detect the entire bandwidth transmitted by the aluminum filter. Since different harmonic orders are phase matched at different pressures, the maximum photon yield curve will be broadened with pressure.

The highest photon yield occurs for a higher pulse energy than expected. For a 23 fs pulse, the critical ionization for phase matching of argon occurs at the peak of the pulse with an energy of 250 μJ. In this situation, the waveguide and free electron dispersion are balanced with the neutral gas dispersion, allowing pressure tuned phase matching. However, the highest photon yield, more than twice the yield under phase matching conditions, was found for an input energy of 1.07 mJ. Here, phase matching happens on the rising edge of the pulse. The higher flux in this case may be due

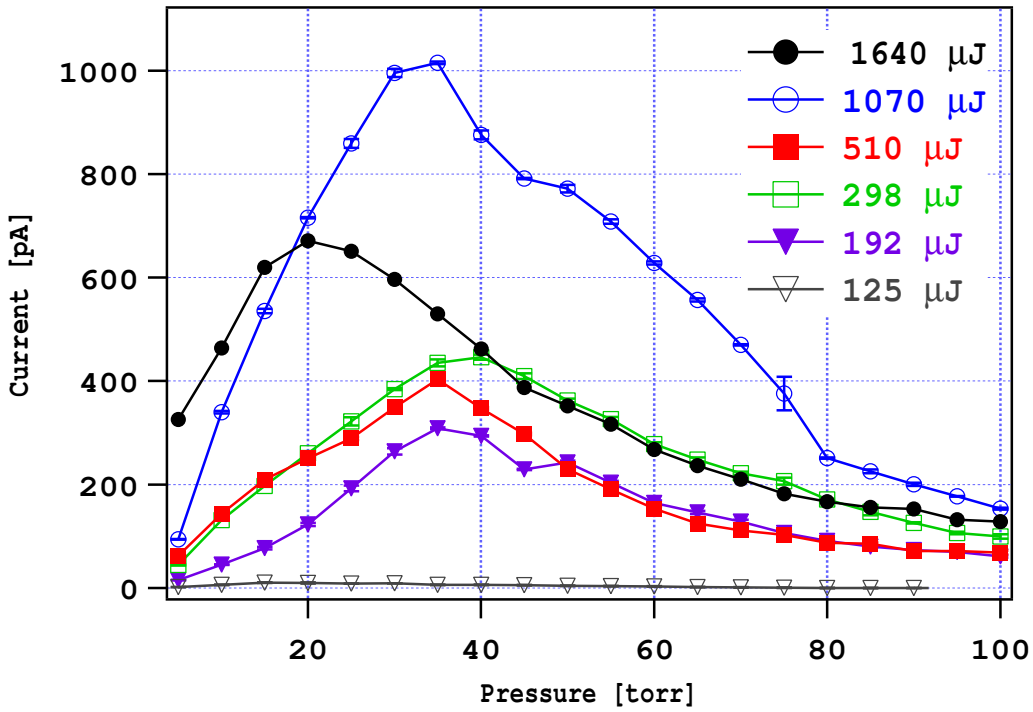

Figure 3.8: Current measured from a vacuum photodiode as a function of pressure, for several different input pulse energies.

to a larger spatial volume of emission, since there is more energy in the pulse. Pulse compression was also observed at higher pulse energies [87,117], which could allow phase matching at a higher ionization rate.

The fact that the peak current for every pulse energy, except the highest (1640 μJ), occurs at roughly the same pressure could indicate one or both of the following mechanisms. First, phase matching could occur always at the ionization just below critical. For this ionization fraction, phase matching will be observed at the same peak pressure that minimizes the phase mismatch. As the pulse energy increases, phase matching will occur earlier and earlier in the pulse, before the ionization fraction is raised above critical. Second, the decrease at high pressures occurs due to reabsorption by the argon gas medium. For the highest energy, the falloff occurs at a lower pressure. This could indicate that the limiting mechanism is energy loss, described in further

detail in the following section.

Estimation of the harmonic yield at 45 eV was relatively straightforward. The current was scaled by three factors: the Al filter transmission (0.1 ± 0.05), the quantum efficiency of the diode at 45 eV (0.050 ± 0.003), and since five harmonic orders were visible with similar brightness, another factor of 5 ± 1. The photon yield is given by:

$$yield = \frac{current}{eQEt_{Al}5} \approx 2 \pm 1 \text{ x } 10^{11} photons/sec \tag{3.1}$$

where e is the electron charge, QE is the quantum efficiency of the diode at 45 eV, and t_{Al} is the transmission of the Al filter at 45 eV. This corresponds to an energy of $\sim 2\ nJ/harmonic/pulse$. Given a driving pulse energy of ~ 1 mJ, the conversion efficiency is approximately 2 x 10^{-6}. In comparison, phase matching at the peak of the pulse occurs for a pulse energy of 298 μJ. In this case, given the peak diode current of $\sim 450\ pA$, the photon yield is $1.1 \pm 0.5\ photons/sec$, and the conversion efficiency is approximately 3 x 10^{-6}. A more accurate estimate of the photon yield would require the use of energy-selective EUV optics.

In the past, phase matching was investigated only at low pulse energies, for which the ionization level remained low throughout the duration of the pulse. In this case, phase matching could occur near the peak of the pulse. When harmonics are generated using high pulse energies, the gas may be fully ionized. In this situation, the characteristic harmonic spectra are quite different. To further illustrate the behavior of the harmonic emission generated at such a high pulse energy ($\sim 1\ mJ$), harmonic spectra were recorded concurrently with a measurement of the photon yield. The diode current as a function of pressure is shown in Fig. 3.9e) along with selected spectra (Figs. 3.9a)-d)) recorded at corresponding experimental conditions. For these data, the power recorded exiting the waveguide when under vacuum was 990 mW, and the pulse duration was $\sim 20\ fs$.

One of the features of the diode current data in Fig. 3.8 noted above is the

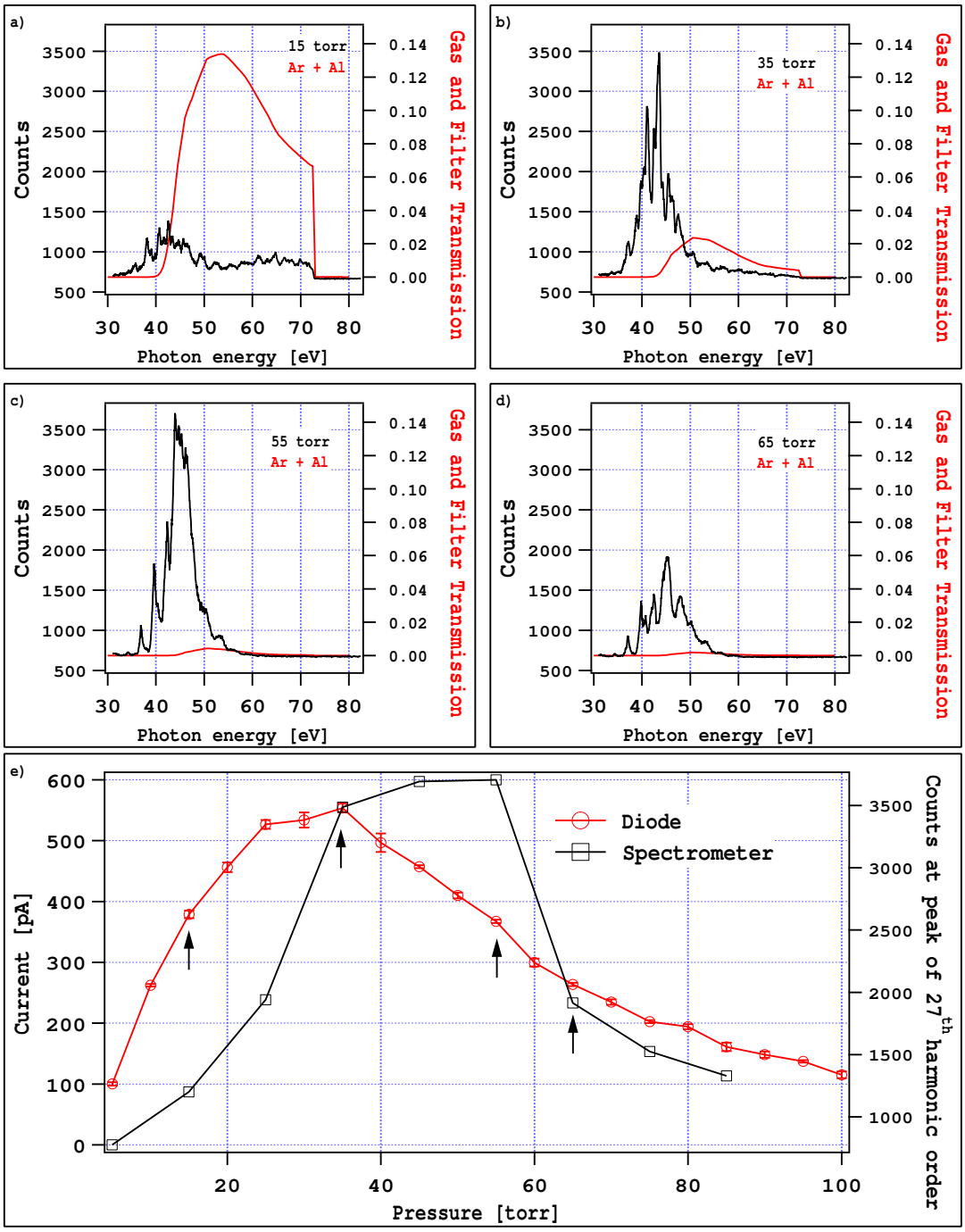

Figure 3.9: e) Current measured from a vacuum photodiode and counts from a CCD camera measured at the peak of the 27th harmonic, as a function of pressure. For several of the pressures, indicated by arrows, the spectra are plotted (a)-d)), along with the transmission of the gas and filters used.These data were generated at a high pulse energy of 990 μJ, for which argon is fully ionized.

fact that the pressure tuning curves are quite broad. Plotted in Fig. 3.9e) along with the diode current is the number of counts recorded at the peak of the 27^{th} harmonic order as a function of pressure. This provides a comparison of the photon yield for all harmonics detected with the photon yield for a single harmonic. Figure 3.9e) shows that the pressure tuning curve for a single harmonic order is narrower than that for all the harmonics together. While the diode current peaks at a pressure of 35 $torr$, the 27^{th} harmonic, as detected by the CCD camera, peaks at 55 $torr$.

The harmonic spectra generated using a high pulse energy are also qualitatively different than the spectra generated with a low energy, such as those presented in previous work (i.e., Ref. [70]). The red curves in Figs. 3.9a)-d) show the transmission of the Al filter used in addition to the transmission of argon at the pressure used. For lower pressures, photon energies are generated over the entire observable bandwidth of $\sim 35\ eV$ up to the Al absorption edge at 72 eV. The absorption depth at low pressures is long enough to transmit a significant amount of energy. Pulse compression has also been observed at high pulse energy combined with low pressure [87, 117], which can allow the generation of high photon energies. At higher pressures, however, the strong emission is limited to photon energies below 55 eV. In this case, energy loss may prevent the generation of high photon energies. The pressure of the brightest emission from the 27^{th} harmonic order is higher than the predicted phase matching pressure. However, neglecting phase matching effects, the brightness of the harmonic emission depends on the square of the pressure. This, in combination with the smoothing effects of higher absorption could result in an optimal pressure higher than that predicted by the phase matching equation.

The spectra also appear to cover a continuum, rather than exhibit well-separated peaks. This could be due to self-phase modulation from the generation of a plasma, which broadens the driving laser spectrum and hence the harmonic spectrum as well. Also easily possible is the presence of non-adiabatic blue-shifting. Since the argon is

fully ionized by the peak of the pulse, the emission is likely from the leading edge of the pulse, where the intensity is changing rapidly.

3.4 Ionization Loss

Loss of intensity in the driving laser beam is one of several effects that limit the total harmonic intensity achievable. One of the loss mechanisms, common to both free-focus and hollow waveguide geometries, is ionization loss. Because of the necessary process of photoionization that occurs during HHG, some of the laser energy is transferred in creating a plasma. Since this mechanism should depend on gas species, density, and intensity, the transmission of several waveguides were measured as a function of pressure and for a few intensities and gases. Ionization loss was also simulated using a simple numerical propagation code, the results of which are compared to the data.

Figure 3.10 shows the measured output of a 3.5 *cm* total length waveguide as a function of pressure for three different gases and three different input powers. The gas pressure was constant at the value indicated for the central 2.5 *cm* of the waveguide, and the 5 *mm* segments on either end were used for differential pumping. The input power is indicated for each graph. (Figure 3.11 shows the same for a 11 *cm* total length waveguide.) The input power was measured before the vacuum window, and the output power was measured after reflection from a silver mirror mounted in a vacuum feedthrough, and transmission through a second, uncoated glass window. A density-independent loss originates from these reflective and transmissive optics.

The ionization loss simulation models the amount of energy lost to ionization using the ADK ionization rates (Eqns. **??**). The code was a 2D propagation code, in which the energy was assumed to be distributed radially in the EH_{11} mode. The intensity was calculated for an array of annular segments. For each radial intensity value, the ionization fraction was calculated. The number of atoms was determined from the

density and the volume of the annular segment for a small propagation increment. For each atom, an energy equivalent to the ionization potential plus the ponderomotive potential ($I_p + U_p$) was subtracted from the pulse energy. A new intensity was calculated and then applied to the next propagation segment, etc., for the full length of the waveguide. Because the initial intensity was highest on-axis, the highest ionization rate and therefore the highest loss was also on-axis. The final output power was determined by summing the energy over the radial direction after propagation.

The ionization loss simulation does capture some of the significant elements of the loss as a function of pressure. The density-independent loss was neglected by fixing the incident power to that measured at the exit of the waveguide under vacuum. Higher loss was measured for the gas species with a smaller ionization potential, as expected. For helium and neon, the loss is relatively constant with pressure, however, with argon, the loss is very sharp at first, then levels out at higher pressure. This is reproduced and explained well by the simulation. What happens is that at low pressures, the gas is fully ionized throughout the waveguide. In this case, an increase in pressure simply results in more atoms to ionize, leading to a sharp loss with propagation distance. At some pressure, the rate of loss will be high enough that the intensity is reduced to a point where the ionization is less than 100% before the pulse reaches the end of the waveguide. After this point in the waveguide, the loss with further propagation is less rapid. The loss then levels out and changes only slowly with pressure. For example, in the data of the center plot of Fig. 3.10, at the beginning of the waveguide, with a power of 1.05 W and a pulse duration of 25 fs, the total ionization fractions are: helium: 4.5%, neon: 35%, and argon: 100%.

Although it appears to account for a large fraction of the density-dependent loss, the ionization loss simulation decidedly underestimates the loss in each case. One of the mechanisms for the loss of energy is due to coupling of the light into the cladding material of the waveguide. The attenuation of energy from the excited modes of the

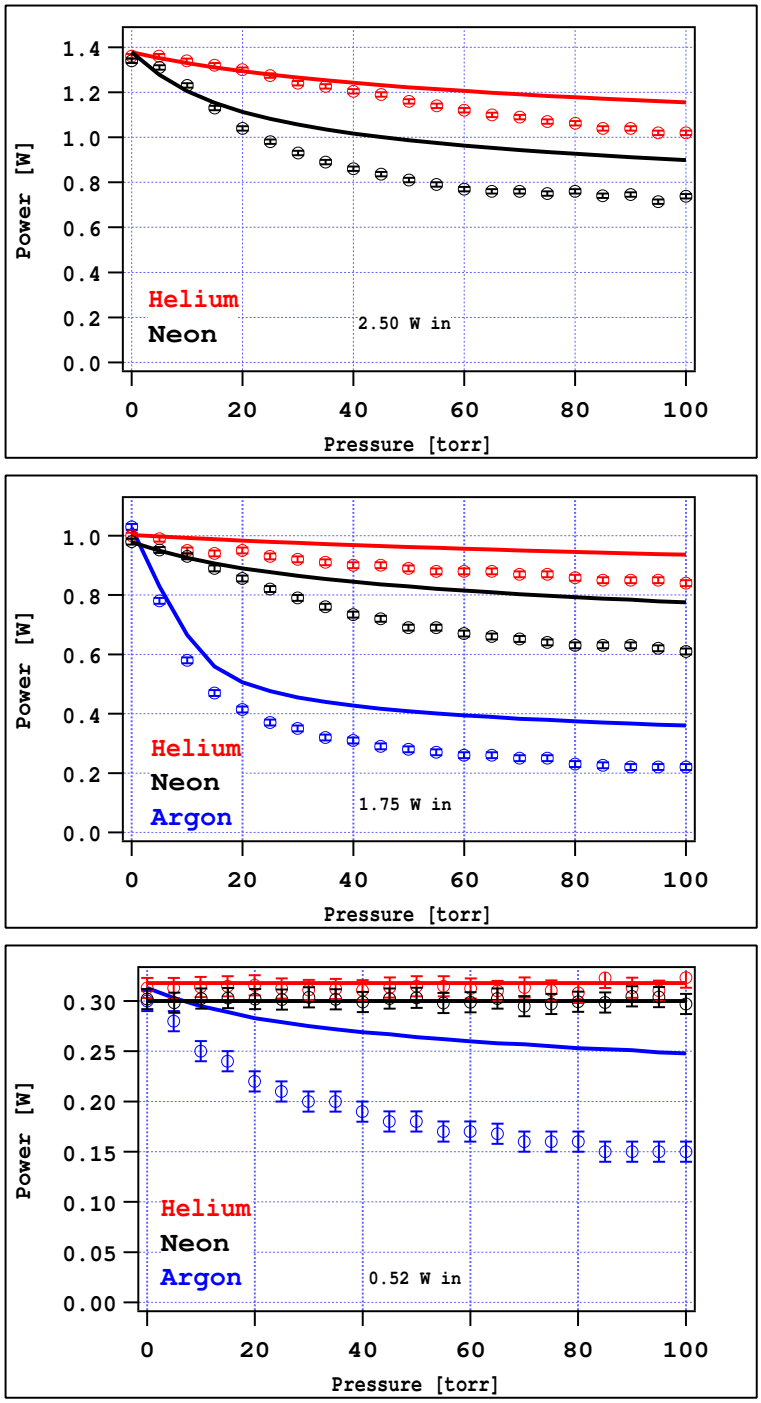

Figure 3.10: Measured output power from a 3.5 cm length waveguide, inner radius 150 μm, as a function of gas pressure, for three different gases (open circles) and three different input powers (individual plots). Repetition rate of the pulses was 1 kHz. Gas pressure was constant at the value indicated over a distance of 2.5 cm in the waveguide, with 5 mm differential pumping sections on either side. Solid curves show the results of a simulation of ionization loss.

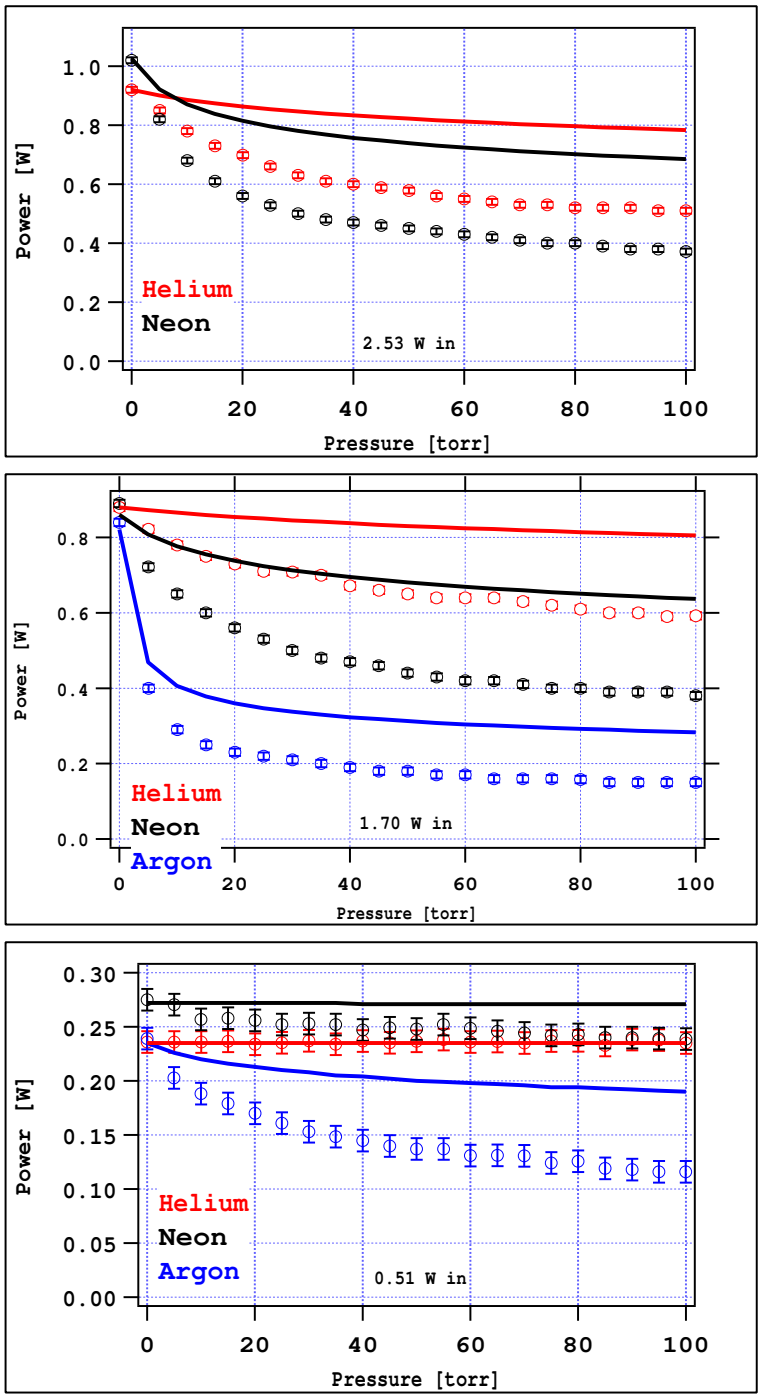

Figure 3.11: Measured output power from a 11 cm length waveguide, inner radius 150 μm, as a function of gas pressure, for three different gases (open circles) and three different input powers (individual plots). Repetition rate of the pulses was 1 kHz. Gas pressure was constant at the value indicated over a distance of 10 cm in the waveguide, with 5 mm differential pumping sections on either side. Solid curves show the results of a simulation of ionization loss.

waveguide depends on specific mode. This attenuation is described in Chapter 2, and the attenuation distances for several modes are listed in Table 2.2. Another unavoidable mechanism is coupling loss at the entrance to the waveguide. These two mechanisms cannot account, however, for the discrepancy between the ionization loss model and the loss measurement. Neither is dependent on the pressure of the gas within the waveguide, and so they instead account for the reduction of energy present when the waveguide is at vacuum.

Ionization-induced defocusing is likely the density-dependent loss mechanism not taken into account by the simulation. First, at high pressures, residual gas may be present in the region just in front of the entrance to the waveguide, due to inefficient pumping. Ionization in this region will reduce the coupling efficiency into the waveguide. Inside the waveguide, ionization-induced defocusing causes the driving laser light either to refract strongly into the cladding material, or to couple into higher order modes which are attenuated more quickly. In fact, especially for high pressures, ionization-induced blueshifting is clearly evident in the shifting of the laser beam to higher, visible frequencies. Coupling of light into the cladding is visible under these conditions, and a portion of the beam exiting the waveguide is highly divergent. In the experimental setup used for measuring loss, the steering optics aperture the exit beam, so that some of the energy does not reach the power meter detector. This also explains why the simulations appear to agree more closely with the data for the shorter waveguide.

Some of the assumptions inherent to the code will result in an underestimate of the ionization loss. First, the code calculates free electron density only from single ionization. When the singly ionized population is high early in the pulse, there is a possibility for multiple ionization, which will reduce the beam energy further. This will only reasonably effect situations where the ionization fraction is very high. The code also assumes the propagation of only the lowest order mode. The intensity fluctuations that result from mode beating can also alter the rate of ionization loss.

The maximum possible harmonic yield will depend strongly both on the transmission of the waveguides and the absorption depth of the gas. For the first case, Fig. 3.12 shows an interesting correlation between the density-dependent loss of the waveguide and the measured flux. For these data, a low pulse energy of $\sim 300\ \mu J$ was used, so that phase matching will occur near the peak of the pulse, and so that ionization loss is not too rapid. Figure 3.12a) shows the measured transmission as a function of pressure in 3.5 cm and 11 cm waveguides. Figure 3.12b) shows the diode current measured through a 200 nm thickness aluminum filter under corresponding experimental conditions. A pressure tuning curve is evident for both waveguides. However, for the 11 cm waveguide the peak of the curve is at a very low pressure, while for the 3.5 cm waveguide, the peak is at the expected phase matching pressure. It is interesting to note that the beginning of the decrease in photon yield is located at the pressure that results in the same fractional transmission ($\sim 32\%$) for both waveguides. This suggests that energy loss with increased pressure in the longer waveguide overcomes the increase in brightness due to phase matching effects.

Absorption, of course, also plays a major role, especially for photon energies around 50 eV, which are strongly absorbed by argon. The data in Fig. 3.12b) are consistent with the predictions of Constant et al. [75], as outlined in Eqn. 2.34. Recall that maximum conversion efficiency occurs when the interaction region is $> 3L_{abs}$. Near the phase matching pressure of 45 $torr$, the absorption depth of argon at 50 eV is $L_{abs} \approx 0.9\ cm$. This corresponds well to a waveguide with a 2.5 cm constant pressure region. The peak in photon yield for the 11 cm waveguide occurs at 20 $torr$. Here, the absorption depth of argon at 50 eV is $L_{abs} \approx 2\ cm$. However, energy loss in the waveguides, even at the low level of ionization present for these data, will establish an upper limit to the length of the waveguide that will produce bright, phase matched HHG. The analysis by Constant assumes that the generation of harmonics has a constant strength throughout the interaction region. However, in practice, it is clear that in the presence of loss, the

harmonic production is shut down after a given propagation distance. This could explain why high pulse energies produce a higher flux, since sufficient energy is maintained over a longer propagation distance.

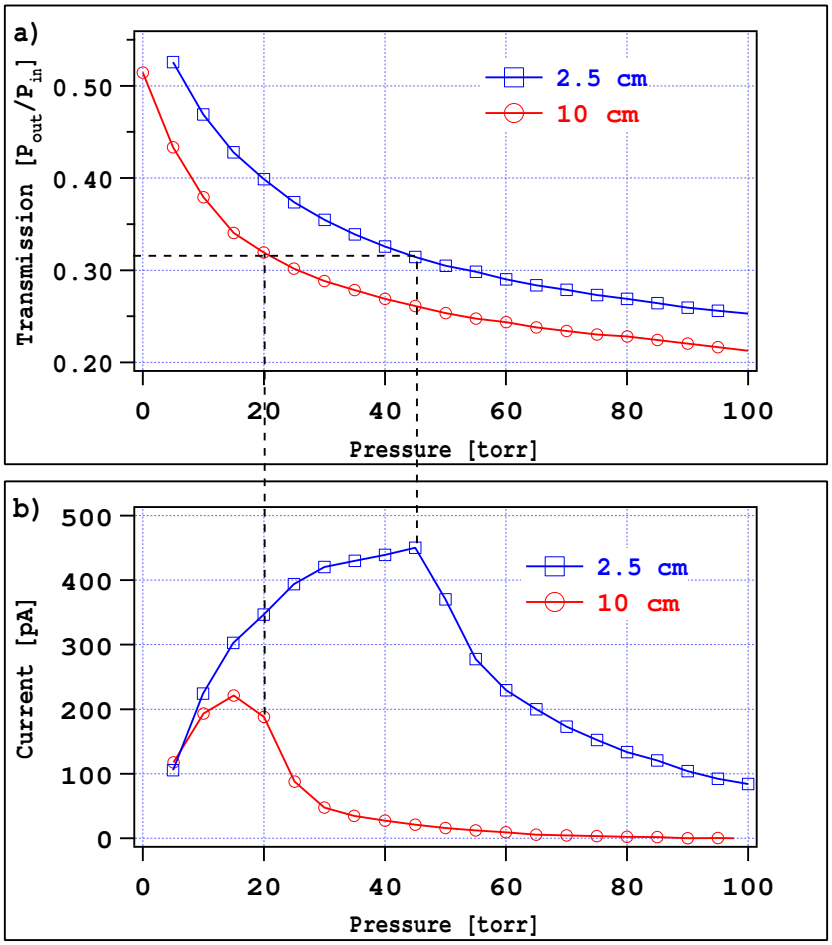

Figure 3.12: Correlation between loss and harmonic photon yield. a) Measured transmission from 3.5 cm and 11 cm total length (2.5 cm and 10 cm constant pressure regions) as a function of argon pressure. b) Corresponding measured diode current. Input power was $\sim$ 300 mW, corresponding to an ionization low enough to allow pressure-tuned phase matching.]

3.5 Modulated Waveguides

As discussed in Chapter 2, quasi-phase matching using a hollow waveguide with a modulated inner diameter is achieved through a periodic modulation of the intensity [29]. In this scheme, the cutoff photon energies are generated only in the regions of highest intensity. When this periodicity is matched to the coherence length, the conversion process can be quasi-phase matched. Figure 3.13 shows a schematic of the modulated waveguide design used in the experimental demonstration of QPM.

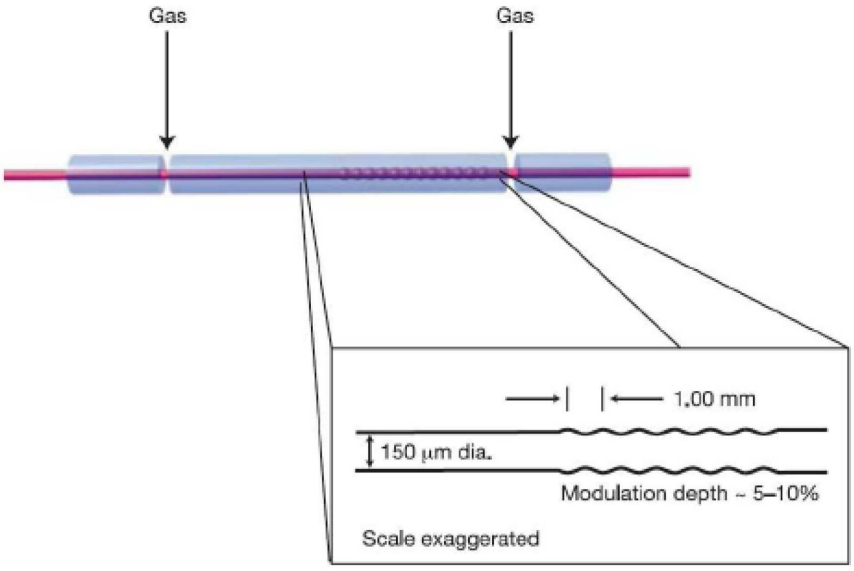

Figure 3.13: Schematic of a hollow waveguide with a modulated inner diameter, including typical physical parameters.

Among the first measurements made using the new and more reproducible v-groove mounting design were a measurement of HHG yield using modulated waveguides. In previous work [34, 35], enhancements of around 1 to 2 orders of magnitude of the photon yield, over a broad range of photon energies were demonstrated. However, while these initial measurements showed great potential for enhancement of HHG at high photon energies, it was unclear how the enhancement depended on the specific waveguide characteristics. Systematic measurements were impossible until the use of

the v-groove mount, since there was a large variation between individual waveguides. Using the v-groove setup, previous results were subsequently reproduced. Figures 3.14 and 3.15 show typical enhancements seen for HHG in helium and neon, respectively.

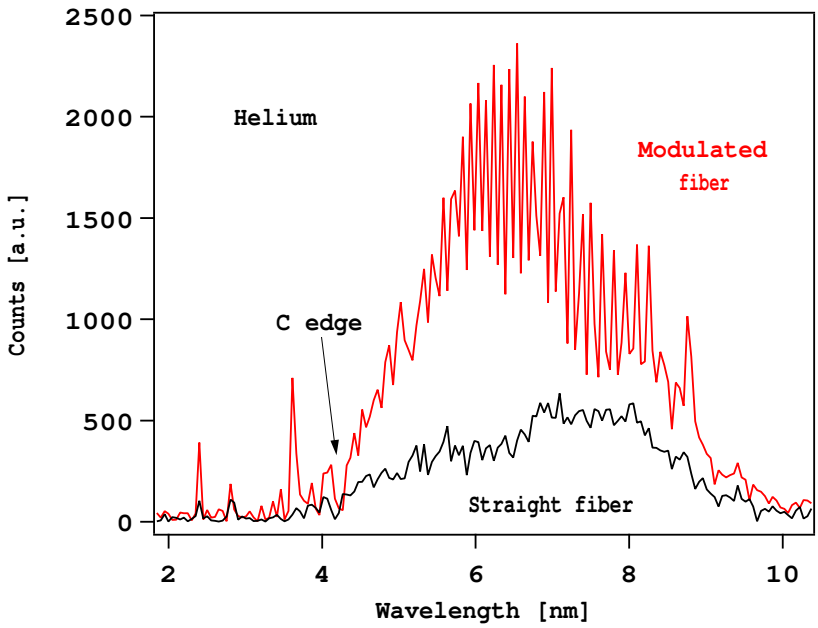

Figure 3.14: Data showing enhancement of HHG in helium through QPM using modulated waveguides.

The experimental parameters for the data in Figs. 3.14 and 3.15 were as follows. For data collected in helium, a 6 cm waveguide was used, with a constant pressure of 10 $torr$ throughout the waveguide. Modulations of depth $\sim 1.5\%$ of the inner diameter and periodicity 0.5 mm extended through the final 1 cm before the exit of the waveguide. The input pulse energy was ~ 1 mJ. The harmonic emission was detected using the SB grating, and was transmitted through 400 nm thickness Ti and 150 nm thickness Ag filters. For data collected in neon, all parameters were the same as in helium except for the following. In this case, a 3.5 cm waveguide was used, with a constant pressure of 10 or 12 $torr$ throughout the waveguide. Also, the modulations extended throughout the waveguide.

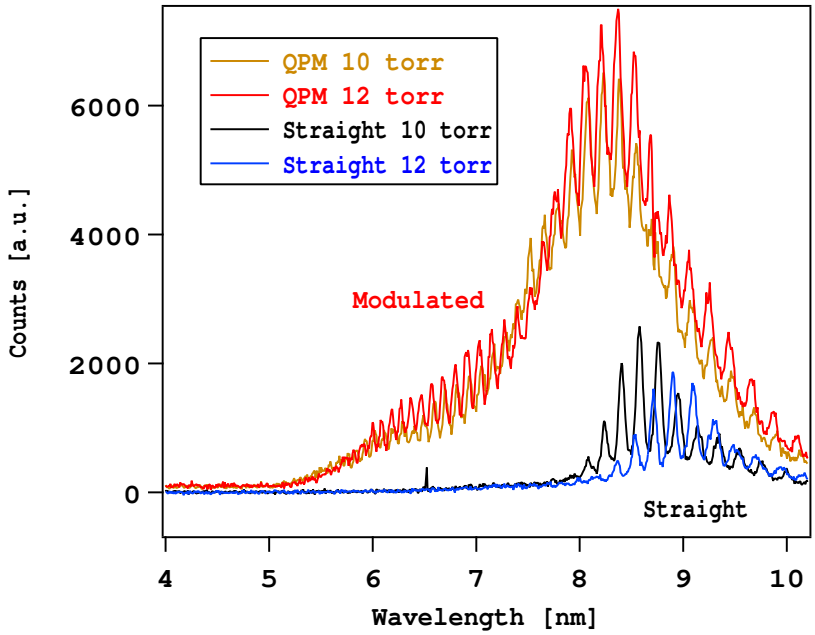

Figure 3.15: Data showing enhancement of HHG in neon through QPM using modulated waveguides.

The main effect of the modulated waveguides, in each case, is to enhance the photon yield by a factor of 2-20x higher than that produced from a waveguide with no modulations. The enhancement occurs, again, over the entire observed bandwidth. In the case of neon, the highest observable photon energy was also dramatically extended, from $\sim 7\ nm$ down to $\sim 5\ nm$. This type of enhancement was reproducible for moderate pulse energies of $\sim 1\ mJ$. At this pulse energy, the ionization level reaches $\sim 30\%$ by the end of the pulse in neon, and only $\sim 4\%$ in helium. At such low ionization levels, energy loss and refraction effects from the plasma are kept to a minimum, and the intensity modulation is expected to be dominated by the guiding effects of the modulated inner wall of the waveguide.

However, with the implementation of the v-groove mounting, an extension of the cutoff was observed for unmodulated waveguides as well. Figure 3.16 shows a spectrum generated in 15 *torr* helium that extends into the "water window" region

of the spectrum, in an unmodulated waveguide. For this spectrum, the pulse energy used was $\sim 4\ mJ$. At this pulse energy, the gas is fully ionized, and the plasma would be expected to have a significant effect on the propagation of the driving laser beam. Under these conditions, higher order modes may be excited in the waveguide, producing short regions of higher-than-expected intensity. This boost in intensity could explain the very high cutoff photon energies observed. Pulse compression may also play a role: pulse compression in argon was observed under similar ionization conditions [87, 117]. Although it was not measured in this case, it is possible that self-pulse compression contributed to the generation of very high photon energies seen in Fig. 3.16.

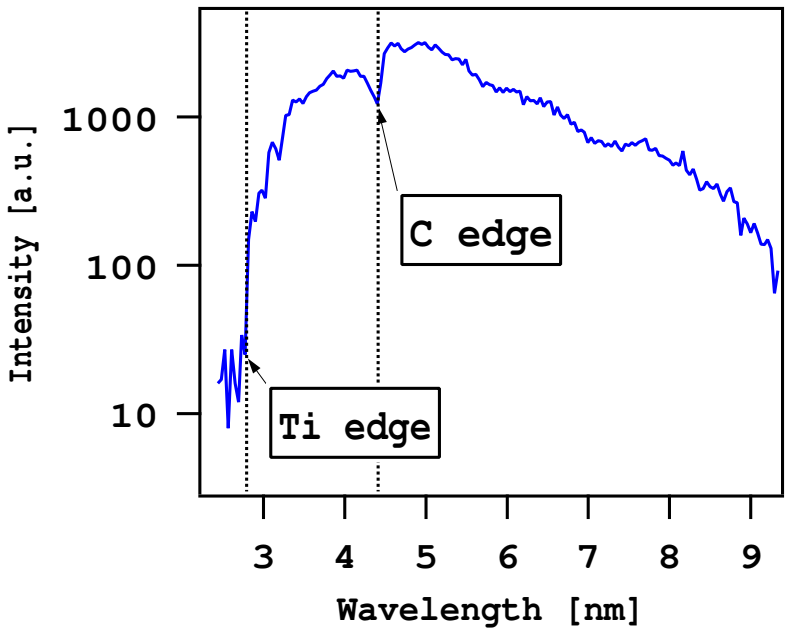

Figure 3.16: Data showing HHG emission from helium extending into the "water window" up to the Ti L edge.

Without the ability to measure intensity fluctuations in the waveguides, however, it is difficult to make further claims, either about the nature of QPM using modulated waveguides, or the generation of high photon energies in unmodulated waveguides. The need to understand the dynamics of the intensity was, in part, the motivation to develop

the probing technique described in Chapter 4. A better understanding of the spatio-temporal dynamics of the driving laser beam is essential to further progress in quasi-phase matching techniques.

Modulation Depth Dependence

Another measurement performed using the v-groove mounting was a study of how the modulation depth affects the enhancement. The goal of the modulation depth study was to determine the optimal modulation depth for QPM enhancement. In past studies, it had been found that modulation depths estimated to be a few percent of the inner diameter of the waveguide had produced the highest enhancements. However, a careful measurement and correlation had never been performed.

Modulated waveguides were manufactured using the glassblowing lathe setup described above (and in more detail in Ref. [1]). In order to characterize the waveguides, the modulation depth was measured by placing the waveguide in an index-matching fluid to eliminate lensing effects by the curved outer surface of the waveguide. The waveguides were placed in the fluid in a such a way that the inner bore remained filled with air, to provide a good contrast for measurement. Images of each waveguide were recorded using a digital camera equipped microscope. With the magnification used, the pixel size was estimated to be roughly 1 μm. For each waveguide used, a consistent modulation depth was confirmed. The transmission efficiency of each waveguide was also tested using a HeNe laser to ensure consistency. Waveguides with a transmission of less than 90% of the energy, or with a mode that did not appear symmetrically round, were rejected. The only exception to this was the largest modulation depth tested, for which mode degredation and reduced transmission was consistent. Six different modulation depths were tested: 0%, or the "straight," control waveguides, $0.8 \pm 0.7\%$, $1.6 \pm 0.3\%$, $2.4 \pm 0.6\%$, $4.2 \pm 1.6\%$, $6.5 \pm 2.5\%$, where the uncertainties are the standard devations of the measured modulations.

The measurements were performed in very low pressure neon ($0.7 - 3$ $torr$), for

several pulse energies (in the range $0.85 - 1.70\ mJ$). Low pressures and pulse energies were chosen in order to minimize detrimental effects due to ionization. The waveguides each had a total length of 3.5 cm, with a central constant pressure region 2.5 cm long, and a 5 mm pumping section on either end. The modulations had a periodicity of 0.5 mm and were present throughout the 2.5 cm central section. For the data collection, the wavelength scale was calibrated using boron and carbon filters, and for each data set, an identical background scan was taken in which the harmonic emission was suppressed by rotating a quarter-waveplate in the driving laser beam path. The integration time on the camera was 240 s, and 6 pixels were binned in the direction of the diffraction, in order to increase signal-to-noise. The grating used was the SB survey grating, and the driving laser wavelengths were attenuated using a 400 nm Ti and a 150 nm Ag filter.

For each modulation depth, five individual waveguides were tested. The plots in Fig. 3.17 include the averaged spectra from each of the five modulation depths. Typical standard devation error bars are included on the spectrum average for the modulation depth of 4.2%. Five "straight," or unmodulated, waveguides were also measured. The shaded region on the graph represents the range included in one standard deviation above and below the average straight fiber spectrum.

Figure 3.17 shows the results for the lowest pulse energy tested, which is representative of the general trends of the data. Enhancements were observed only for the smallest modulation depths of 0.8 and 1.6% of the inner diameter. The enhancement is typically broadband, extending from $\sim 8\ nm$ to the cutoff at $\sim 8\ nm$. The signal tends to exhibit a general decrease with increasing modulation depth, however. The only exception to this was the modulation depth of 2.4%, which consistently produced the weakest HHG signal. For the largest depths, the HHG signal drops dramatically, which is consistent with their reduced transmission of the driving laser beam. It seems that in general, however, the optimal modulation depth is <2%, since for greater depths, the loss appears to counteract any gains from a quasi-phase matching effect.

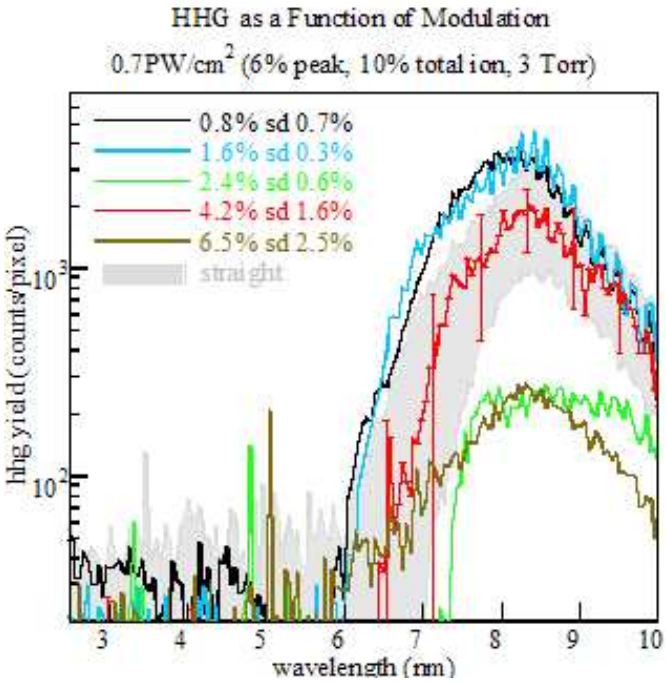

Figure 3.17: HHG yield from neon as a function of wavelength, generated in modulated waveguides with varying modulation depth, for a pulse energy of 0.7 mJ and a pressure of 3 $torr$.

Chapter 4

Probing and Quasi-Phase Matching of High-Order Harmonic Generation Using Counterpropagating Light

4.1 Introduction

In this chapter, I describe the use of counterpropagating pulses for probing and manipulating HHG. Counterpropagating light is used to selectively suppress the coherent buildup of HHG, leading to several new types of measurements. In particular, information about the coherence of HHG and evolution of the phase of the generated harmonic field with propagation is revealed. Accurate measurements are shown of the in-situ coherence length of the nonlinear conversion process. From the direct measurement of the coherence of HHG, new information may be indirectly obtained about several different aspects of this process. First, the evolution of the coherence, or phase mismatch, is sensitively dependent on the local and instantaneous driving laser intensity. Fluctuations of the intensity due to loss or interference mechanisms are thus directly mapped onto the coherence, and can hence be inferred from a measurement of coherence length. Until now, the precise location of harmonic emission within the waveguide was not known. By probing with a counterpropagating pulse, the location of brightest generation of a given harmonic order may be mapped within the waveguide, and it has been found to be more complex than previously thought. Even temporal dynamics can be inferred from measurements of coherence with sub-cycle resolution.

Careful measurements of the coherence length are then used to implement a

new, all-optical technique for quasi-phase matching. Using trains of counterpropagating pulses, enhancement of HHG is demonstrated for high photon energies, for which conventional phase matching techniques are not possible. In two different cases, the HHG signal is enhanced by more than two orders of magnitude. The photon yields obtained with all-optical QPM are shown to be comparable to those obtained with conventional phase matching techniques at lower photon energies. Further enhancements should be straightforward with with implementation of longer pulse trains. This technique is shown to be flexible, applying to range of photon energies and ionization levels, and customizable for compensating a wide range of phase mismatch. All-optical QPM is also shown to provide a mechanism for controlled enhancement of HHG. Selectivity and tunability of the enhanced photon energy is shown, along with selectivity of either of the two quantum paths that contribute to HHG emission. This selectivity could, in the future, allow temporal and spatial manipulation of high harmonic generation, as well as provide a mechanism for improved temporal and spatial coherence.

This importance of this work is in gaining insight and information on previously unknown and inaccessible physics of the HHG process in hollow waveguides. This information will be invaluable in overcoming the present limitations on HHG to make it possible to implement a useful, tabletop source of ultrafast, coherent, soft x-ray light.

4.2 Experimental Setup

The laser source, HHG waveguide setup, vacuum setup, and EUV detection used for the studies described in this chapter are the same as were described in Chapter 3. The parts of the setup relevant to the counterpropagating pulse scheme are outlined here.

The initial setup for creating counterpropagating pulses is shown in Fig. 4.1. The output of a Ti:sapphire CPA system is split after compression; part of the energy, compressed to $25 - 30\ fs$, is coupled into a hollow waveguide to drive the harmonic

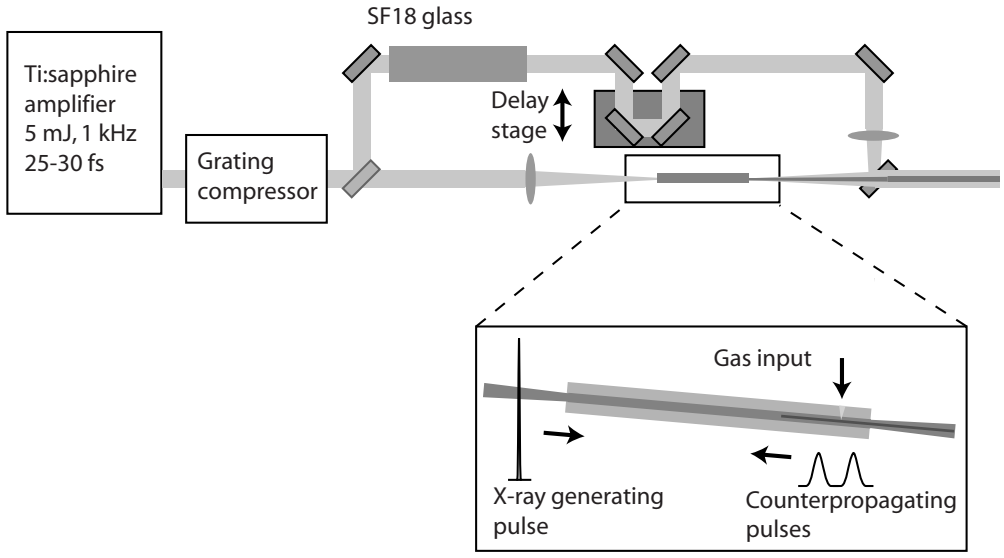

Figure 4.1: Experimental setup for generation and coupling of a single counterpropagating pulse, using bulk material for stretching the pulse. Delay lines are not to scale.

generation. The other part of the beam propagates through 10 cm of SF18 glass, stretching the pulse through normal material dispersion to around 1.6 ps. This pulse then propagates through a delay line, which allows relative adjustment of the timing of the forward and counterpropagating pulses. A polarizer in the delay line is adjusted to assure a close match in the polarizations of the forward and counterpropagating beams. Finally the beam is coupled into the opposite end of the waveguide using a lens. Since the orientation of the waveguide is fixed for optimal alignment of the HHG beam into the spectrometer, fine adjustments to the coupling of the counterpropagating beam were accomplished by adjusting the X-Y position of the lens. The forward and counterpropagating pulses have the same propagation distance between the splitting of the beam and the coupling into the waveguide, so that they overlap in space and time in a small region the waveguide.

To allow propagation of the harmonic light to the detection system, a 3 mm hole is drilled into a mirror at a 45° angle past the exit of the waveguide. This mirror then directs most of the energy of the counterpropagating beam into the waveguide. The

mirror is located between the focusing lens and the end of the waveguide. The annular shape of the counterpropagating beam focuses to a nearly Gaussian beam, as shown in Ref. [118]. However, diffraction at the sharp edges degrades the quality of the beam at the focal spot, leading to poor coupling. At high intensities, imperfect coupling also results in ablation of glass at the entrance to the waveguide, further degrading the coupling efficiency. The counterpropagating beam, when focused with a 50 *cm* focal length lens, positioned about 15 *cm* before the mirror, loses about 30% of its total energy due to this hole.

This setup was used for initial measurements of coherence length, but was eventually changed for several reasons. First, the ultimate pulse duration was determined by the length of the material and was not continuously adjustable. Adjustment of the pulse duration by using different lengths of material was prohibitively expensive. Second, since the pulse was compressed in time before propagating through the SF18 glass, nonlinear phase accumulated while the intensity remained high in the first several millimeters of propagation. This distorted the beam, making coupling of the light into the waveguide more difficult. Finally, there was no simple method for creating multiple pulses for all-optical QPM. The use of a thin sapphire substrate to create a series of pulses was briefly explored. By exploiting the birefringence of sapphire, a beam passed through the plate with its polarization at 45° relative to the optic axis. This produced two slightly delayed pulses. generating a sinusoidally modulation of the intensity. However, this configuration did not yield significant enhancements, mostly due to the inflexibility of the design.

Figure 4.2 shows a revised design for the creation of a counterpropagating pulse train. Instead of splitting the beam after the compressor, the beam was split before compression. Each beam propagated through separate, grating pulse compressors, so that the pulse durations could be adjusted separately and continuously. The advantage of splitting the beam before compression is that each beam propagates only once through

the grating pulse compressors, each having a throughput efficiency of about 60%. This allows the new design the same overall efficiency as the material stretcher design.

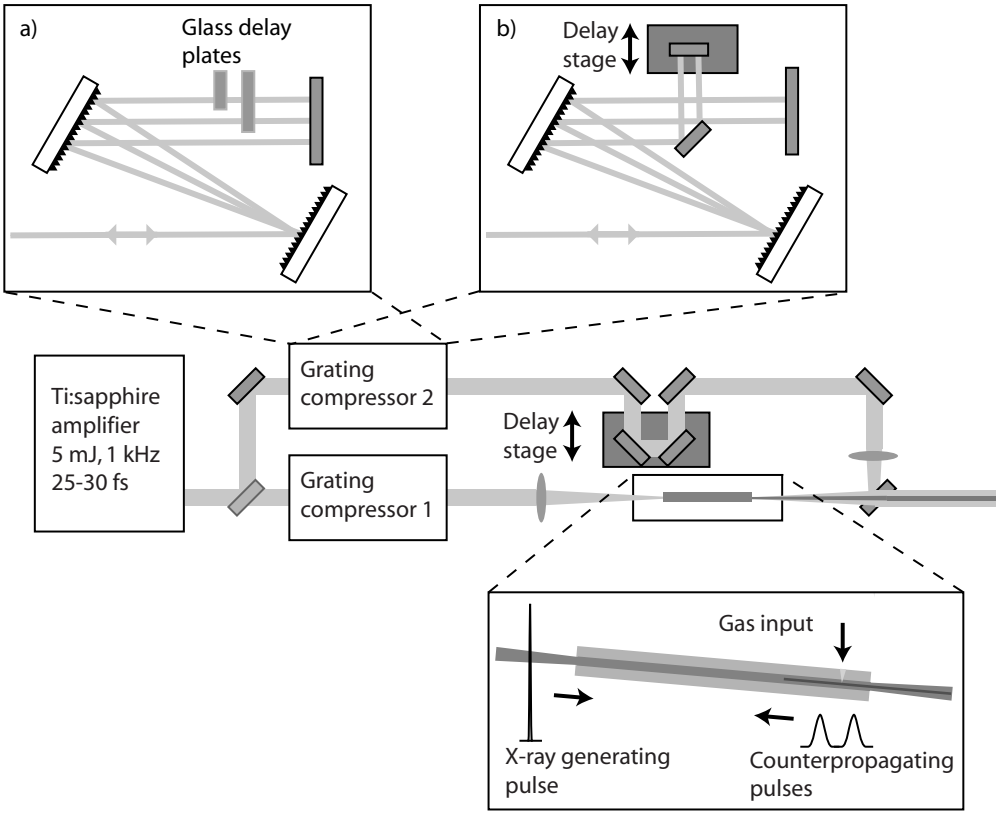

Figure 4.2: Experimental setup for the generation and coupling of one or more counterpropagating pulses, using phase masks within a grating pulse compressor.

Insets a) and b) in Figure 4.2 illustrate diagrammatically how multiple counterpropagating pulses, separated by a small time delay, were created using the grating pulse compressor. In a), glass plates are inserted in the beam path at the frequency-dispersed plane of the compressor (see Ref. [7] for details on grating-based stretcher/ compressor designs). By propagating different frequency components through different amounts of material, a series of pulses with differing center wavelength were created. The frequency range was typically chosen so that each delayed component had approximately the same total energy. The separation is static and depends on the thickness and index of the glass used. For data presented in this chapter, the counterpropagating beam was lin-

early chirped by the compressor, so that the low frequency light preceded the higher frequency light. Third order dispersion was minimized. Combinations of 2 mm and 5 mm thickness, uncoated BK7 plates, were used to create 3 pulses in sequence at various delays.

In principle, the setup of Fig. 4.2 could serve as an almost lossless technique. However, efficient implementation requires some care. First, the windows must have sufficiently parallel surfaces, so that one part of the beam is not deflected relative to the other. Even a very small wedge can severely affect coupling into a 150 μm inner diameter waveguide several meters away. Second, with about 4% loss at each surface, multiple windows can add up to significant loss without proper antireflection coatings. For the data presented here, the windows used were not coated, however, they were selected for minimum deflection of the beam.

Inset b) of Fig. 4.2 shows a second iteration of this setup. In this case, a mirror directs half the beam's energy to a second retroreflector which is mounted on a motorized delay stage. The advantage of setup b) relative to setup a) is that the time delay between the two pulses can be adjusted continuously. However, this is a more complex setup and requires additional care in alignment. First, the two retroreflectors in the compressor are ideally identical, and have very little deviation of the beam with vertical tilt. The mirror reflecting light to the moveable retroreflector must be large enough in area to reflect both the incoming and vertically displaced outgoing beams. It is oriented as indicated in inset b) of Fig. 4.2 so that the depth of the substrate and mount do not clip the beam on either side. The static retroreflector may be moved farther from gratings to accommodate this mirror. However, minimal propagation of the beam in the frequency-dispersed region reduces instability due to air currents. Properly recombining the two time-delayed beams requires two additional alignment considerations. First, the beam must encounter both retroreflectors at the same height so that the outgoing beams return at the same height. Second, the delay stage must translate smoothly and parallel

to the direction of the beam, so that the coupling into the fiber (again, several meters away) is not altered significantly.

In order for the two pulses to interfere within the waveguide, the path lengths of the forward propagating beam line and the counterpropagating beam line must be equal (Figs. 4.1, 4.2 are hence not drawn to scale). For the present work, this was accomplished by careful, manual measurement of the two path lengths from the beamsplitter that separates the beams combined with adjustment of the path lengths through static, optical delay lines. The path length of each beam was ∼10 m. For stability, these beam lines were enclosed by custom acrylic boxes and beam tubing constructed to minimize air currents. Maintaining efficient and consistent coupling into the waveguide is a particular challenge when using this setup. However, especially in the initial stages of setup and testing, a long path length was preferable, for flexibility. Furthermore, it is likely that the long path length partially prevented feedback into the amplifier from the counterpropagating beams. Upon exiting the waveguide, the counterpropagating light was refracted strongly by the plasma, and this strong divergence limited the energy propagating back through the delay lines.

Information about the coherence of HHG was inferred by observing the HHG output while scanning the suppression region where the two pulses collide along the common axis of propagation. This scan was performed using a motorized delay stage in the counterpropagating beam line (see Figs. 4.1 and 4.2). A hollow corner cube retroreflector was mounted on the delay stage. Adjustment of the delay stage position changes the relative path lengths of the forward and counterpropagating pulses, so that the position of the collision point can be adjusted. One of two microstepper motors was used: a Melles Griot Nanomover, with a range of approximately 1 in, and a Thorlabs NRT motor, with a range of 10 cm. Typical step sizes used for data collection were $50 - 200\ \mu m$. For the experimental setup used, the step size of the motor corresponded directly to the change in position of the collision region. For example, when the motor

moves a distance 1 mm, the change in path length for the counterpropagating pulse is 2 mm due to the retroreflection. However, since the two pulses propagate in opposite directions, each pulse makes up half this distance before colliding, so that the position of the collision point moves 1 mm.

Identification of the collision point of the two pulses was accomplished as follows. The pulse for each beam was fully compressed through optimization of the grating pulse compressor. The two beam lines were propagated to the interaction region, but with the waveguide removed, and the delay was adjusted so that the pulses were focused at the same location in space. Both the forward and counterpropagating pulses were capable of generating a visible filament of plasma ($\sim 2-3$ cm in length). Astigmatism was minimized by slight tilting of the lenses to minimize the length of the filament. Once the two counterpropagating plasma filaments were overlapped well in space, the collision point could readily be observed as a brighter spot in the plasma that moved when the relative path lengths of the two pulses were adjusted. A photograph of the filament with a bright collision point, along with a schematic of the beams, is shown in Fig. 4.3.

If the collision point could not be located this way, it was possible that the collision point occurred on either side of the filament, where the beam was not focused strongly enough to ionize the air. The bright collision point will be visible only when the two pulses are overlapped well in space and in time. However, the collision point could be located indirectly. When the air is ionized, self-phase modulation generates new frequencies which lie outside the reflectivity bandwidth of the steering mirrors for each beam. This means that there is visible light that can easily be observed leaking through the steering optics. Consider the following example. If the forward pulse collides with the counterpropagating pulse *before* it reaches the plasma region at the focus, it will propagate through the counterpropagating pulse's plasma wake and be spatially distorted by refraction of the plasma. The plasma will diffract away the central part of

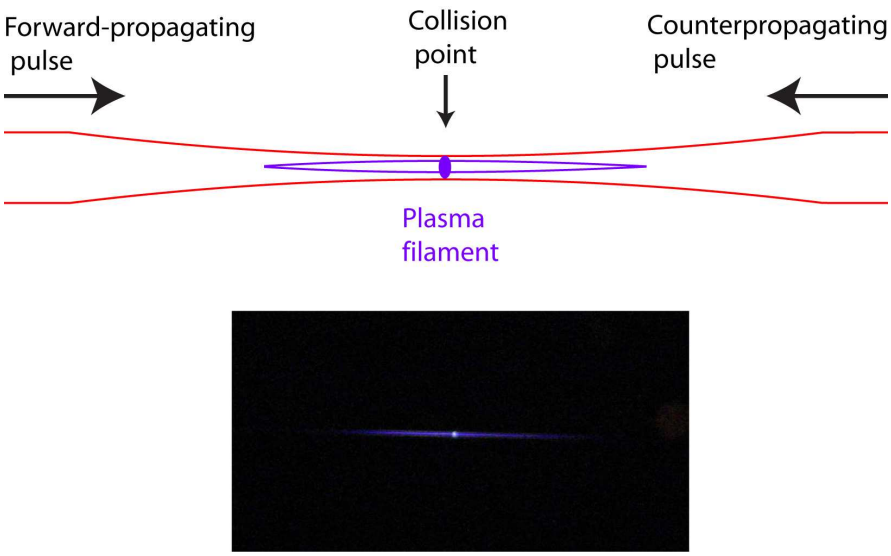

Figure 4.3: Photograph of the air plasma filament created in the free focus of the counterpropagating beams. The bright point of plasma emission occurs at the collision point of the two pulses.

the forward beam. However, the counterpropagating pulse will not propagate through the forward pulse's plasma, since it collides *after* the focus region, and hence the beam will not be distorted. By identifying which beam is distorted, it can be deduced on which side of the filament the collision point is located.

4.3 Single Pulse Probing

One of the more revealing and useful measurements that can be accomplished with counterpropagating light is that of the local coherence length of high-order harmonic generation. In fact, this technique is capable of measuring coherence lengths in-situ, over several harmonic orders simultaneously, and over an extended length. The coherence length is shown to evolve with propagation distance in the waveguide. This measurement provides previously unknown detail in the evolution of the phase of harmonic light, and indirectly, the evolution of the intensity and phase of the driving laser light.

The coherence length can be measured by using the counterpropagating pulse to

suppress the harmonic field buildup in the overlap region of the forward and counter-propagating pulses. This overlap region is then scanned along the propagation direction of the waveguide by adjusting the time delay between the forward and counterpropagating pulses. Figure 4.4 shows the result of such a scan. Harmonic spectra, generated in argon, are shown as a function of the position of the collision point of the two pulses.

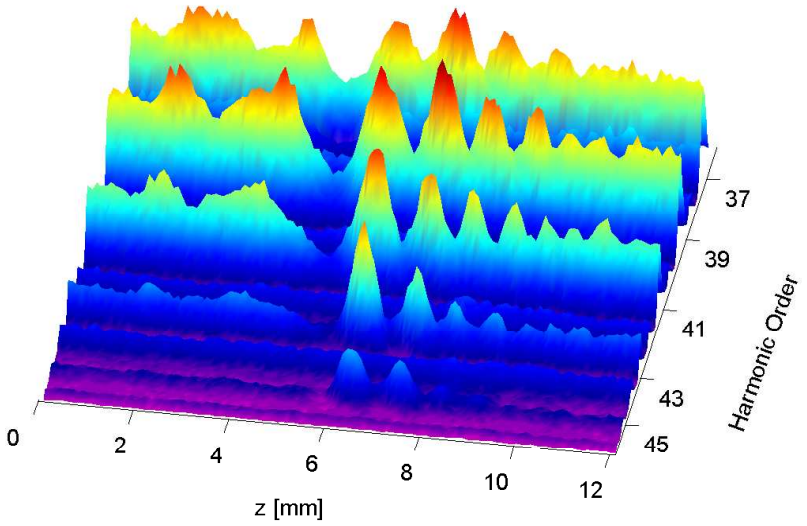

Figure 4.4: The effect of a single counterpropagating pulse on the high harmonic emission from orders q = 37-45 in low pressure argon. The local coherence length can be directly measured in-situ from the coherence fringes which appear as a function of the intersection point, z, of the forward and counterpropagating pulses [119].

For these data, a 3.5 cm waveguide was used, with 5 $torr$ of argon introduced approximately 5 mm from each end of the waveguide, producing a constant pressure throughout most of the waveguide, and a rapid pressure drop at either end. In Fig. 4.4, the exit of the waveguide is located at z = 0 mm, the differential pressure region at z = 0 to 5 mm, and the gas inlet at z = 5 mm. The forward pulse duration and energy were 27 fs and 0.65 mJ, respectively, while the counterpropagating pulse duration and energy were 1.6 ps and 0.155 mJ, respectively. The fundamental light is suppressed with two

200 nm thickness aluminum filters. The integration time of the CCD camera was 0.2 s, and the spectrometer grating used was SC (see Chapter 3 for grating information).

When the overlap region is approximately the same width as the coherence length for the generation of a particular harmonic order, the counterpropagating light can have a significant effect on the overall output harmonic intensity. In the absence of phase matching, the observed harmonic signal originates from a single coherence length. Suppression of the harmonic light originating from a similar strength coherence zone will thus have a large effect on the observed signal. Consider a simple picture of the nonlinear conversion process in which the phase slip (coherence length) and harmonic emission strength are constant with propagation distance (see Fig. 4.5). The final, N^{th} coherence length is the one detected, while the zones preceding it will have alternating overall phase values. If the harmonic field from zone N-1 is suppressed, then it will no longer be destructively interfering with the harmonic light immediately preceding it, from the zone N-2. Now zone N-2 interferes **constructively** with zone N, doubling the overall detected field strength (the intensity increasing by 4x). This will be referred to as suppression from an "out-of-phase" coherence zone. Conversely, suppression of harmonic buildup from an "in-phase" coherence zone will cause an overall decrease in the detected harmonic signal.

As can be seen in Fig. 4.4, distinct modulations are observed in the intensity of each harmonic order, as the overlap region that suppresses harmonic buildup is scanned through the interaction region. The periodicity of these modulations is twice the coherence length, $2L_c$, allowing the local coherence length of the process to be directly measured from these data. The contrast of the modulations can be seen to vary with both location and harmonic order. This is due to the fact that the coherence length and harmonic emission strength vary with both position and harmonic order. These variations are described in more detail below. The greatest contrast will occur when the overlap region precisely matches that of the coherence length, and when the signal

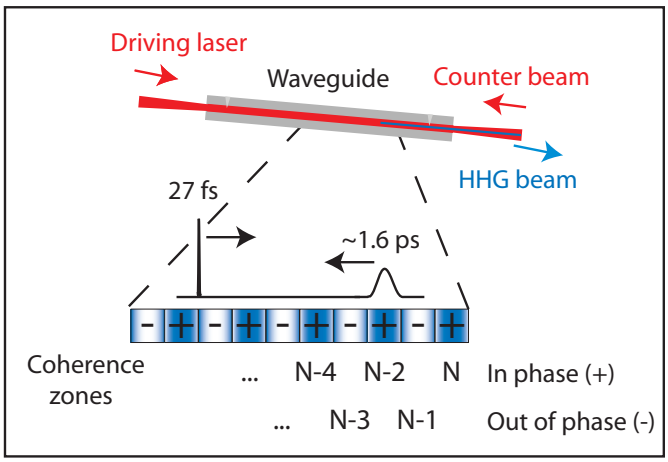

Figure 4.5: Measuring the coherence length of HHG in a hollow waveguide. A schematic of the coherence zones present within a waveguide when the phase mismatch is nonzero. For N total coherence zones, the total harmonic signal detected is only from the final, N^{th}, zone, since all other "in-phase" zones can be paired with a destructively interfering, "out-of-phase" zone.

strength of the two constructively interfering zones is the same. When the counter-propagating light permits transmission from a coherence zone that has a smaller field strength than the final zone, either due to absorption by the gas medium, or a weaker harmonic emission, the contrast of the fringes will decrease. In these cases, however, weak contrast of the modulations is not an indication of poor relative coherence.

Strong contrast in the measured interference fringes, over an extended interaction distance is then not a necessary, but is a sufficient, indication of strong relative coherence between harmonic emission from different locations in the waveguide. The longer the distance over which the harmonic emission maintains a good relative coherence, the greater the potential for enhancing HHG using QPM. Strong contrast of the modulations have been observed for distances over 1 cm in hollow waveguides (see, e.g., Fig. 4.6). This shows that the waveguide geometry provides the long range coherence necessary for implementing all-optical QPM. Especially when the coherence length is very short, in the case of high photon energies, substantial enhancements could be made by correction of

the phase mismatch over a long propagation distance. Ultimately, the absorption depth of the gas medium for the photon energy of interest is what will limit the obtainable flux [75]. For certain photon energies, such as the "water window" region at $\sim 2-4$ nm, helium has a very long absorption length at typical useful gas pressures ($\sim$10's of cm), much longer than the typical coherence length there ($\sim$10's of μm). In this type of situation, all-optical QPM in a hollow waveguide is an ideal solution for improving the conversion efficiency. For example, if L_c was approximately constant at 10 μm, and all-optical QPM can be implemented over a distance of 1 cm, the total enhancement of the conversion efficiency would be nearly six orders of magnitude.

Spatial Dynamics

While the hollow waveguide geometry provides a long interaction distance by maintaining a high intensity through guiding of the driving laser, the HHG process is sensitive even to small variations in the peak intensity and pulse shape of the driving field. Probing with a single counterpropagating pulse can provide information about the variation of the intensity of the driving laser. As described in Chapters 2 and 3, the energy of the driving laser pulse will vary with propagation distance. In particular, the intensity decreases with propagation due to various loss mechanisms: from the imperfect guiding of the hollow waveguide, from the energy lost to the ionization process, and from defocusing of the light by the plasma. The effect of this decreasing intensity on the coherence length is through the level of ionization. The free electrons are strongly dispersive, and even a slight change in their density will affect the phase mismatch. As the intensity decreases, the ionization level follows, reducing the phase mismatch. The expected effect is an increase in the coherence length toward the exit of the waveguide. This effect is shown in Fig. 4.6: the periodicity of the modulations increases toward the exit, indicating a lower density of free electrons, and hence a decreasing intensity.

Another source of variation in the driving laser intensity is the interference of propagating modes of the waveguide. When there is a significant amount of energy

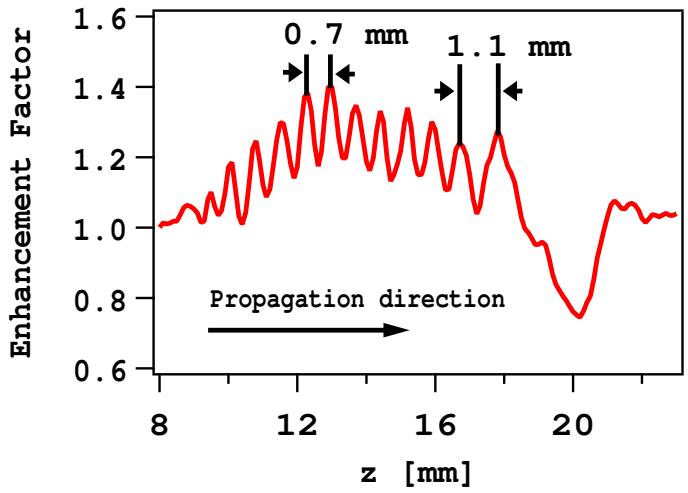

Figure 4.6: Intensity modulations of the 41^{st} harmonic order generated in argon. A changing periodicity of the intensity modulation with propagation distance indicates a reduction in the intensity of the driving laser toward the exit of the waveguide [120].

propagating in both of the two lowest-order modes, EH_{11} and EH_{12}, of a waveguide with inner diameter 150 μm, an on-axis intensity modulation forms with a period of $\sim 2.2\ cm$. (See Chapter 2 for details on mode propagation.) In fact, a modulation of the brightness of the plasma emission with roughly this periodicity is typically observed, similar to those shown in Ref. [32]. For a sufficiently strong modulation of the intensity, the harmonic generation will be limited to the regions of highest on-axis intensity. This effect is shown in Fig. 4.7, which shows modulations in the intensity of harmonics 25 and 39, generated in a 6 cm waveguide filled with argon.

The periodicity in the data of Fig. 4.7 agrees well with that observed in a simulation of the modebeating effect, shown in Fig. 4.8. For this calculation, the energy of the driving laser beam was divided between two modes, with 67% of the laser energy in the EH_{11} mode and 33% of the energy in the EH_{12} mode. Decreasing energy with propagation distance can been seen in the simulation, as a result of guiding loss and simulation of ionization loss as described in Chapter 3. The intensity profile is plotted as a function of both propagation distance and waveguide radius.

Another aspect worth noting about the data of Fig. 4.7 is where within the waveguide the different harmonic orders are generated. At z $\approx$ 5 cm, there is detectable emission from the 25^{th}, but not the 39^{th} harmonic order. This makes sense from the standpoint that, due to loss, the driving field does not maintain sufficient intensity to generate the higher photon energies further in the waveguide. Additionally, the absorption depth of the 25^{th} harmonic is $\sim$ 0.5 cm at the pressure used here, while the absorption depth of the 39^{th} harmonic is $\sim$ 4 cm. This explains why there is no detectable response at the 25^{th} harmonic order to the counterpropagating light near the entrance of the waveguide, at z $\approx$ 0.8 cm.

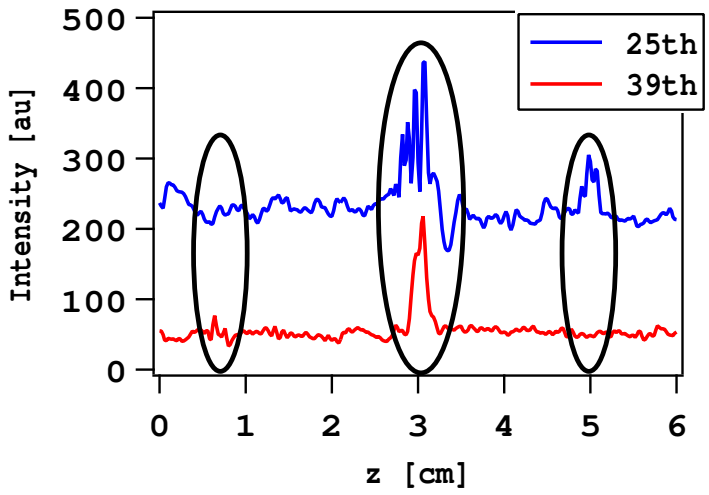

Figure 4.7: Variation of the harmonic emission generated in argon as function of the overlap region of the forward and counterpropagating pulses, for two harmonic orders, q = 25 and 39. In the figure, the harmonic light propagates toward increasing z. Modulations appear only in limited locations within the 6 cm length waveguide (circled), with a periodicity corresponding to the periodicity of intensity modulations due to modebeating [120].

Modulations were often observed only in limited regions within the waveguide. Two possible reasons for this observation are absorption of harmonic light by the gas medium and a restricted region of high intensity due to modebeating. Another possible reason is that modebeating can occur for the counterpropagating as well as the for-

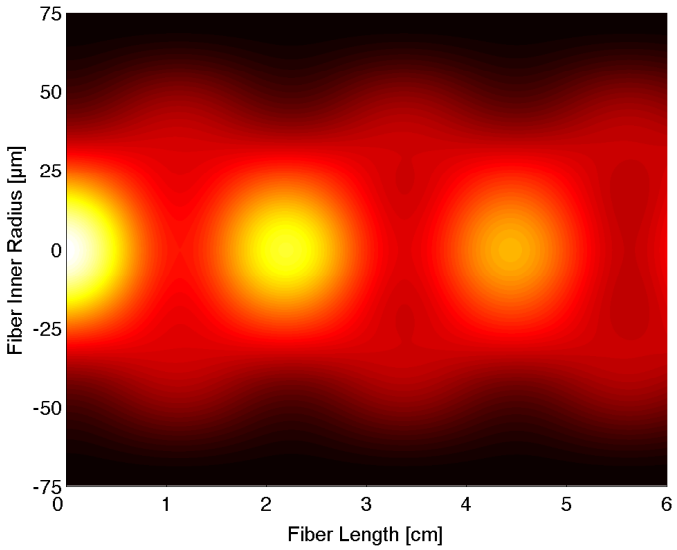

Figure 4.8: Calculated intensity of the driving laser as a function of propagation distance and inner radius of the waveguide. Simulation includes interference of the two lowest order modes (beam energy: 67% EH_{11} and 33% EH_{12}) of a waveguide with 150 μm inner diameter, as well as numerically calculated ionization loss [120].

ward propagating beam. The ability of the counterpropagating light to suppress HHG depends on the ratio of intensities of the counter- and forward propagating pulses. Modebeating in each of the beams can result in a periodic variation of the intensity ratio. Figure 4.9 shows a model of on-axis intensity modulations due to modebeating present for both the forward and counterpropagating beams for two different length waveguides. For the 6 *cm* waveguide (Fig. 4.9a)), the oscillations of the intensity do not coincide, meaning that in the regions of high intensity for the driving laser beam, where harmonics are expected to be strongly generated, the counterpropagating beam has a low intensity, and therefore may not suppress the HHG strongly enough to disrupt the detected signal. In contrast, the intensity modulations do coincide in an 11 *cm* waveguide (Fig. 4.9b)). The intensity ratios for each of these waveguides as a function of propagation distance are shown in Fig. 4.9c). For the 6 *cm* waveguide, the intensity ratio varies greatly with propagation distance, and may prevent efficient suppression of

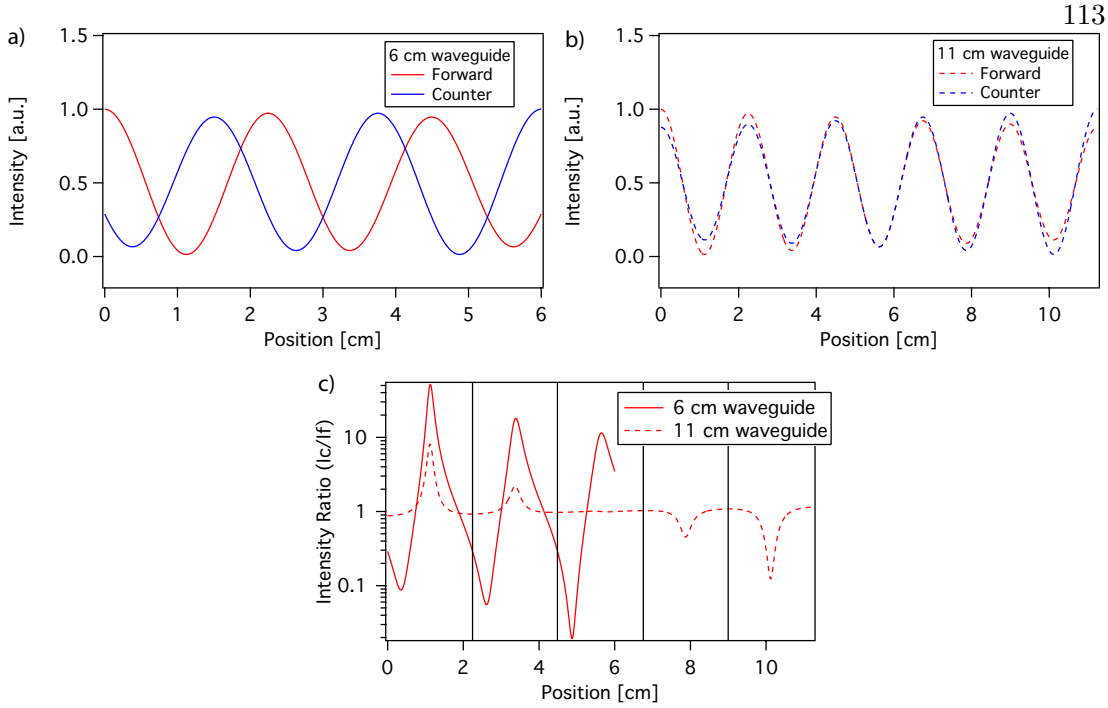

Figure 4.9: On-axis intensity modulations due to modebeating between the first two coupled modes of a hollow waveguide, both for the forward- (red) and counterpropagating (blue) modes. Intensity peaks of the modulations do not coincide well for a 6 *cm* waveguide (a), but do for an 11 *cm* waveguide (b). c) The on-axis intensity ratio of the counterpropagating to the forward propagating beams. In the 6 *cm* waveguide (solid curve), this ratio fluctuates more strongly with position in the waveguide than in the 11 *cm* waveguide (dashed curve), and is lower at the regions of highest intensity of the driving laser (indicated by vertical lines).

HHG. An insufficient intensity ratio could also account for less-than-complete suppression of the HHG signal, causing weak modulations in the HHG signal as the collision region is scanned.

Temporal Dynamics

The counterpropagating pulse probing technique has also been used to gather information about the temporal dynamics of HHG. Under constant experimental conditions (i.e., gas pressure, laser intensity, ionization fraction, waveguide diameter, etc.), the coherence length is expected to vary inversely with the harmonic order, due to the plasma-induced frequency dependence of the dispersion. This inverse relationship can

be seen in the calculated (solid and dashed) curves of Fig. 4.10a, which are based on the phase mismatch equation (Eqn. 2.32) including the major dispersion source terms of the neutral atoms, free electrons, and the waveguide.

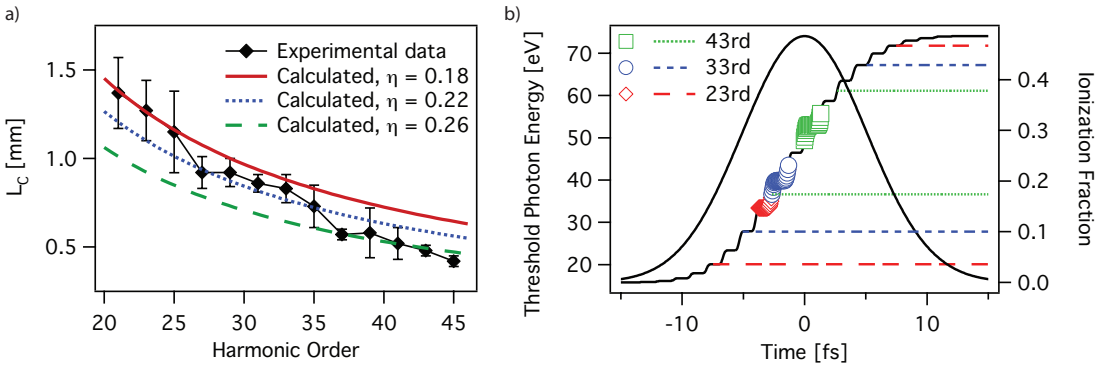

Figure 4.10: Probing temporal dynamics of HHG. a) Coherence length vs. harmonic order at a single location in the hollow waveguide (black diamonds), as well as calculated dependences at different levels of ionization (solid and dashed curves). Measured L_c decreases faster than 1/q due to increasing ionization levels with harmonic order. b) Time of harmonic generation within the generating ultrafast pulse for three harmonic orders, based on the measured coherence length, and the inferred ionization level using ADK ionization rates. Dotted lines indicate the energetically allowed ranges for the same harmonics, based on the cutoff rule [121].

For the data in Fig. 4.10a) (black diamonds), the coherence length for several harmonics, generated in 5 *torr* argon, was measured at the same location, near the exit of the waveguide. The driving laser pulse had a duration of $\sim$ 24 fs and an energy of 375 μJ, while the counterpropagating pulse had a duration of $\sim$ 2.5 ps, and an energy of 210 μJ. Error bars indicate standard devation of measurements of coherence length from several scans. When the data are compared to the calculated curves of the coherence length, however, it seems that higher harmonic orders are generated at increasing levels of ionization. Thus, such a measurement of coherence length can be used to infer the ionization level at which each harmonic order was generated in this region of the waveguide, using Eqn. 2.32. Knowledge of the ionization level then allows us to determine at what time within the laser pulse a particular harmonic order

was generated. Fig. 4.10b) shows the result of such a calculation, using the ADK tunneling ionization rates [47], for three of the harmonic orders: q = 23, 33, and 43. The range of ionization levels corresponding to the uncertainty in the coherence length is superimposed on a plot of ionization level vs. time within the ultrafast pulse. The different levels of ionization indicate that the brightest signal for each harmonic is not generated simultaneously. Instead, the lower photon energies are generated earlier in the pulse, at a lower ionization level, compared with the higher photon energies. This leads to a stronger variation in the coherence length with harmonic order, since the higher harmonic orders are generated in a more highly ionized, and hence more dispersive, medium.

Another time domain phenomenon is indicated by the data in Fig. 4.10b). According to the cutoff rule (Eqn. 2.7), a given energy harmonic may only be generated within a limited time range of the pulse, during which the intensity is high enough. Thus, lower harmonic orders may be generated over a longer range than higher harmonic orders. The horizontal dashed lines in the plot indicate this range for each of the three harmonic orders. The data in Fig. 4.10b) indicate that harmonics are generated, not necessarily at the peak of the pulse, where the ionization rate is expected to be highest, nor even throughout the energetically allowed region, but closer to the time when the intensity reaches threshold. The ability to probe these sub-optical cycle dynamics of harmonic generation may lead to further characterization and temporal control of the HHG process using all-optical QPM.

Limitations to Single Pulse Probing

There are, of course, several limitations to this single-pulse probing technique for measuring coherence length. First, the counterpropagating pulse will have a significant effect on the harmonic signal only when its width is similar to the local coherence length of the process. Simulations indicate that modulations should be clearly visible when the overlap region of the pulses is within the range of $\sim$0.1-2L_c. An overlap

region of $2L_c$ would be expected to have no effect, since it would suppress emission from both an in-phase and an out-of-phase zone. An overlap region much smaller than the coherence length would not suppress enough of the emission to interfere strongly enough. In practice, signal-to-noise ratio in the detection of the harmonic spectrum is what will ultimately limit resolution of the coherent oscillations when using a pulse shorter than the coherence length. Unless the duration of the counterpropagating pulse used is similar to the local coherence length, modulations will not be observed, even though there may be HHG emission from the probed region.

Second, there is a limit to what size coherence length may be conveniently measured. For nearly all the data presented in this thesis, the coherence lengths were on the order of $\sim 100\ \mu m$. The larger the coherence length, the greater the strength of the harmonic signal. However, coherence lengths much larger than a few millimeters are problematic since there is an energy limit to how long the counterpropagating pulse can be made while still having enough intensity to efficiently suppress the HHG. For small coherence lengths (less than about $50\ \mu m$) noise in the detection will limit the resolution, regardless of how well matched the overlap region is to the coherence length. Also, smaller step sizes in the time delay scan increase the data collection time. Since all-optical QPM is expected to be most useful for compensating phase mismatch in the case of very small coherence lengths, the signal-to-noise must be improved. The two major sources of noise in the current setup are the inherent intensity fluctuations of the laser system, and pointing stability associated with large propagation distances.

An experimental example demonstrating the limitation in probing long coherence lengths involves the idea of waveguide phase matching [23]. When the ionization level is below critical (i.e., 5% for argon), phase matching may be achieved through tuning the pressure of the gas within a waveguide to minimize the phase mismatch. Until now, the evidence for this process was a measurement of the harmonic signal as a function of pressure, which peaked at the expected phase matching pressure of $30 - 40\ torr$, in

the case of argon gas and in a 150 μm waveguide [23].

Probing with a counterpropagating pulse confirms phase matching of HHG under these conditions. A counterpropagating pulse was used to probe the coherence length of the 27^{th} harmonic generated in argon over a range of gas pressures from far below to far above the optimal phase matching pressure. The normalized harmonic intensity as a function of pulse collision point and pressure is shown in Fig. 4.11a. In this case the counterpropagating pulse had a duration of about 2.5 ps, resulting in an overlap region with the driving laser pulse of $\sim$ 375 μm. Modulations are clear at low pressures (5 $torr$) and high pressures ($>$ 60 $torr$), but disappear near the phase matching pressure (25 and 45 $torr$). Figure 4.11b shows the average (unnormalized) harmonic intensity vs. pressure, showing the distinct rise in intensity at these mid-range pressures.

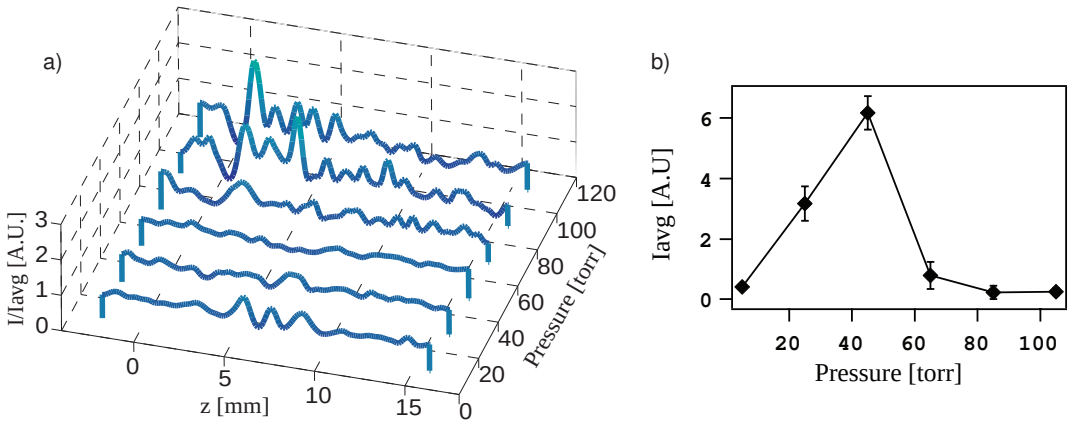

Figure 4.11: a) Enhancement factor (I/I_{avg}) of the 27th harmonic as a function of gas pressure and position of the pulse collision point in the waveguide. The coherence length increases as expected near the phase matching pressure of 45 $torr$, leading to a disappearance of the modulations. The position within the waveguide at which the harmonic is strongly generated also changes with pressure. b) Average harmonic output (I_{avg}) as a function of pressure, demonstrating phase matching at $\sim$ 45 $torr$.

It can also be seen in Fig. 4.11a that the modulations appear at different locations in the waveguide for different pressures. These data were collected by scanning the pulse

collision point from the exit of the waveguide toward the front. The horizontal axis indicates distance from the exit of the waveguide. Strong modulations appear closer to the exit of the waveguide at high pressure. There are two different reasons for this. First, the absorption depth of the gas decreases from $\sim 18\ cm$ at $5\ torr$ to $\sim 2\ mm$ at $105\ torr$. The strongest modulations at high pressure are therefore visible in the $5\ mm$ differential pumping end section of the waveguide. At low pressures, the strongest modulations are visible in the center, constant pressure section. Second, the phase mismatch will be lowest where the pressure is closest to the correct pressure ($\sim 30 - 40\ torr$), and therefore the strongest contributions at high pressure are in the differential pumping region since the pressure ramps down through the phase matching pressure in this section of the waveguide. For the low pressure case, the modulations occur where the pressure is highest, near the gas input in the central section.

4.4 Double Pulse Probing

As shown in the previous section, the local phase mismatch is sensitive to changes in the intensity of the driving laser pulse, leading to spatial variations of the measured coherence length with propagation distance. In hollow waveguides, one of the effects examined was the interference of excited propagation modes, which depend sensitively on the coupling of the laser beams into the waveguide (see Section 2.6). This effect influences harmonic generation in several ways. As shown in Fig. 4.7, emission of the highest harmonics may be confined longitudinally to regions corresponding to maximum laser intensity. In addition, since the ionization rate of the gas medium is proportional to the intensity, there will also be a variation in the single-atom efficiency of harmonic emission. This variation in efficiency significantly influences the harmonic signal detected at the exit of the waveguide.

A scan of the collision region of the driving laser pulse and a single counterpropagating pulse through several coherence zones can result in coherent oscillations in the

detected HHG signal, such as that shown in Fig. 4.4. In this case, the length and harmonic emission efficiency of the zones are approximately constant with propagation distance. As discussed above, the size of the coherence lengths, as well as the spatial dynamics of the HHG, can be obtained from the periodicity of these oscillations. This information is essential for understanding how harmonics are generated and how the phase mismatch evolves. However, when the harmonic emission varies significantly along the propagation direction (e.g., due to mode interference and nonlinear laser-plasma interactions), a scan of a single counterpropagating pulse will not give rise to clear oscillations in the HHG signal. Instead, regions of large enhancement in the HHG signal are typically observed. Thus, a new technique is necessary for probing HHG coherence under these conditions.

It is possible to demonstrate strong coherence and probe the coherence lengths, even in the presence of intensity oscillations, by using two counterpropagating pulses. When the scan of a single counterpropagating pulse does not show coherent oscillations, the relative phase between emission from different locations in the waveguide may be measured using two counterpropagating pulses whose separation is continuously varied. The following analysis illustrates the case where the collision region of one of the pulses is fixed in space, while the other is scanned through the region of interest, to determine the mutual phase of the HHG emission from the two regions.

A simple model of HHG emission under the influence of counterpropagating pulses reproduces many of the qualitative and quantitative features of a counterpropagating pulse scan. The harmonic field at the output of the nonlinear medium, of length L, can be expressed as

$$E_{HHG}(L) = \int_0^L E^o_{HHG}(z) \exp\left(i\frac{\pi}{L_c(z)}\right) dz \tag{4.1}$$

where $E^o_{HHG}(z)$ is the strength of the generated harmonic field as a function of the propagation distance, z, and $L_c(z)$ is the z-dependent coherence length. Two represen-

tative regimes may be considered which correspond to the experimental observations described above.

Regime 1: Constant Emission Strength (CES). $E^o_{HHG}(z) \approx E^o_{HHG}$ and $L_c(z) \approx L_c$

This regime is characterized by oscillation of the detected HHG signal as the collision region of a counterpropagating pulse and the driving laser pulse is scanned through the interaction region (as seen in Fig. 4.4). In this regime, the strength of the harmonic emission and the coherence length are both approximately constant with propagation distance. Except for the final, N^{th}, coherence zone, all the preceding zones are paired with an identical zone of opposite overall phase that destructively interferes (see Fig. 4.5). Without a counterpropagating pulse, the only emission detected is that from the N^{th} zone. When a counterpropagating pulse suppresses the emission from one of the preceding zones, the emission from its "partner" zone will interfere with the N^{th} zone. If all zones are constant in length and emission strength, the suppression of any zone will either double the total field exiting the waveguide, or completely suppress it. Thus, as the collision region is scanned through the nonlinear medium, high contrast fringes appear in the detected HHG signal.

A simple calculation of this effect is shown in Fig. 4.12. For this calculation, E^o_{HHG} is assumed to be constant with propagation distance and proportional to the ionization rate, calculated for typical parameters for HHG in argon. Fig. 4.12a) shows the constant ionization rate profile as a function of propagation distance. The simulation of the counterpropagating pulse scan is performed by calculating Eqn. 4.1 as a function of the collision region of the pulses, from which the HHG emission is subtracted. The counterpropagating pulse is approximated as square in time, with an effective width equal to the coherence length, and with the optimal laser intensity needed to suppress HHG emission completely. Figure 4.12b) shows the coherent oscillations which appear for such a scan in this regime.

Regime 2: Varying Emission Strength (VES). $E^o_{HHG}(z)$ and/or $L_c(z)$ vary signif-

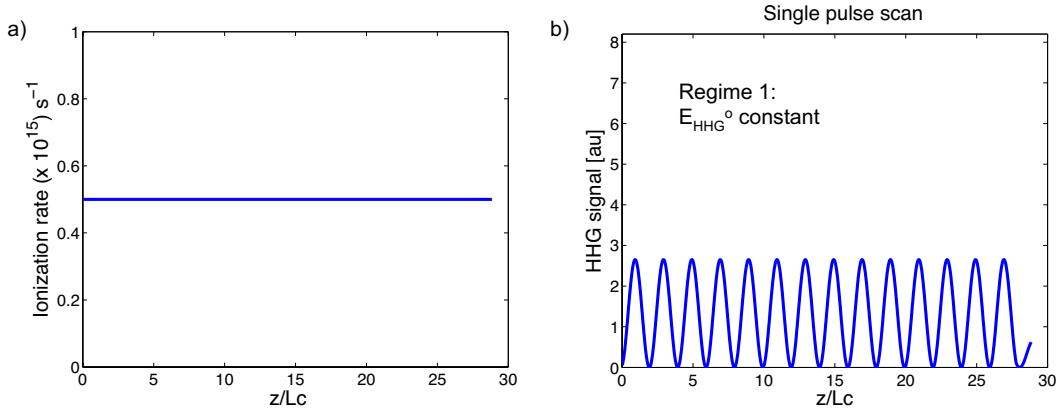

Figure 4.12: Simulation of a scan of a single counterpropagating pulse when the single-atom strength of the harmonic emission and the coherence length do not vary with propagation distance. a) A constant ionization rate with propagation and b) the variation in the intensity of the detected harmonic signal for the scan of a single counterpropagating pulse, showing coherent oscillations [120].

icantly with z.

This regime is characterized by a significant change of the detected HHG signal when the collision region of a single counterpropagating pulse and the driving laser pulse is scanned through the interaction region. A significant variation in $E^o_{HHG}(z)$ and/or $L_c(z)$ means that the emitted harmonic signal is varying significantly along its propagation. As an example, we consider the case where L_c is constant with propagation distance and the harmonic emission strength oscillates with propagation distance (Fig. 4.13a)). (This is the case almost always observed experimentally. However, future study could elaborate on what happens when $L_c(z)$ varies with z.) Now the final coherence zone is weak relative to the preceding zones. If the collision point suppresses harmonic emission from a zone that has a much stronger emission, then its "partner" zone will dominate the spectrum, exhibiting only a small modulation due to interference from the much weaker N^{th} zone. Figure 4.13 shows the results of the propagation simulation in this case. Figure 4.13a) shows the profile of the ionization rate as a function of distance in the medium for a changing laser intensity. This profile was generated taking into

account the interaction of the two lowest order coupled modes of a hollow waveguide with inner diameter 150 μm. For this calculation, the intensity variation used was the same shown in Fig. 4.8. The 1D ionization rate was calculated from the intensity variation at the central axis of the waveguide. For the simulation of a single pulse scan, the same calculation was performed as for Fig. 4.12b), but now with a longitudinally varying ionization rate. The coherent oscillations disappear, and the HHG signal can be greatly enhanced using a single counterpropagating pulse (Fig. 4.13b)).

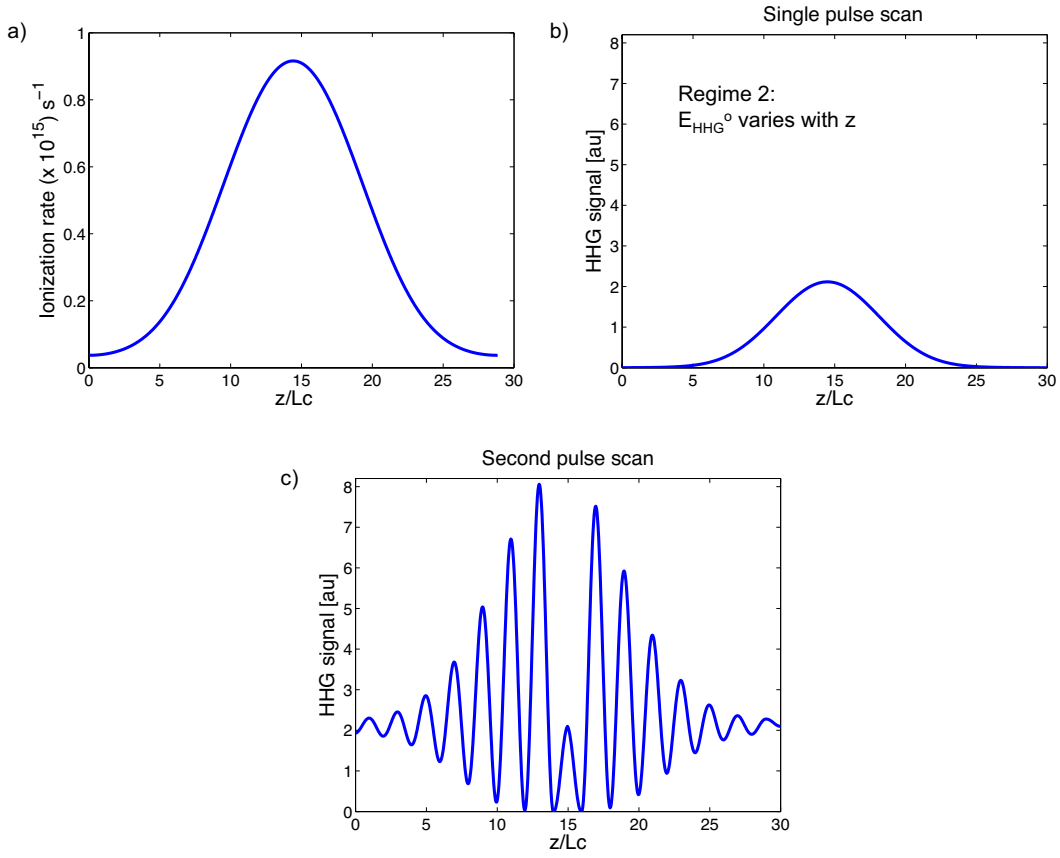

Figure 4.13: Simulation of a scan of one and two counterpropagating pulses when the single-atom strength of the harmonic emission varies with propagation distance due to modebeating. a) A varying intensity due to modebeating leads to a varying ionization rate. b) A single counterpropagating pulse does not reveal coherent oscillations, since the harmonic emission is much stronger at $z/L_c = 15$ than at 5 or 25. c) A second counterpropagating pulse, scanned while the first is held fixed at $z/L_c = 15$ gives rise to clear oscillations [120].

In order to measure the coherence length in this second regime, a second counterpropagating pulse is required so that clear coherent oscillations can be observed. For these experiments, the first counterpropagating pulse is held at a fixed position where the emission strength is high, while the second counterpropagating pulses is scanned through the nonlinear medium. The second scan probes the relative coherence between the bright emission now detected due to the presence of the first pulse, and the HHG emission throughout the rest of the region. In this case, the harmonic emission from the zone detected due to the second pulse is of similar or lesser strength, resulting in strong contrast fringes. A simulation of this effect is shown in Fig. 4.13c), where the first pulse is held fixed near $z/L_c = 15$. When the two pulses are exactly overlapped, the signal remains as though only one pulse was present. However, when the pulses are separated by a distance $2L_c$, the signal further increases by about a factor of four, which is the increase in intensity expected when the harmonic field is doubled. The ability to continuously change the distance between the two counterpropagating pulses pinpoints the exact separation of the pulses required for the greatest enhancement of the HHG signal. Additionally, the periodicity of the fringes provides a measurement of the local coherence length in this second regime, which was previously inaccessible.

Experimentally, both of the above regimes have been observed by scanning a single counterpropagating pulse through the interaction region. Figure 4.4 shows an example of the Constant Emission Strength (CES) regime, in which strong modulations are resolved using a single counterpropagating pulse scan. Figure 4.14a) shows a typical data set showing the Varying Emission Strength (VES) regime, obtained by scanning a single counterpropagating pulse through a region of strong intensity variation. For these data, the interaction region consists of 8 *torr* argon in a 6 *cm* long waveguide. The driving laser pulse had a duration of 27 fs and an energy of 470 μJ, while the counterpropagating pulse had a duration of $\sim$ 1 ps, and an energy of 80 μJ. The integration time of the CCD camera was 0.5 s, the grating used was SC, and two 200

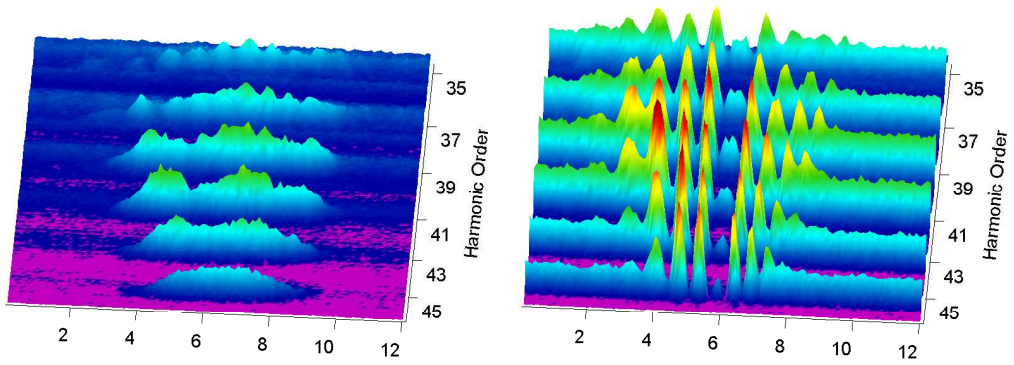

Figure 4.14: Harmonic spectra as a function of the collision region of one and two counterpropagating pulses. a) A single counterpropagating pulse is scanned through the interaction region, showing no coherent oscillation. b) A second counterpropagating pulse is scanned through the interaction region while the first remains stationary at z $\approx$ 6 mm [120].

nm thickness aluminum filters attenuated the driving laser.

The effect of the single counterpropagating pulse is to strongly enhance the harmonic flux over a distance of 4 mm or more. The result of scanning a second counterpropagating pulse, while holding the first fixed in position, is shown in Fig. 4.14b). This plot reveals the relative coherence of the harmonic emission in this region. The first counterpropagating pulse is held stationary at position z $\approx$ 6 mm, while the second pulse is scanned through the same region. Modulations appear with strong visibility, demonstrating the strong relative coherence and also providing a measurement of the coherence length. The signal is weak at the position where the two counterpropagating pulses are exactly overlapped, since they suppress coherent addition in the same region of emission. However, when the pulses are separated by $2L_c$, the signal is enhanced dramatically, because two coherence zones from a region of strong emission are permitted to add coherently. Further enhancement could be achieved by adding more counterpropagating pulses, while optimizing the width and separation of each pulse.

The ratio of the coherence length compared with the region suppressed by each of the counterpropagating pulses can also be inferred from the data. Figure 4.15 shows the results of the two pulse scan simulation for parameters mimicking the experimental conditions. The length of the region suppressed by each of the counterpropagating pulses, L_s, is held constant, while the coherence length is varied. It is clear that the periodicity of the modulations matches the coherence length, regardless of the counterpropagating pulse length. Also the appearance of a double peak near the first, stationary pulse, when $L_s < L_c$, matches the behavior seen in Fig. 4.14. This is a good indicator of the width of the effective suppression region, which could be used to select the appropriate width of the counterpropagating pulse for maximum enhancement. The agreement with the experimental data also supports the validity of the simple model used in the simulation.

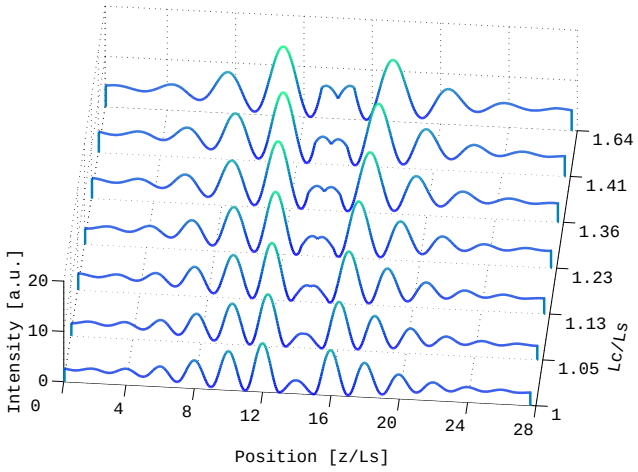

Figure 4.15: Simulation of a scan of two counterpropagating pulses when the single-atom strength of the harmonic emission varies with propagation distance due to modebeating. For each of the curves, the suppression region (L_s) is constant, while the coherence length (L_c) varies. The simulation reproduces features visible in Fig. 4.14b.

This measurement constitutes a new technique for probing the local phase mismatch as well as the spatial and temporal emission of HHG in hollow waveguides. The simulations of the counterpropagating pulse scans presented show clear qualitative

agreement with the observed data, providing evidence for the validity of the simple model presented. Because the largest enhancements due to all-optical QPM have been observed in this second regime, where the harmonic emission varies strongly with propagation distance, this approach yields the necessary information required to achieve further enhancement.

One future application of this two-pulse probing technique is to determine the relative coherence of HHG at greater separations ($> 1\ cm$) within the hollow waveguide. Because HHG is most strongly generated in regions of strong laser intensity on-axis, nonlinear reshaping and modebeating can limit strong emission to a several millimeter length region separated by cm-scale distances. For a 6 cm length, 150 μm hollow waveguide, there are three regions of high laser intensity, assuming most of the energy is propagating in the two lowest order modes. The coherent addition of light from each of these three intense regions could lead to significant further enhancements of HHG.

4.5 Quasi-Phase Matching

Once the coherence length has been measured, a train of counterpropagating pulses with the correct width and separation can be designed that suppresses emission from multiple, out-of-phase coherence zones [119,122]. This enables buildup of the x-ray signal from in-phase zones only, leading to enhancement of the HHG signal. The first attempts to implement all-optical QPM of HHG with counterpropagating pulses were performed by the Peatross group. In their work, they used a free focus geometry. As described in Chapter 2, they were not able to increase the harmonic signal above what could be obtained by optimizing phase matching conditions. This work, in contrast, deals with regimes where the photon energies cannot be truly phase matched, because of the high level of ionization. In further contrast with previous work, hollow waveguides are shown to be an ideal medium for all-optical QPM due to the long-range coherence described in the previous section.

Here, all-optical QPM of HHG is demonstrated in two different cases. An enhancement of ∼300 was obtained using three counterpropagating pulses in argon at 65 eV, and an enhancement of ∼150 was obtained using only two counterpropagating pulses in helium at 140 eV. In both cases, the photon yield increased to a level comparable to or higher than that which could be obtained for either photon energy by optimizing the pressure and intensity level. In particular, HHG at 65 eV may be phase matched in helium. At 140 eV, however, HHG cannot be conventionally phase matched in any gas for the driving laser wavelength used. These preliminary results showcase the great potential of all-optical QPM for further substantial enhancements of HHG when longer trains of counterpropagating pulses are employed. All-optical QPM is particularly promising, as will be described below, for enhancing emission at very high, soft and hard x-ray photon energies, where the photon yield is currently severely limited by a large phase mismatch.

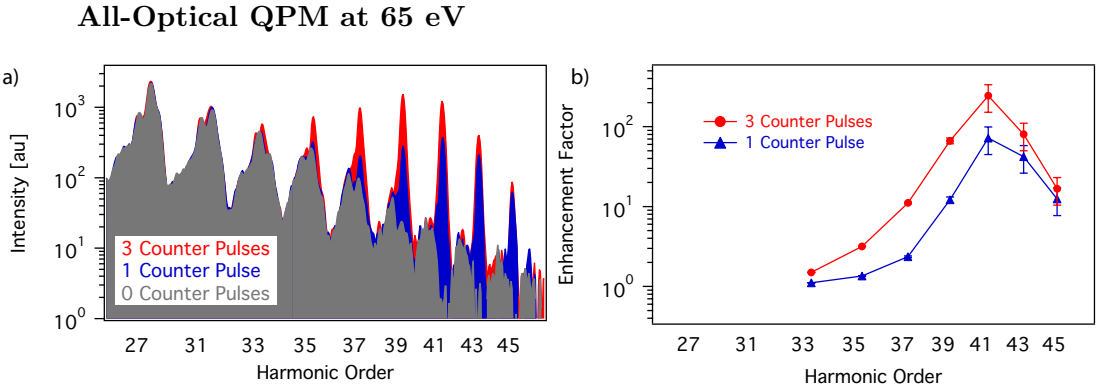

Figure 4.16: Data demonstrating all-optical QPM at 65 eV in argon. a) Observed harmonic emission from argon with no (gray), one (blue), and three (red) counterpropagating pulses present. b) Enhancement factor as a function of harmonic order, for one (blue) and three (red) counterpropagating pulses [119].

Figure 4.16 shows the enhancement of HHG at 65 eV in argon using three counterpropagating pulses. The gas was introduced at a pressure of 10 $torr$ at about 7 cm from the entrance of an 11 cm long, 150 μm inner diameter waveguide. Thus, instead

of having a long constant pressure region, this waveguide had a long pressure ramp region that increased with the direction of propagation of the driving laser pulse. The collision point of the forward and counterpropagating pulses was scanned over a 2 cm region around 4 cm from the entrance, in the center of this pressure ramp. In this experiment, the separation of the counterpropagating pulses was set using a static phase mask (shown in inset a) of Fig. 4.2). The integration time for the CCD camera was 0.5 s, the grating used was SC, and the fundamental light was attenuated using two 200 nm thickness aluminum filters. The approximate effective pulse separation was 1.1 mm and each counterpropagating pulse had a FWHM effective extent of about 340 μm. The HHG spectra detected in the presence of zero, one, and three counterpropagating pulses are shown in Fig. 4.16a).

For this experiment, the harmonic emission varied significantly along the propagation direction due to strong modebeating modulation of the laser intensity, corresponding to the VES regime described in the previous section. In this regime, a single counterpropagating pulse can significantly enhance the total output of the HHG signal without producing coherent oscillations of the signal. Indeed, in this experiment, any one of the three counterpropagating pulses enhances the 41^{st} harmonic order by approximately two orders of magnitude, which can be seen in Fig. 4.16b. The first pulse intersects with the driving laser pulse within the region where the harmonic emission is strongest. As a result, bright harmonic generation from that region is now detected at the output of the waveguide. The second and third pulses enhance the signal further, but by a much smaller factor, corresponding to the addition of similar strength coherence zones. The enhancement in this case is likely limited by imperfect delay between the counterpropagating pulses, since the pulse train is created using a static, nonadjustable, phase mask. The thickness of the plates was selected to match the observed coherence length, and the gas pressure and driving laser intensity were optimized for the greatest enhancement. However, it is possible that further enhancement could be

obtained through finer adjustment of the counterpropagating pulses.

The enhancement factor was calculated for each harmonic order and is shown in Fig. 4.16b). Enhancement factor is defined as the ratio of integrated counts from the spectrum with quasi-phase matching compared to the spectrum without quasi-phase matching. Specifically, an enhancement factor was calculated for each harmonic order within a narrow bandwidth around the harmonic peak. Uncertainty originates with the detection noise of the CCD camera. Error bars indicate the standard deviation of the CCD signal for the average pixel.

Even though this photon energy range may be phase matched in helium, all-optical QPM is found to enhance the photon yield to a level comparable to true phase matching. The photon yield of the 41^{st} harmonic order was estimated to be $\sim 10^10$ photons/sec, based on roughly calibrated estimates of the detection efficiency. The CCD count rates for phase matched emission at the 27^{th} harmonic order, which have a corresponding measured photon yield using a vacuum photodiode (described in Chapter 3) are compared to the CCD count rates for the 41^{st} harmonic order enhanced by all-optical QPM. Corrections were made for differences in efficiency of the filter transmission, the optical components of the spectrometer, and the quantum efficiency of the CCD camera. This photon yield is comparable to that of phase matched emission from helium at these wavelengths, which is mostly limited by the absorption depth of helium at the high pressures required for phase matching. At 65 eV, the absorption depths of helium and argon are ~ 3 mm and ~ 3 cm, respectively. Hence further enhancements are possible in argon by the addition of more counterpropagating pulses, since the absorption depth is still much longer than the region over which QPM was implemented, ~ 3 mm.

Selectivity of Photon Energy

A consequence of the strong coherence of HHG generated in hollow waveguides is that all-optical QPM will be selective, enhancing a narrow bandwidth. For example,

the enhancement in Fig. 4.16 is selective, enhancing the the 41^{st} harmonic order more strongly than the adjacent orders. Because the coherence length of the harmonics varies by at least 1/q, as described earlier in the chapter, a pulse train with a given delay between the individual pulses will selectively enhance a single harmonic order. The addition of more counterpropagating pulses will not only enhance the HHG signal further, but will become more selective of a narrower bandwidth. This feature of all-optical QPM is particularly attractive for applications of HHG that require a narrow bandwidth, e.g., for coherent imaging [15] or selective energetic excitation of chemical or electronic processes [19].

The selectivity of all-optical QPM can be improved further if the counterpropagating pulses suppress out-of-phase coherence zones that are not adjacent, but are farther apart. Figure 4.17 illustrates this effect: the size of the coherence zones for two different harmonic orders will be slightly different due to the frequency dependence of the dispersion. A given pair of counterpropagating pulses can be adjusted to match the spacing of out-of-phase coherence zones for one harmonic order, but will not match the spacing of another harmonic order. This effect becomes more prominent the greater the spacing between the pulses, or the more counterpropagating pulses that are used.

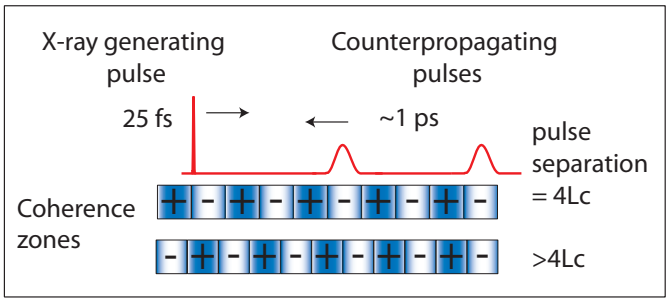

Figure 4.17: A schematic illustrating the selectivity and tunability of all-optical QPM using two counterpropagating pulses, by varying their separation [120].

An example of this selectivity of photon energy is shown in Fig. 4.18. This plot shows enhanced spectra of HHG from argon, at different pulse separations. The

width of each counterpropagating pulse was kept constant at $\sim 300\ \mu m$, but the delay between them was varied around a pulse separation of approximately $4L_c$. As the pulse separation is changed, the harmonic order that is most strongly enhanced is shifted. Essentially, the pulse separation will precisely match a distance of $4L_c$ for different harmonic orders as the separation is varied.

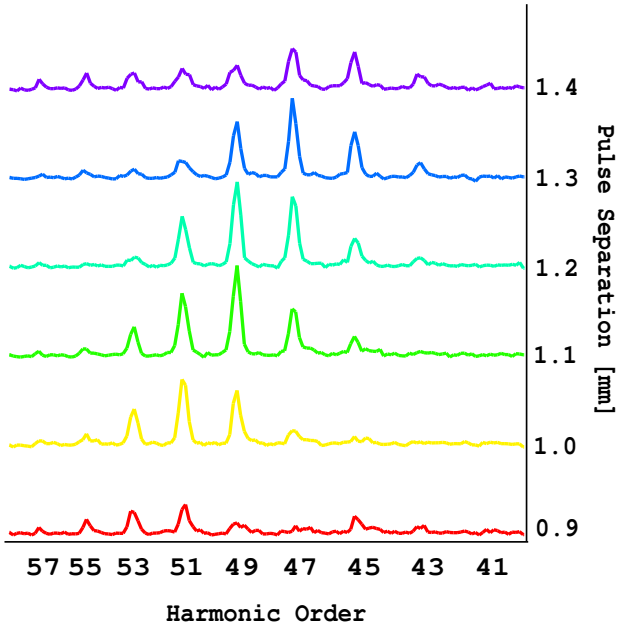

Figure 4.18: Selectivity and tunability of all-optical QPM using two counterpropagating pulses with variable separation. Enhancement occurs when the pulse separation is $2^N L_c$. Selectivity improves when $N > 1$. HHG spectra in argon show the shift of the enhancement with harmonic order as the separation between the pulses is varied [120].

Figure 4.19 includes the same data, and further illustrates both the selectivity and tunability capabilities of all-optical QPM. Two of the spectra from Fig. 4.18 are plotted along with the spectrum observed when only one of the two counterpropagating pulses is present. Without all-optical QPM, no harmonic peaks are visible. The blue curve, for which the pulses were separated by 1.0 mm, shows in particular the selectivity of all-optical QPM. Only three of the harmonic orders, q = 49, 51, and 53, are enhanced

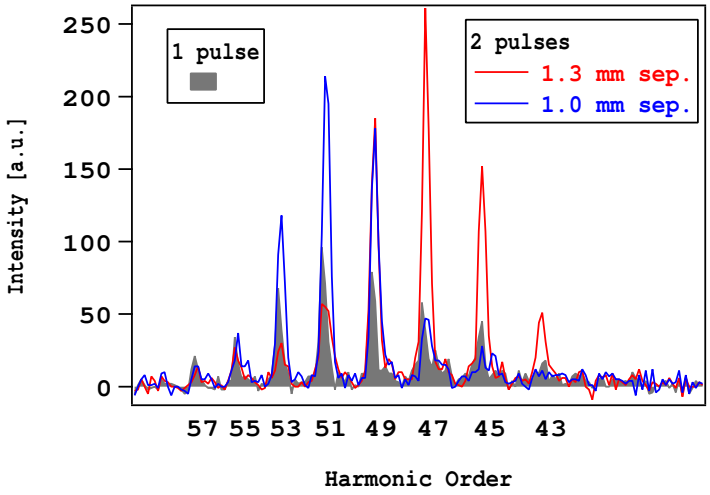

Figure 4.19: Selectivity and tunability of all-optical QPM using two counterpropagating pulses with variable separation. The spectrum enhanced by one pulse (solid gray) is plotted along with spectra enhanced by two pulses, for two different pulse separations: 1.3 mm (red) and 1.0 mm (blue).

further by the addition of the second pulse. In fact, for orders 45 and 47, the second counterpropagating pulse actually reduces the degree of enhancement to below that with the first counterpropagating pulse. The red spectrum illustrates the tunability. For a slightly different pulse separation, 1.3 mm, the harmonic orders enhanced shift to lower photon energy.

All-Optical QPM at 140 eV

All-optical QPM has also been used to demonstrate enhancement of HHG at high photon energies in helium [122]. Helium has the highest ionization potential of the noble gases, at 24 eV, and thus offers the highest possible photon energies that can be phase matched. The upper limit of the phase matching region for helium is $\sim$ 130 eV, when using a driving laser wavelength of 800 nm. Higher photon energies can only be produced at higher laser intensities, which necessarily results in a higher degree of ionization of the gas medium. Above the critical fraction of ionization, η_{cr} (Eqn. 2.33), the dispersion from the free electrons is too strong to be compensated by that from the

neutral atoms. Therefore, QPM techniques are required for enhancing HHG at high photon energies.

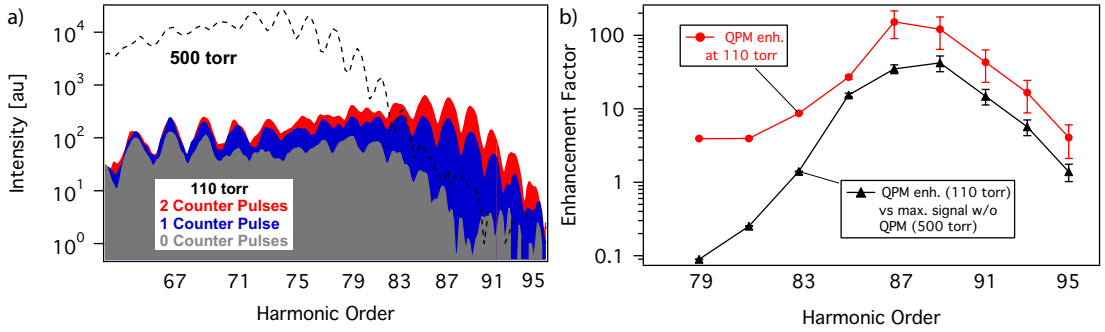

Figure 4.20: Data demonstrating all-optical QPM at 140 eV in helium. a) Observed harmonic emission from helium for no (gray), one (blue), and two (red) counterpropagating pulses. The dotted curve shows harmonic emission under similar laser conditions, but at a pressure of 500 $torr$, which is optimal for conventionally phase matching lower harmonic orders, below q = 77. b) Enhancement factors for harmonic orders 79-95. Red circles show the ratio of the QPM emission obtained using a two counterpropagating pulses to that without counterpropagating light at a pressure of 110 $torr$. Black triangles show the ratio of QPM emission at 110 $torr$ to that without counterpropagating light at a pressure of 500 $torr$.

Figure 4.20 shows the enhancement of HHG in helium using two counterpropagating pulses. The gas was introduced at a pressure of 110 $torr$ at 5 mm from the exit of a 6 cm, 150 μm inner diameter waveguide. The forward propagating pulse had a duration of 27 fs and an energy of ~ 1 mJ. The collision point of the forward and counterpropagating pulses was scanned over a 2 cm region near the exit of the waveguide. Since the gas was introduced only at the exit of the waveguide, there was a long section of the waveguide with a pressure ramp increasing with propagation distance. The separation between the two counterpropagating pulses was adjusted using the setup shown in inset b) of Fig. 4.2. The coherence length was measured using the two pulse method, since these data were observed in VES regime. This also allowed careful tuning of both the width of each pulse and their separation to produce the maximum enhancement. The width of each pulse was approximately 750 fs FWHM, and the approximate pulse

separation at highest enhancement was 3 ps, making the effective separation about 1.5 ps. The energy in each counterpropagating pulse was $\sim$ 200 μJ. The integration time for the CCD camera was 1 s, the grating used was SC, and the fundamental light was attenuated using one 200 nm thickness silver filter, and one 200 nm thickness zirconium filter. The HHG spectra with zero, one, and two counterpropagating pulses are shown in Fig. 4.20a).

Without the counterpropagating pulses present, harmonics are observed from helium at a pressure of 110 $torr$ up to the 87^{th} order at 134 eV. The presence of even one counterpropagating pulse increases the brightness of several harmonic orders. At the laser intensity used, the cutoff is well above the highest photon energies observed, indicating that the falloff of the 87^{th} harmonic is due to phase mismatch. As in the data presented in Fig. 4.16 in argon, the enhancement is selective, occurring only over a limited range of photon energies whose coherence length matches that of the counterpropagating pulse train used. The enhancement factor obtained using two counterpropagating pulses is shown in Fig. 4.20b, reaching factors of 150 and 120 of the 87^{th} and 89^{th} harmonic orders, respectively. The highest observable harmonic is also extended from the 87^{th} to the 95^{th}, due to partial suppression of out-of-phase zones. Error bars are calculated in a similar way to those of Fig. 4.16b.

The efficiency of all-optical QPM was maximized through fine-tuning of the width and separation of the counterpropagating pulses. The coherence length, for q = 89, for example, was measured to be 217 $\pm$ 25 μm near the region of highest harmonic emission, through the observed oscillations of the harmonic signal. This was used to determine the optimal separation of the two pulses, which was independently measured as $\sim$3 ps, appropriate for enhancing a coherence length of 225 $\pm$ 25 μm. The measured single pulse FWHM of 225 $\pm$ 15 μm approximately matches the prediction [106] that the largest QPM enhancement occurs when the Sech^2 pulse width corresponds to $\sim 0.92 L_c \approx 203$ μm.

This measured coherence length can be used to calculate the ionization level at which the harmonics were generated, using the phase mismatch equation: Eqn. 2.32. Solving this equation gives an ionization level of $\eta \approx 1.7\%$, for the above experimental conditions. This number is also consistent with the ionization level predicted at the time when the cutoff intensity reaches 140 eV, as calculated using the ADK tunneling ionization rates [47]. The critical ionization for helium may be determined using Eqn. 2.33, giving 0.5% for a driving laser wavelength of 800 nm. The measured harmonics, then, are generated at a level of ionization three times that which can be conventionally phase matched.

For these data, the pressure of the gas at the input to the waveguide was kept constant at 110 $torr$. To get a sense of the absolute enhancement obtained using all-optical QPM, a comparison was made between the emission with all-optical QPM at a pressure of 110 $torr$, and the emission for which the pressure was optimized for the brightness of the highest harmonic orders. All other experimental parameters were similar to those described above. Overlaid in Fig. 4.20a) is a spectrum taken at a pressure of 500 $torr$, which is near the phase matching pressure for q = 79 and below. Fig. 4.20b) shows the enhancement factor obtained by the two-pulse all-optical QPM at 110 $torr$ compared to the maximum emission without QPM at 500 $torr$ (black triangles). The 89^{th} harmonic order in particular is enhanced by a factor of 40, and all harmonic orders $>$ q = 83 are enhanced using all-optical QPM above that which can be obtained simply by optimizing the pressure.

4.6 Quantum Electronic Trajectories

As described in Chapter 2, in the semi-classical picture of HHG, there are two distinct paths an electron may travel in the continuum and return to the parent ion with the same kinetic energy, hence producing the same harmonic order. These paths are the so-called "long" and "short" trajectories, referring to the relative time the electron

spends as a "free" electron in the time interval between field-ionization and recombination with the parent ion. These different quantum trajectories can often be distinguished in spectral measurements. Non-adiabatic blueshifting of the harmonics is stronger for the long trajectories than the short trajectories, leading to a splitting of the harmonic peaks. When driven with a high pulse energy, HHG spectra in argon often show strong peak splitting between the two trajectories in Fig. 2.10. In some cases, even more complicated structures can be seen due to multiple trajectory peaks. This differential blueshifting of the different quantum trajectories allows distinction of the effects of counterpropagating pulses in the spectral data, allowing insight into, and even control of, sub-cycle time scale processes.

The phase modulations induced by the counterpropagating pulse affect the long trajectories more strongly than the short, as described in Chapter 2 and Ref. [119]. Emission originating from the long trajectory may in fact be suppressed at a lower counterpropagating intensity than that from the short, due to the greater contribution from the intensity-dependent phase. In Figs. 4.14 and 4.4, for example, it is emission from the long trajectory that exhibits modulations, while emission from the short trajectory is unaffected. For Fig. 4.4, the cutoff photon energy for the driving laser intensity used is about 100 eV. Thus, the harmonic orders shown are well within the plateau region, where the intensity-dependent phase accumulation is significantly different for the long and short trajectories. For these data, the ratio of the counter- to the forward propagating intensities, I_C/I_F, is about 0.25%. Calculations have shown that for such a small intensity ratio, there is a significant difference in the degree of suppression between the two trajectories, mostly owing to intensity-dependent phase fluctuations [119].

Information may be also be extracted that relates to the difference in the macroscopic phase evolution with propagation between the two different quantum paths. The data set shown in Fig. 4.21 was taken in argon using the two-pulse probing technique.

For some of the harmonic orders, the two distinct long and short peaks are readily apparent, as for orders 35-39. At the higher orders, modulations extend through the spectral region between the bright, long trajectory peaks. The probing of coherence reveals

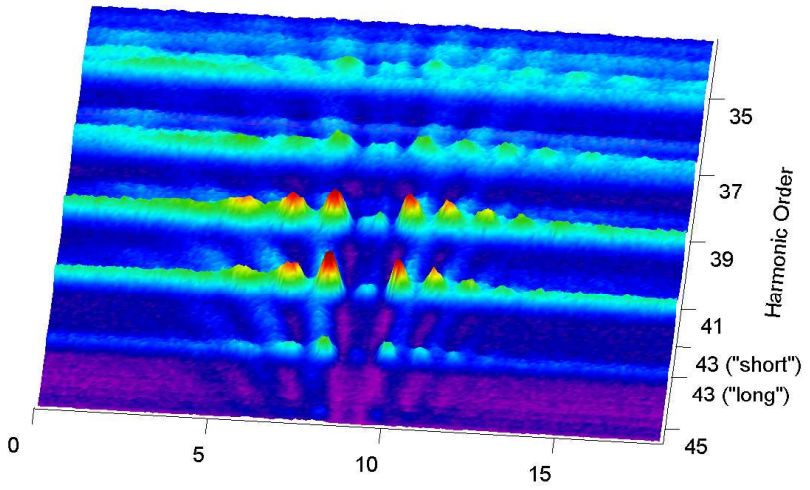

Figure 4.21: HHG spectra from argon in the presence of one counterpropagating pulse held fixed in position at z $\approx$ 9 mm, while a second counterpropagating pulse is scanned through a 2 cm region of the waveguide. Variation of the periodicity of the oscillations with harmonic order (photon energy) reveal dependences of the phase on the time the electron spends in the continuum before recombination.

several interesting features. First, the enhancement peaks, which correspond to suppression of out-of-phase regions, appear to fan out in the direction of longer wavelength (lower photon energy). This means that the less blue-shifted, short trajectories have longer coherence lengths than do the long trajectories. In fact, it is apparent that the coherence lengths change more rapidly among different trajectories which correspond to the same harmonic order than do coherence lengths from harmonic peak to peak. One possible explanation for this is that the electron wavefunction acquires more phase the longer it is present in the continuum. Therefore the long trajectories will have a greater phase mismatch, and hence shorter coherence length than the short trajectories.

Another thing revealed by the probing is simply the existence of emission from the short trajectories. Because of the ringdown of harmonic signal due to intensity fluctuations, the emission from the short trajectories is not detectable without counterpropagating light, especially for the 43^{rd} and 45^{th} harmonic orders. In other words, the harmonic emission from the short trajectories is of the VES regime described in Section 4.4.

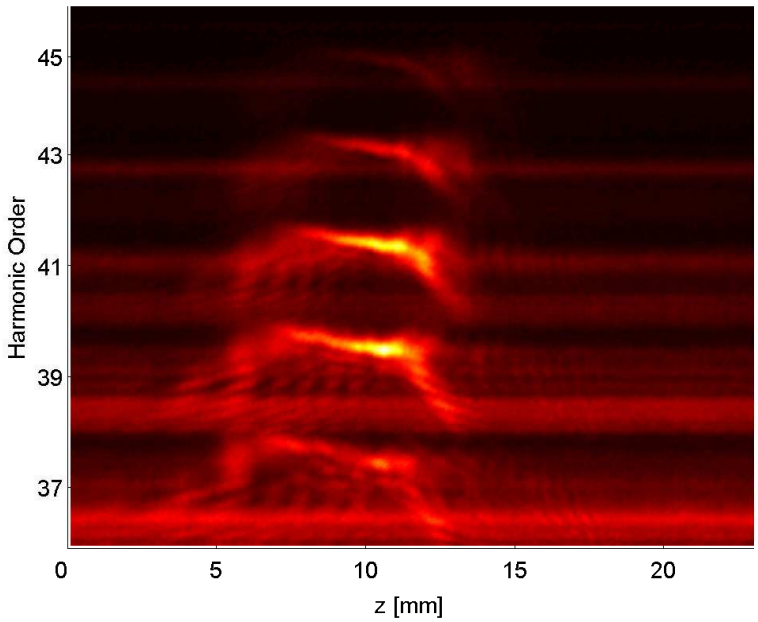

Figure 4.22: Harmonic spectra in argon as a function of the collision position of the driving laser pulse and a single counterpropagating pulse, revealing the presence of several quantum trajectories with different coherence properties.

Probing with counterpropagating pulses has revealed even more complex trajectory phase information which is not easily explainable. Figure 4.22 shows a plot of harmonic spectra from argon as a function of the collision point of a single counterpropagating pulse, showing a more complex structure than in Fig. 4.21. In particular, this plot shows the difference in the brightness of emission from different trajectories as a function of position within the waveguide. This plot was again acquired in the center of a high intensity region of modebeating. Short trajectories (toward the low photon

energy or low harmonic order) appear to be strongly generated in two general regions along the axis of propagation, while the long trajectories are located in one. Numerical simulations may be required to describe the coherence properties of different trajectories, as well as the relative emission strength of trajectories as a function of driving laser intensity.

A direct consequence of the fact that different trajectories have different coherence lengths is that all-optical QPM may be used to selectively enhance a single trajectory. In fact, since the coherence length changes more rapidly with time of recombination than with harmonic order, the distinction between trajectories is expected to be even stronger than between harmonic orders. The harmonic spectra in Fig. 4.23 illustrate this ability to preferentially enhance one electronic trajectory over the other using all-optical QPM with two counterpropagating pulses.

The experimental parameters for the data in Fig. 4.23 were as follows. The harmonics were generated in 200 $torr$ helium. The gas was introduced into an 11 cm waveguide at about 7 cm from the entrance. The pulse collision point was scanned through a 2 cm region just ahead of the gas input. The driving laser pulse had a duration of 27 fs, and an energy of 1.3 mJ, while each counterpropagating pulse had a duration of ~ 750 fs and an energy of ~ 0.2 mJ. The driving laser light was attenuated by a 200 nm silver and a 200 nm zirconium filter, and the spectrometer grating used was SB. Integration time of the CCD camera was 1 s, and each point shows the sum of three pixels, binned in order to reduce integration time. Two counterpropagating pulses were generated using the static delay method shown in inset a) of Fig. 4.2.

In the figure, the gray curve shows a typical spectrum detected in 200 $torr$ helium without the use of counterpropagating pulses. In this case the spectrum is dominated by the short trajectory. As shown by the red spectrum, all-optical QPM enhances these short trajectory peaks when two counterpropagating pulses with a pulse separation of ~ 840 μm are used. Dashed lines show that the peaks of the gray and red spectra occur

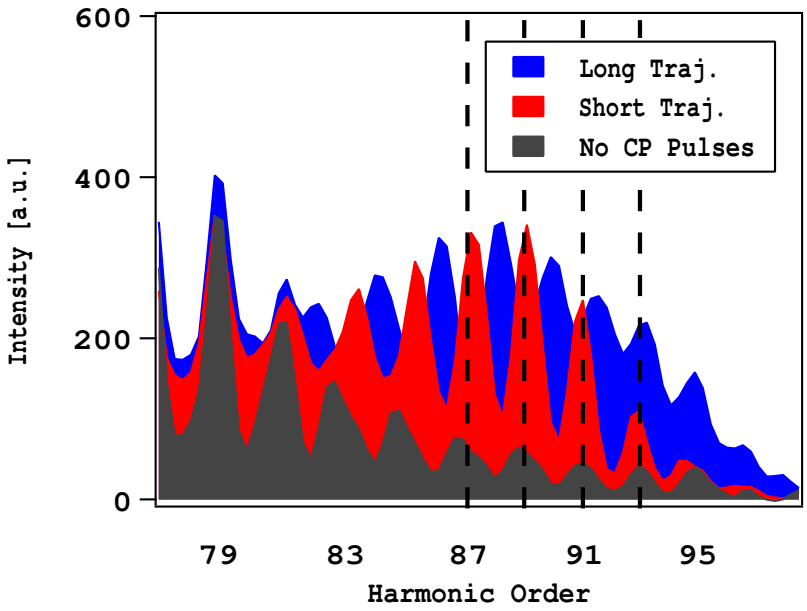

Figure 4.23: Selective enhancement of either the long or short quantum trajectories using all-optical QPM in helium. The dashed lines indicate the position of the harmonic peaks for the short trajectories. Harmonic spectra are show for no counterpropagating pulses (gray) or two counterpropagating pulses present at pulse separations of ~ 350 μm (blue) or ~ 840 μm (red). (These data were obtained from the same data set as Figure 3 in [69]

at the same approximate photon energy. In neither of these two spectra are double peaks, indicating the absence of strong emission from the long trajectory; only the short trajectory is enhanced. The blue spectrum, on the other hand, shows a two-pulse enhancement with a pulse separation of ~ 350 μm. The enhanced peaks are clearly blue-shifted relative to the short trajectory peaks, especially for harmonic orders 81-91, indicating that it is the long trajectory which has been enhanced. Furthermore, the short trajectory peaks are clearly not enhanced as well as in the red spectrum.

The only difference between these two enhanced spectra is the separation between the counterpropagating pulses. Further analysis reveals that for the blue spectra, the pulse separation corresponds to adjacent out-of-phase coherence zones, separated by $2L_c$, while for the red spectra, the pulse separation corresponds to $4L_c$. The distinction

between the two trajectories diminishes closer to the higher orders, $q > 91$. These harmonic orders are close to the cutoff photon energy for the laser parameters used, and the two trajectories merge near cutoff.

This ability to selectively enhance a single trajectory has great implications for spatio-temporal control of HHG. In particular, selection of a single quantum trajectory improves both the temporal and spatial coherence of HHG. These coherence properties are especially important for applications of HHG such as coherent imaging techniques [15,123]. Emission from long trajectories is strongly divergent compared to short trajectories for a couple of different reasons. First, the long trajectories have stronger coupling to the intensity dependent phase, and hence have a stronger modulation of the wavefront from a Gaussian or Bessel-shaped laser mode [65]. Second, better phase matching conditions off-axis will result in a more divergent harmonic spatial mode for the long trajectories, as described in Refs. [73] and [74].

Spatial and temporal coherence can be degraded due to interference of emission from different quantum trajectories. Previously, coherence properties have been improved through aperturing of the harmonic beam in the far field [8], or the use of long waveguides [68]. All-optical QPM not only isolates a single trajectory with good coherence properties, but also enhances its conversion efficiency, without the need for previous techniques which tend to be lossy. These qualities will become especially important as imaging and measurements requiring strong coherence move toward ever smaller wavelengths. Additionally, preferential selection of emission from a single trajectory has great implications for temporal shaping of HHG. The ability to control the generation of harmonic on a sub-cycle time scale can lead to the shaping of attosecond pulse trains, or even isolated attosecond pulses. Attosecond sources based on HHG have already been shown to be quite powerful in time-resolved measurements of electronic processes [21,124], and as attosecond sources become more accessible and tunable, new discoveries are sure to follow.

Chapter 5

Summary and Future Work

5.1 Summary

The work presented in this thesis includes several advances in the understanding and ability to control high-order harmonic generation. Energy loss in the driving laser beam obviously limits both the observable cutoff energy and the total harmonic intensity, and is documented here, illustrating its dependence on pressure. Simulations of ionization loss show that this is one of the major mechanisms for loss, but consistently accounts for only a portion of the total loss, regardless of the degree of ionization or free electron density. The use of a new experimental waveguide setup allowed two updated measurements: a higher harmonic photon yield estimate at 45 eV, and a systematic study of QPM with modulated waveguides. Concerning the modulated waveguides, enhancements at high photon energies ($150 - 250\ eV$) were shown to be reproducible in the new waveguide setup. A study of modulation depth showed that the optimal modulation is $< 2\%$ of the inner diameter. It is possible that the use of counterpropagating pulses to probe the generation process in modulated waveguides would further illustrate this QPM technique.

Probing the harmonic generation process with counterpropagating pulses has proven invaluable in providing previously unknown information about the coherence and the dephasing of HHG in hollow waveguides. Knowledge of the local, dynamically varying phase mismatch will be crucial in any quasi-phase matching scheme for HHG,

regardless of the geometry used or the QPM mechanism. Counterpropagating light has also shown some of the limitations, as well as advantages, of the use of hollow waveguides for HHG that could not have been easily predicted. Modebeating limits the longitudinal regions of high intensity, and therefore strong harmonic emission. However, the mutual coherence of harmonic emission from hollow waveguides was shown to be strong over extended interaction distances of at least 1 cm and possibly more. This fact makes the possibility for enhancing conversion efficiency through quasi-phase matching very promising.

Probing of the local coherence length also showed that the brightest emission of several harmonic orders occurs at different times within the femtosecond driving laser pulse. Temporal information such as this will provide information about the temporal structure of harmonic emission and how best to control it. Evidence for pressure-tuned phase matching in a hollow waveguide was also observed as an evident divergence of the coherence length when close to the optimal pressure. Intensity modulations from energy loss and modebeating were also unambiguously observed through variation of the local phase mismatch. Until now, the location of harmonic emission within the waveguide was not known. This type of characterization may be important in demonstrating the effect of plasma dynamics on HHG.

Two different regimes of coherent buildup of HHG were identified through probing, one where the harmonic emission strength is constant with propagation, and the other varying with propagation. In the first regime, strong coherent modulations are observed with the scan of a single counterpropagating pulse. In the second regime, a single counterpropagating pulse can lead to strong enhancement, but coherent modulations are not observed. The coherence in this region, as well as a measurement of the coherence length, can be demonstrated using a two-pulse probing technique. The ability to measure coherence length in both of these regimes is crucial to implementing QPM.

Counterpropagating pulses suppress the coherent buildup of the harmonic field by modulating the phase of the driving laser pulse over a small region. When destructive interference is suppressed using a series of counterpropagating pulses, the HHG process can be quasi-phase matched. All-optical quasi-phase matching using multiple counterpropagating pulses was demonstrated, producing enhancements of more than two orders of magnitude, both for emission from argon and helium. In each of these media, QPM was shown for photon energies that could not be phase matched using conventional techniques. The main advantages of this QPM technique are its flexibility, scalability, and efficiency. The coherence length was similar for both of the experimental demonstrations, however, the degree of ionization was quite different, demonstrating the applicability of all-optical QPM to varying plasma conditions. Since the coherence length can be measured carefully, the destructive interference can be suppressed efficiently. A larger enhancement simply requires a greater number of pulses. All-optical QPM is easily scaled to the shorter coherence lengths expected at higher photon energies.

Finally, all-optical QPM of HHG is selective, enhancing a narrow bandwidth of harmonic frequencies. This feature is especially attractive for applications requiring monochromaticity. Contributions to the harmonic emission from either of the electronic trajectories can also be selectively enhanced. This has important implications for improving the spatial coherence and transverse mode profile of harmonic emission, as well as manipulation of the temporal structure of the emission.

5.2 Future Work

Enhancements from all-optical QPM could certainly be improved beyond the results presented here. The enhancement is expected to increase with the addition of multiple counterpropagating pulses. For the shorter coherence lengths present at high harmonic orders, less energy is required in each counterpropagating pulse. The phase of

a higher harmonic order can be sufficiently modulated by a lower counterpropagating intensity. Also, for a short coherence length, the counterpropagating pulse duration is also shorter, lowering the total required energy. This will permit the generation of a train of many pulses for all-optical QPM for high harmonic orders. This is particularly beneficial, since the highest orders are currently the least efficiently generated.

To date, all-optical QPM has only been demonstrated for relatively long coherence lengths of $\sim$ 100's of μm. In this situation, the harmonic signal can be increased substantially even with a few pulses, since each coherence length summed adds a relatively large amount to the total intensity. All-optical QPM using shorter counterpropagating pulses is technically more difficult. The detection noise can mask the effect of a single, probing pulse, and necessarily longer integration times makes the data collection time-consuming. One way of extending efficient phase matching to higher photon energies is to use a longer driving laser wavelength [81, 83, 84]. However, the longer wavelengths reduce the recombination probability [85]. All-optical QPM used in combination with a longer driving laser wavelength could be a good compromise.

The addition of shaping techniques could allow more precise control over both HHG and all-optical QPM. In previous work, temporal [125] and spatial [103] shaping of the driving laser beam have led to greater conversion efficiency and manipulation of the harmonic beam. In our work, temporal pulse shaping was not used, but could be applied to generating a shorter driving laser pulse, or to carefully shaping the counterpropagating pulse train. As a first step, the optimal counterpropagating pulse shape could be determined using a pulse shaper to obtain the highest enhancement from a single pulse. More sophisticated shaping could be used to generate custom sequences of counterpropagating pulses. Genetic algorithms for pulse optimization may even provide new information on the QPM mechanism. Spatial shaping of either beam could be used to produce more optimal coupling conditions. Intensity fluctuations from modebeating may be reduced or selected for advantageous conditions.

Pulse trains could also be extended to different regions of the waveguide for substantially higher enhancements. As shown in Fig. 4.7, the harmonic generation is sometimes limited to local regions of the waveguide by guided mode interactions. So far, pulse trains used for QPM have been limited to only one of these regions at a time. By adding more pulses, delayed to interact in other regions of high intensity, more in-phase harmonic emission could be coherently summed. As a first step, it should be determined, through two-pulse probing, whether the emission from different regions is mutually coherent. This technique would be also be limited by the absorption depth of the gas used.

It is likely that in the regimes used for pressure-tuned phase matching in waveguides, low ionization and moderate pressure, the conversion efficiency is not maximized. The ionization loss and modebeating simulations and measurements presented above show that the intensity is likely not contained to the lowest-order, EH_{11}, propagation mode. Varying intensities and localized regions of harmonic generation can lead to an inefficient compensation of the phase mismatch, or unavoidable ringdown in the harmonic signal. Counterpropagating pulses may be useful for improving the obtainable harmonic signal. A long counterpropagating pulse could suppress out-of-phase emission from a long coherence length or a region of coherent ringdown of the signal in a region of strong intensity fluctuation. Another option is to use a compressed counterpropagating pulse to pre-ionize the gas. This is a potential way of suppressing the harmonic generation over an extended longitudinal region. At the low intensities used for pressure-tuned phase matching, insufficient for generating harmonics from ions, the harmonic generation will be essentially shut down in the region after the collision of the two pulses. The plasma will also tend to refract the driving laser beam. This technique was explored briefly, but without definitive results.

Several proposals [26,30] and one experimental demonstration [36] have dealt with the manipulation of the gas density as a means of quasi-phase matching. Certainly, the

gas density has a significant effect on HHG in many different ways. In the demonstrations of all-optical QPM and exploratory studies not presented here, it has been found that pressure ramps rather than constant pressure regions inside the waveguide produce higher harmonic orders, or a brighter harmonic signal. One possible area of future study is modeling of how pressure ramps affect both the local phase matching conditions and how different pressure profiles could be used to facilitate pressure-tuned phase matching, minimization of the detriments of ionization loss, or to facilitate all-optical QPM.

Absolute harmonic photon yield, however, can sometimes be secondary to the quality of the harmonic beam. For certain applications of HHG, such as coherent imaging, the spatial coherence and mode quality of the harmonic beam is just as crucial as the number of photons. Also important to imaging as well as molecular dynamics studies is the monochromaticity of the harmonic beam. Often multilayer mirrors and metal filters are used to select a narrow bandwidth, but these techniques often have a poor transmission efficiency. All-optical QPM has been shown to be effective in selecting a single harmonic, and selectivity is predicted to improve with both number of pulses and the order of QPM. It is also effective in selectively enhancing a single trajectory. Interference between multiple trajectories can lead to a degredation of the spatial coherence, and so a strong selection of a single trajectory should improve the spatial coherence, although this effect has yet to be shown experimentally. It is also likely that the selectivity of all-optical QPM will affect the spatial mode profile of the harmonic beam, since different trajectories have different phase fronts due to the intensity-dependent phase accumulation. This is also an effect that has not yet been measured and compared with predictions. Finally, all-optical QPM should have an effect on the temporal structure of the attosecond pulse train, and further studies could show if proper implementation of QPM with counterpropagating pulses would give more desirable temporal structures. Pulse and beam shaping would be powerful tools in manipulating the properties of the harmonic beam in combination with all-optical QPM.

Lastly, in a proposal by Oren Cohen, QPM with counterpropagating light could be extended to very short coherence lengths, on the order of a few microns, through a technique called grating-assisted phase matching (GAPM) [126]. In this technique, a quasi-cw counterpropagating beam, rather than a series of pulses, is used to modulated the phase of the driving laser. However, instead of using the counterpropagating light to suppress harmonic generation, in GAPM the counterpropagating field periodically corrects for the phase mismatch. When the wavelength of the counterpropagating light is matched to twice the coherence length, the phase of the driving laser is shifted at every coherence length in order to allow coherent buildup throughout the interaction medium. Optical parametric amplifiers (OPA's) are likely necessary to generate enough energy in the counterpropagating beam at the correct wavelength, on the order of microns. This technique is promising in combination with plasma waveguiding for generating very high photon energies. In plasma waveguides, harmonics can be generated in a pre-ionized gas medium, giving higher photon energies due to the higher ionization potential of the ions [127]. However, due to the high free electron density, the phase mismatch is very high, creating ideal conditions for GAPM. Variations in the local phase mismatch could be compensated through the use of pulse shaping to create the ideal counterpropagating field.

Bibliography

[1] H. Shin, D. Lee, Y. Cha, J.-H. Kim, K. Hong, and C. Nam, "Nonadiabatic blueshift of high-order harmonics from ar and ne atoms in an intense femtosecond laser field," Physical Review A, vol. 63, p. 053407, 2001.

[2] Z. Chang, A. Rundquist, H. Wang, I. Christov, H. Kapteyn, and M. Murnane, "Temporal phase control of soft-x-ray harmonic emission," Physical Review A, vol. 58, pp. R30–R33, 1998.

[3] C. Kan, C. Capjack, R. Rankin, and N. Burnett, "Spectral and temporal structure in high harmonic emission from ionizing atomic gases," Physical Review A, vol. 52, no. 6, pp. R4336–4339, 1995.

[4] M. B. Gaarde, F. Salin, E. Constant, P. Balcou, K. Schafer, K. Kulander, and A. L'Huillier, "Spatiotemporal separation of high harmonic radiation into two quantum path components," Physical Review A, vol. 59, no. 2, pp. 1367–1373, 1999.

[5] P. Salieres, A. L'Huillier, and M. Lewenstein, "Coherence control of high-order harmonics," Physical Review Letters, vol. 74, no. 19, pp. 3776–3779, 1995.

[6] C. Durfee, A. Rundquist, S. Backus, Z. Chang, C. Herne, H. Kapteyn, and M. Murnane, "Guided-wave phase-matching of ultrashort-pulse light," Journal of Nonlinear Optical Physics and Materials, vol. 8, no. 2, p. 23, 1999.

[7] E. Constant, D. Garzella, P. Breger, E. Mevel, C. Dorrer, C. Le Blanc, F. Salin, and P. Agostini, "Optimizing high harmonic generation in absorbing gases: Model and experiment," Physical Review Letters, vol. 82, no. 8, p. 4, 1999.

[8] M. Schnurer, Z. Cheng, M. Hentschel, G. Tempea, P. Kalman, T. Brabec, and F. Krausz, "Absorption-limited generation of coherent ultrashort soft-x-ray pulses," Physical Review Letters, vol. 83, no. 4, pp. 722–725, 1999.

[9] I. Christov, H. Kapteyn, and M. Murnane, "Quasi-phase matching of high-harmonics and attosecond pulses in modulated waveguides," Optics Express, vol. 7, no. 11, pp. 362–367, 2000.

[10] E. Gibson, A. Paul, N. Wagner, R. Tobey, D. Gaudiosi, S. Backus, I. Christov, A. Aquila, E. Gullikson, D. Attwood, M. Murnane, and H. Kapteyn, "Coherent soft x-ray generation in the water window with quasi-phase matching," Science, vol. 302, no. 5642, pp. 95–97, 2003.

[11] O. Cohen, A. Lytle, X. Zhang, M. Murnane, and H. Kapteyn, "Optimizing quasi-phase matching of high harmonic generation using counter propagating pulse trains," Optics Letters, vol. 32, no. 20, pp. 2975–2977, 2007.

[12] S. Voronov, I. Kohl, J. Madsen, J. Simmons, N. Terry, J. Titensor, Q. Wang, and J. Peatross, "Control of laser high-harmonic generation with counterpropagating light," Physical Review Letters, vol. 87, no. 13, p. 133902, 2001.

[13] A. J. Paul, "Coherent euv light from high-order harmonic generation: Enhancement and applications to lensless diffractive imaging," Ph.D. dissertation, University of Colorado at Boulder, 2007.

[14] W. Silfvast, Laser Fundamentals, 2nd ed. Cambridge, UK: Cambridge University Press, 2004.

[15] J. J. Rocca, "Table-top soft x-ray lasers," Review of Scientific Instruments, vol. 70, no. 10, pp. 3799–3827, 1999.

[16] D. Attwood, K. Halbach, and K.-J. Kim, "Tunable coherent x-rays," Science, vol. 228, no. 4705, pp. 1265–1272, 1985.

[17] K.-J. Kim and A. Sessler, "Free-electron lasers: Present status and future prospects," Science, vol. 250, no. 4977, pp. 88–93, 1990.

[18] D. Strickland and G. Mourou, "Compression of amplified chirped optical pulses," Optics Communications, vol. 56, no. 3, pp. 219–221, 1985.

[19] S. Backus, C. Durfee, M. Murnane, and H. Kapteyn, "High power ultrafast lasers," Review of Scientific Instruments, vol. 69, no. 3, p. 15, 1998.

[20] M. Bellini, C. Lynga, A. Tozzi, M. B. Gaarde, T. W. Hansch, A. L'Huillier, and C. G. Wahlstrom, "Temporal coherence of ultrashort high-order harmonic pulses," Physical Review Letters, vol. 81, no. 2, pp. 297–300, 1998.

[21] R. Bartels, A. Paul, H. Green, H. Kapteyn, M. Murnane, S. Backus, I. Christov, Y. Liu, D. Attwood, and C. Jacobsen, "Generation of spatially coherent light at extreme ultraviolet wavelengths," Science, vol. 297, no. 5580, pp. 376–377, 2002.

[22] J. Seres, E. Seres, A. Verhoef, G. Tempea, C. Strelill, P. Wobrauschek, V. Yakovlev, A. Scrinzi, C. Spielmann, and F. Krausz, "Source of coherent kilo-electronvolt x-rays," Nature, vol. 433, no. 7026, p. 3, 2005.

[23] I. Christov, M. Murnane, and H. Kapteyn, "High-harmonic generation of attosecond pulses in the "single-cycle" regime," Physical Review Letters, vol. 78, no. 7, pp. 1251–1254, 1997.

[24] P. Paul, E. Toma, P. Breger, G. Mullot, F. Auge, P. Balcou, H. G. Muller, and P. Agostini, "Observation of a train of attosecond pulses from high harmonic generation," Science, vol. 292, no. 5522, p. 3, 2001.

[25] M. Hentschel, R. Kienberger, S. C., G. Reider, N. Milosevic, T. Brabec, P. Corkum, U. Heinzmann, M. Drescher, and F. Krausz, "Attosecond metrology," Nature, vol. 414, no. 6863, pp. 509–512, 2001.

[26] R. Tobey, M. Siemens, O. Cohen, M. Murnane, and H. Kapteyn, "Ultrafast extreme ultraviolet holography: Dynamic monitoring of surface deformation," Optics Letters, vol. 32, p. 286, 2007.

[27] R. Sandberg, A. Paul, D. Raymondson, S. Hadrich, D. Gaudiosi, J. Holtsnider, R. Tobey, O. Cohen, M. Murnane, H. Kapteyn, C. Song, J. Miao, Y. Liu, and F. Salmassi, "Lensless diffractive imaging using tabletop, coherent, high harmonic soft x-ray beams," Physical Review Letters, vol. 99, no. 9, p. 098103, 2007.

[28] M. Wieland, C. Spielmann, U. Kleineberg, T. Westerwalbesloh, U. Heinzmann, and T. Wilhein, "Toward time-resolved soft x-ray microscopy using pulsed fs-high-harmonic radiation," Ultramicroscopy, vol. 102, no. 2, pp. 93–100, 2005.

[29] H. Niikura, F. Legare, R. Hasbani, M. Y. Ivanov, D. M. Villeneuve, and P. B. Corkum, "Probing molecular dynamics with attosecond resolution using correlated wave packet pairs," Nature, vol. 421, no. 6925, pp. 826–829, 2003.

[30] N. Wagner, A. West, I. Christov, T. Popmintchev, X. Zhou, M. Murnane, and H. Kapteyn, "Monitoring molecular dynamics using coherent electrons from high-harmonic generation," Proceedings of the National Academy of Sciences of the United States of America, vol. 103, p. 13279, 2006.

[31] E. Gagnon, P. Ranitovic, X.-M. Tong, C. Cocke, M. Murnane, H. Kapteyn, and A. Sandhu, "Soft x-ray driven femtosecond molecular dynamics," Science, vol. 317, no. 5843, pp. 1374–1378, 2007.

[32] J. Itatani, J. Levesque, D. Zeldler, H. Niikura, H. Pepin, J. Kieffer, P. Corkum, and D. Villeneuve, "Tomographic imaging of molecular orbitals," Nature, vol. 432, no. 7019, pp. 867–871, 2004.

[33] M. Drescher, M. Hentschel, R. Kienberger, M. Uiberacker, V. Yakovlev, A. Scrinzi, T. Westerwalbesloh, U. Kleineberg, U. Heinzmann, and F. Krausz, "Time-resolved atomic inner-shell spectroscopy," Nature, vol. 419, 2002.

[34] A. Baltuska, T. Udem, M. Uiberacker, M. Hentschel, E. Goulielmakis, C. Gohle, R. Holzwarth, V. S. Yakoviev, A. Scrinzi, T. W. Hansch, and F. Krausz, "Attosecond control of electronic processes by intense light fields," Nature, vol. 421, no. 6923, pp. 611–615, 2003.

[35] A. Rundquist, C. Durfee, Z. Chang, C. Herne, S. Backus, M. Murnane, and H. Kapteyn, "Phase-matched generation of coherent soft x-rays," Science, vol. 280, no. 5368, pp. 1412–1414, 1998.

[36] E. Takahashi, Y. Nabekawa, M. Nurhuda, and K. Midorikawa, "Generation of high-energy high-order harmonics by use of a long interaction medium," Journal of the Optical Society of America B - Optical Physics, vol. 20, p. 158, 2003.

[37] E. Takahashi, Y. Nabekawa, and K. Midorikawa, "Low-divergence coherent soft x-ray source at 13 nm by high-order harmonics," Applied Physics Letters, vol. 84, p. 4, 2004.

[38] P. Shkolnikov, A. Lago, and A. E. Kaplan, "Optimal quasi-phase-matching for high-order harmonic-generation in gases and plasma," Physical Review A, vol. 50, no. 6, pp. R4461–R4464, 1994.

[39] J. Peatross, M. Fedorov, and K. Kulander, "Intensity-dependent phase-matching effects in harmonic-generation," Journal of the Optical Society of America B - Optical Physics, vol. 12, no. 5, p. 7, 1995.

[40] J. Peatross, S. Voronov, and I. Prokopovich, "Selective zoning of high harmonic emission using counter-propagating light," Optics Express, vol. 1, no. 5, pp. 114–124, 1997.

[41] T. Auguste, B. Carre, and P. Salieres, "Quasi-phase-matching of high-order harmonics using a modulated atomic density," Physical Review A, vol. 76, p. 011802, 2007.

[42] B. Dromey, M. Zepf, M. Landreman, and S. M. Hooker, "Quasi-phasematching of harmonic generation via multimode beating in waveguides," Optics Express, vol. 15, no. 13, pp. 7894–7900, 2007.

[43] T. Pfeifer and M. C. Downer, "Direct experimental observation of periodic intensity modulation along a straight hollow-core optical waveguide," Journal of the Optical Society of America B-Optical Physics, vol. 24, no. 5, pp. 1025–1029, 2007.

[44] A. Paul, R. Bartels, R. Tobey, H. Green, S. Weiman, I. Christov, M. Murnane, H. Kapteyn, and S. Backus, "Quasi-phase-matched generation of coherent extreme-ultraviolet light," Nature, vol. 421, no. 6918, pp. 51–54, 2003.

[45] J. Seres, V. Yakovlev, E. Seres, C. Streli, P. Wobrauschek, C. Spielmann, and F. Krausz, "Coherent superposition of laser-driven soft-x-ray harmonics from successive sources," Nature Physics, vol. 3, pp. 878–883, 2007.

[46] R. R. Freeman, P. H. Bucksbaum, H. Milchberg, S. Darack, D. Schumacher, and M. E. Geusic, "Above-threshold ionization with subpicosecond laser-pulses," Physical Review Letters, vol. 59, no. 10, pp. 1092–1095, 1987.

[47] M. Ferray, A. L'Huillier, X. Li, L. Lompre, G. Mainfray, and C. Manus, "Multiple-harmonic conversion of 1064 nm radiation in rare gases," Journal of Physics B: Atomic, Molecular, and Optical Physics, vol. 21, pp. L31–L35, 1988.

[48] J. Macklin, J. Kmetic, and C. Gordon, "High-order harmonic-generation using intense femtosecond pulses," Physical Review Letters, vol. 70, no. 6, p. 3, 1993.

[49] J. Krause, K. J. Schafer, and K. C. Kulander, "High-order harmonic generation from atoms and ions in the high intensity regime," Physical Review Letters, vol. 68, pp. 3535–3539, 1992.

[50] K. Kulander, K. Schafer, and J. Krause, "Dynamics of short-pulse excitation, ionization, and harmonic conversion," in Super-Intense Laser-Atom Physics, B. Piraux, A. L'Huillier, and K. Rzazewski, Eds., vol. 316. Han-sur-Lesse, Belgium: Plenum, 1993, pp. 95–110.

[51] P. Corkum, "Plasma perspective on strong-field multiphoton ionization," Physical Review Letters, vol. 71, no. 13, p. 4, 1993.

[52] M. Lewenstein, P. Balcou, M. Ivanov, A. L'Huillier, and P. Corkum, "Theory of high-harmonic generation by low-frequency laser fields," Physical Review A, vol. 49, no. 3, p. 15, 1994.

[53] R. Boyd, Nonlinear Optics, 2nd ed. New York: Academic Press, 2003.

[54] T. Brabec and F. Krausz, "Intense few-cycle laser fields: Frontiers of nonlinear optics," Reviews of Modern Physics, vol. 72, no. 2, pp. 545–591, 2000.

[55] L. V. Keldysh, "Ionization in field of a strong electromagnetic wave," Soviet Physics Jetp-Ussr, vol. 20, no. 5, p. 1307, 1965.

[56] M. Ammosov, N. Delone, and V. Krainov, "Tunnel ionization of complex atoms and atomic ions in a varying electromagnetic field," Zhurnal Eksperimentalnoi I Teoreticheskoi Fiziki (JETP), vol. 91, no. 6, pp. 2008–2012, 1986.

[57] V. P. Krainov, "Ionization rates and energy and angular distributions at the barrier-suppression ionization of complex atoms and atomic ions," Journal of the Optical Society of America B-Optical Physics, vol. 14, no. 2, pp. 425–431, 1997.

[58] C. Spielmann, C. Kan, N. Burnett, T. Brabec, M. Geissler, A. Scrinzi, M. Schurer, and F. Krausz, "Near-kev coherent x-ray generation with sub-10-fs lasers," IEEE Journal of Selected Topics in Quantum Electronics, vol. 4, no. 2, p. 17, 1998.

[59] H. Tawara and T. Koto, "Total and partial ionzation cross sections of atoms and ions by electron impact," Atomic Data and Nuclear Data Tables, vol. 36, no. 2, pp. 167–353, 1987.

[60] I. Christov, J. Zhou, J. Peatross, A. Rundquist, M. Murnane, and H. Kapteyn, "Nonadiabatic effects in high-harmonic generation with ultrashort pulses," Physical Review Letters, vol. 77, no. 9, pp. 1743–1746, 1996.

[61] Z. Chang, A. Rundquist, H. Wang, M. Murnane, and H. Kapteyn, "Generation of coherent soft x rays at 2.7 nm using high harmonics," Physical Review Letters, vol. 79, no. 16, p. 3, 1997.

[62] P. Balcou, P. Salieres, A. L'Huillier, and M. Lewenstein, "Generalized phase-matching conditions for high harmonics: The rold of field-gradient forces," Physical Review A, vol. 55, no. 6, pp. 3204–3210, 1997.

[63] M. J. Landreman, "Quasi-phase matching techniques for high harmonic generation," Ph.D. dissertation, University of Oxford, 2007.

[64] C. Froud, E. Rogers, D. Hanna, W. Brocklesby, M. Praeger, A. de Paula, J. Baumberg, and J. Frey, "Soft-x-ray wavelength shift induced by ionization effects in a capillary," Optics Letters, vol. 31, no. 3, pp. 374–376, 2006.

[65] Z. Fangchuan, L. Zhong, Z. Zhinan, Z. Zhengquan, L. Ruxin, and X. Zhizhan, "Spectral splitting of high-order harmonic emissions from ionizing gases," Physical Review A, vol. 65, p. 033808, 2002.

[66] S. Rae, K. Burnett, and J. Cooper, "Generation and propagation of high-order harmonics in a rapidly ionizing medium," Physical Review A, vol. 50, no. 4, pp. 3438–3446, 1994.

[67] D. M. Gaudiosi, "High power ultrafast laser design and high-order harmonic generation in capillary discharge plasmas," Ph.D. dissertation, University of Colorado at Boulder, 2006.

[68] G. R. Fowles, Introduction to Modern Optics. New York: Holt, Rinehart and Winston, 1968.

[69] S. Rae, "Ionization-induced defocusing of intense laser pulses in high-pressure gases," Optics Communications, vol. 97, no. 1-2, pp. 25–28, 1993.

[70] C. Altucci, T. Starczewski, E. Mevel, C. G. Wahlstrom, B. Carre, and A. L'Huillier, "Influence of atomic density in high-order harmonic generation," Journal of the Optical Society of America B - Optical Physics, vol. 13, no. 1, pp. 148–156, 1996.

[71] T. Ditmire, E. Gumbrell, R. Smith, J. Tisch, D. Meyerhofer, and M. Hutchinson, "Spatial coherence measurement of soft x-ray radiation produced by high order harmonic generation," Physical Review Letters, vol. 77, no. 23, pp. 4756–4759, 1996.

[72] P. Salieres, T. Ditmire, M. Perry, A. L'Huillier, and M. Lewenstein, "Angular distributions of high-order harmonics generated by a femtosecond laser," Journal of Physics B: Atomic, Molecular, and Optical Physics, vol. 29, pp. 4771–4786, 1996.

[73] X. Zhang, A. R. Libertun, A. Paul, E. Gagnon, S. Backus, I. P. Christov, M. M. Murnane, H. C. Kapteyn, R. A. Bartels, Y. Liu, and D. T. Attwood, "Highly coherent light at 13 nm generated by use of quasi-phase-matched high-harmonic generation," Optics Letters, vol. 29, no. 12, pp. 1357–1359, 2004.

[74] X. Zhang, A. Lytle, O. Cohen, M. Murnane, and H. Kapteyn, "Quantum path control in high-order harmonic generation at high photon energies," New Journal of Physics, vol. 10, p. 025021, 2008.

[75] A. Rundquist, "Phase-matched generation of coherent, ultrafast x-rays using high harmonics," Ph.D. dissertation, Washington State University, 1998.

[76] A. L'Huillier and P. Balcou, "High-order harmonic-generation in rare-gases with a 1-ps 1053-nm laser," Physical Review Letters, vol. 70, no. 6, p. 4, 1993.

[77] A. L'Huillier, P. Balcou, and L. Lompre, "Coherence and resonance effects in high-order harmonic generation," Physical Review Letters, vol. 68, no. 2, pp. 166–169, 1992.

[78] G. Tempea, M. Geissler, M. Schnurer, and T. Brabec, "Self-phase-matched high harmonic generation," Physical Review Letters, vol. 84, no. 19, pp. 4329–4332, 2000.

[79] P. Leonard, "Refractive indices, verdet constants, and polarizabilities of the inert gases," Atomic Data and Nuclear Data Tables, vol. 14, pp. 21–37, 1987.

[80] www.cxro.lbl.gov.

[81] J. Zhou, J. Peatross, M. M. Murnane, and H. C. Kapteyn, "Enhanced high-harmonic generation using 25 fs laser pulses," Physical Review Letters, vol. 76, no. 5, pp. 752–755, 1996.

[82] A. Paul, E. Gibson, X. Zhang, A. Lytle, T. Popmintchev, X. B. Zhou, M. Murnane, I. Christov, and H. Kapteyn, "Phase-matching techniques for coherent soft x-ray generation," IEEE Journal of Quantum Electronics, vol. 42, no. 1-2, p. 12, 2006.

[83] P. Colosimo, G. Doumy, C. Blaga, J. Wheeler, C. Hauri, F. Catoire, J. Tate, R. Chirla, A. March, G. Paulus, H. G. Muller, P. Agostini, and L. DeMauro, "Scaling strong-field interactions towards the classical limit," 23 March 2008 2008.

[84] A. Gordon and F. X. Kartner, "Scaling of kev hhg photon yield with drive wavelength," Optics Express, vol. 13, no. 8, pp. 2941–2947, 2005.

[85] B. Shan and Z. H. Chang, "Dramatic extension of the high-order harmonic cutoff by using a long-wavelength driving field," Physical Review A, vol. 65, no. 1, 2002, 011804.

[86] T. O. Clatterbuck, C. Lynga, P. Colosimo, J. D. D. Martin, B. Sheehy, L. F. Dimauro, P. Agostini, and K. C. Kulander, "Scaled intense laser-atom physics: the long wavelength regime," Journal of Modern Optics, vol. 50, no. 3-4, pp. 441–450, 2003.

[87] J. Tate, T. Auguste, H. G. Muller, P. Salieres, P. Agostini, and L. F. DiMauro, "Scaling of wave-packet dynamics in an intense midinfrared field," Physical Review Letters, vol. 98, no. 1, 2007, 013901.

[88] T. Popmintchev, M.-C. Chan, O. Cohen, M. Grisham, J. Rocca, M. Murnane, and H. Kapteyn, "Extended phase-matching of high-order harmonics driven by mid-infrared light," Optics Letters, submitted for publication.

[89] N. Wagner, E. Gibson, T. Popmintchev, I. Christov, M. Murnane, and H. Kapteyn, "Self-compression of ultrashort pulses through ionization-induced spatiotemporal reshaping," Physical Review Letters, vol. 93, no. 17, p. 173902, 2004.

[90] J. A. Armstrong, N. Bloembergen, J. Ducuing, and P. S. Pershan, "Interactions between light waves in a nonlinear dielectric," Physical Review, vol. 127, no. 6, p. 1918, 1962.

[91] P. A. Franken and J. F. Ward, "Optical harmonics and nonlinear phenomena," Reviews of Modern Physics, vol. 35, no. 1, p. 23, 1963.

[92] M. M. Fejer, G. A. Magel, D. H. Jundt, and R. L. Byer, "Quasi-phase-matched 2nd harmonic-generation - tuning and tolerances," Ieee Journal of Quantum Electronics, vol. 28, no. 11, pp. 2631–2654, 1992.

[93] G. A. Magel, M. M. Fejer, and R. L. Byer, "Quasi-phase-matched second-harmonic generation of blue light in periodically poled linbo3," Applied Physics Letters, vol. 56, pp. 108–110, 1990.

[94] D. H. Jundt, G. A. Magel, M. M. Fejer, and R. L. Byer, "Periodically poled linbo3 for high-efficiency second-harmonic generation," Applied Physics Letters, vol. 59, pp. 2657–2659, 1991.

[95] E. A. Gibson, "Quasi-phase matching of soft x-ray light from high-order harmonic generation using waveguide structures," Ph.D. dissertation, University of Colorado at Boulder, 2004.

[96] E. Marcatili and R. Schmeltzer, "Hollow metallic and dielectric waveguides for long distance optical transmission and lasers," Bell System Technical Journal, vol. 43, p. 24, 1964.

[97] R. Abrams, "Coupling losses in hollow waveguide laser resonators," IEEE Journal of Quantum Electronics, vol. 8, no. 11, p. 5, 1972.

[98] M. Geissler, G. Tempea, A. Scrinzi, M. Schnurer, F. Krausz, and T. Brabec, "Light propagation in field-ionizing media: Extreme nonlinear optics," Physical Review Letters, vol. 83, no. 15, pp. 2930–2933, 1999.

[99] C. Courtois, A. Couairon, B. Cros, J. Marques, and G. Matthieussent, "Propagation of intense ultrashort laser pulses in a plasma filled capillary tube: Simulations and experiments," Physics of Plasmas, vol. 8, no. 7, p. 11, 2001.

[100] D. Homoelle and A. Gaeta, "Nonlinear propagation dynamics of an ultrashort pulse in a hollow waveguide," Optics Letters, vol. 25, no. 10, pp. 761–763, 2000.

[101] O. Kolevatova, A. Naumov, and A. Zheltikov, "Guiding high-intensity laser pulses through hollow fibers: self-phase modulation and cross-talk of guided modes," Optics Communications, vol. 217, pp. 169–177, 2003.

[102] G. Tempea and T. Brabec, "Theory of self-focusing in a hollow waveguide," Optics Letters, vol. 23, no. 10, p. 3, 1998.

[103] M. Zepf, B. Dromey, M. Landreman, P. Foster, and S. M. Hooker, "Bright quasi-phase-matched soft-x-ray harmonic radiation from argon ions," Physical Review Letters, vol. 99, no. 14, p. 143901, 2007.

[104] T. Pfeifer, R. Kemmer, R. Spitzenpfeil, D. Walter, C. Winterfeldt, G. Gerber, and C. Spielmann, "Spatial control of high-harmonic generation in hollow fibers," Optics Letters, vol. 30, no. 12, pp. 1497–1499, 2005.

[105] P. Arpin, A. Lytle, M. Murnane, and H. Kapteyn, "High-order harmonic generation from argon ions up to the ti l edge using pulse compression," Optics Letters, in preparation.

[106] M. Landreman, K. O'Keefe, T. Robinson, M. Zepf, B. Dromey, and S. M. Hooker, "Comparison of parallel and perpendicular polarised counter-propagating light for suppressing high harmonic generation," Journal of the Optical Society of America B - Optical Physics, vol. 24, no. 9, pp. 2421–2427, 2007.

[107] M. Y. Ivanov, T. Brabec, and N. Burnett, "Coulomb corrections and polarization effects in high-intensity high-harmonic emission," Physical Review A, vol. 54, no. 1, pp. 742–745, 1996.

[108] P. Antoine, A. Lhuillier, M. Lewenstein, P. Salieres, and B. Carre, "Theory of high-order harmonic generation by an elliptically polarized laser field," Physical Review A, vol. 53, no. 3, pp. 1725–1745, 1996.

[109] K. S. Budil, P. Salieres, A. Lhuillier, T. Ditmire, and M. D. Perry, "Influence of ellipticity on harmonic-generation," Physical Review A, vol. 48, no. 5, pp. R3437–R3440, 1993.

[110] J. Madsen, L. Hancock, S. Voronov, and J. Peatross, "High-order harmonic generation in crossed laser beams," Journal of the Optical Society of America B - Optical Physics, vol. 20, no. 1, p. 4, 2003.

[111] J. Peatross, J. Miller, K. Smith, S. Rhynard, and B. Pratt, "Phase matching of high-order harmonic generation in helium- and neon-filled gas cells," Journal of Modern Optics, vol. 51, no. 16-18, p. 8, 2004.

[112] J. Sutherland, E. Christensen, N. Powers, S. Rhynard, J. Painter, and J. Peatross, "High harmonic generation in a semi-infinite gas cell," Optics Express, vol. 12, no. 19, p. 6, 2004.

[113] D. Gaudiosi, E. Gagnon, A. Lytle, J. Fiore, E. Gibson, S. Kane, J. Squier, M. Murnane, H. Kapteyn, R. Jimenez, and S. Backus, "Multi-kilohertz repetition rate ti : sapphire amplifier based on down-chirped pulse amplification," Optics Express, vol. 14, no. 20, p. 6, 2006.

[114] R. Trebino and D. Kane, "Using phase retrieval to measure the intensity and phase of ultrashort pulses - frequecy-resolved optical gating," Journal of the Optical Society of America A - Optics Image Science and Vision, vol. 10, no. 5, p. 10, 1993.

[115] physics.nist.gov/Divisions/Div841/Gp1/xuv.detectors/Al.detector.html.

[116] J. Yeager and M. Hrusch-Tupta, Low Level Measurements Handbook: Precision DC Current, Voltage, and Resistance Measurements, 5th ed. Cleveland: Keithley Instruments, Inc., 1998.

[117] X. Zhang, A. Lytle, T. Popmintchev, A. Paul, N. Wagner, M. Murnane, H. Kapteyn, and I. Christov, "Phase matching, quasi-phase matching, and pulse compression in a single waveguide for enhanced high-harmonic generation," Optics Letters, vol. 30, no. 15, p. 3, 2005.

[118] J. Peatross, J. Chaloupka, and D. Meyerhofer, "High-order harmonic generation with an annular laser beam," Optics Letters, vol. 19, p. 942944, 1994.

[119] X. Zhang, A. Lytle, T. Popmintchev, X. Zhou, M. Murnane, H. Kapteyn, and O. Cohen, "Quasi-phase matching and quantum path control of high harmonic generation using counterpropagating light," Nature Physics, vol. 3, no. 4, pp. 270–275, 2007.

[120] A. Lytle, X. Zhang, R. Sandberg, O. Cohen, H. Kapteyn, and M. Murnane, "Quasi-phase matching and characterization of high-order harmonic generation in hollow waveguides using counterpropagating light," Optics Express, vol. 16, no. 9, pp. 6544–6566, 2008.

[121] A. Lytle, X. Zhang, J. Peatross, M. Murnane, H. Kapteyn, and O. Cohen, "Probe of high-order harmonic generation using counterpropagating light in a hollow waveguide," Physical Review Letters, vol. 98, no. 12, p. 123904, 2007.

[122] A. Lytle, X. Zhang, P. Arpin, O. Cohen, M. Murnane, and H. Kapteyn, "Quasi-phase matching of high order harmonic generation at high photon energies using counterpropagating pulses," Optics Letters, vol. 33, no. 2, pp. 174–176, 2008.

[123] W. F. Schlotter, R. Rick, K. Chen, A. Scherz, J. Stohr, J. Luning, S. Eisebitt, C. Gunther, W. Eberhardt, O. Hellwig, and I. McNulty, "Multiple reference fourier transform holography with soft x rays," Applied Physics Letters, vol. 89, no. 16, 2006, 163112.

[124] E. Goulielmakis, V. S. Yakovlev, A. L. Cavalieri, M. Uiberacker, V. Pervak, A. Apolonski, R. Kienberger, U. Kleineberg, and F. Krausz, "Attosecond control and measurement: Lightwave electronics," Science, vol. 317, no. 5839, pp. 769–775, 2007.

[125] R. Bartels, S. Backus, E. Zeek, L. Misoguti, G. Vdovin, I. Christov, M. Murnane, and H. Kapteyn, "Shaped-pulse optimization of coherent emission of high-harmonic soft x-rays," Nature, vol. 406, no. 6792, p. 2, 2000.

[126] O. Cohen, X. Zhang, A. Lytle, T. Popmintchev, M. Murnane, and H. Kapteyn, "Grating-assisted phase matching in extreme nonlinear optics," Physical Review Letters, vol. 99, no. 5, p. 053902, 2007.

[127] D. Gaudiosi, B. Reagan, T. Popmintchev, M. Grisham, M. Berrill, O. Cohen, B. Walker, M. Murnane, H. Kapteyn, and J. Rocca, "High-order harmonic generation from ions in a capillary discharge," Physical Review Letters, vol. 96, no. 20, p. 203001, 2006.

[128] D. Spence, P. Kean, and W. Sibbett, "60-fsec pulse generation from a self-mode-locked ti-sapphire laser," Optics Letters, vol. 16, no. 1, p. 3, 1991.

[129] M. Asaki, C. Huang, D. Garvey, J. Zhou, H. Kapteyn, and M. Murnane, "Generation of 11-fs pulses from a self-mode-locked ti-sapphire laser," Optics Letters, vol. 18, no. 12, p. 3, 1993.

[130] A. Baltuska, Z. Wei, M. Pshenichnikov, D. Wiersma, and R. Szipocs, "All-solid-state cavity-cumped sub-5-fs laser," Applied Physics B - Lasers and Optics, vol. 65, no. 2, p. 13, 1997.

[131] Y. Liau, A. Unterreiner, D. Arnett, and N. Scherer, "Femtosecond-pulse cavity-dumped solid-state oscillator design and application to ultrafast microscopy," Applied Optics, vol. 38, no. 36, p. 6, 1999.

[132] A. Libertun, R. Shelton, H. Kapteyn, and M. Murnane, "A 36-nj - 15.5 mhz extended-cavity ti:sapphire oscillator," presented at the Conference on Lasers and Electro-Optics, 1999.

[133] A. Kowalevicz, A. Zare, F. Kartner, J. Fujimoto, S. Dewald, U. Morgner, V. Scheuer, and G. Angelow, "Generation of 150-nj pulses from a multiple-pass cavity kerr-lens mode-locked ti:al2o3 oscillator," Optics Letters, vol. 28, no. 17, p. 3, 2003.

[134] J. Sung, K. Hong, Y. Cha, and C. Nam, "13-fs, 1-mw ti:sapphire laser oscillator in a long-cavity configuration," Japanese Journal of Applied Physics part 2 - Letters, vol. 41, no. 8B, p. 3, 2002.

[135] A. Fox and T. Li, "Computer-simulation of laser resonators - retrospective view," IEEE Journal of Quantum Electronics, vol. 15, no. 9, p. 1, 1979.

[136] S. Chu, T. Liu, and C. Sun, "Real-time second-harmonic generation microscopy based on a 2-ghz repetition rate ti:sapphire laser," Optics Express, vol. 11, no. 8, p. 5, 2003.

[137] A. Bartels, T. Dekorsy, and H. Kurz, "Femtosecond ti:sapphire ring laser with a 2-ghz repetition rate and its application in time-resolved spectroscopy," Optics Letters, vol. 24, no. 14, p. 3, 1999.

[138] A. Bartels and H. Kurz, "Generation of a broadband continuum by a ti:sapphire femtosecond oscillator with a 1-ghz repetition rate," Optics Letters, vol. 27, no. 20, p. 3, 2002.

[139] M. Ramaswamy-Paye and J. Fujimoto, "Compact dispersion-compensating geometry for kerr-lens mode-locked femtosecond lasers," Optics Letters, vol. 19, no. 21, p. 3, 1994.

[140] Z. Liu, S. Izumida, C. Liu, N. Sarukura, T. Hikita, Y. Segawa, T. Hatani, T. Sugaya, T. Nakagawa, and Y. Sugiyama, "1-ghz repetition-rate mode-locked ti:sapphire laser using a saturable bragg reflector," Conference on Lasers and Electro-Optics, OSA Technical Digest Series, p. 29, 1996.

[141] A. Stingl, C. Spielmann, R. Szipocs, and F. Krausz, "Compact high-repetition-rate femtosecond lasers using chirped mirrors," Conference on Lasers and Electro-Optics, OSA Technical Digest Series, pp. 66–67, 1996.

[142] V. Magni, G. Cerullo, and S. DeSilvestri, "Closed-form gaussian-beam analysis of resonators containing a kerr medium for femtosecond lasers," Optics Communications, vol. 101, no. 5-6, p. 5, 1993.

[143] C. Spielmann, P. Curley, T. Brabec, and F. Krausz, "Ultrabroadband femtosecond lasers," IEEE Journal of Quantum Electronics, vol. 30, no. 4, p. 14, 1994.

[144] O. Martinez and J. Chilla, "Self-mode-locking of ti-sapphire lasers - a matrix formalism," Optics Letters, vol. 17, no. 17, p. 3, 1992.

[145] I. Christov, V. Stoev, M. Murnane, and H. Kapteyn, "Mode-locking with a compensated space-time astigmatism," Optics Letters, vol. 20, no. 20, p. 3, 1995.

[146] I. Christov, H. Kapteyn, M. Murnane, C. Huang, and J. Zhou, "Space-time focusing of femtosecond pulses in a ti:sapphire laser," Optics Letters, vol. 20, no. 3, p. 3, 1995.

[147] A. Penzkofer, M. Wittmann, M. Lorenz, E. Siegert, and S. MacNamara, "Kerr lens effects in a folded-cavity four-mirror linear resonator," Optical and Quantum Electronics, vol. 28, no. 4, p. 19, 1996.

[148] H. Kogelnik, C. Shank, A. Dienes, and E. Ippen, "Astigmatically compensated cavities for cw dye lasers," IEEE Journal of Quantum Electronics, vol. 8, no. 3, p. 1, 1972.

[149] S. Uemura and K. Miyazaki, "Femtosecond cr:lisaf laser pumped by a single diode laser," Optics Communications, vol. 138, no. 4-6, p. 3, 1997.

[150] J. Hopkins, G. Valentine, B. Agate, A. Kemp, U. Keller, and W. Sibbett, "Highly compact and efficient femtosecond cr:lisaf laser," IEEE Journal of Quantum Electronics, vol. 38, no. 4, p. 8, 2002.

[151] E. Seres, J. Seres, F. Krausz, and C. Spielmann, "Generation of coherent soft x-ray radiation extending far beyond the titanium l edge," Physical Review Letters, vol. 92, p. 163002, 2004.

[152] F. Powell, P. Vedder, J. Lindblom, and S. Powell, "Thin film filter performance for extreme ultraviolet and x-ray applications," Optical Engineering, vol. 29, pp. 614–624, 1990.

[153] R. Falcone and J. Bokor, "Dichroic beamsplitter for extreme-ultraviolet and visible radiation," Optics Letters, vol. 8, pp. 21–23, 1983.

[154] E. Takahashi, H. Hasegawa, N. Nabekawa, and K. Midorikawa, "High-throughput, high-damage-threshold broadband beam splitter for high-order harmonics in the extreme ultraviolet region," Optics Letters, vol. 29, pp. 507–509, 2004.

[155] J. Monga, "Double-layer broadband antireflection coatings for grazing incidence angles," Applied Optics, vol. 31, no. 4, p. 546, 1992.

[156] H. McLeod, Thin Film Optical Filters. Bristol, UK: Hilger, 1986.

[157] S. Kohli, C. D. Rithner, P. K. Dorhout, A. M. Dummer, and C. S. Menoni, "Comparison of nanometer-thick films by x-ray reflectivity and spectroscopic ellipsometry," Review of Scientific Instruments, vol. 76, no. 2, 2005, 023906.

[158] F. Krausz, M. Fermann, T. Brabec, P. Curley, M. Hofer, M. Ober, C. Spielmann, E. Wintner, and A. Schmidt, "Femtosecond solid-state lasers," IEEE Journal of Quantum Electronics, vol. 28, no. 10, pp. 2097–2122, 1992.

[159] H. Haus, J. Fujimoto, and E. Ippen, "Analytic theory of additive pulse and kerr lens mode locking," IEEE Journal of Quantum Electronics, vol. 28, no. 10, pp. 2086–2096, 1992.

Appendix A

Variable Repetition-Rate Ti:Sapphire Oscillators

A.1 Introduction

Since the first demonstration of self-modelocking [128], ultrafast Ti:sapphire lasers have become the workhorse devices for generating ultrafast pulses in the near infrared. Typical modelocked oscillators operate at a repetition rate between 70 and 100 MHz, with an output power of about 500 mW when pumped with 5 W of CW green laser radiation. This corresponds to a pulse energy of about 6 nJ. Since the gain bandwidth of Ti:sapphire is so large, pulse durations of 10 fs and shorter are routinely achievable [129]. Thus the typical peak output power of the standard oscillator is about 0.6 MW.

Several techniques have been demonstrated for increasing the peak power directly from an oscillator without the use of extracavity amplification. Cavity dumping has been shown to generate peak powers of up to 5 MW [130, 131]. However, cavity dumped lasers are complex, expensive, and generally more difficult to operate than a simple laser oscillator. Recently, alternative approaches to increasing the peak power from oscillator have been developed by increasing the cavity length [132–134]. The lower repetition rate allows for more energy in a single pulse for a given average power. However, simply increasing the length of a Ti:sapphire laser cavity quickly results in an unstable geometry. By inserting a telescope, or multiple telescopes, into the cavity, the overall physical length of the cavity can be increased without changing the round-trip "ABCD" matrix [135] that determines the stability of the laser. This procedure

has been demonstrated for repetition rates as low as 5.85 MHz with pulse durations as short as 43 fs [133]. In some of these designs, the use of saturable Bragg mirror reflectors (SBR) to prevent multiple pulsing limits the pulse duration obtainable from the laser. Alternatively, there has also been interest in the development of compact, high repetition rate lasers, which have applications in frequency metrology, high speed communications, and biological imaging [136]. Several examples of high repetition rate oscillators have been demonstrated [137–141], some of which have repetition rates of 1 GHz or more. However, these designs are also more specialized and expensive, requiring custom coatings and optics, and are not tunable. Most are forced to sacrifice bandwidth, average output power, or experimental robustness. The Kerr lens modelocking (KLM) mechanism that results in ultrashort pulse generation is simple in principle, but is complex and incompletely understood in practice. Extensive work has been done in modeling KLM laser resonators using ABCD formalisms [142–144], and also using more rigorous approaches including full space-time propagation models [145]. However, dynamics such as space-time focusing and self- phase modulation in the Ti:sapphire crystal [146] are complex enough that modeling gives limited guidance on real world usability and stability issues. As a consequence, experimentation is necessary for each new cavity design, and few variations have a robustness comparable to the "standard" modelocked Ti:sapphire cavity design [129].

In this Appendix, I describe a very simple approach that can be applied to both extending and shortening the length of a Ti:sapphire cavity. We use a simple asymmetric focusing geometry that alters the cavity length while preserving the overall cavity propagation, and that provides the exceptional stability and ease of use inherent to the standard cavity configuration.

A.2 Theory

The basic cavity configuration of the modelocked Ti:sapphire laser is shown in Fig. A.1, along with definitions of various cavity parameters.

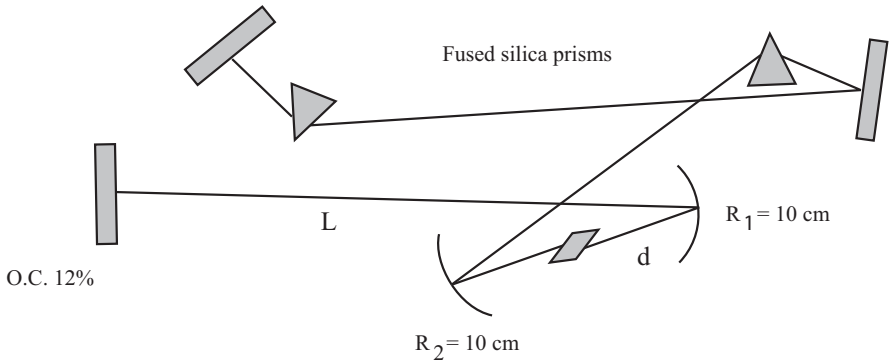

Figure A.1: Diagram of the standard Ti:sapphire cavity.

Calculations were performed to determine how the stability could be maintained as the cavity length was altered. The dynamics of modelocking are neglected in the calculation. As in previous research [133], the goal of these calculations is to construct a round-trip ABCD matrix that is effectively the same as the standard cavity, even as the overall cavity length is altered. We can do this by changing the length L and the radius of curvature R, of one or both "arms" of the cavity, as referenced to the Ti:sapphire crystal. If the q-parameter is the same for the asymmetric cavity as for a standard cavity in cw operation, the idea is that the modelocking initiation procedure and behavior will be the same as well. Ignoring the astigmatism in the cavity introduced by the off-axis reflection, the round trip ABCD matrix for one arm of the cavity, starting from the edge of the crystal, reflecting from the curved mirror and to the plane mirror and back, is given by

$$\begin{pmatrix} \frac{1}{R}\left(R-4\left(L+d\right)+\frac{8Ld}{R}\right) & \frac{2}{R}\left(R\left(L+d\right)-4Ld-2d^2+\frac{4Ld^2}{R}\right) \\ \frac{4}{R}\left(\frac{2L}{R}-1\right) & \frac{1}{R}\left(R-4\left(L+d\right)+\frac{8Ld}{R}\right) \end{pmatrix} \tag{A.1}$$

where L is the distance from the curved mirror to the output coupler, d is the distance from the curved mirror to the crystal, and R is the radius of curvature (ROC) of the mirror. Generally in the cw Ti:sapphire cavity, R ≈ 2d. Setting R = 2d simplifies the matrix considerably to

$$\begin{pmatrix} -1 & 0 \\ \frac{4}{R}\left(\frac{2L}{R}-1\right) & -1 \end{pmatrix} \tag{A.2}$$

By equating the value of the "C" element of the matrix for two different cavities, we determine cavity parameters (L_b, R_b), that give an overall ray matrix similar to the standard cavity (L_a, R_a). L_b corresponds to

$$L_b = \frac{1}{2}\left[\left(\frac{R_b}{R_a}\right)^2 (2L_a - R_a) + R_b\right] \tag{A.3}$$

Using the parameters from the standard cavity, Table A.1 lists the corresponding values for two possible asymmetric cavities, having altered the output coupling arm, which give the same ABCD matrix in this approximation.

Standard cavity	Low rep rate cavity	High rep rate cavity
L = 60 cm	L = 230 cm	L = 16.25 cm
d = 5 cm	d = 10 cm	d = 2.5 cm
R_1 = 10 cm	R_1 = 20 cm	R_1 = 5 cm

Table A.1: Cavity parameters for ABCD matrices

Without changing the q parameter of the Gaussian beam, and therefore without changing the laser stability, the distance to the output coupler may be nearly quadrupled by using a 20 cm ROC as one of the focusing optics, and it may be nearly quartered by using a 5 cm ROC optic. The length of the prism arm of the cavity could be altered in a similar way.

The radii of curvature of the two focusing mirrors are different, and therefore the incidence angles must also be different in order to compensate for astigmatism. The

incidence angles for this laser were calculated using ABCD matrices [147, 148].

$$\cos\theta = \frac{l_c}{2n_L R}\left(\frac{1}{n_L^2} - 1\right) \mp \frac{1}{R}\sqrt{\left(\frac{l_c}{2n_L}\right)^2\left(1 - \frac{1}{n_L^2}\right)^2 + R^2} \tag{A.4}$$

Here l_c is the length and n_L is the refractive index of the Brewster angled crystal, R_1 and R_2 are the radii of curvature of the mirrors as indicated in Fig. A.1, and θ is the incidence angle. The angles of incidence for each of the curved mirrors were calculated using Eqn. A.4 and are listed in Table A.2. In all cases, $n_L = 1.75$.

Standard cavity	Low rep rate cavity	High rep rate cavity
l_c = 4.75 mm	l_c = 4.75 mm	l_c = 3.00 mm
$R_{1,2}$ = 10 cm	R_2 = 100 mm, $\theta = 7.5°$	R_2 = 50 mm, $\theta = 8.7°$
	R_1 = 200 mm, θ =5.3°	R_1 = 75 mm, $\theta = 7.1°$

Table A.2: Astigmatism compensation angles

A.3 Low Repetition Rate Laser

Design

Our design for extending the cavity length of the Ti:sapphire laser requires changing only two optics in a standard Ti:sapphire laser: the output coupler and one of the curved mirrors. Instead of using two identical mirrors with the same radius of curvature to focus the beam into the Ti:sapphire crystal, this laser uses one mirror with twice the ROC (20 cm) of the other (10 cm). This is the first time to our knowledge that such an asymmetric cavity has been employed for the purpose of changing the repetition rate of a modelocked Ti:sapphire laser, although past ABCD analyses for modelocked Ti:sapphire lasers have included the possibility of an asymmetric cavity [143]. Asymmetric cavities have been demonstrated [149, 150] in modelocked Cr:LiSAF systems so that they may be directly pumped by a single diode laser and have a small footprint. In this case, the larger ROC optic allows the distance to the output coupler to be increased

significantly, while maintaining cavity stability as discussed above. The length of the prism arm remains unchanged. This results in a laser with approximately twice the cavity length and therefore half the repetition rate of the standard Ti:sapphire laser.

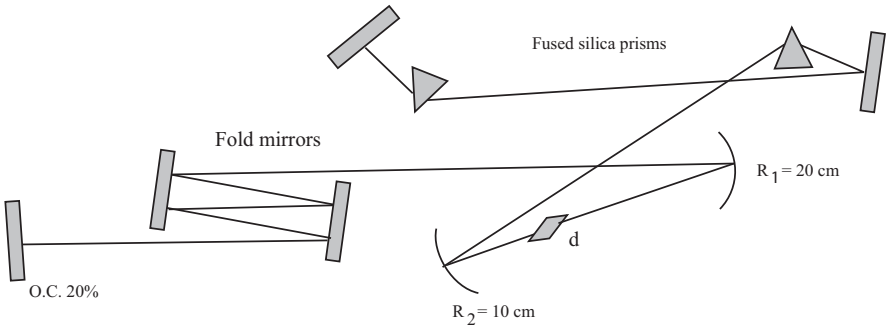

Figure A.2: Diagram of the low repetition rate cavity.

The setup, shown in Fig. A.2, is quite similar to that of a standard Ti:sapphire laser. The laser has two flat end mirrors, three flat fold mirrors, two curved mirrors focusing into a Ti:sapphire crystal, and two prisms for intracavity dispersion compensation. The Ti:sapphire crystal is 4.75 mm long, doped at 0.15%. The three fold mirrors and one of the end mirrors are dielectric and $> 99\%$ reflective at center wavelength 800 nm. A larger output coupler of 20% is used to suppress multiple pulsing and to increase the output power. The curved mirrors, with radii of curvature 10 cm and 20 cm, are aligned in an astigmatism compensated X configuration about the crystal. The 10 cm mirror was set to an astigmatism compensation angle of $7.5 \pm 1.0°$, and the 20 cm was set to an angle of $5.3 \pm 1.0°$. The Ti:sapphire crystal is pumped by 4.75 W from a frequency doubled Nd:Vanadate laser (Coherent Verdi) at 532 nm. The pump beam is focused into the cavity with a lens of focal length 10.5 cm through the R = 10 cm optic. The flat side of the mirror was AR coated for 532 nm to minimize loss. The prisms are Brewster cut fused silica, at a separation of $\sim$63 cm. The total length of the single pass cavity is $\sim$333 cm, resulting in a pulse repetition rate of 45 ± 1 MHz, as measured by a fast photodiode.

Performance

An extracavity prism pair compensated for the dispersion of the output coupler, crystal, and pulse measurement optics. Calculations indicated that the equilateral, fused silica prisms should be separated by about 100 cm in order to correct for GVD. The compressed pulse was measured using SHG FROG [114]. The FROG trace was deconvolved using Femtosoft FROG3 software to yield a FWHM pulse duration of 15 ± 2 fs, shown in Fig. **??**(a). The pulse duration was limited by uncompensated third order dispersion, as can be seen as a "ringing" effect at the leading edge of the pulse. This and the 1 fs resolution of the FROG setup were the main sources of uncertainty in the measurement of the pulse duration. The transform limited pulse duration, determined by an inverse Fourier transform of the experimental spectrum shown in Fig. A.3(b), is $\sim$13 fs.

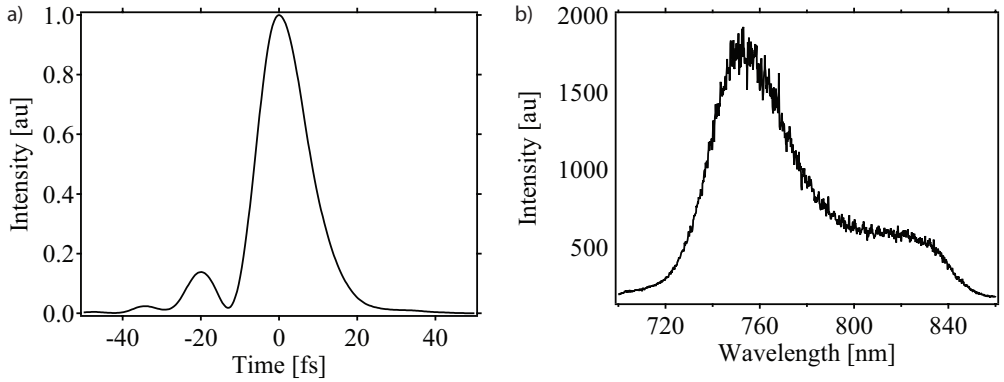

Figure A.3: (a) The deconvolved pulse width and (b) experimental spectrum for the low repetition rate laser.

When modelocked in the standard negative dispersion regime, stable, $\sim$15 fs pulses were obtained at an average output power of 400 mW, with a typical power discrimination of 50 mW. At a repetition rate of 45 MHz, this corresponds to a pulse energy of 10 nJ, or twice that usually obtained from a standard Ti:sapphire laser operating at such short pulse widths.

In order to initiate modelocking, we decrease the length d until the intracavity power reaches a value that favors stably modelocked operation, then introduce a brief disturbance to initiate a pulse. This is the same procedure used for a standard Ti:sapphire laser. However, for a similar bandwidth, the extended cavity laser operates at a slightly lower average output power of ∼400 mW, likely the result of a somewhat lower than optimum output coupling. Modelocking is achieved as a result of gain-aperturing, as in the standard Kerr lens modelocked Ti:sapphire laser. Stability is limited mainly by environmental factors- in our case from air currents and significant temperature fluctuations. The laser would persist in modelocked operation for several hours uncovered in the lab. The absence of multiple pulse instabilities, self Q-switching, and double pulsing was confirmed by observation of the pulse train by a fast photodiode and a spectrometer.

A.4 High Repetition Rate Laser

Design

To shorten the cavity length, we incorporated asymmetric focusing mirrors along with other techniques. Since the main limit on the length of the cavity is determined by the prism pair, two steps were taken to minimize the prism separation. First, a shorter Ti:sapphire crystal was used, introducing less dispersion. Second, chirped mirrors were added to the cavity, adding negative chirp and thereby reducing the prism separation. This allowed us to shrink both cavity arm lengths. We also further shortened the cavity by shrinking the arm lengths while maintaining the same arm-length ratio, until the laser operation became noticeably less stable. The output coupling was also reduced to 3.5%, to compensate for a lower intracavity peak intensity.

The optimal length for the output coupling arm (L in Fig. A.1) is smaller than that predicted by Eqn. A.2. The value of this distance in the cavity demonstrated was 11.5 cm, compared with the predicted 16.5 cm. According to ray-propagation

simulations, the astigmatism is quite large (a factor of 1.5 difference between the two dimensions of the beam waist) at stable resonator values of the ABCD matrix when L = 16.5 cm. This astigmatism caused the unstable modelocking observed with this configuration. Another reason for this discrepancy is that the dispersive arm of the cavity was also altered. Had the dispersive arm of the cavity remained similar to that of the standard cavity, the prediction of Eqn. A.2 results in a stable, non-astigmatic beam in the cavity, according to the ray-propagation calculations.

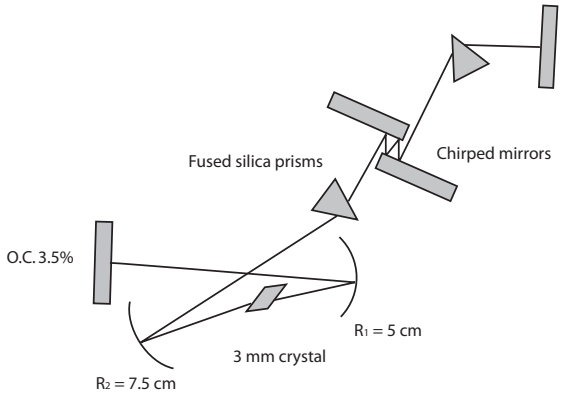

Figure A.4: Diagram of the high repetition rate cavity.

The setup for the high repetition rate laser is shown in Fig. A.4. The laser has two flat end mirrors, two flat chirped mirrors, two curved mirrors focusing into a Ti:sapphire crystal, and two prisms for intracavity dispersion compensation. The Ti:sapphire crystal is 3 mm long, doped at 0.25%. One of the end mirrors is dielectric and $> 99\%$ reflective at center wavelength 800 nm. The chirped mirrors are a dispersion compensated pair with a GVD of $\sim -60fs^2$ each, introducing a total of $\sim -480fs^2$ GVD with eight bounces round-trip. The OC is 3.5% transmissive. The curved mirrors, with ROC 7.5 cm and 5 cm, are aligned in an astigmatism compensated X configuration about the crystal. The 7.5 cm mirror was set to an astigmatism compensation angle of $7.1 \pm 1.0°$, and the 5 cm was set to an angle of $8.7 \pm 1.0°$. The Ti:sapphire crystal is pumped by 4.0 W from a frequency doubled Nd:Vanadate laser (Spectra-Physics Millennia) at 532 nm.

The pump beam is focused into the cavity with a lens of focal length 10.5 cm through the R = 7.5 cm optic. The flat side of the mirror was AR coated for 532 nm to minimize loss. The prisms are Brewster cut fused silica, at a separation of about 25 cm. The total length of the single pass cavity is ∼54.5 cm, resulting in a pulse repetition rate of 275 ± 1 MHz.

Performance

The pulse was compressed as described for the low repetition rate cavity, and the pulse duration was again measured by SHG FROG. The FROG trace was deconvolved to yield a FWHM pulse duration of 14 ± 2 fs, shown in Fig. A.5(a), limited by uncompensated third order dispersion. The transform limited pulse duration, determined by a Fourier transform of the experimental spectrum shown in Fig. A.5(b), is ∼10.3 fs. When modelocked in the standard negative dispersion regime, stable, ∼14 fs pulses were obtained at an average output power of 400 mW, with a typical power discrimination of 50 mW. At a repetition rate of 275 MHz, this corresponds to a pulse energy of about 1.5 nJ.

Modelocking is again achieved as a result of gain-aperturing. The procedure for initiating and maintaining modelocking is also nearly identical to that of a standard laser, except that the spatial mode of the output is not TEM_{00} at bandwidths greater than ∼40nm. These larger bandwidths are likely caused by single-pass self-phase modulation, which is not governed by the spatial modes of the cavity. However, stability is again limited mainly by environmental factors. The laser would persist in modelocked operation for several hours uncovered in the lab. The group of spectral peaks around 875 nm is due to unidentified cavity dynamics, but contributes only a small amount to the spectrum and does not affect the cavity perfomance. Although the spectra in Figs. A.3(b) and A.5(b) have different structure, Fourier analysis shows that they will each support a short pulse (13 fs and 10.3 fs respectively). The fact that the pulses shown in the time domain, Figs. A.3(a) and A.5(a), appear similar, is a result of the fact that the

same compression scheme, with limiting third order dispersion, was used. The shape of the pulses presented is dominated by the spectral phase rather than the shape of the spectrum. The particular shapes of the spectra are likely determined by the dispersion of the respective optics, particularly the chirped mirrors in the high repetition rate cavity, and the coating of the output couplers. The absence of multiple pulse instabilities, self Q-switching and double pulsing, was confirmed by observation of the pulse train by a fast photodiode and a spectrometer.

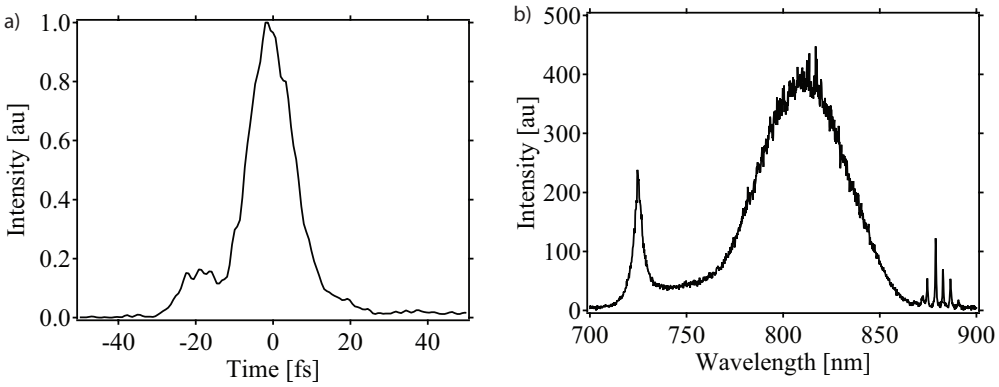

Figure A.5: (a) The deconvolved pulse width and (b) experimental spectrum for the high repetition rate laser.

We also investigated a symmetric cavity of comparable repetition rate which employs two R = 5 cm curved mirrors in place of the asymmetric pair. This cavity was observed experimentally to be unstable in modelocked operation and overall quite sensitive to alignment. ABCD matrix models confirmed this alignment sensitivity. The asymmetric cavity did not have these stability issues, and operated with generally the same stability observed in a standard 100 MHz laser.

A.5 Conclusions

In conclusion, we have demonstrated the operation of Ti:sapphire oscillators with novel geometries. By constructing cavities with asymmetric pairs of curved mirrors,

we have demonstrated a simple method of altering the repetition rate of a Ti:sapphire oscillator while maintaining the simplicity of the standard cavity.

This technique is useful especially for applications in which a repetition rate within a factor of 2-3 of the standard 80-100 MHz is needed. Only slight changes to a standard Ti:sapphire oscillator are needed to effect this result. For repetition rates outside this range, other techniques, such as cavity-dumping or chirped mirror based cavities, may be appropriate. However, the cavities described above maintain characteristics similar to a standard 100 MHz oscillator. Our results indicate that for low- and high-repetition rate asymmetric cavities, both laser geometries are stable, easy to construct and to use, and can support the generation of sub-20 fs pulses, limited only by dispersion and the onset of multiple pulse instabilities.

Appendix B

High Harmonic/ Fundamental Beamsplitter

B.1 Introduction

High-order harmonic generation (HHG) has the potential to be a unique source of coherent, ultrafast light at high photon energies. One of the technical challenges to the development of this source is the attenuation of the high-power fundamental laser beam that typically propagates colinearly with the harmonic beam. In current systems for generating high harmonics, either in guided [23, 35] or free space [10, 24] propagation, the fundamental laser beam has a necessarily high fluence, which provides the intensities required for driving the extreme nonlinear process. Pulse energies for the highest demonstrated fluxes of HHG to date [24, 151] can reach up to tens of millijoules within a duration of tens of femtoseconds. This level of power can optically damage EUV optics or samples under study, saturate sensitive detectors, or indeed interfere with a physical process due to the strength of the optical field.

Thin metal filters [152] are commonly used as a way of separating the two beams. The fundamental light is reflected, since its frequency is below that of the plasma frequency. Harmonic frequencies, on the other hand, are above the plasma frequency, allowing passbands which depend on the absorption characteristics of the given metal. However, metal filters are certainly a less than ideal solution. Filters with thicknesses of hundreds of nanometers are quite delicate, and are often not robust enough to withstand handling or the high fluence of the fundamental beam. Heat dissipation can be

a significant problem at the high vacuum ($\sim 10^{-}5$ torr) needed for EUV propagation. Oxidation of the metals over time leads to degradation of the transmission of harmonic light. Multiple filters, in combination with apertures, are required if the fundamental transmission is to be kept at a minimum, and combinations of materials can be required to achieve the necessary robustness and desired passband of photon energies. Hence thin filters can become an expensive, consumable solution for this problem. Other techniques have also been proposed and in some cases implemented successfully, including the use of an annular fundamental beam [118] which can be apertured after some propagation distance from the HHG interaction region, a dichroic beam splitter [153] for separating narrowband fundamental and lower order harmonic frequencies, and recently, a beamsplitter of Si, SiC, or Mo oriented at the Brewster angle of the fundamental frequency [154]. The major advantage of each of these techniques is their high damage threshold or lack of consumables, reducing the costs of operation.

In this appendix, I describe a new dielectric beam splitter for separating the fundamental and high-order harmonic beams. The design involves a multilayer coating which is antireflective for the broadband and powerful fundamental beam at a grazing angle of incidence, allowing the much shorter wavelength harmonic light to be reflected from the top surface. An estimate of the performance was made for 45 eV light. Compared to the transmission of two aluminum foil filters, the combination of the beamsplitter with one aluminum filter improves the efficiency by about 5x and reduces the risk of burning filters and/or samples.

B.2 Design

The particular design for this beam splitter exploits the large difference between the wavelengths of the light to be separated. The thin film structure is constructed entirely for interaction with the long wavelength light, near 800 nm, while the short wavelengths (10-40 nm) interact only with the surface layer of SiO_2. Since EUV is

strongly absorbed by bulk material, the reflectivity is not achieved through a quarter-wave or other thin film structure but through reflectivity at a grazing incidence angle from the top surface. One great advantage of this strategy is the broad nature of the reflectivity, allowing this design to be useful for a very broad range of harmonic wavelengths, limited ultimately by the absorption characteristics of the surface material. Unfortunately, since light near 800 nm is not absorbed by the materials used for this design, it is also strongly reflected at grazing incidence. Furthermore, since the fundamental light is ultrafast, its bandwidth can be very broad, exceeding 50 nm FWHM. Hence the multilayer structure must achieve the difficult combination of antireflection (AR) both for grazing incidence, and for a broad bandwidth [155]. The tradeoff then, involves minimizing the total reflected energy of the fundamental beam, made easier at low angles of incidence, while maximizing the total reflected energy of the harmonic beam, which is easier at high angles of incidence.

Under these conditions, a good balance between reasonable reflection of EUV and transmission of 800 nm was achieved at an incidence angle of 82-85° (8-5° grazing incidence). The coating was an alternating material, 10-layer design, using SiO_2 and HfO_2. Table B.1 lists the layer thicknesses for the original AR coating design. (This original design was based on previously developed broadband antireflection coatings found in Ref. [156].) The transmission curve at 85° incidence is shown in Figure B.1a in the red curve, showing a peak in transmission of ~ 0.9 near 800 nm.

A sample coating was produced by collaborators at Colorado State University using reactive ion beam sputtering with a Veeco SPECTOR IBS deposition system. Ref. [157] describes some of the capabilities of this system. Characterization of the sample's layer thicknesses was done in two ways: using a spectrophotometer and an ellipsometer. The layer thicknesses obtained from these measurements are also listed in Table B.1, along with estimated uncertainties, described in more detail below.

Characterization was essential to calibration of the deposition source as well as

Material	Design	Measured (Spectrophotometer)	Measured (Ellipsometer)
HfO_2	448.16 nm	472 ($\pm$ 5) nm	464 ($\pm$ 3) nm
SiO_2	181.49 nm	188 nm	189 nm
HfO_2	112.05 nm	117 nm	115 nm
SiO_2	181.73 nm	186 nm	185 nm
HfO_2	111.46 nm	115 nm	120 nm
SiO_2	545.87 nm	547 nm	535 nm
HfO_2	111.36 nm	115 nm	117 nm
SiO_2	545.95 nm	547 nm	540 nm
HfO_2	111.94 nm	120 nm	118 nm
SiO_2	363.48 nm	358 nm	354 nm

Table B.1: Layer thicknesses for broadband, grazing incidence, antireflection coating at 800 nm.

the efficiency of the AR coating. Several iterations led to the production of the sample described in this appendix. The optical properties are quite sensitive to variations in the thicknesses at such a large angle of incidence, requiring a significant degree of precision in the deposition. The measurement of the layer thicknesses using the spectrophotometer was performed as follows. A spectrophotometer was used to measure the transmission of the sample over a large range of wavelengths at normal incidence. This data is plotted in Figure B.1b as the violet curve. Although the design for antireflection was for a grazing incidence angle, the spectrophotometer alignment was much simpler for normal incidence, and this measurement could be easily compared with the predicted behavior of the design at normal incidence. In addition, small differences in the layer thicknesses may have a small effect at grazing incidence, but are more distinguishable at normal incidence (as can be seen above in Figure B.1). Data from the spectrophotometer measurement were used as fit criteria for determining the actual layer thicknesses using an optimization routine in TFCalc (an optical thin film design software). Once layer thicknesses were determined which matched the behavior at normal incidence (listed in Table B.1), a prediction of the transmission at 85° incidence was generated and is shown in Figure B.1a. This method of determining the sample's actual

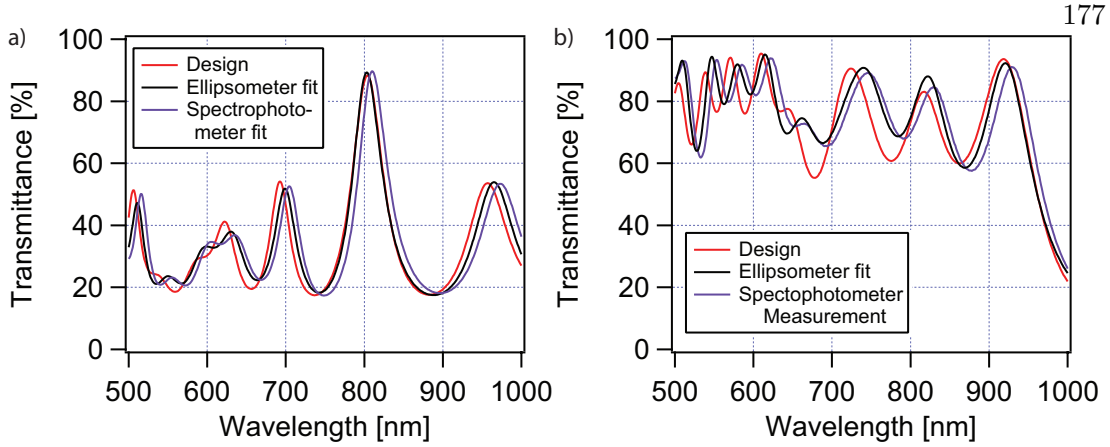

Figure B.1: Calculated transmission of the beamsplitter at 85° (a) and normal (b) incidence, including the original coating design, and the fits corresponding to spectrophotometer and ellipsometer measurement.

layer thicknesses involved uncertainty in both the fit, but also the spectrophotometer measurement, which is difficult to calibrate, since it is normally used to determine relative, rather than absolute absorption. However, the spectrophotometer measurement was less sensitive to the smoothness of the surface. This uncertainty is reflected in the estimated error for the layer thicknesses listed in Table B.1.

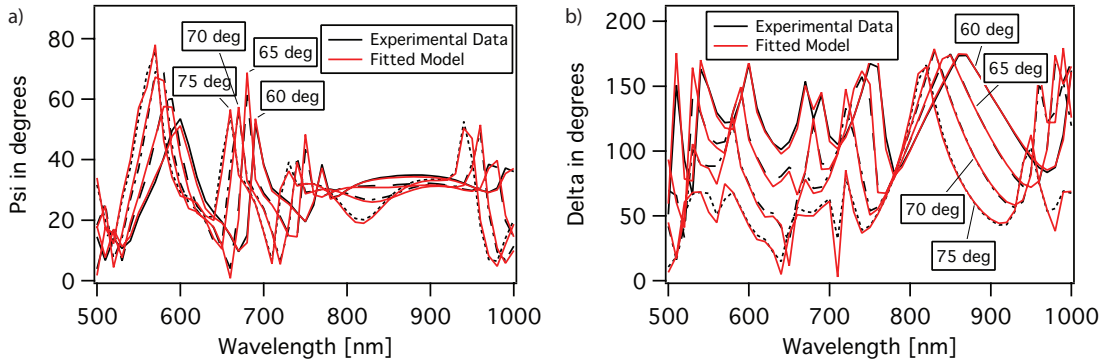

Figure B.2: Ellipsometer measurements (black curves) and fitted model calculations (red curves) for Ψ (a) and Δ (b).

A more reliable measurement of the layer thicknesses was made using a J.A.

Woollam ellipsometer. This measurement characterizes thin film coatings by comparing the reflectivities at various incidence angles of s and p polarizations. Specifically, given the quantity

$$\frac{R_p}{R_s} = \tan \Psi e^{i\Delta}, \tag{B.1}$$

where R_p and R_s are the Fresnel reflection coefficients for s and p polarizations, respectively, the ellipsometer measures the values of Ψ and Δ as a function of both specified wavelength and incidence angle. From this information, it can fit the measured data to a given coating structure to determine the specific layer thicknesses. The raw data, along with the fits produced by the accompanying software, are shown in Figure B.2. Data was collected at 60°, 65°, 70°, and 75° incidence, over the wavelength range 500-1000 nm. One aspect which proved to be significant in the correspondence of the fits and the measured layer thicknesses was the particular indices of refraction. Measurements of the indices of SiO_2 and HfO_2, provided by researchers at CSU, allowed much closer fits than those obtained with the default data provided with the software. The measured layer thicknesses and corresponding transmission curves are also presented in Table B.1 and Figure B.1, respectively. Uncertainty estimates include both the error in the fit, as well as measurement error. These error values are smaller due to the careful calibration routines performed and the closeness of the fits.

B.3 Beam Splitter Performance

The beam splitter sample was found to allow significant reflection of the EUV wavelengths from the top surface of SiO_2 at grazing incidence. Figure B.3 shows the predicted [78] reflectivity calculated assuming a thick (>100 nm), perfectly flat top layer of SiO_2. The blue curve shows the reflectivity, at 8° grazing incidence of the the sample described above in Section B.2. This measurement was performed at the Advanced Light Source by collaborators at the Lawrence Berkeley Laboratory. The measured reflectivity

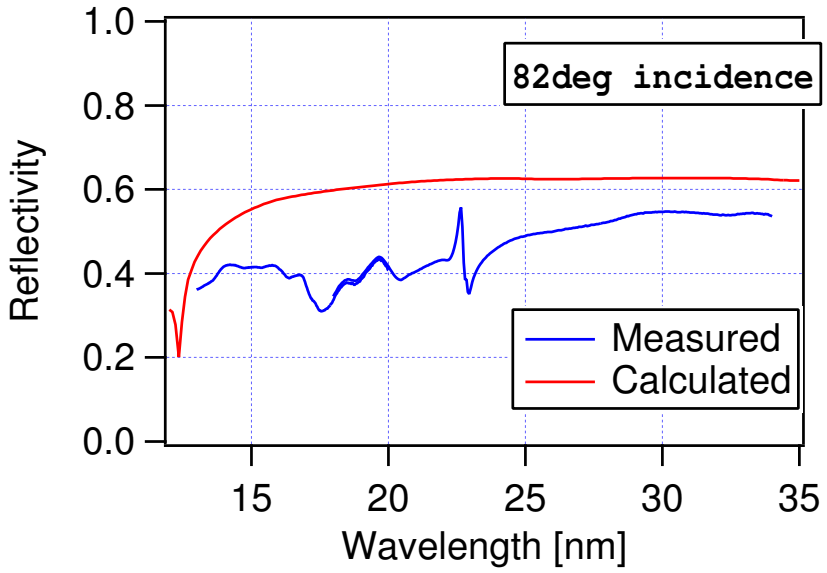

Figure B.3: Predicted (red) and measured (blue) reflectivities of the beam splitter at EUV wavelengths.

is significantly smaller than that predicted. This discrepancy is most likely due either to variations in the flatness of the surface, caused by variations in the deposition of the AR coating, or absorptive surface contamination. The surface smoothness and flatness are mostly likely the limiting factors in the ultimately achievable reflectivity of the harmonic (EUV) wavelengths. Especially at such large incidence angles, even a relatively small beam of $\sim$ 1-2 mm in diameter will reflect from a much larger area on the substrate. Further improvements could include the use of superpolished substrates, and development of the coating capabilities and performance.

After the characterization of the EUV reflectance, a study was made of the transmission of typical spectra present in the fundamental beam. In particular, since the antireflection efficiency of the coating is highly dependent on the incidence angle, it was important to determine at which angle the beam splitter should be oriented for efficient and broadband transmission of the NIR light. Because of the slight differences between the design and the produced sample coating, measurements were needed to determine

whether the AR coating was efficient at an incidence angle high enough for significant reflection of the EUV. This was also a secondary evaluation of the accuracy of the prepared AR coating sample. Figure B.4 shows the typical spectrum from a broadband

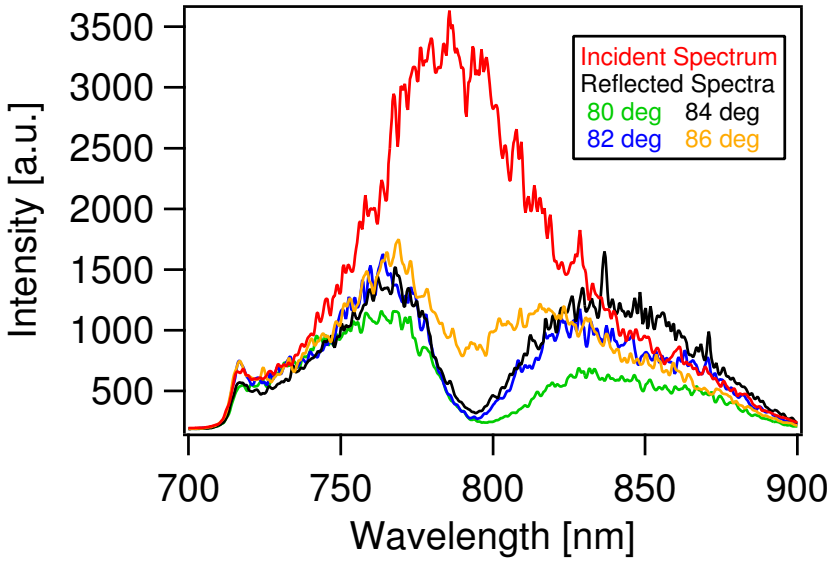

Figure B.4: Measured spectral reflectance of a typical broadband spectrum from a Ti:sapphire oscillator, for a variety of incidence angles.

Ti:sapphire oscillator along with the spectra reflected from the beam splitter sample at various angles of incidence. It is clear that the reflectance of the beam splitter far from the transmission peak increases with increasing angle of incidence, as expected. However, at the transmission peak of the AR coating, the reflectance remains low up to an angle of 84°. In fact, the integrated reflectance of the beamsplitter over 700-900 nm is ∼45% of the incident spectrum. If the spectrum is truncated to 750-830 nm, as a mimic of the bandwidth of a typical amplified spectrum, this efficiency is improved to a reflectance of ∼30% of the spectral energy.

B.4 Analysis and Conclusions

The beam splitter design presented here is a robust and useful way of reducing the transmission of high fluence 800 nm light which propagates colinearly with high harmonic generation. However, the design has certain limitations which must be considered before using the beam splitter as a replacement for the more costly method of thin metal filters. Ultimately, this design's utility will be determined by its ease of use and efficiency compared to other techniques. As an example, consider the harmonic wavelength of 30 nm (45 eV), which can be well phase matched, and is therefore used often in HHG applications. The fundamental light may be effectively rejected by two 200 nm thickness aluminum filters in series. The typical transmission of a single filter, taking into account the transmission of aluminum and aluminum oxide, is about 0.1, making the total transmission 0.01. Using a single beam splitter with an efficiency of 0.5-0.6 in combination with a single aluminum filter should also eliminate the fundamental light and increase the total efficiency by a factor of 5-6, while reducing the risk of burning the filter.

One consideration unmentioned so far is scattering of the fundamental light. Samples produced so far were coated on round substrates of 1 inch diameter, which was determined to be large enough to reflect the entire HHG beam at a reasonable distance ($\sim$50cm) from the nonlinear generation region for the optics to be mounted under vacuum. However, this aperture is significantly smaller than the width of the fundamental beam at this distance ($\sim$ 2-3 cm). Thus precautions must be taken against the scatter of light, either which does not encounter the surface of the beam splitter, or that which transmits through the beam splitter. It is likely that an optic coated on both sides, allowing transmission of the beam completely through the optic would allow easier management of the scattered light than a wedged optic.

Related to the reduction of scattered light is the engineering consideration of the

beam splitter's mounting in the vacuum line which allows propagation of the harmonic light. Takahashi et al. [154] use two Brewster-angled Si beam splitters in series, so that the harmonic light has only a lateral offset, but propagates parallel to its original direction. An advantage of this setup is that it could be aligned at atmosphere with a visible light source. However, two reflections, while reducing the fundamental light power, would not eliminate it below a factor of $\sim 10^{-2}$, and for some applications may require an additional thin metal filter. If such strong attenuation of the fundamental light is required, the transmission of the EUV may not ultimately be improved over the use of metal filters alone.

Another limitation to the beam splitter described above is the limited reflection bandwidth in the EUV. In this design, the surface layer used was SiO_2, which has an absorption resonance at 99 eV, limiting the range of efficient reflection of harmonic light. Since HHG photon energies extend well above 99 eV, variations in this design will be required to extend the reflection bandwidth. The use of this material was determined by availability of deposition materials, but other low index materials, such as ZrO_2, or other low/high index combinations of dielectrics may be considered.

Appendix C

Alignment Procedure for a Ti:Sapphire Oscillator

C.1 Introduction

This appendix contains an informal manual for alignment and operation of a Ti:sapphire oscillator of the type described in Ref. [129]: a prism-based dispersion compensation, soft-apertured, Kerr-lens modelocked (KLM) oscillator. This is the type of oscillator commonly used in our labs, and the following manual was written with the uninitiated in mind. In that spirit, the origin of different mechanisms and physical principles are not cited within. For the interested reader, there is a vast amount of literature on the operation and nonlinear optical dynamics in such lasers. As a starting point, there are the original report of KLM in Ti:sapphire [128], a review on femtosecond solid-state lasers [158], and theory of KLM [159].

C.2 Components

The efficiency and stability of a Ti:sapphire femtosecond laser are only as good as its components. It pays to use very stable optomechanics. In particular, the mounts used in the cavity are most preferably Lees, Newport Ultima, or similar quality mounts on 1" diameter posts for stability. Posts of 1/2" diameter in combination with post holders will noticeably affect the stability of modelocking and the output power of the laser, as well as beam steering. Also, stability counts in preventing misalignment from external vibrations and bumps.

The cw pump laser should have a Gaussian, TEM_{00} mode, and a wavelength near the peak of the absorption bandwidth of Ti:sapphire. Often used are frequency-doubled, diode pumped Nd:Vanadate lasers at 532 nm or flashlamp-pumped argon ion lasers operated at the 514 nm line. For pump beam steering, broadband or green dielectric mirrors are necessary. Silver coated mirrors are less efficient, and will also distort or even burn with the intensity from a 4-5 W pump laser. This affects not only the efficiency of the oscillator, but the stability of the modelocking, since this is very sensitive to the mode of the pump beam focus at the crystal.

The fused silica, Brewster angle prisms must be mounted so that they are flat on the translation stages, and that the base of the prism is parallel to the side of the translator. If this is not carefully done, the translation of the prisms will cause unwanted deflection of the beam. For a typical, "standard" cavity, the titanium-doped sapphire crystal has 0.33% doping, figure of merit (FOM) >150, and a path length of 4 mm. The amount of doping influences the intracavity power, and hence the amount of pump power needed for a given output coupling. The length of the crystal will affect the total intracavity dispersion, and hence the separation of the prisms.

All mirrors except the output coupler should have a highly reflective (>0.99), broadband coating. The reflection bandwidth and dispersion of the output coupler are often limiting factors in the achievable output bandwidth. The curved mirrors should be antireflection (AR) coated for the pump laser's wavelength on the planar side, and have a curvature of R = 10 cm on the concave side. The output coupling should be ∼12%, for a pump power of ∼4.5 - 5 W. Different amounts of output coupling will determine the appropriate pump power, and will affect the amount of average output power. In order to work stably in the "standard" configuration, the oscillator needs an approximately constant intracavity power.

Figure C.1 shows relevant parameters in the cavity, as well as the beam path of the linear resonant cavity. The light has, in a single round trip of the cavity, one bounce

each on the end mirror (EM) and output coupler (OC), and two bounces each on the two curved mirrors and the fold mirror (FM), and passes through the crystal and each of the prisms twice. These must all be considered when determining the round trip dispersion or loss.

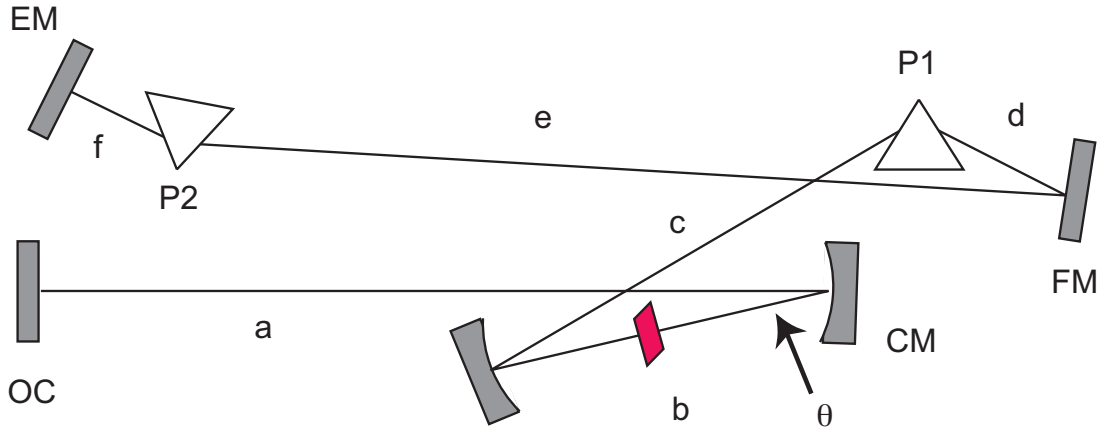

Figure C.1: Parameters of a standard Ti:sapphire laser cavity. a∼62 cm, b∼10.4 cm, θ ∼16°, c∼22 cm, total prism separation (d+e)∼62 cm, f∼5 cm Abbreviations are defined in Table C.1.

OC	Output Coupler
FM	Fold Mirror
CM	Curved Mirror
EM	End Mirror
P1	First Prism
P2	Second Prism

Table C.1: Abbreviations for cavity elements (shown in Figure C.1) used throughout the appendix.

The path lengths within the cavity are important for correct dispersion compensation and modelocking, and the reflection angles from the curved mirrors compensate the astigmatism caused by the crystal. The crystal should be mounted at Brewster angle, and this can be adjusted by eye (at low pump power) by adjusting the angle until the reflected pump beam is at minimum intensity. Incidentally, the polarization of the

pump beam must be parallel to the table for the Brewster angle of the crystal as shown in Figure C.1.

C.3 Alignment

Step 1: Align the pump beam along the rail, at low power ($\sim$ 10 mW or less). For consistency, the pump beam should be parallel to both the rail (in the horizontal plane) and the table (in the vertical plane) when there are no optics present. This may be done by removing all optics and aligning with two mirrors and two pinholes. The height of the beam may be established, if necessary, by the height of the crystal. Next, replace the green focusing lens so that the beam passes through the center of the lens, and translating the lens does not deflect the beam from the second pinhole (this is more accurately done by propagating the beam farther, if possible). Then the curved mirrors and crystal may be replaced. The beam should pass through the crystal at the focus of the lens, and roughly through the centers of the curved mirrors. There may be defects in the crystal which scatter the pump beam and therefore must be avoided. The two curved mirrors should be symmetric about the crystal, roughly 10.4 cm apart. The laser is easier to align when the curved mirror, through which the pump beam passes, is stationary and all translational adjustments are made with the other curved mirror, denoted CM in Figure C.1. For detail of the crystal and both curved mirrors, see Fig. C.2.

Step 2: The KMLabs commercial rail is designed so that the beam which propagates toward the OC should line up with the tapped-hole grid of the table. In other words, the central translational axis of the rail rests at an angle of 16° to the grid of breadboard or table. The reflection of the CM to the OC should be parallel to the grid. Use the green light to retroreflect from the OC to the CM.

Step 3: Now the pump power should be increased, with care, to 4.5 5.0 W. At this pump power, there will be a bright, reddish fluorescence propagating through the

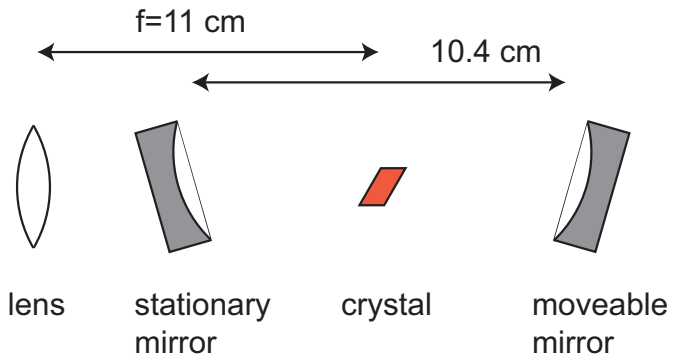

Figure C.2: Positions of optics on rail.

cavity to allow alignment for lasing. Low room lights will improve the visibility of the fluorescence. For convenience, set the prism translation stages at the middle of their scale when the maximum amount of visible fluorescence passes through. (Eventually, the prisms will be adjusted so that the beams propagate through the minimum amount of glass, to reduce total dispersion. However, this does not affect cw operation, and alignment is easiest with the greatest amount of fluorescent light propagating through the cavity.) Set P1 at minimum deviation, adjust the FM so that the incidence angle is small, then set P2 at minimum deviation. Finally, retroreflect the fluorescence spot with the EM.

Note: Minimum deviation describes the angle at which the beam both enters and leaves the prism at Brewster angle, and so passes through the material of the prism parallel to its base. Of course, this is precisely true for only one wavelength, so with a broad band of fluorescence, the spot will be slightly dispersed horizontally by the prisms. To find the proper angle, rotate the prism on its mount (preferably with the prism centered on the rotation axis) to change the propagation direction of the fluorescence through it. Rotate in one direction until the deflection of the fluorescence spot reaches a point where it stops and begins to reverse direction. This point where the movement of the propagating light changes direction is the minimum deviation angle.

Greater accuracy can be achieved by propagating the beam over a long distance ($\sim$ 1 m or more).

Step 4: If the OC is retroreflecting well, and the rail optics are close to their optimal positions, there should be a characteristic shape to the fluorescence at P1, as shown in Fig. C.3a. The diameter of the larger, diffuse red spot should be roughly the size of the prism. This is the light reflected directly from the crystal, and its size may be adjusted by the position of the crystal. The smaller, focused spot is the light reflected from the OC. It may not be in focus at P1, but this can be achieved by adjusting the translational position of the CM reflecting to the output coupler. Once this shape is seen at P1, the spatially dispersed shape to the fluorescence should be seen at P2, seen in Fig. C.3b. If this is not what the fluorescence looks like, small adjustments can be made in the translational positions of the CM and crystal.

Figure C.3: Appearance of fluorescence at P1 (a) and P2 (b).

Step 5: At this point, the retroreflected beam from the EM must be aligned to overlap with that of the OC. The two beams can be viewed with an index card at the FM between the prisms. The retroreflected beams can be viewed often only one at a time, since the index card blocks the propagating fluorescent light. If the crystal and CM can be adjusted so that the two spots of fluorescence are focused at the FM, this is much easier to do. When the beams are aligned, lasing can be initiated by small adjustments to the OC, EM, and the position of the CM. (In fact, optimum alignment for lasing often occurs for a different position of the CM than was convenient for viewing and aligning the fluorescence.) The oscillator will lase only when the mirrors

are aligned fairly accurately, and the curved optics and crystal are in approximately the correct positions. The distances between the curved mirrors and the endmirrors (a and c-f in Fig. C.1) are not as crucial for cw operation; these become more important for modelocking stability. It is helpful to make sure that the fluorescence is passing through the centers of the prisms (keep in mind that some of the fluorescence is infrared, and therefore invisible). When modelocking later, the prism insertion will likely require adjustment for optimal dispersion compensation.

Step 6: Once the laser lases, the peak power can be increased by careful alignment. One method which seems to work well for this is iterative adjustment of: the horizontal and vertical tilt of the EM and OC, then small tweaks on the CM, crystal, and lens translational positions. At 4.5 - 5.0 W of pump power, the laser should easily have an output power of about 600-700 mW, and with a very careful alignment and depending on the exact output coupling, up to 1 W. If it is difficult to achieve these output powers, it may be that the optics are backwards in their mounts, there is clipping of the intracavity beam, or that the relative distances of the rail optics are incorrect. Using a tape measure to set the positions of the rail optics should be sufficient to correct the latter problem.

Another diagnostic strategy for tweaking up the cw power is to align the green and red beams in the crystal so that there is efficient coupling between the pump beam and the red beam. To do this, look at the scatter of both beams (this works best with amber goggles intended to block 514 nm) on the surface of either of the curved mirrors. The red beam may be made more visible by adding more prism glass until the laser lases at shorter, visible wavelengths. The red beam should appear very slightly to the right of the green beam (see fig. C.4). This is because the two different wavelengths will be refracted at slightly different angles by the crystal. The exact positions of the two beams is not as important as getting the best coupling between the two modes. Alignment for highest power should correlate with this configuration, unless the red beam is clipped somewhere within the cavity. High power with significant separation

between the red and green beams, or with the red to the left of the green beam suggest that the red beam may be clipped.

Figure C.4: Appearance of the green and red beams at either of the curved mirrors for maximum coupling between the pump beam and the red beam.

For modelocking, one of the critical parameters is the distance between the CM and the crystal. In the "standard" configuration, the oscillator will lase for a range of values for this distance. When the oscillator is running well for cw operation, as described above, there will be two "stability regions" in which lasing will occur. Starting with the largest distance between the CM and the crystal at which the cavity is still lasing, and moving the CM inward, the laser will at one point stop lasing, start again as the mirror is moved further, then stop a second time. Modelocking will occur most stably when the CM has been moved to the "inside" of the "outer" stability region, or in other words, just before the first cease of lasing as the CM is moved inward toward the crystal. When the laser is aligned well in cw operation, it should have highest power when the CM is farthest from the crystal.

Step 7: Running at high output powers and aligned well for cw operation, the laser may now be slightly misaligned in a specific way to favor pulsed operation. This effect is commonly known as Kerr-Lens Modelocking (KLM), and is a passive modelocking mechanism. First, pull the prisms back so that the beam passes through their tips, taking care that the beam is no clipped, especially at the first prism. Move the CM toward the crystal until the output power is reduced to about 350 mW, or until the shape of the mode beyond the OC is elongated slightly to an oval shape (see Fig. C.5). Use only the OC and EM to tweak up the power as high as it will go. Then repeat these two steps until the power no longer increases with adjustment of the OC and EM.

Give the translation stage of one of the prisms a quick, slight push to introduce a brief fluctuation in the intensity of the beam. Sometimes a tap on one of the mirror mounts is also sufficient. Because the cavity is aligned to favor modelocked operation, a small peak in the intensity of the beam will be amplified into a pulse train by the Kerr lens effect of the crystal.

Figure C.5: Appearance of the (cw) output mode when the laser is aligned to favor modelocked operation. When in a stable modelocking configuration, the modelocked mode should collapse to a more circular shape.

Once the oscillator is modelocked, the beam should collapse into a more circular shape and will lose its characteristic cw speckle. The power may be be tweaked up by very slight adjustments to the EM and OC. Typical average powers from a "standard" modelocked oscillator are 400-500 mW. The modelocking is most stable when there is "positive discrimination" in the average output power, meaning that the power increases when the laser switches from cw to modelocked operation. For stability, the discrimination should fall within the range of 50-100 mW difference in the power. The second prism may be translated to adjust the dispersion characteristics of the cavity to facilitate modelocking. The laser will modelock stably when there is a small, net negative, linear dispersion. This is because the self-phase modulation in the Ti:sapphire crystal gives a slight positive dispersion.

C.4 Diagnostics and Common Instabilities

Intracavity Power

Stable, long-term operation of a modelocked Ti:sapphire oscillator depends on

mechanical and temperature stability. However, there are certain common problems associated with drift of the cavity alignment that can be readily diagnosed and addressed. One easy way to tell if the oscillator is close to modelocking is to look at the output with a fast photodiode and an oscilloscope, or a spectrometer. When it is close to modelocking, the oscilloscope signal should show a pulse train briefly when you tap the prism. Among the common reasons that the oscillator does not modelock is that the intracavity power is too high or too low, or that the total intracavity dispersion is incorrect. Intracavity power may be adjusted by the amount of pump power. For a 10% output coupler, 4-5 W is appropriate, for 20%, 6-7 W. Also, the peak power at the crystal increases with the amount of bandwidth, as the pulse duration is assumed to be transform-limited at the crystal.

Intracavity Dispersion

The intracavity dispersion may be adjusted by the amount of prism glass. The separation of the prisms determines the amount of negative second order dispersion; inserting more prism glass adds more positive second order dispersion. Stable, broadband operation is optimal in the so-called "negative dispersion" regime. This refers to the net amount of dispersion from the prism separation (anomalous) and prism glass and sapphire material dispersion (normal). When there is slightly more anomalous dispersion from the prisms, it can partially compress the extra frequencies generated in the crystal due to self-phase modulation. In this regime, the spectrum may be broadened by adding more prism glass into the beam path. When there is a net normal, or "positive dispersion," the output spectrum will appear truncated, and narrow with added glass.

Second order is the only adjustment with the prisms. Third order dispersion may be minimized by setting the prisms at a separation such that there is the minimum amount of prism glass in the beam path. The third order dispersion of fused silica has the opposite sign of that of sapphire, making it a good choice for the prism material. For cavities which use fused silica prisms as the sole dispersion compensation mechanism,

third order dispersion will always be the limiting factor in the number of modes which can propagate with the same round-trip time.

Despite third order dispersion, very broad bandwidths can be achievable directly from Ti:sapphire oscillators. This is often due to spectral broadening in the sapphire crystal due to the third order nonlinear effect known as self-phase modulation. For very broad spectra ($\geq$200 nm tail-to-tail), often this broadening is achieved in the final pass through the crystal, and has a characteristically poor mode quality. This is because the optical coatings are often not reflective over such a large bandwidth, and leakthrough of the visible wavelengths can be observed in this situation. Thus, there is often a tradeoff between bandwidth and mode quality. For a poorly shaped mode which is not due to this effect, corrections can often be made through adjustment of the crystal position.

Double Pulsing

Double pulsing is a common instability which occurs when there is too much intracavity power for the Kerr lensing mechanism to passively modelock the cavity stably. Symptoms of double pulsing are a large output power, a periodically modulated spectrum, or a pulse train at double the expected repetition rate of the cavity. This may most often be remedied by reducing the pump power. However, double pulsing may occur when the CM has not been moved close enough to the crystal (see step 7 on modelocking the oscillator) or is otherwise in the wrong stability region.

Spontaneous Q-switching

Self-Q switching is another common instability. This is an unstable periodic modulation on the pulse train with a period on the order of picoseconds, and is easily seen with a fast photodiode. It often appears when the prism is inserted in order to increase the bandwidth. The beam intensity may also appear to flicker. This problem may be fixed by turning the pump power up or adjusting the EM or OC. It can also be eliminated by changing the position of the CM or crystal.

CW-Breakthrough

Another power-related instability is referred to as cw-breakthrough. This occurs when the intracavity power is too high for purely modelocked operation, and an extra cw mode propagates simultaneously. This can be corrected by reduction of the pump power, or moving the CM toward the crystal slightly.